“*Unus pro omnibus, omnes pro uno*”

Using single amino acids as templates for biomineralization, and small self assembling peptides for the preparation of metal oxides, organization of metal nanoparticles and creation of new porous materials.

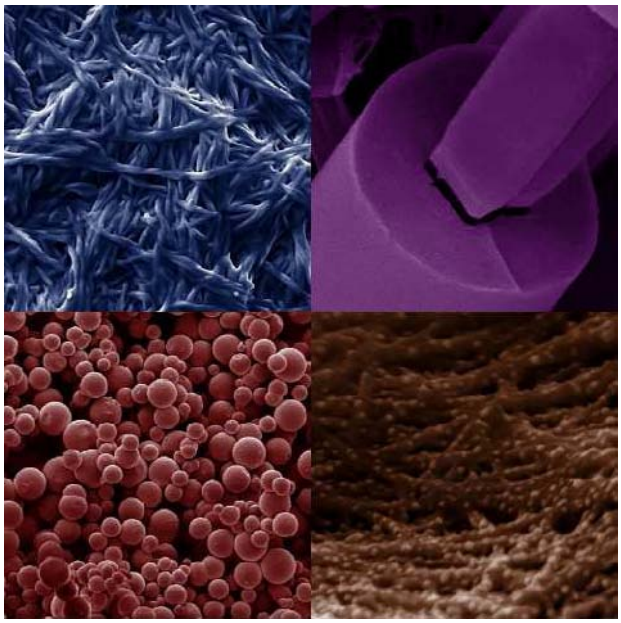

Inauguraldissertation

Zur

Erlangung der Würde eines Doktors der Philosophie

Vorgelegt der

Philosophisch-Naturwissenschaftlichen Fakultät

Der Universität Basel

Von

Alexandre MANTION

Aus Belfort, Frankreich

BASEL, 2007

UNI BASEL

Genehmigt von der Philosophisch-Naturwissenschaftlichen Fakultät auf Antrag von

Prof Dr Andreas Taubert, University of Potsdam / DE

Prof Dr Katharina Fromm, University of Fribourg / CH

Prof Dr Wolfgang Meier, University of Basel / CH

Prof Dr Catherine Housecroft, University of Basel / CH

Prof Dr Markus Meuwly, University of Basel / CH

Basel, den 20. November 2007

Prof. Dr. Hans-Peter Hauri

Dekan

Fasten your seatbelts. It's going to be a bumpy night.
Everybody has a heart. Except some people.
Bette Davis, *In All About Eve*

Attempt the impossible in order to improve your work.
If you've never been hated by your child, you've never been a parent.
I am doomed to an eternity of compulsive work. No set goal achieved satisfies. Success only breeds a new goal. The golden apple devoured has seeds. It is endless.
Bette Davis

Nowdays, If a news report does not tie up loose ends as neatly as 'The A Team', it is considered a flop.
Richard Nixon, In The Arena (1990)

Apprécier les circonstances dans chaque cas particulier, tel est donc le rôle essentiel du chef. Du fait qu'il les connaît, qu'il les mesure, qu'il les exploite, il est vainqueur ; du fait qu'il les ignore, qu'il les juge mal, qu'il les néglige, il est vaincu.
Charles de Gaulle, Le fil de l'épée

$$H(t)\,|\psi(t)\rangle = i\hbar\frac{\partial}{\partial t}\,|\psi(t)\rangle$$

The Schrödinger Equation, *Annalen der Physik*, "Quantisierung als Eigenwertproblem", (1926)

The more precise the measurement of position, the more imprecise the measurement of momentum, and vice versa. In the most extreme case, absolute precision of one variable would entail absolute imprecision regarding the other. The Uncertainty principle in "Über den anschaulichen Inhalt der quantentheoretischen Kinematik und Mechanik" in Zeitschrift für Physik, 43 (1927), Heisenberg

Where are they?
Enrico Fermi

When you are solving a problem, don't worry. Now, after you have solved the problem, then that's the time to worry.
Richard Feynmann

[The Many-worlds interpretation is the] only completely coherent approach to explaining both the contents of quantum mechanics and the appearance of the world.
Hugh Everett

$$n\lambda = 2d \cdot \sin\theta$$

Bragg's Law

Individual science fiction stories may seem as trivial as ever to the blinder critics and philosophers of today — but the core of science fiction, its essence has become crucial to our salvation, if we are to be saved at all.
The most exciting phrase to hear in science, the one that heralds new discoveries, is not 'Eureka!', but 'That's funny ...'
Isaac Asimov

Each success only buys an admission ticket to a more difficult problem.
In crises the most daring course is often safest.
Dr Henry Kissinger

Visum der Fakultätsverantwortlich

Gemäß das abgegebene Dokument „Bestimmungen über die Ablieferung der Pflichtexemplare und den Druck der Dissertation“, Februar 2006 :

„Ein Exemplar der vollständigen Fassung ist vom Fakultätsverantwortlichen visieren zu lassen und dem Dekanat gegen Bestätigung vorzuweisen.“

Basel, den _____

Prof Dr Wolfgang Meier, Universität Basel / CH

Summary

Visum der Fakultätsverantworlich 1
Summary 2
Acknowledgements 4
Impact of this work 6
Declaration of Originality 9
Summary of the PhD Thesis 10
1. Introduction 13
1.1 Proteins, peptides and amino-acids: a general introduction 14
1.2 Proteins, peptides, and amino-acids: self-assembling modalities [PPAS-1] - [PPAS-8] 16
1.3 Proteins as templates: biomineralization as a tool to prepare new functional structures 17
1.4. Low-molecular weight organogelators: preparation and properties [Gel-1] 18
1.5 Metal-Peptide Framework: a next step towards new metal-organic frameworks 20
1.6 Scope of the work 23
1.7 References 25
2. Amino acid-controlled iron oxide polymorph selection 32
2.1 Introduction 33
2.2 Experimental 34
2.3 Results 35
2.4 Discussion 45
2.5 Conclusion 49
2.6 Acknowledgement 49
2.7 References 49
2.8 Supplementary material 52
3. Concentration-induced TiO_2 sphere-tube-fiber transition in oligovaline organogels and silica structure preparation 55
3.1 Introduction 56
3.2 Experimental Section 56
3.3 Results and Discussion 62
3.3.1. Gels from the methyl esters 1a, 2a, and 3a 64
3.3.2. Gels from the free carboxylic acids 1b, 2b, and 3b. 70
3.3.3 Titania formation in the gels 73
3.3.4 Silica formation. 78
3.4 Conclusions 82
3.5 Acknowledgement 82
3.6 References 82
4. Silver nanoparticle growth controlled by modular oligovaline organogels 87
4.1 Introduction 88
4.2 Experimental 89
4.3 Results 92
4.4 Discussion 112
4.5 Conclusion 115
4.6 Acknowledgement 115
4.7 References 116
5. Metal-peptide frameworks (MPFs) – “bioinspired” metal organic frameworks 119
5.1 Introduction 120

5.2 Experimental 121
5.3 Results and discussion 125
5.4 Conclusion 142
5.4 Acknowledgements 143
5.5 References 143
5.6 Supplementary material 147
Conclusions - Outlook 156
Curriculum Vitae & Collaboration list 159
Appendix 1 Ionic liquid crystal precursors for inorganic particles: phase diagram and thermal properties of a CuCl nanoplatelet precursor 166
Appendix-1.1 Introduction 167
Appendix-1.2 Experimental Section 168
Appendix-1.3 Results and Discussion 169
Appendix-1.3 Conclusion 182
Appendix-1.4 Acknowledgement 183
Appendix-1.5 References 183

Acknowledgements

The present work has been performed in the laboratories of the „Department of Chemistry“ at the University of Basel under the supervision of Prof. Dr. Andreas Taubert. I would like to express my gratitude to have accepted me in his group. I would also like to stress the patience, freedom and suggestions Prof. Dr. Taubert has given me during my PhD time in his group. I would also like to thank the support of Prof. Dr. Taubert to start my scientific career.

I would like to thank Prof. Dr. Katharina M. Fromm for acting as a referee and her constant support for starting my scientific career, Prof. Dr. Catherine Housecroft and Prof. Dr. Edwin Constable to accept the invitation as specialists. Prof. Dr. Wolfgang Meier is acknowledged for his role as Faculty delegate in the examination board and Prof. Dr. Markus Meuwly for chairing the PhD examining board.

I would like to thank all the members of the collaborative network I started: Dr. Markus Neuburger (Uni Basel), Dr. Lynne McCusker (ETHZ D-MATL), Dr. Lars Massüger (ETHZ D-MATL), Dr. Pierre Rabu (ICPMS), Dr. Annette Foelske (PSI), Dr. Bernd Schmidt (PSI), Dr. Fabia Gozzo (PSI), Dr. Cornelia Palivan (Uni Basel), Yvonne Gerber, Prof. Dr. Willem-B. Stern (Uni Basel), Dr. Alexandre Tarantola (Uni Bern), Monika Painsi (Uni Bern), Prof. Dr. Larry Diamond (Uni Bern), Francisca Schmitt (Uni Basel), Prof. Dr. Markus Meuwly (Uni Basel) and Prof. Dr. Thomas Bürgi (Uni Neuchatel) and Dr. Ovidiu Ersen (IPCMS). Access to analytical tools belonging to Prof. Dr. J. Wirz, Prof. Dr. Katharina M. Fromm, Prof. Dr. Catherine Housecroft, and Prof. Dr. Edwin Constable is warmly acknowledged. The time they gave me for general and scientific discussions, as continuously supporting my scientific career is greatly thanked.

I would also like to thank the technicians of the Zentrum für Microscopy at the University of Basel (Daniel Mathys, Marcel Düggelin, Vesna Olivieri, and Gianni Morson), Werner Kirsch for the elemental analysis and Dr. Heinz Nadig for MS Measurements.

My thanks also go to Daniela Tischhauser and Esther Stalder for their help and support in solving administrative problems.

I would like to thank some of my colleagues: Dr. Adeline Robin, for her strong personality, sense of dramatization and capacity to collect and summarize any sort of information, Laurent Mirolo for his support in measurements and dedication to make the diffractometer working, Tünde Vig for her funny conversation and Dr. Rémi Bergougnant for discussions and his ability to generate any kind of surrealistic conditions at free will. I also thank Lucy Kind simply for her fun and to have given me some times the occasion to escape of my projects, Rainer Nehring for sharing some rigoristic but fair consideration of chemistry teaching in Praktikum, Dr. Caroline Fraysse for his sense of humor, ability to give his fun and useful discussions. I would also to stress the role of Dr. Alessandro Napoli, Dr. Susana Moreno and Dr. Violeta Malinova for useful comments and discussions.

I would like to thank my family for its *important and capital* support, my parents Gilbert and Marie-Marthe and my sisters Maryline, Ingrid, and Elodie. More specifically I would like to thank Maryline for her *indefectible* support all along my University curriculum. Corinne, Patricia, Chantal, Odile, and others are acknowledged for the fun I had with them in the public transportation system. Régine Herrmann is thanked for her help before I started my PhD and to have given me taste to study Science.

The Swiss National Foundation, the NCCR Nanosciences,
the University of Potsdam,
and the Max-Planck-Institut of Colloids and Interfaces
are acknowledged for financial support.

Impact of this work

- ***Peer-reviewed articles:***

Ionic Liquid Crystal Precursors for Inorganic Particles: Phase Diagram and Thermal Properties of a CuCl Nanoplatelet Precursor.
Andreas Taubert, Pascal Steiner and Alexandre Mantion, *J. Phys. Chem. B*, *2005*, 109 (32), 15542 – 15547.

Concentration-induced TiO2 sphere-tube-fiber transition in oligovaline organogels
Alexandre Mantion and Andreas Taubert
Macromolecular Bioscience (Special Issue on Bioinspired Materials for the Chemical Industry), *2007*, 7, 208.

Amino acid-controlled iron oxide polymorph selection
Alexandre Mantion, Fabia Gozzo, Bernd Schmitt, Willem B. Stern, Yvonne Gerber, Adeline Y. Robin, Katharina M. Fromm, Monika Painsi, and Andreas Taubert
J. Chem. Phys. C., to be accepted after minor revisions

Silver nanoparticle growth controlled by modular oligovaline organogels
Alexandre Mantion, Annette Foelske, Laurent Mirolo, Katharina M. Fromm, Monika Painsi, and Andreas Taubert
Soft Matters, to be accepted after minor revisions

Metal peptides frameworks : new peptide based chiral equivalent to MOF's
Alexandre Mantion, Cornelia Palivan, Pierre Rabu, Lars Massuger, Lynne MacCusker and Andreas Taubert
J. Am. Chem. Soc., accepted

- ***Oral presentations:***

X-Ray Diffraction and Raman Microscopy: Complementary Tools for Iron Oxide Biomineralization studies Alexandre Mantion, Andreas Taubert
Scholarship from The German Chemical Society obtained to present this talk
GDCh JCF Frühjahrsymposium 2005
07-09/04/05 Humboldt-Universität zu Berlin, Institut für Chemie, Berlin/D

Amino acids: Bioinspired templating agent for iron oxyde and hydroxide templating
Alexandre Mantion, Andreas Taubert
SFC Eurochem 2005
28-1/08/05, Nancy/F

Bioinspired iron oxide synthesis
Alexandre Mantion, Andreas Taubert
European Congress of Young Chemists, Youngchem 2005
12-16/10/05 Rydzyna/PL

Peptide-based low molecular weight organogelators and their transcription in inorganic materials
Alexandre Mantion, Andreas Taubert
EMPA PhD Day 2006
19/10/06 St Gallen/CH

- ***Poster presentations:***

From rust to magnet: Nature triggers structures of iron oxide
Alexandre Mantion, Andreas Taubert
Informal Discussion Workshop “Growth Control”
09-10/09/04 Faculté Science et Techniques, Mulhouse/F

Bioinspired Iron Oxide Synthesis

Alexandre Mantion, Andreas Taubert

NRP 47 Summer school - 11-15/04/05 Löwenberg center, Murten/CH

Self assembling peptides as new inorganic materials templates

Alexandre Mantion, Andreas Taubert

BASF Symposium on Bioinspired Materials - 07-08/08/06 Strasbourg/F

A simple model for iron oxide biomineralization - synchrotron X-ray scattering analysis of iron oxide precipitated in the presence of amino acids

Alexandre Mantion, Andreas Taubert

7th Swiss Light Source Users' Meeting - 28-29/09/06 Paul Scherrer Institute, Villingen/CH

Self assembling small peptides and their use to prepare new materials

Alexandre Mantion, Andreas Taubert

Swiss Chemical Society - Fall Meeting - 13/10/2006 Irchel Campus, Zurich/CH

Declaration of Originality

I declare that I wrote this thesis

"*Unus pro omnibus, omnes pro uno*"
Using single amino acids as templates for biomineralization, and small self assembling peptides for the preparation of metal oxides, organization of metal nanoparticles and creation of new porous materials.

with the help indicated and only handed it in to the Faculty of Science of the

University of Basel and to no other faculty and no other university.

Alexandre MANTION

Basel, 24/08/2007

Summary of the PhD Thesis

Introduction

General concepts involved in the scope of this PhD Thesis are briefly presented.

Part I: Bioinspired iron oxide mineralization

Using single amino acids may be thought an over-simplification of larger proteins or peptides. However, their use as model system already enables the understanding of some crystalline phase selection processes. Some general rules about iron oxide biomineralization in the presence of amino acids and thus, as an extension, in the presence of proteins are drawn out of this study.

Part II: Small self assembling peptides and the transcription of their chiral information into inorganic materials

Small self assembling peptides can be tuned to self assemble in organogels. The 3D organogel self-organization scheme can be transcribed into inorganic materials using processes involving metal alkoxide (sol-gel) technologies. The peptide synthesis and the self-assembling motives, material synthesis (silica and anatase based materials) and characterization are described in this part.

Part III: Using organogels to synthetize nanoparticles and to orient them on a peptide fiber

Organogels prepared from two chemically and structurally similar peptides can be mixed to prepare a homogenous 3D network which will present on its surface complexing properties depending on the structure of the peptides chosen. This scaffold could be used to organize nanoparticles or to prepare silver-based nanostructures. Peptides involved, their self assembling schemes, the structures created and rationalization of this approach will be presented in this part.

Part IV: Using small self assembling peptides to create new porous materials

The preparation of metal-organic frameworks using a slightly modified version of the model peptide which was used througout the PhD Thesis is possible. We present here the synthesis and spectroscopic and crystallographic characterization of the materials obtained.

Conclusions

In this section the achievements realized during the PhD will be discussed. Some new tracks to further exploit these systems will also be introduced.

1. Introduction

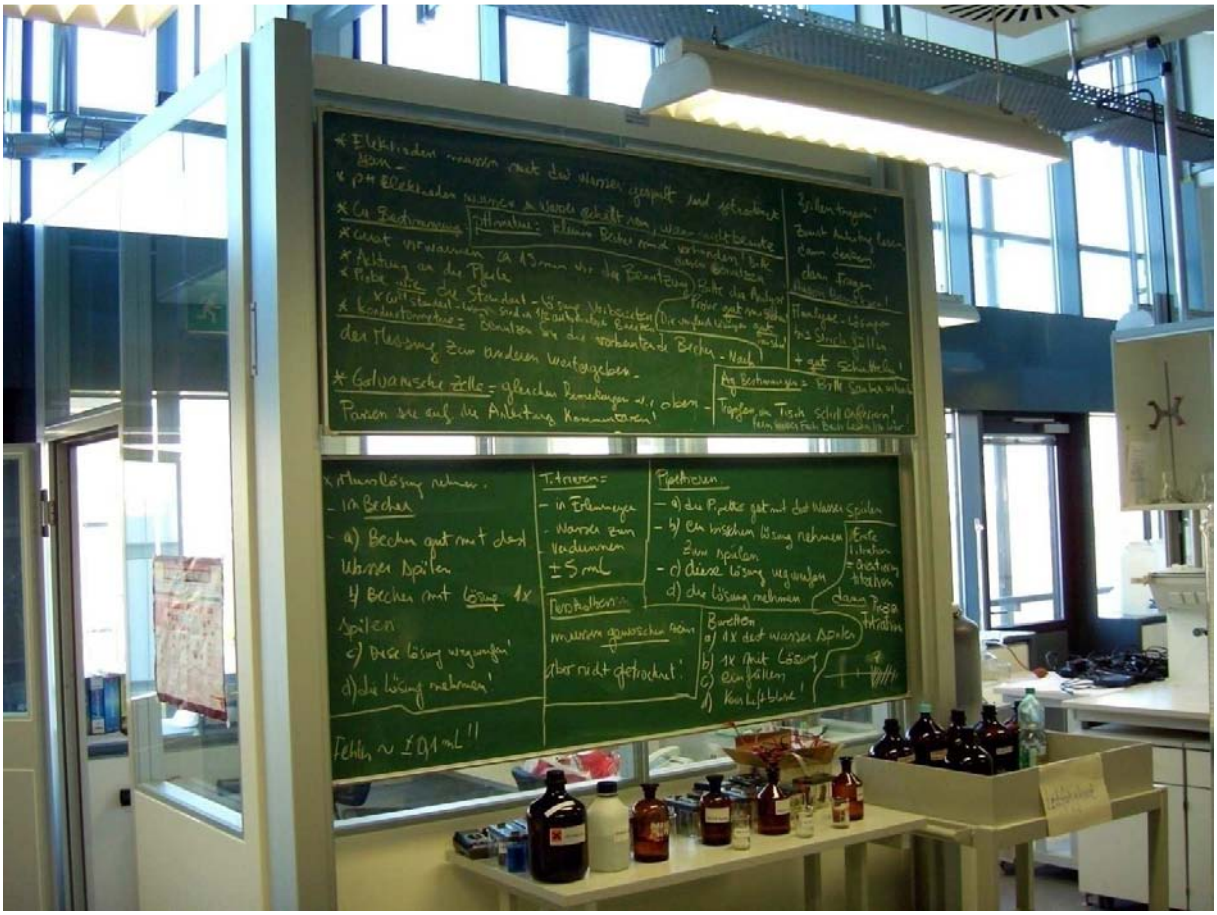

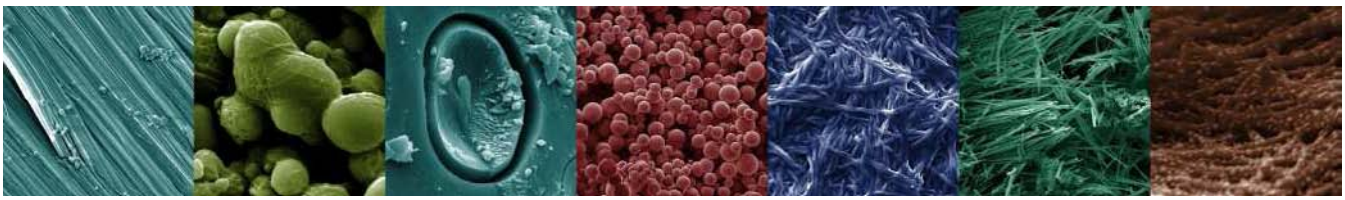

1.1 Proteins, peptides and amino-acids: a general introduction

Proteins are highly evolved structures ubiquitious in the living reign. An example of a protein is given in figure 1. Proteins, based on precisely tuned defined sequences of amino-acids are the basis of life. They are involved in catalysis, can have mechanical functions like actin and myosin in muscles, or involved in the skeleton of cells. Others are involved into signaling or immune response, to give only some examples.

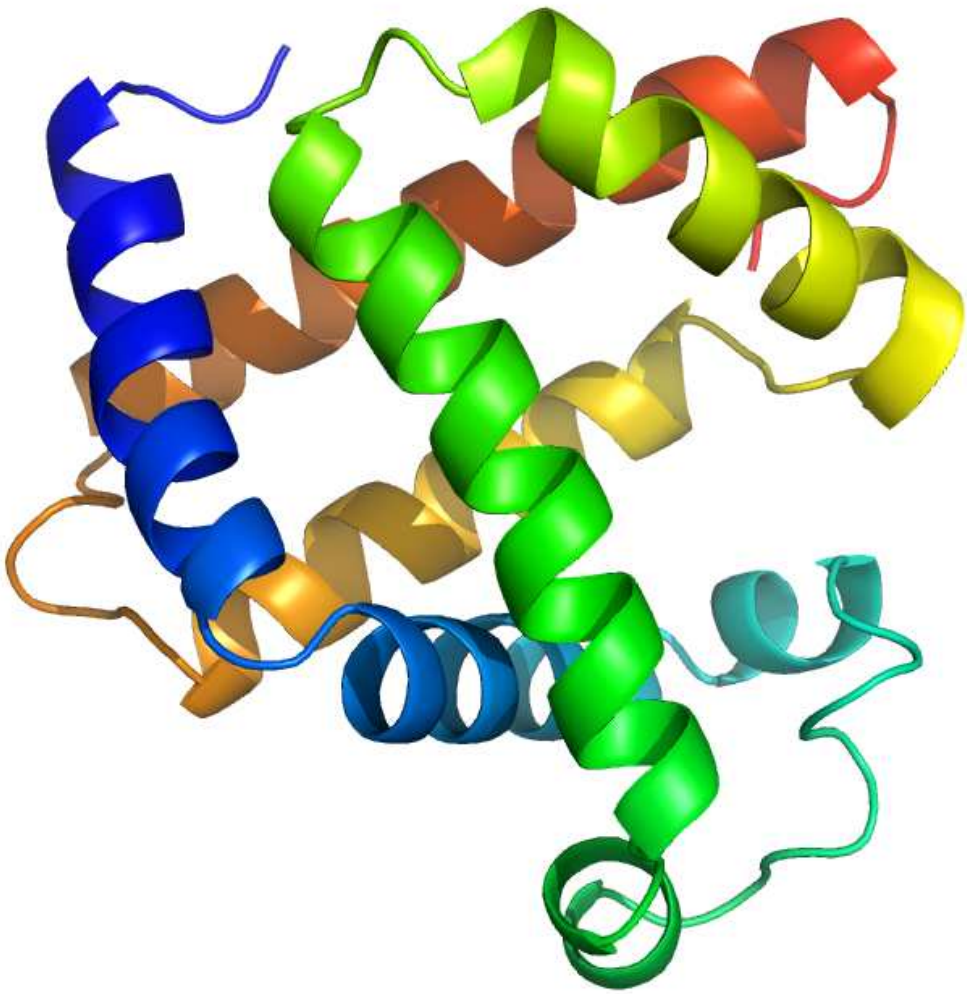

Figure 1: Structure of oxymyoglobin at 1.6 angstroms resolution (PDB reference: 1MBO, rendered with Pymol [PPA-1]) [PPA-2]. The heme was not represented for simplicity.

Proteins are polymers prepared from the 20 different L-amino acids. The amino acids are composed around a common scaffold: an amino group, a carboxyl group, and a residue.

They are connected to a Cα carbon, which is chiral (except for glycine). According to the Cahn-Ingold-Prelod rule the naturals amino acids are S for except for glycine (only H as residue) or L-cysteine (because of the sulfur) which is R. L-proline is different, because of the special spatial requirement imposed by the structure of this amino acid. A table summarizing the different amino acids is given figure 2.

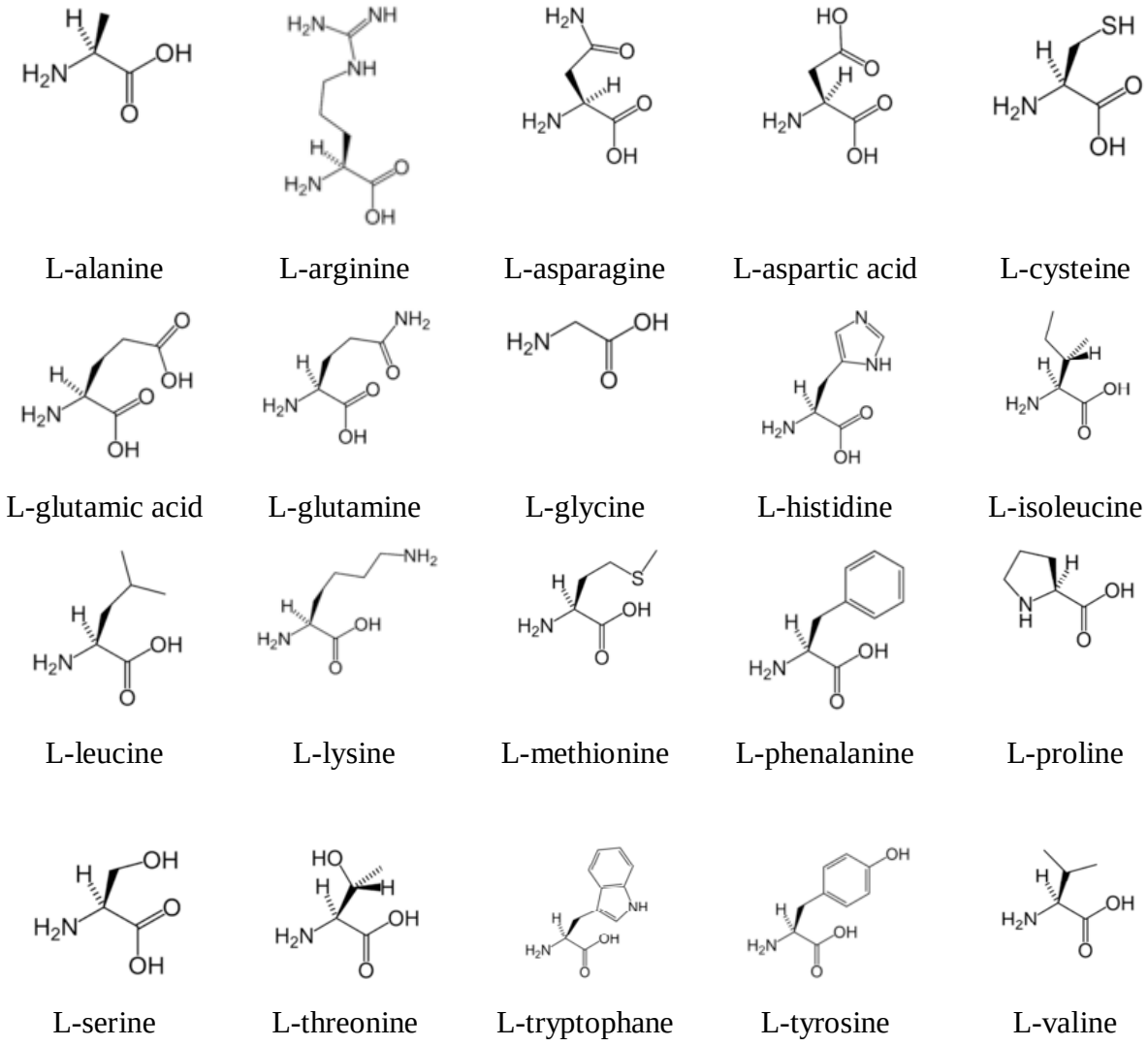

Figure 2: Natural amino-acids

All amino acids in a protein are connected by peptide bonds, formally formed by a dehydration of the carboxylic acid with an amine nitrogen, as depicted figure 3. Because of the way the protein is created, one protein end has a free carboxylic group; this end is called C-terminus. The second end will be terminated with an amine and is called N-terminus. Electronically, the peptide bond can exist in two mesomeres forms and thus are coplanar.

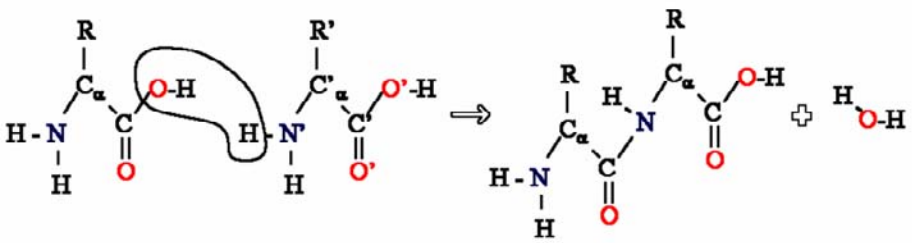

Figure 3: Peptide synthesis

There is no clear limit in size between the notions of protein, polypeptide, and peptide. Proteins refer to the complete self-organized and functional structure, but peptide refers to a small excerpt of this protein but sometimes without a stable 3D structure. There are also proteins without a stable 3D structure. Polypeptides refer to a single linear chain irrespective to size and there may be several conformations for this polypeptide sequence.

1.2 Proteins, peptides, and amino-acids: self-assembling modalities [PPAS-1] - [PPAS-8]

The polypeptide may fold in various conformations, which could be sorted in four different classes, depending on the scale choosen to describe the self assembly motif. The primary structure is composed of the amino-acid sequence. The secondary structure is composed for repeating units of (very commonly) alpha helices and beta sheets self assembling under the influence of hydrogen bonding. The tertiary structure describes the overall shape of a single protein molecule. The overall shape can be controlled by hydrophobic interaction, salt bridges, hydrogen bonds, disulfide bonds. The quaternary structure is the shape obtained by the interactions of many proteins (which can be seen as protein subunits) leading to protein aggregates and complex structures.

The major leading to structure in organogels is the β sheet pattern. Discovered by William Astbury (around 1930) [PPAS-6] – [PPAS-8], the β sheet structure was refined by Linus Pauling and Robert Corey in 1951 [PPAS-2]. A β sheet structure forms via hydrogen bonding through the peptide bonds of parallel or antiparallel extended β strands (with respect to their relative directionality) and forms a twisted, pleated sheet. A β strand is constituted by a strech of amino acids (from 5 to 10) with amino acids fully extended. A β sheet presents two

extreme variations: antiparallel β sheet (figure 4) and parallel β sheet (figure 5) and could also present a mixed structure of alternating antiparallel-parallel strands. Besides the respective directionalities of the strands, there is a clear modification of the hydrogen bonding pattern. Figure 4 and 5 shows the different types of β sheets and for comparison, a α helix is displayed on figure 6.

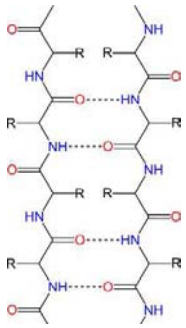

Figure 4: General structure of antiparallel β sheet

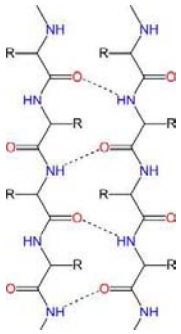

Figure 5: General structure of parallel β sheet

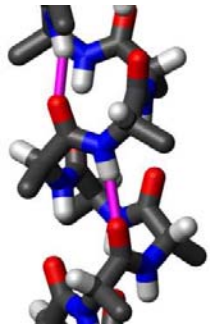

Figure 6: Comparison with an α helix

1.3 Proteins as templates: biomineralization as a tool to prepare new functional structures

Biomineralization [Bio-1], [Bio-2] is the synthesis of poorly soluble minerals from simple compounds by organisms. Biomineralization is an increasingly important domain interested in understanding what are the forces and mechanisms leading to the selectivity of organisms towards the synthesis of inorganic materials, sometimes against the thermodynamic relative stability of the materials. Biominerals are functional materials: they are bones or act as passive mechanical protection *via* shells (any exoskeleton) using calcium carbonate. They also help magnetotactic bacteria or pigeons to orient using magnetite particles [Bio-3], act as storage of iron in ferritin in living organisms [Bio-4], or as a part of mechanically robust instruments or weapons (teeth). Examples of biominerals are silicates in algae, carbonates in diatoms and invertebrates, calcium carbonates and phosphates in mammals and birds, iron oxides in limpets [Bio-5] and birds [Bio-3], strontium and barium sulfates in unicellular plancton, or even metals in bacterias [Bio-6], [Bio-7].

Modern material science is concerned by these bio-inspired materials not only because of academic interest but also because of their very interesting properties for industrial or biomedical applications. Namely, these hybrid materials will exhibit properties of hardness and mechanical stress resistance conferred by the inorganic part and elasticity and tensile strength given by the organic part (collagen, glycoproteins, and polysaccharides). But the organic part also plays an important role in the phase selection, morphology, and other parameters controlled by a template. [Bio-9]-[Bio-15]

1.4. Low-molecular weight organogelators: preparation and properties [Gel-1]

An organogel is a thermally-reversible viscoelastic liquid-like or solid-like material based on a organic liquid and low concentration (usually under 2 weight%) of low molecular weight molecules (the gelators). An example of organogel prepared in our group is displayed figure 7. There are also hydrogels, where water is used in place of organic solvent. The physical properties of organogels range from surfactant in solution [Gel-2] or polymers [Gel-3] and are at the limit between complex fluids [gel-4] and phase separated materials. The thermoresponsive nature is based on the fact that the supramolecular architecture can be melted and individual molecules (or separated strands of aggregated molecules) can be redispersed in the bulk solution. Organogels can be used as templates for new materials preparation, drug delivery, cosmetics, metallurgy, and food processing.

Figure 7: Example of an organogel. Left vial: n-butanol without gelator; Right vial: n-butanol gel with ZVVVOMe (20 mg/mL solvent) as gelator

There is no simple definition of a gel [Gel-5]-[Gel-8]. A substance is considered a gel if it is solid-like in its rheological properties and if has a continuous structure in a macroscopic range and the structure is stable during the analytical determination. Factors affecting the aggregation process are relevant for describing the gelation phenomenon. They include the solvent nature, the polarity, conformational lability, and molecular shape of the gelator, the temperature, and the possible participation of cosurfactants [Gel-9]-[Gel-11]. Some structural and kinetic aspects of the aggregation/gelation process are also consistent with the gelation process being viewed as a phase separation involving a nucleation reaction, thus emphasizing the role of the interfacial free energy of the gelators.

Morphology, consistency, or chemical and mechanistic considerations can be used to describe the macroscopic recognition of a gel state, although this is under debate [Gel-12]-[Gel-14]. Rheological properties appear to be the best diagnostics to follow the changes in gelator aggregation during the sol-to-gel and gel-to-sol (melting) phase transitions [Gel-15].They can be described by statistical physics. In particular, percolation models [Gel-16]-[Gel-17] can simulate the mechanical behavior near the critical gelation threshold. Physical properties of organogels are dependent upon the nature of their networks. The two network types are i) "strong" gels with permanent solid-like networks in which the nodes are spatially extended (pseudo)crystalline microdomains, and ii) "weak" gels with transient networks exhibiting no elasticity over long time periods in which the nodes are entanglements or spatially limited organized microdomains.

An organogel is very easily prepared. The organogelator is mixed with a solvent, the mixture is then heated until the solid is dissolved and slow cooling of the solution to below the gelation temperature, temperature at which the liquid does not flow anymore. The resulting material is described as a gel or “jelly-like” depending on the rheological properties of the material. The colloidal aggregates (of size 20 to 2000 Å) are linked together in a 3D network, which immobilizes the liquid component by principally surface tension.

Rodlike assemblies are the most efficient way to immobilize a large mount of solvent using the minimum amount of organogelator. The structure of the linear aggregates is determined by the direction and strength of the binding forces associated with the aggregation process. As the organogels form in organic solvents, hydrophobic interactions are not enough

to ensure aggregation [Gel-18]. Much rather, the interactions are dipolar and, possibly, specific intermolecular hydrogen bonds, π–π stacking or metal-coordination bonds [Gel-9]-[Gel-11]. Their intensity must balance the free energy increase that accompanies reductions in translational and rotational freedom of motion.

There are a large amount of organogelator classes: fatty acid derivatives, steroid derivatives, anthryl derivatives, steroidal and condensed aromatic rings, azobenzene steroid-based, amino acid based organogelators, organometallic compounds, and sorbitols. Other, more complex systems are based on multi-component systems, for a review see ref [Gel-1].

1.5 Metal-Peptide Framework: a next step towards new metal-organic frameworks

Metal organic frameworks (MOFs) are among the most promising materials for applications requiring on porous structures [MPF-1]-[MPF-3]. They are constructed from relatively simple organic building blocks (which are connectors) and transition metals or lanthanides (which are the connecting points). They can be defined as porous inorganic polymers [MPF-4]. An illustration of a MOF is displayed figure 8. Contrary to zeolithes and mesoporous materials, which have a purely crystalline inorganic structure, MOF's are highly crystalline organic-inorganic hybrids. These structures are synthesized using a broad variety of methods from hydrothermal to simple diffusion methods.

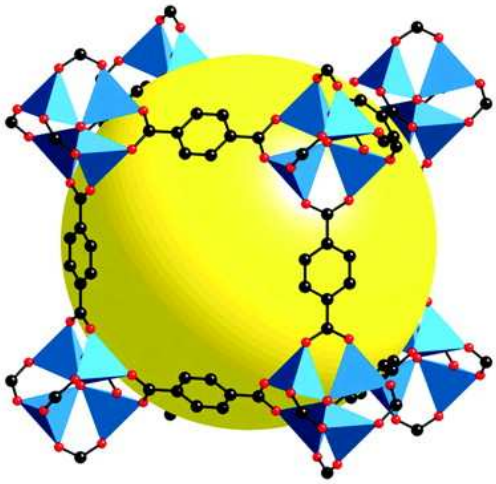

Figure 8: MOF-5 as designed by Yaghi [MPF-6] Yellow ball is void.

Despite their organic-inorganic hybrid nature, MOF's are extremely robust and have valuable properties like high gas sorption [MPF-5], filtration [MPF-6], optical [MPF-7] and magnetical [MPF-8] properties. Currently, some MOF's are under investigation for large scale applications: hydrogen car fuel storage or combustible gases like methane [MPF-9]. Other MOF's can be used as small nanocontainers able to release their inner content for biological applications.[MPF-10]

The molecular control over arrangement and inter-metal distances is one of the major advantages of this family of materials. The rationalization of the geometries prepared from these simple di-, tri-, or higher range complexing molecules (examples are given figure 9) with metals has allowed for the elaboration of rules for topologies selection and modelizing of the self-assembly behaviour of these units and is known as reticular grammar [MPF-5]-[MPF-8]. The usual connectors under investigation can very often be viewed as linear rods, triangles or cubes. This, in conjunction with the connectivity given by the metal, gives the whole range of structure theoretically predictable. However, the majority of the considered ligands are rigid and there are quite limited investigations on flexible and self-assembling connectors. Small peptides or peptidomimetic units have not been studied to date.

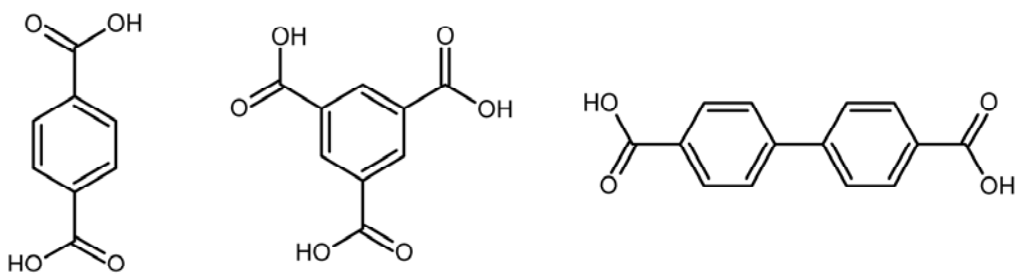

Figure 9: Example of ligands for MOFs synthesis

The connection between the metal centers and the connectors are generally performed through carboxylate moieties [MPF-15], less often through amine functionalities [MPF-16] or both [MPF-17]. Carboxylate-metal bonds are ideal for the preparation of materials because of the bond strength [MPF-18], conferring thermal (comparable to covalent systems) and chemical stability to the MOF's. Interestingly, the carboxylate moiety can transfer magnetization over long distances, making this functionality also interesting for the preparation of magnetic substances without incorporation of counter-ion in the structure

[MPF-4]. Careful control of the pH in the synthesis conditions allows the fine tuning of the ligation properties. Finally, carboxylate groups can bind metals through a wide range of possibilities: monodentate, bidendate, or bridging the metals centers, which broadens the range of possible structures ever known.

The metal plays a dual role: it has a major influence on the structural connectivity of the assembly [MPF-14] but also confers magnetic or optical properties to the material. Lanthanides [MPF-19] will allow the preparation of optically active materials with tunable optical emittive properties, pressure-sensitive materials using Samarium (III) or magnetic materials using high spin compounds like Gadolinium (III). However, the complexing modes of these metals are difficult to predict, as they have coordination numbers of up to 9. The rational design of structures is made more difficult but in turn allows for a topological diversity with new functionalities. In contrast to 4f elements, 3d metals as connectors allow for a better control of the whole structure and predictability [MPF-4].

There is a growing interest in the field of chiral MOF's [MPF-19]-[MPF-23], [MPF-26]. Chiral MOF's find a very important audience in the scientific community because of their application as asymmetric catalysts, in chiral recognition and non-centrosymmetric phenomena, and a more fundamental level for the preparation of new topologies. Essentially, there are mostly three different ways to prepare chiral MOF's: using a system which will self-resolve [MPF-24], a chiral co-ligand [MPF-20], and a chiral ligand [MPF-25]-[MPF-26]. The chiral ligand approach is preferred by the community because of its viability, see [MPF-20]-[MPF-25]. Indeed, the intrinsic chiral information is entirely transferred to the structured material, because the ligand is part of the structure. This contrasts zeolithes and mesoporous materials where the chiral information has to be transfered from a chiral template on very long range crystalline structure. However, and interestingly, there have been no peptides or peptidomimetics used in MOFs so far, despite their self assembling properties and their chiral information, which would make them of first interest for many applications.

Only a few 1D (linear), 2D (plane), and 3D (space) arrangements prepared from amino acids and metal ions are described in the literature. Examples of 3D networks can be found with L-glutamic acid and cobalt (II) [MPF-27], 1D single helical structures with L-glutamic acid and copper (II) [MPF-28], homochiral chains with L-asparagine and zinc phosphite

[MPF-29], 1D helical chains with L-aspartic acid and nickel (II) [MPF-29], 3D structures with l-histidine and zinc phosphite [MPF-31], chains and sheets with imidazole and zinc phosphate [MPF-32], 1D helices with L-arginine (with bpy) and copper (II) [MPF-33]. Lanthanide complexes linked through amino acids were also investigated [MPF-34]-[MPF-35].

Adipic acid, although not an amino acid itself, can in a sense be compared to L-glutamic acid, adipic acid being one carbon longer as L-glutamic acid. Cahill et al [MPF-36]-[MPF-38], [MPF-47] (and other groups [MPF-39]-[MPF-48]) have studied the structures obtained from adipic acid (1,6-hexanedioic acid), auxiliary bases (templating agent) and Ca^{2+}, lanthanides or 3d transition metals. Porous structures with various topologies were prepared either for their optical or structural properties.

1.6 Scope of the work

Peptides and peptidomimetics constitute the next step after extensive investigations of polymers and surfactants for materials templating and hybrid materials preparation. This constitutes a new challenge to be taken. Proteins are the only tool of Nature to control shape, functionality, and structure selectivity in living systems. Because of their ubiquitous presence in living organisms, the fact that the proteins can be codded (and modified) trough genetics and for the important potential industrial applications, it is of interest to either study the full proteins or small replicas of larger proteins for potential applications in Material Science.

One point where proteins can be used and should be investigated as templates is the biomineralization field. We decided to study the iron oxide biomineralization, because of the potential and innovation rich area which may arise from our studies, especially for the creation of magnetic materials. Because there is no extensive study of the effects of the amino acid on the precipitation of iron oxides, we decided to investigate this point first to help for the further design of more complex peptide (or protein) templates for iron oxide material preparation. This study involves Rietveld refinement, size-strain analysis, TGA (thermogravimmetric analysis), Raman Spectroscopy and microscopies (transmission electron microscopy, scanning electron microscopy).

The next point is the preparation of inorganic structures from organogels. Structural information of organogels can be transferred into inorganic materials. We decided to synthesize L-valine based materials, because of the chiral information present in these systems, the fact that the proteins can self assemble in gel-like structures and because of the ubiquitous presence of L-valine (beside L-alanine and hydrophobic amino acids) in proteins. The inorganic materials prepared are silica structures and anatase, because of the interest to prepare nano-objects from these materials, as catalysts.

Unlike in biomineralization, the structural information is transcripted using sol-gel chemistry processes via metal alkoxides technology. The metal alkoxide is slowly hydrolized by air moisture and not by more biologically inspired conditions. A next step which is not present in the biomineralization process is the calcination of the structure to remove the organic embedded part and to finish the reticulation process of the inorganic material, generally an inorganic metal oxide. Motivation to investigate these small-self assembling peptides as templates are their availability, low price, and structural models for more complex structures and robustness when compared to other systems of higher complexity. This study involved the synthesis of small peptides and characterization of their self assembling scheme, preparation of inorganic structures based on titanium dioxide or silica based materials. Techniques used are Rietveld refinement, small peptides synthesis in solution, IR spectroscopy, TGA and various microscopies.

After having successfully converted the structural information of the L-valine based small peptides into inorganic materials, we decided to investigate the possibility to prepare self-organized nanoparticles around peptidic fibers. Besides the interest in having methodologies to synthesize silver nanoparticles or metal-based nanostructures using peptides for both industrial and academic reasons, the formation of complex structures from two peptides by co-assembly has not been studied often. Creating complex structures from simple systems constitutes a motivating challenge and in this part we propose to investigate the mixture of a non functionalized self-assembling peptide with a functionalized self-assembling peptide to see if the mixture is homogenous or segregates. Silver nano-objects are interesting as they present original optical properties and they can be used as antiseptic additives in plasters to give only two examples.

After mineralization of the fiber in a gel with silver using DMF as a reductant, we were able to generate various silver-based structures from silver nanoparticles to silver triangles or hexagons. Understanding self-assembly and silver growth is a first step to understand artificial systems when peptides are involved in the synthesis of nano-metallic structures. After the synthesis of sulfur-based peptides, which is based on the already developed methodology in the previous section, the synthesis of the metal-based hybrid was performed by the *in situ* reduction of silver(I) using DMF. Characterization of the structures was performed using X-Rays diffraction, X-Ray photoelectron spectroscopy, Raman (incl SERS), UV-Vis, IR spectroscopy and NMR.

The last part of this manuscript is dedicated to the understanding of how it is possible to create 3D porous and chiral materials as a new variety of Metal-Organic Frameworks from small self-assembling peptides (which are models for larger systems). These chiral MOFs, or better Metal-Peptide Frameworks (MPFs) motivates serious research efforts because of the implications of such a system in asymmetric catalysis, asymmetric filtration or gas storage. The concept is to use the self assembly propensity of a small peptide via hydrogen bonds, π–π stacking and the coordination of metal centers to generate chiral and (possibly) porous material. Interest to use a peptide arises from the chiral information transfer from the ligand into the hybrid structure. This system constitutes a good prototype for further and more complex structures. The crystal structure was determined using *ab initio* direct methods, and confirmed via magnetic (SQUID), EPR, FT-IR and TGA/elemental analysis.

1.7 References

- **Proteins, peptides and amino-acids: a general introduction section:**

[PPA-1] Software available at www.pymol.org

[PPA-2] Phillips, S.E.; *J.Mol.Biol.*, **1980**, *142*, 531-554

- **Proteins, peptides, and amino-acids: self-assembling modalities section:**

[PPAS-1] Eisenberg, D.; *Proc. Natl. Acad. Sci. USA*, **2003**, *100*, 11207-11210.

[PPAS-2] Pauling, L.; Corey, R. B.; *Proc. Natl. Acad. Sci. USA*, **1951**, *37*, 251–256

[PPAS-3] Pauling, L., Corey, R. B.; Branson, H. R.; *Proc. Natl. Acad. Sci. USA*, **1951**, *37*, 205–211

[PPAS-4] Branden, C.; Tooze, J.; Introduction to Protein Structure (2nd ed.), 1999, Garland Publishing: New York, NY.

[PPAS-5] Kabsch, W.; Sander, C.; Dictionary of Protein Secondary Structure: Pattern Recognition of Hydrogen Bonded and Geometrical Features. Biopolymers 22: 2577-2637 (1983)

[PPAS-6] Astbury, W.T.; Street, A.; *Trans. R. Soc. Lond.*, **1931**, *A230*, 75-101.

Astbury, W.T.; *Trans. Faraday Soc.*, **1933**, *29*, 193-211.

[PPAS-7] Astbury, W.T.; Woods, H.J.; *Trans. R. Soc. Lond.*, **1934**, *A232*, 333-394.

[PPAS-8] Astbury, W.T.; Sisson, W.A.; *Proc. R. Soc. Lond.*, **1935**, *A150*, 533-551.

- **Biomineralization section:**

[Bio-1] Baeuerlein, E., Biomineralization : Progress in Biology, Molecular Biology and Application (Second Edition), 2004, Wiley-VCH Verlag

[Bio-2] Mann, S., Biomineralization: Principles and Concepts in Bioinorganic Materials Chemistry, 2001, Oxford Chemistry Masters

[Bio-3] Kirschvink, J. L, Gould, J. L., *Bio Systems*, **1981**, *13*(3), 181-201

[Bio-4] Waldo, G. S., Theil, E. C., Comprehensive Supramolecular Chemistry, **1996**, *5*, 65-89

[Bio-5] Webb, J.; Brooker, L. R.; Lee, A. P.; Hockridge, J. G.; Liddiard, K. J.; Macey, D. J.; Van Bronswijk, W., *Aust. J. Chem.*, **2001**, *54*(9 & 10), 611-613

[Bio-6] Rashamuse, K. J.; Whiteley, C. G., *Appl. Microbiol. Biotechnol.*, 2007, 75(6), 1429-1435

[Bio-7] Rusin, P., Cassells, J., Sharp, J., Arnold, R.; Sinclair, N. A., *Miner. Eng.*, 1**992**, *5*(10-12), 1345-1354

[Bio-8] Lins, U., Keim, C. N., Evans, F. F.; Farina, M., Buseck, P. R., *Geomicrobiol. J.*, **2007**, 24(1), 43-50

[Bio-9] Lang, C., Schueler, D., *Microbial Bionanotechnology*, **2006**, 107-124

[Bio-10] Matsunaga, T., Suzuki, T., Tanaka, M., Arakaki, A., *Trends Biotechnol.*, **2007**, 25(4), 182-188

[Bio-11] Dujardin, E., Mann, S., *Adv. Mat.*, **2002**, *14*(11), 775-788

[Bio-12] van Hest, J. C. M., Tirrell, D. A., *Chem. Comm.*, **2001**, 19, 1897-1904

[Bio-13] Yao, N., Wang, R., Ku, A. Y., Saville, D. A., Aksay, I. A., Handbook of Nanophase and Nanostructured Materials, **2003**, *4*, 237-256

[Bio-14] Douglas, T., *Science*, **2003**, *299*(5610), 1192-1193

[Bio-15] Sanford, K., Kumar, M., *Curr. Opin. Biotechnol.*, 2005, 16(4), 416-421

- **Low molecular weight organogelator section:**

[Gel-1] Terech, P., Weiss, R. G., *Chem. Rev.*, **1997**, 97, 3133-3159

[Gel-2] Hoffmann, H., *Adv. Colloid Interface Sci.*, **1990**, 32, 123

[Gel-3] De Gennes, P. G., Scaling Concepts in Polymer Physics; **1979**, Cornell University Press: Ithaca, NY

[Gel-4] Gelbart, W. M.; Ben-Shaul, A., *J. Phys. Chem.*, **1996**, *100*, 13169¨

[Gel-5] Jordon Lloyd, D., Colloid Chemistry; **1926**, Alexander, J., Ed.; The Chemical Catalog Co.: New York, 1, 767

[Gel-6] Graham, T,. Phil., *Trans. Roy. Soc.*, **1861**, 151, 183

[Gel-7] Hermans, P. H., Colloid Science, 1947, Kruyt, H. R., Ed.; Elsevier: Amsterdam, Vol. II, p 483.

[Gel-8] Flory, P., *J. Discuss Faraday Soc.*, **1974**, *57*, 7

[Gel-9] Eicke H. F. Topics in Current chemistry; Springer-Verlag: Berlin, 1980; Vol. 87, p. 91

[Gel-10] Bourrel, M.; Schechter, R. S., Surfactant Science Series; Dekker, M.: New York, **1988**; Vol. 30, p 111

[Gel-11] Ruckenstein, E.; Nagarajan, R., *J. Phys. Chem*,. **1980**, *84*, 1349

[Gel-12] Ferry J. D., *Viscoelastic Properties of Polymers*; Wiley: New York, 1980

[Gel-13] Hermans, P. H., Colloid Science; Kruyt, H. R., Ed., Elsevier: Amsterdam, **1969**; Vol II.

[Gel-14] Russo, P. S., Reversible polymeric gels and related systems; **1987**, Russo, P. S., Ed.; ACS Symposium Series 350; American Chemical Society: Washington, DC,; Chapter 9

[Gel-15] Almdal, K.; Dyre, J.; Hvidt, S.; Kramer, O., Polym. Gels Networks, **1993**, *1*, 5

[Gel-16] Stauffer, D., Introduction to percolation; **1985**,Taylor and Francis: London,.

[Gel-17] Stanley, H. E.; Family, F.; Gould, H., *J. Polym. Sci.: Polym. Symp.*, **1985**, *73*, 19

[Gel-18] Israelachvili, J. N., Intermolecular and surface forces, 3rd ed.; Academic Press: London, **1992**, pp 341-435

- **Metal peptide frameworks section:**

[MPF-1] James, S. L., *Chem. Soc. Rev.*, **2003**, 32, 276

[MPF-2] Rowsell, J. L. C. , Yaghi, O. M. , *Micro. Meso.*, **2004**, 73, 3-14

[MPF-3] Yaghi, O. M. , Li, H. , Davis, C. , Richardson, D. , Groy, T., *Acc. Chem. Res.*, **1998**, *31*, 474-484

[MPF-4] Barton, T. J., Bull, L. M., Klemperer, W. G., Loy, D. A., McEnaney, B., Misono, M., Monson, P. A., Pez, G., Scherer, G. W., Vartuli, J. C., Yaghi, O. M., *Chem. Mater.*, **1999**, *11*(10) , 2633 - 2656

[MPF-5] Robin, A. Y. , Fromm, K. M., *Coord. Chem. Rev.*, **2006**, *250*(15+16), 2127-2157

[MPF-6] Rosi, N. L., Eckert, J., Eddaoudi, M., Vodak, D. T., Kim, J., O'Keeffe, M., Yaghi, O. M., *Science*, **2003**, 300(5622), 1127-1130.

[MPF-7] Chen, B., Liang, C., Yang, J., Contreras, D. S., Clancy, Y. L., Lobkovsky, E. B., Yaghi, O. M., Dai, S., *Angew. Chem. Int. Ed.*, **2006**, *45*(9), 1390

[MPF-8] Fan, J., Zhu, H-F. Okamura, T-A., Sun, W-Y., Tang, W-X., Ueyeama, N., *New. J. Chem.*, **2003**, *27*, 1409-1411

[MPF-9] Ye, Q., Song, Y-M., Wang, G-X., Chen, K., Fu, D-W., Wai Hong Chan, P., Zhu, J-S., Huang, S. D., Xiong, R-G., *J. Am. Chem. Soc.*, **2006**, *128*(20), 6554 -6555

[MPF-10] Düren, T., Sarkisov, L., Yaghi O. M., Snurr, R. Q., *Langmuir*, **2004**, *20*, 2683-2689

[MPF-11] Horcajada, P., Serre, C., Vallet-Regi, M., Sebban, M., Taulelle, F., Ferey, G., *Angew . Chem. Int. Ed.*, **2006**, *45*(36), 5974-5978

[MPF-12] Ockwig, N. W., Delgado-Friedrichs, O., O'Keeffe, M., Yaghi, O. M., *Acc. Chem. Res.*, **2005**, *38*(3), 176-182

[MPF-13] Eddaoudi, M., Kim, J., Vodak, D., Sudik, A., Wachter, J., O'Keeffe, M., Yaghi, O. M., *P. Nat. Acad. U.S.*, **2002**, *99*(8), 4900-4904

[MPF-14] Yaghi, O. M, O'Keeffe, M., Ockwig, N. W., Chae, H. K, Eddaoudi, M., Kim, J., *Nature* , **2003**, *423*(6941), 705-714

[MPF-15] Kim, J., Chen, B., Reineke, T. M., Li, H., Eddaoudi, M., Moler, D. B., O'Keeffe, M., Yaghi, O. M.. A, *J. Am. Chem. Soc.*, **2001**, 123(34), 8239-8247.

[MPF-16] Eddaoudi, Mohamed, Moler, David B., Li, Hailian, Chen, Banglin, Reineke, Theresa M., O'Keeffe, Michael, Yaghi, Omar M. , *Acc. Chem. Res.*, **2001**, 34(4), 319-330

[MPF-17] Fletcher, A. J, Cussen, E. J, Bradshaw, D., Rosseinsky, M. J, Thomas, K M., *J. Am. Chem. Soc.*, **2004**, *126*(31), 9750-9759

[MPF-18] Lin, X., Blake, A. J., Wilson, C., Sun, X. Z., Champness, N. R., George, M. W., Hubberstey, P., Mokaya, R., Schroeder, M., *J. Am. Chem. Soc.*, **2006**, *128*(33), 10745-10753

[MPF-19] Pearson, R. G., *Coord. Chem. Rev.*, **1990**, *100*, 403-425

[MPF-20] Hill, R. J., Long, De-L., Hubberstey, P., Schröder, M., Champness, N. R., *J. Solid State Chem.*, **2005**, *178*(8), 2414-241

[MPF-20] Bradshaw, D., Claridge, J. B., Cussen, E. J., Prior, T. J., Rosseinsky, M. J. , *Acc. Chem. Res.*, **2005**, *38*, 273

[MPF-21] Kesanli, B., Lin, W.-B. , *Coord. Chem. Re*v., **2003**, *246*, 305.

[MPF-22] Zang, S., Su, Y., Li, Y., Zhu, H., Meng , Q., *Inorg. Chem.*, **2006**, *45*(7), 2972 - 2978,

[MPF-23] Sun, D., Ke, Y., Collins, D. J., Lorigan, G. A., Zhou, H.-C.., *Inorg. Chem.*, **2007**, *46*(7), 2725-2734

[MPF-24] Gao, E.-Q. , Yue, Y.-F. , Bai, S.-Q. , He, Z. , Yan, C.-H. , *J. Am. Chem. Soc.*, **2004**, 126, 1419

[MPF-25] Wu, C.-D., Hu, A., Zhang, L., Lin, W. , *J. Am. Chem. Soc.*, **2005**, *127*, 8940

[MPF-26] Lin, W., *J. Solid State Chem.*, **2005**, *178*, 2486

[MPF-27] Zhang, Y., Saha, M. K., Bernal, I. , *CrystEngComm.*, **2003**, *5*(5), 34-37

[MPF-28] Mizutani, M., Maejima, N., Jitsukawa, K., Masuda, H., Einaga, H. , *Inorg. Chim. Acta* , **1998**, *283*, 105-110.

[MPF-29] Gordon, L. E., Harrison, W. T. A. , *Inorg. Chem.*, **2004**, *43*, 1808-1809

[MPF-30] Anokhina, E. V., Jacobson, A. J. , *J. Am. Chem. Soc.*, **2004**, *126*, 3044-3045

[MPF-31] Chen, Lan, Bu, Xianhui., *Chem. Mat.*, **2006**, *18*(7), 1857-1860

[MPF-32] Fan, J., Slebodnick, C., Angel, R., Hanson, B. E., *Inorg. Chem.*, **2005**, *44*, 552-558

[MPF-33] Zhou, X., Yang, C., Le, X., Chen, S., Liu, J., Huang, Z., *J. Coord. Chem.*, **2004**, *57*(5), 401-409

[MPF-34] Wang, R., Liu, H., Carducci, M. D., Jin, T., Zheng, C., Zheng, Z.., *Inorg. Chem.*, **2001**, *40*(12), 2743-2750

[MPF-35] Wang, R., Zheng, Z., Liu, Q.-D., Wang, S., *Inorganic Syntheses* , *2004*, **34**, 184-187

[MPF-36] de Lill, D. T., Bozzuto, D. J., Cahill, C. L. , *Dalton Transactions*, **2005**, *12*, 2111-2115

[MPF-37] de Lill, D. T., Gunning, N. S., Cahill, C. L., *Inorg. Chem.*, **2005**, 44(2), 258-266

[MPF-38] Borkowski, L. A., Cahill, C. L., *Inorg, Chem.*, **2003**, *42*(22), 7041-7045

[MPF-39] Hao, N., Shen, E., Li, Y., Wang, E., Hu, C., Xu, L., *Inorg. Chem. Comm.*, **2004**, *7*(4), 510-512

[MPF-40] Dimos, A., Tsaousis, D., Michaelides, A., Skoulika, S., Golhen, S., Ouahab, L., Didierjean, C., Aubry, A. , *Chem. Mat.*, **2002**, *14*(6), 2616-2622.

[MPF-41] Kiritsis, V., Michaelides, A., Skoulika, S., Golhen, S., Ouahab, L., *Inorg. Chem.*, **1998**, *37*, 3407-3410

[MPF-42] Duan, L.-M., Xu, J.-Q., Xie, F.-T., Liu, Y.-B., Ding, H. , *Inorg. Chem. Commun.*, **2004**, *7*, 216-219

[MPF-43] Lobo, R. F., Zones, S. I., Davis, M. E. , *J. Inclusion Phenom.*, **1995**, *21*, 47-78

[MPF-44] Zheng, Y. Q., Zhou, L. X., Lin, J. L. *Z. Kristallogr.*, **2001**, *216*, 351-352

[MPF-45] Kim, YooJin , Jung', Duk-Young , *Bull. Korean Chem. Soc.*, **2000**, *21*(6), 656-658

[MPF-46] Kim, Y., Suh, My., Jung, D.-Y., *Inorg. Chem.*, **2004**, *43*(1), 245-250.

[MPF-47] Borkowski, L. A., Cahill, C. L., *Inorg. Chem. Comm.*, **2004,** 7(6), 725-728

[MPF-48] Sun, Z-G., Ren, Y-P., Long, L-S., Huang, R-B., Zheng, L-S.., *Inorg. Chem. Comm.*, **2002**, *5*(8), 629-632

2. Amino acid-controlled iron oxide polymorph selection

Alexandre Mantion,[1] Fabia Gozzo,[2] Bernd Schmitt,[2] Willem B. Stern,[3] Yvonne Gerber,[3] Adeline Y. Robin,[4] Katharina M. Fromm,[5] Monika Painsi,[6] and Andreas Taubert[1,7,*]

1 Department of Chemistry, University of Basel, CH-4056 Basel, Switzerland

2 Swiss Light Source, Paul-Scherrer-Institute, CH-5232 Villigen, Switzerland

3 Department of Environmental Geosciences, University of Basel, CH-4056 Basel, Switzerland

4 Laboratoire de cristallogénèse et cristallographie des protéines, Institut de Biologie Structurale Jean-Pierre Ebel, CEA-CNRS-University J. Fourier, F-38027 Grenoble, France

5 Department of Chemistry, University of Fribourg, CH-1700 Fribourg, Switzerland

6 Institute of Geological Sciences, University of Bern, CH-3012 Berne, Switzerland

7 Institute of Chemistry, University of Potsdam, Karl-Liebknecht-Str. 24-25, Building 26, D-14476 Golm, Germany, and Max-Planck-Institute of Colloids and Interfaces, D-14476, Golm, Germany. Tel.: ++49 (0)331 977 5773, Email: ataubert@uni-potsdam.de

Submitted as a paper to *J. Chem. Phys. C*

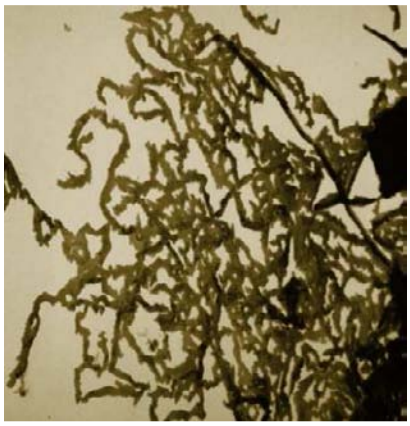

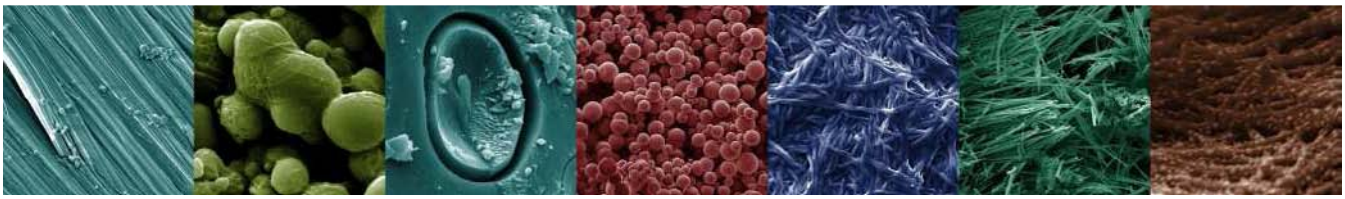

2.1 Introduction

Iron oxides and hydroxides are among the most important biominerals. Among others they are used for navigation and iron storage in biology.[1-3] Moreover, the advantageous poperties of biogenic iron oxide particles have also been exploited for several applications, mainly in the medical field.[4] As a result, iron oxide biomineralization has attracted quite some attention; biological aspects of magnetite biomineralization in bacteria[1,2,5,6] and biotechnology of iron oxide nanoparticles have also been studied in detail.[4,7]

Bacterial magnetite particles have found application in drug delivery, for example by incorporation in liposomes. The resulting magnetoliposomes can be disrupted in a rotating magnetic field, leading to a simple and controlled released pathway for drugs.[8] Bacterial magnetite particles can also be used for DNA extraction; they have the advantage over synthetic magnetite nanoparticles that they are less prone to (unfavorable) aggregation,[9] although it has been shown that further functionalization is necessary for good DNA extraction efficiencies.[10] Subsequently, also an automated procedure for DNA extraction based on the same particles has been proposed.[11]

Despite the successful implementation in several branches of technology and some successful attempts to mineralize (genetically modified) (apo)ferritin cages with inorganics in vitro,[12-16] the colloid chemistry of iron oxide (bio)mineralization is a subject of ongoing research.[17-27] For example, Mann et al. have studied the formation of iron oxides and oxyhydroxides in “biomimetic magnetosomes” using phospholipid vesicles as a model system.[17] Banfield and coworkers have studied the biomineralization of iron oxides on a polymer-based scaffold and have suggested reasons why some microbes release polysaccharides-templated iron oxohydroxides.[22,24] The thermochemistry of iron oxides and oxyhydroxides is also still under investigation,[20] in particular interconversion processes.[21,23,25-27]

Although it is known that peptides and proteins control the growth of biogenic minerals, the interaction of peptides with growing iron oxides has remained elusive. Arakaki et al. have found an acidic protein tightly bound to magnetite, Fe_3O_4.[28] Moreover, Prozorov et al. have described a protein which is able to induce the formation of magnetic nanoparticles.[29]

Similar interactions exist for other inorganic/peptide combinations,[30] but even the mineralization of a simple compound like ZnO has been shown to be more complex with peptides[31,32] than with synthetic polymers.[33-35]

Indeed, one of the most complex questions in (bio)mineralization is how peptides select a specific crystal phase of a (bio)mineral. Brown has shown that proteins containing a basic oligopeptide, Arg-Arg-Val-Thr-Lys-His-His-Val-Asn, adsorb on Fe_2O_3 but not on Fe_3O_4.[36,37] To determine, whether or not the individual building blocks (that is, the single amino acids) of this nonapeptide have a different influence on iron oxide mineralization, we have precipitated iron oxide in the presence of different concentrations of these amino acids. For comparison, we have also included the sulfur-containing amino acids methionine and cysteine, because they are often found in iron containing proteins and peptides.[38] The paper clearly shows that already single amino acids have a strong influence on iron oxide crystal phase selection from aqueous solution.

2.2 Experimental

Preparation of iron oxides. Chemicals were obtained from Fluka and used as received. For precipitation, 50 mL of an aqueous amino acid solution and 20 mL of an aqueous 80 mM $FeSO_4(NH_4)_2SO_4$*6 H_2O solution were mixed under stirring. Then 10 mL of a 12 M aqueous ammonia solution were added under stirring. Amino acid concentrations were set such that the final concentration after mixing these solutions was 0.1, 1, 10, or 100 mM. In the case of histidine and threonine, the maximum concentrations were 60 and 80 mM, respectively, due to their limited solubility. During the whole process, air was bubbled through the reaction solution with an aquarium pump at 10 L/hr. During reaction, the pH remained at pH 9. After 24 hours, the suspensions were centrifuged, the supernatant was decanted, and the solids were air-dried at 40 ºC.

Characterization. XRD was done at the Swiss Light Source, Paul-Scherrer-Institute, Beamline X04SA. Patterns were recorded from 1° to 60° 2θ using the MYTHEN microstrip detector.[39] Samples were mounted in 1 mm mark tubes (Hilgendorf) and measured while rotating. X-ray wavelength λ was 0.708 Å and electron energy was 17.5 keV. Peaks were

modeled using a Pseudo Voigt model (Thompson-Cox-Hastings pseudo-Voigt * Axial divergence asymmetry) using Fullprof.[40] Atomic positions were used as published.[3] For TEM, particles were dispersed in ethanol and deposited on carbon coated copper grids. Samples were imaged with a Philips Morgagni TEM at 80 kV. TGA was done on a Mettler Toledo TGA/SDTA851e from 25 °C to 600 °C with heating rates of 10 to 40 °C/min under nitrogen (10 mL/min) in alumina crucibles. IR spectra were recorded on a Shimadzu FTIR 8300 with a Golden Gate ATR probe from 650 to 4000 cm^{-1}. Raman microscopy was done with an Olympus BX 41 (100 x objective) optical microscope coupled to a Labram HR800 Jobin Yvon Horiba Raman spectrometer with a 514 nm laser with a power of 5.20 mW. XRF spectra were recorded on an energy-dispersive Spectro X-LAB 2000 using the “police tape” method.

2.3 Results

Scheme 1 shows the amino acids used in this study. Crystal phases of the precipitates were determined via synchrotron powder X-ray diffraction (XRD). Rietveld refinement was used to determine the relative amounts of individual crystal phases present in each sample. Figure 1 shows a set of representative XRD patterns. Already visual inspection of the patterns shows that there are big differences between individual samples. Some samples appear well crystallized, which is indicated by the rather narrow reflections, whereas others are so poorly crystalline that Rietveld refinement was only possible with rather large errors or not possible at all.

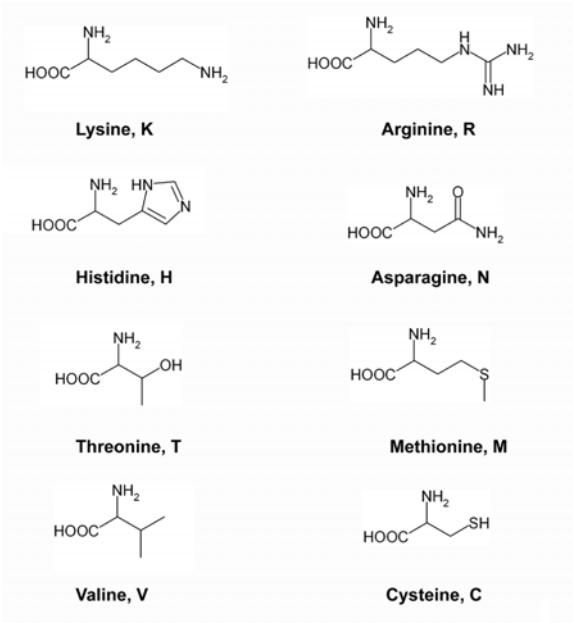

Scheme 1. Amino acids used in this study; all amino acids used were L-amino acids.

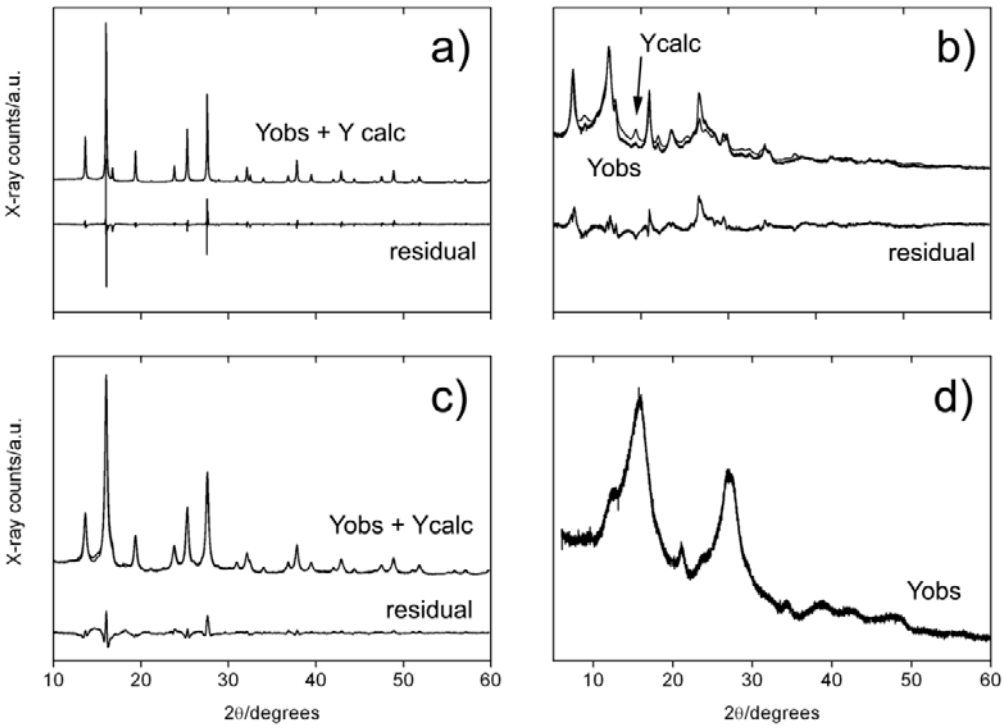

Figure 1. Representative X-ray patterns and Rietveld refinement of samples precipitated in the presence of (a) L-asparagine (100 mM), (b) L-valine (1 mM), (c) L-arginine (10 mM), (d) L-threonine (80 mM). The peak width increases from (a) to (d), which affects the quality of the refinement. The peaks in (d) are too broad for a successful refinement.

Table 1 and Figure 2 summarize the results from XRD and Rietveld refinement. Overall, the precipitates can be classified in two groups, which are plotted as the left and right column of Figure 2, respectively. Figure 2 shows that L-valine, L-methionine, L-asparagine and L-arginine have a similar effect on mineralization. At low amino acid concentration, the sample is over 95 % magnetite. Only with L-arginine, at 10 mM, a small fraction of goethite is found. At 100 mM of amino acid, other crystal phases are present in significant amounts: L-valine and L-methionine lead to mixtures of magnetite and lepidocrocite, whereas in the presence of L-asparagine and L-arginine ternary mixtures of magnetite, goethite, and lepidocrocite form. Furthermore, the weight fraction of magnetite decreases from L-valine to L-arginine and the fraction of goethite and the fraction of the less stable crystal phase lepidocrocite increases.

The second group of precipitates does not exhibit as clear trends, but a few features can be found: L-lysine differs from the aforementioned samples in that already at 10 mM of amino acid, a significant decrease in the magnetite content and corresponding increase in goethite content is found. At 100 mM, goethite is replaced by lepidocrocite and the magnetite fraction has further decreased. At this point, it is interesting to compare the samples precipitated with L-asparagine, L-arginine and L-lysine: these amino acids are more efficient stabilizers for metastable crystal phases in increasing order. L-asparagine only leads to a small fraction of goethite and lepidocrocite at high amino acid concentration. The fraction of these two crystal phases increases further with arginine and finally L-lysine. Moreover, lysine has this effect at lower concentration.

L-cysteine shows the same trend as lysine, but is more efficient in that it already at low concentrations of 1 mM reduces the amount of magnetite to close to zero. Cysteine efficiently traps goethite and lepidocrocite at 1 mM and exclusively stabilizes lepidocrocite at 10 and 100 mM. Similar to cysteine, threonine leads to goethite at 1 mM, lepidocrocite at 10 mM, and 2-line ferrihydrite at 100 mM. Histidine is exotic in that it does not appear to have an impact on the mineralization until at high concentrations of 100 mM. However, at this concentration, exclusively the rather unstable ferrihydrite forms.

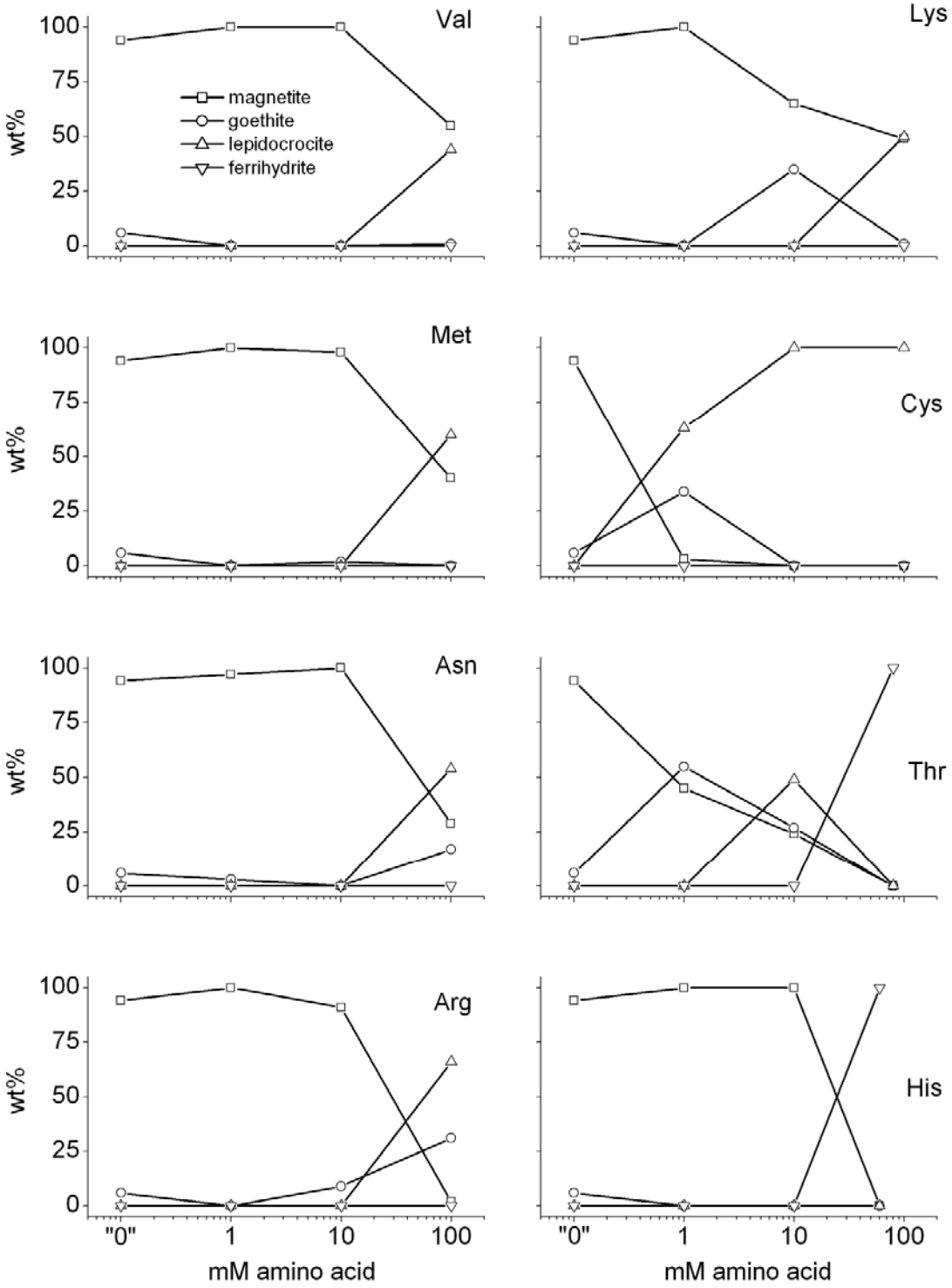

Figure 2. Phase composition of the precipitate as a function of the amino acid chemistry and concentration. "0" denotes the control sample, which, for simplicity of data representation, was also kept on the log scale of the x-axis. For experimental values, see Table 1.

Table 1. Iron oxide composition (weight %) as a function of the amino acid (AA).[a,b]

Amino acid	1 mM	%	10 mM	%	100 mM[c]	%
L-valine	Magnetite	100	Magnetite	100	Magnetite Goethite Lepidocrocite	55 1 44
L-lysine	Magnetite	100	Magnetite Goethite	65 35	Magnetite Goethite Lepidocrocite	49 1 50
L-methionine	Magnetite	100	Magnetite Goethite	98 2	Magnetite Lepidocrocite	40 60
L-asparagine	Magnetite Goethite	97 3	Magnetite	100	Magnetite Goethite Lepidocrocite	29 17 54
L-arginine	Magnetite	100	Magnetite Goethite	91 9	Magnetite Goethite Lepidocrocite	2 31 66
L-histidine	Magnetite	100	Magnetite	100	2-line Ferrihydrite	100[d]
L-threonine	Magnetite Goethite	45 55	Magnetite Goethite Lepidocrocite	24 27 49	2-line Ferrihydrite	100[d]
L-cysteine	Magnetite Goethite Lepidocrocite	3 34 63	Lepidocrocite	100	Lepidocrocite/cystine hybrid[e]	n/a

a The control sample is composed of 94 % magnetite and 6 % goethite.

b Representative X-ray patterns are given in Figure 1, crystallite sizes in Table 2, and stress-strain data are given in the supporting information, Table S2.

c Maximum concentrations are 80 mM for L-threonine and 60 mM for L-histidine due to solubility limits.

d These reflections are too broad for Rietveld refinement. Minor amounts of other crystal phases may have gone undetected.

e See discussion below.

The above results clearly show that amino acids trap kinetically favored iron oxide crystal phases. The amino acids can be roughly arranged in order of increasing trapping efficiency. On this scale, valine is the least efficient additive, followed by methionine, asparagine, arginine, lysine, cysteine, and finally threonine. The latter two stabilize lepidocrocite and ferrihydrite, respectively, at high concentrations, but they also trap goethite and lepidocrocite at concentrations as low as 1 mM.

Figure 3 shows representative transmission electron microscopy (TEM) images of some samples. Control samples and samples precipitated with 1 mM of amino acid (predominantly) contain rounded particles with a broad size distribution. At 10 and 100 mM the morphologies vary, but all samples exhibit morphologies that are essentially given by the crystal structure and not the additive. There is no amino acid-morphology correlation, that is, the amino acid additives do not change the morphology in a specific manner (with the exception of cysteine, see below). Much rather, in all cases, where magnetite forms, roughly spherical particles are observed and so on. For example, the control sample and the samples precipitated at 1 mM of lysine are predominantly magnetite, thus spherical particles are observed (Figure 1a, b).

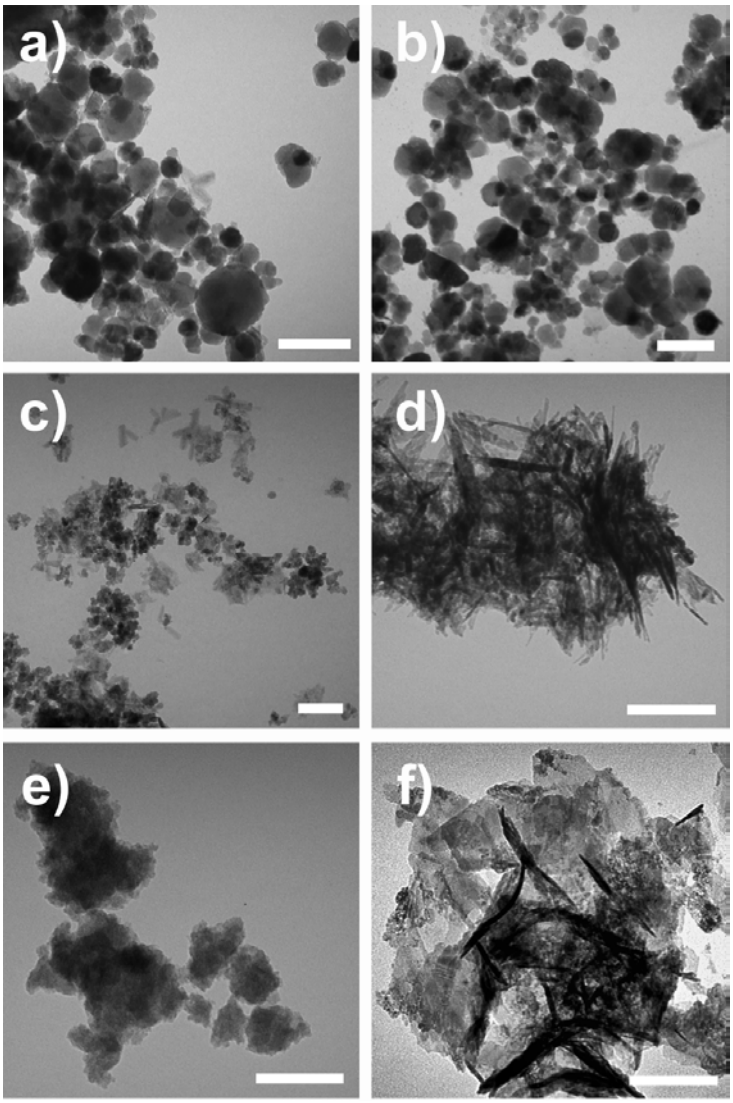

Figure 3. TEM images of (a) control sample, (b) L-lysine 1 mM, (c) L-lysine 10 mM, (d) L-lysine 100 mM, (e) L-histidine 60 mM, (f) L-methionine 100 mM. Scale bars are 100 nm.

Figure 4 shows that L-cysteine is the only amino acid that also affects the particle morphology to some extent. At 1 mM, the samples consist of plates and parallel rods; at 10 mM of amino acid, the precipitates form wires. In the former case, the precipitate is a mixture of goethite and lepidocrocite, and in the latter case the sample is pure lepidocrocite, see Table 1. As here, the wires observed at 10 mM have no equivalent at 1 mM, TEM indicates that there must be an influence on the morphology.

At 100 mM, TEM reveals large platelets with irregular shapes. Some particles show Moiré patterns or bend contours, demonstrating that they are thin crystalline flakes.

Synchrotron XRD shows a set of sharp reflections that can be assigned to L-*cystine*, that is, the oxidized, dimeric form of L-*cysteine*. Closer inspection of the XRD patterns also reveals very weak and broad reflections at 6.3, 12.2, 16.3, and 21.1 degrees 2θ that can be assigned to the lepidocrocite 200, 210, 301, and 020 reflections (JCPDS 44-1415), respectively. XRD thus suggests that here, a hybrid material and not a predominantly inorganic precipitate forms.

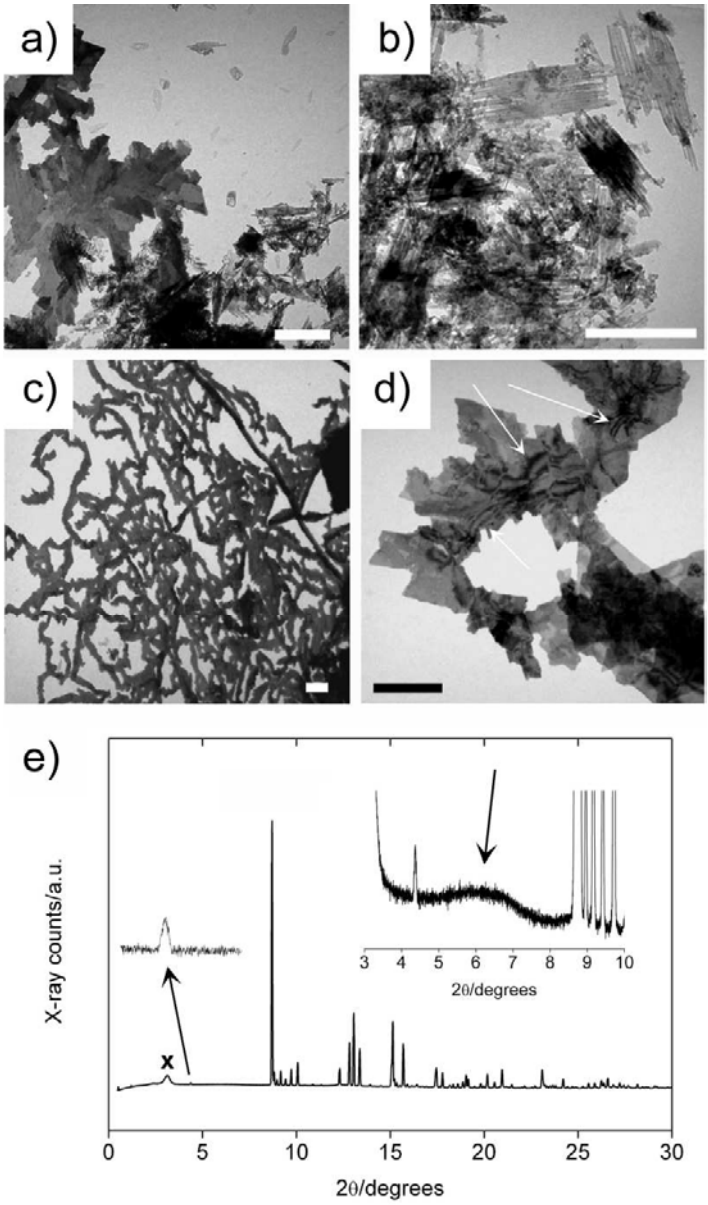

Figure 4. TEM images of precipitates formed in the presence of L-cysteine. (a, b) 1 mM, (c) 10 mM, (d) 100 mM. Scale bars are 250 nm. Dark lines (arrows) are bend contours. (e) X-ray pattern of a sample precipitated from a 100 mM L-cysteine solution; (x) is a peak from the sample support. Inset: very broad lepidocrocite 200 reflection at 6.3 degrees 2θ (arrow).

Raman spectroscopy, Figure 5, confirms the presence of L-cystine in the precipitates obtained with L-cysteine as a starting material. Besides the signals assigned to cystine, the spectra also show a peak at 250 and a shoulder at 377 cm^{-1} assigned to lepidocrocite.[41,42] Moreover, X-ray fluorescence (XRF) shows that the sample contains only ca. 5 % of Fe (from lepidocrocite) and ca. 36 % of S (from L-cystine). This implies, in accordance with the Raman and XRD data, which also indicate a large amount of organic material, that the organic fraction of these samples is very high and that there is a ca. five to sixfold (molar) excess of amino acid in the precipitate. Thermogravimetric analysis (TGA) further confirms these findings. As a result, Raman, XRF, TGA, and XRD show that the precipitate is an L-cystine/lepidocrocite composite with a high organic fraction.

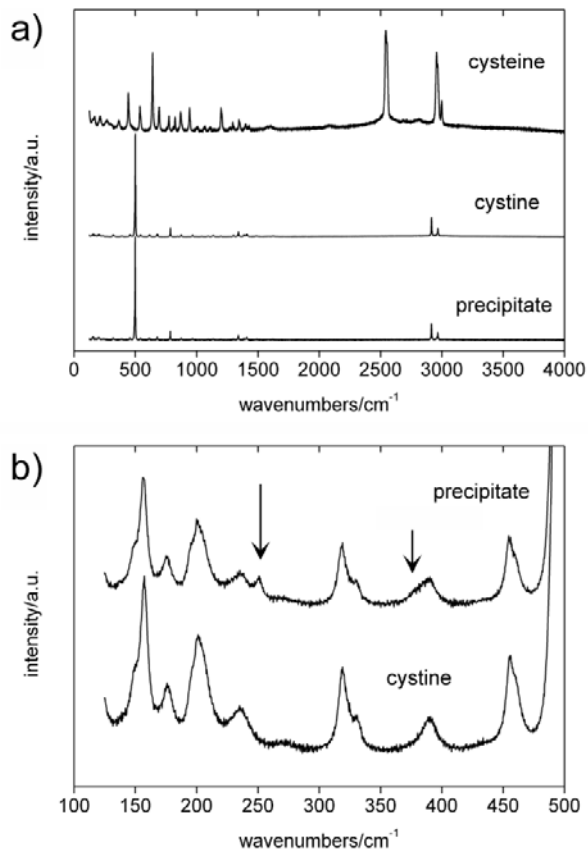

Figure 5. (a) Raman spectra of L-cysteine, L-cystine, and the precipitate. (b) Low wavenumber region. Arrows point to lepidocrocite peak and shoulder.

Amino acid incorporation in the precipitates has been further studied with IR spectroscopy and thermogravimetric analysis (TGA). Figure 6 shows representative TGA curves of a series of samples precipitated with lysine. The control sample and samples precipitated from 1 mM solutions only exhibit a minor weight loss, typically less than 0.5 %, which is presumably due to water desorption. Samples precipitated with threonine and cysteine (with the exception of 100 mM cysteine, see above) and all samples precipitated with higher amino acid concentrations typically exhibit several broad transitions in TGA (labeled 1, 2, and 3 in Figure 6). The samples lose 3 – 5 % at 70 – 80 ºC, followed by an additional loss between 200 and 280 ºC, depending on the amino acid (and hence the crystal phases of the original sample). Finally, often a weight loss between 300 and 380 ºC that again depends on the amino acid, is observed. We assign the first weight loss to weakly bound water leaving the sample; the two latter losses are assigned to decomposition of the amino acids and iron oxide phase transitions to thermodynamically more stable phases, which is accompanied by dehydration. XRD supports this interpretation as we only find hematite after annealing at 400 ºC.

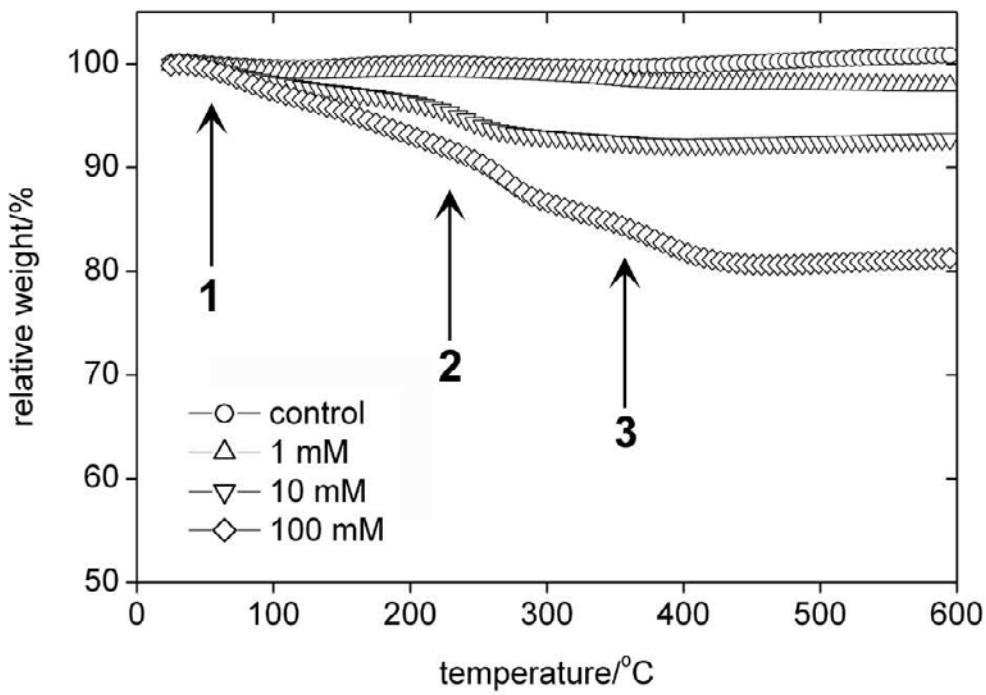

Figure 6. TGA curves of a control sample and samples precipitated with 1, 10, and 100 mM of lysine. Note that the y-axis is only from 50 to 105 % relative weight.

Figure 7 shows IR spectra of a control sample and a sample precipitated with lysine. IR spectroscopy confirms the findings from TGA and (where applicable) Raman spectroscopy as the samples precipitated with amino acids clearly show the presence of organic moieties in the precipitates. Furthermore, many IR spectra show a significant –OH vibration at around 3000 to 3100 cm^{-1}. This band is assigned to both water incorporated into the crystal (lattice), in particular in the case of the hydrated iron oxides, and to adsorbed surface water.

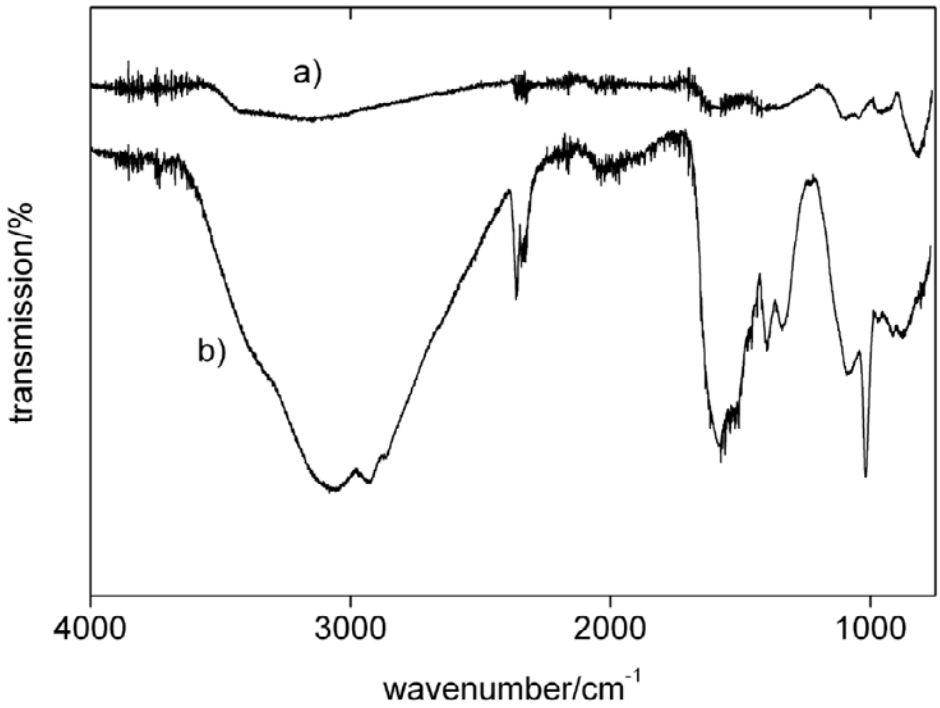

Figure 7. Representative IR spectra of a control sample (a) and a sample precipitated with 100 mM of L-lysine (b). The spectra are drawn to scale and clearly show that some organic components are incorporated into the sample (b).

2.4 Discussion

The current data provide some basic insight into the control that proteins exert on iron oxide biomineralization. Commonly, organic growth modifiers are claimed to adsorb onto growing (inorganic) particles, and indeed, an adsorption mediated process can also be postulated here: valine and methionine are the least effective growth modifiers (or least efficient stabilizers) because they only weakly interact with the precipitates. Magnetite is rather stable and will persist under the conditions chosen here, if the solution only contains a

weak stabilizer or no stabilizer at all. However, the presence of other, more strongly interaction amino acids will prevent further reaction of ferrihydrite with Fe(II) or redissolution/reprecipitation processes.[3]

With asparagine, arginine, lysine, cysteine, and threonine the fractions of metastable crystal phases increase in that order. That is, these amino acids increasingly stabilize metastable precipitates. Moreover, the metastable crystal phases are stabilized at lower amino acid concentrations than with valine and methionine. This especially applies to cysteine (which is also oxidized during the precipitation reaction) and threonine and clearly shows that the interaction strength of amino acids and iron oxide particles increases from asparagine to threonine. Histidine is more difficult to relate to the other amino acids, because it only affects crystal phase selection at rather high concentration.

L-histidine is difficult to compare to L-Lysine and L-arginine, all which contain nitrogen atoms. First, the residue pKa of the histidine residue is lower (5.97) than that of arginine and lysine.[43] This makes an adsorption controlled by electrostatic interactions feasible; at pH 9 only histidine is in its unprotonated form, whereas the two other amino acids are protonated. Moreover, histidine can also behave as a chelator. Indeed the exclusive presence of ferrihydrite at high histidine concentrations suggests that also at lower concentration ferrihydrite should be present. As ferrihydrite is however notoriously poorly crystalline, it is likely that the respective X-ray signals have gone undetected at lower histidine concentrations. Adsorption experiments on ferrihydrite confirm our interpretation on a qualitative level.[44] Matrajt and Blanot have shown that histidine and threonine adsorb much more efficiently on ferrihydrite than the other amino acids used in our study.

However, unlike L-cysteine,[45-47] L-threonine does not favor redissolution/reprecipitation processes at higher concentrations. One possible explanation is that L-threonine effectively complexes Fe(III) present on ferrihydrite surface via the hydroxyl group rather than reducing them (like L-cysteine), preventing further evolution of ferrihydrite to lepidocrocite or other iron (hydr)oxides.

At lower concentrations there is a diverse group of amino acids, which can trap metastable iron oxide crystal phases, however, not usually as single phase materials.

Furthermore, our data show that higher amino acid concentrations in some cases stabilize less stable crystal phases. The most obvious example is threonine, where at 1 mM, ca. 50 % of the sample are goethite, at 10 mM, the fraction of goethite is lower, but an additional ca. 50 % of lepidocrocite form, and at 100 mM only ferrihydrite is observed. This clearly shows that higher amino acid concentrations stabilize less and less stable crystal phases.

The different behaviour of L-lysine and L-arginine can be rationalized via a rather simple electrostatic interaction model. At pH 9, L-lysine is only partially charged (pKa of the residue is 10.28), whereas L-arginine is completely charged (pKa of the residue is 13.28).[43] As the ferrihydrite surface is positively charged,[44,48,49] L-lysine and L-arginine are (in increasing order) repelled from the ferrihydrite surface. Indeed the comparison of samples mineralized at 10 mM suggests a weaker interaction of the L-arginine than the L-lysine with the ferrihydrite. An even stronger interaction has been proposed for L-histidine, which would be in line with the even lower pKa of histidine. Along the same lines, one may argue that because of the weaker and weaker interaction between histidine, lysine, and arginine, L-arginine favors (or at least does not prevent) ferrihydrite redissolution/reprecipitation and the transformation into more stable iron hydr(oxides), lepidocrocite and goethite, similar to additional Fe(II) ions present in solution.[50] In constrast, L-lysine can interact partially with ferrihydrite, leading to trapped lepidocrocite and magnetite.

The above scenario of adsorption and trapping of kinetically favored metastable crystal phases is supported by crystallite size analysis, Table 2. For example, goethite formed in 10 mM solutions of threonine has a coherence length of 47 Å (Table 2). Goethite precipitated with 10 mM solutions of lysine has a coherence length of 148 Å, suggesting a strong affinity of threonine towards strongly hydrated iron (hydr)oxides. This further corroborates stabilization via amino acid adsorption and clearly shows that there are large affinity differences between the amino acids and the different crystal phases. TGA and IR further support this finding by showing evidence for amino acid incorporation into the precipitates.

Table 2. Size (error) of the particles analysis of the samples determined from Rietveld refinement. Mag: magnetite, Goe: goethite, Lep: lepidocrocite, Fer: ferrihydrite, n/a: not applicable due to too low peak intensity or too broad reflections. Sizes are given in Angström.

	1 mM	10 mM	100 mM*
Control sample	Mag: 566.06 (0.36) Goe: 64.47 (0.15)		
L-valine	Mag: 209.27 (0.15)	Mag: 123.89 (0.08)	Mag: 27.07 (0.02) Goe: n/a Lep: 84.48 (0.06)
L-lysine	Mag:172.56 (0.11)	Mag: 148.49 (0.3) Goe: 148.39 (0.3)	Mag: 27.07 (0.02) Goe: n/a Lep: 84.48 (0.12)
L-methionine	Mag: 291	Mag: 62 Goe: 62.24	Mag: 30 Lep: 44.59
L-asparagine	Mag: 175.13 (0.13) Goe: 24.73 (0.04)	Mag: 62.97 (0.08)	Mag: 55.42 (0.06) Goe: 46.61 (0.10) Lep: 69.10 (0.10)
L-arginine	Mag: 255.24 (.04)	Mag: 65.46 (0.06) goe: 126.66 (0.34)	Mag: 53.01 (0.05) Goe:35.66 (0.06) Lep: 69.08 (0.07)
L-histidine	Mag: 294.24 (0.02)	Mag: 104.50 (0.09)	Fer: n/a
L-threonine	Mag: 95.13 (0.13) Goe: 13.95 (0.01)	Mag: 44.04 (0.2) Goe:47.08 (0.03) Lep: 80.27 (0.13)	Fer: n/a
L-cysteine	Mag: 231.69 (0.17) Goe: 113.37 (0.16) Lep: 305.44 (0.31)	Lep: 52.11 (0.06)	n/a

Note: * Maximum concentrations are 80 mM for L-threonine and 60 mM for L-histidine

2.5 Conclusion

In summary, our study shows that (1) there are amino acids, which are more efficient iron oxide crystal phase modifiers than others and (2) even single amino acids exhibit an incomplete selectivity for certain crystal phases. As a result, the peptide controlling the mineralization is a combination of building blocks with a certain preference for one crystal phase. Their combination and chemical connection into a peptide enhances the effect and leads to the more specific selectivity observed in Nature.

2.6 Acknowledgement

We thank M. Neuburger for help with the CSD searches, L. Mirolo for X-ray support, E.C. Constable for access to his IR spectrometer, L. Diamond for access to the Raman spectrometer, and the Swiss National Science Foundation for funding. A.T. thanks the Holcim Stiftung Wissen for a Habilitation Fellowship.

Supplementary information available. Chemical structures of amino acids used in this study. Table with the X-Ray fluorescence analysis result. Table with details of X-ray stress-strain analysis. This material is available free of charge via the Internet.

2.7 References

(1) Bauerlein, E. *Angew. Chem. Int. Ed.* **2003**, *42*, 614.

(2) Bauerlein, E. *Biomineralization - Progress in Biology, Molecular Biology and Application*; Wiley-VCH: Weinheim, 2004.

(3) Cornell, R. M.; Schwertmann, U. *The Iron Oxides: Structure, Properties, Reactions, Occurrences and Uses*; Wiley-VCH: Weinheim, 2003.

(4) Matsunaga, T.; Okamura, T.; Tanaka, T. *J. Mater. Chem.* **2004**, *14*, 2099.

(5) Schüler, D.; Frankel, R. B. *Applied Microbiol. Microtechnol.* **1999**, *52*, 464.

(6) Schueler, D. Biochemical and genetic analysis of the magnetosome membrane in Magnetospirillum gryphiswaldense. In *Biomineralization*; Bäuerlein, E., Ed.; Wiley-VCH: Weinheim, 2004; pp 61.

(7) Matsunaga, T.; Suzuki, T.; Arakaki, A. *Trends Biotechnol.* **2007**, *25*, 182.

(8) Matsunaga, T.; Higashi, Y.; Tsujimura, N. *Cellular Eng.* **1997**, *2*, 7.

(9) Davies, M. J.; Taylor, J. I.; N., S.; Bruce, I. J. *Anal. Biochem.* **1998**, *262*, 92.

(10) Yoza, B.; Matsumoto, M.; Matsunaga, T. *J. Biotechnol.* **2002**, *94*, 217.

(11) Yoza, B.; Arakaki, A.; Matsunaga, T. *J. Biotechnol.* **2003**, *101*, 219.

(12) Meldrum, F. C.; Wade, V. J.; Nimmo, D. L.; Heywood, B. R.; Mann, S. *Nature* **1991**, *349*, 684.

(13) Resnick, D.; Gilmore, K.; Idzerda, Y. U.; Klem, M.; Smith, E.; Douglas, T. *J. Appl. Phys.* **2004**, *95*, 7127.

(14) Wong, K. K. W.; Douglas, T.; Gider, S.; Awschalom, D.; Mann, S. *Chem. Mater.* **1998**, *10*, 279.

(15) Douglas, T.; Stark, V. T. *Inorg. Chem.* **2000**, *39*, 1828.

(16) MacMillan, A. R.; Paavola, C. D.; Howard, J.; Chan, S. L.; Zaluzec, N. J.; Trent, J. D. *Nature Mater.* **2002**, *1*, 247.

(17) Mann, S.; Hannington, J. P.; Williams, R. J. P. *Nature* **1986**, *324*, 565.

(18) Laberty, C.; Navrotsky, A. *Geochim. Cosmochim. Acta* **1998**, *62*, 2905.

(19) Banfield, J. F.; Welch, S. A.; Zhang, H.; Thomsen Ebert, T.; Penn, R. L. *Science* **2000**, *289*, 751.

(20) McGuire, M. M.; Edwards, K. J.; Banfield, J. F.; Hamers, R. J. *Geochim. Cosmochim. Acta* **2001**, *65*, 1243.

(21) Majzlan, J.; Lang, B. E.; Stevens, R.; Navrotsky, A.; Woodfield, B. F.; Boerio-Goates, J. *Am. Mineral.* **2003**, *88*, 846.

(22) Nesterova, M.; Moreau, J.; Banfield, J. F. *Geochim. Cosmochim. Acta* **2003**, *67*, 1177.

(23) Majzlan, J.; Navrotsky, A.; Schwertmann, U. *Geochim. Cosmochim. Acta* **2004**, *68*, 1049.

(24) Chan, C. S.; De Stasio, G.; Welch, S. A.; Girasole, M.; Frazer, B. H.; Nesterova, M. V.; Fakra, S.; Banfield, J. F. *Science* **2004**, *303*, 1656.

(25) Waychunas, G. A.; Kim, C. S.; Banfield, J. F. *J. Nanoparticle Res.* **2005**, *7*, 409.

(26) Mazeina, L.; Navrotsky, A. *Clays and Clay Minerals* **2005**, *53*, 113.

(27) Mazeina, L.; Deore, S.; Navrotsky, A. *Chem. Mater.* **2006**, *18*, 1830.

(28) Arakaki, A.; Webb, J.; Matsunaga, T. *J. Biol. Chem.* **2003**, *278*, 8745.

(29) Prozorov, T.; Mallapragada, S. K.; Narasimhan, B.; Wang, L.; Palo, P.; Nilsen-Hamilton, M.; Williams, T. J.; Bazylinski, D. A.; Prozorov, R.; Canfield, P. C. *Adv. Funct. Mater.* **2007**, *17*, 951.

(30) Sarikaya, M.; Tamerler, C.; Jen, A. K. Y.; Schulten, K.; Baneyx, F. *Nature Mater.* **2003**, *2*, 577.

(31) Gerstel, P.; Hoffmann, R. C.; Lipowsky, P.; Jeurgens, L. P. H.; Bill, J.; Aldinger, F. *Chem. Mater.* **2006**, *18*, 179.

(32) Bauermann, L. P.; Bill, J.; Aldinger, F. *J. Phys. Chem B* **2006**, *110*, 5182.

(33) Taubert, A.; Palms, D.; Glasser, G. *Langmuir* **2002**, *18*, 4488.

(34) Taubert, A.; Palms, D.; Weiss, Ö.; Piccini, M.-T.; Batchelder, D. N. *Chem. Mater.* **2002**, *14*, 2594.

(35) Taubert, A.; Kübel, C.; Martin, D. C. *J. Phys. Chem B* **2003**, *107*, 2660.

(36) Brown, S.; Sarikaya, M.; Johnson, E. *J. Mol. Biol.* **2000**, *299*, 725.

(37) Brown, S. *Proc. Natl. Acad. Sci. USA* **1992**, *89*, 8651.

(38) *Iron-Sulfur Proteins*; Academic Press: San Diego London, 1999; Vol. 47.

(39) Schmitt, B.; Brönnimann, C.; Eikenberrya, E. F.; Gozzo, F.; Hörmann, C.; Horisberger, C.; Patterson, B. *Nuclear Instruments and Methods in Physics Research A* **2003**, *501*, 267.

(40) http://www-llb.cea.fr/fullweb/fp2k/fp2k.htm **2006**, *August*.

(41) Nobuyuki, T.; Kolthoff, I. M.; Stricks, W. *J. Am. Chem. Soc.* **1955**, *77*, 1996.

(42) Chang, S.-G.; Littlejohn, D.; Liu, D. K. *Ind. Eng. Chem. Res.*, **1988**, *27*, 2156.

(43) Windholz, M.; Budavari, S.; Stecher, P. G. *The Merck Index*, 8. ed.; Merck: Rahway, N.J., 1968.

(44) Matrajt, G.; Blanot, D. *Amino Acids* **2004**, *26*, 153.

(45) Cornell, R. M.; Schneider, W. *Polyhedron* **1989**, *8*, 149.

(46) Cornell, R. M.; Schneider, W.; Giovanoli, R. *Clay Minerals* **1989**, *24*, 549.

(47) Amirbahman, A.; Sigg, L.; von Gunten, U. *J. Colloid Interface Sci.* **1997**, *194*, 194.

(48) Charlet, L.; Manceau, A. A. *J. Colloid Interface Sci.* **1992**, *148*, 425.

(49) Davis, J. A.; Leckie, J. O. *J. Colloid Interface Sci.* **1978**, *67*, 90.

(50) Liu, H.; Li, P.; Zhu, M.; Wei, Y.; Sun, Y. *J. Solid State Chem.* **2007**, *180*, 2121.

2.8 Supplementary material

Table S1: X rays fluorescence assay of sulfur and iron (expressed as their oxide)

	L-cysteine	L-methionine
0 uM	98.68 % Fe2O3 - 0.08 % SO3	
100 uM	96.5 % Fe2O3 : 2.037 % SO3	97.68 % Fe2O3 : 0.57 % SO3
1 mM	96.43 % Fe2O3 : 1.93 % SO3	98.47 % Fe2O3 : 0.37 % SO3
10 mM	98 % Fe2O3 : 1 % SO3	97.35 % Fe2O3 : 1.15 % SO3
100 mM	6.8 % Fe2O3 : 89.64 % SO3	94.76 % Fe2O3 : 3.91 % SO3

Table S2. Sizes (error) and strain (anisotropy) analysis of the samples determined from Rietveld refinement. Mag: magnetite, Goe: goethite, Lep: lepidocrocite, Fer: ferrihydrite, n/a: not applicable due to too low peak intensity or too broad reflections.

AA	Crystallite sizes (Å)			Apparent strain (%%)		
	1 mM	10 mM	100 mM*	1 mM	10 mM	100 mM*
Control sample	Mag: 566.06 (0.36) Goe: 64.47 (0.15)			Mag: 36.0825 (0.0028) Goe: 80.7454 (0.1)		
L-val	Mag: 209.27 (0.15)	Mag: 123.89 (0.08)	Mag: 27.07 (0.02) Goe: n/a Lep: 84.48 (0.06)	Mag: 12.0749 (0.0018)	Mag: 12.4325 (0.0168)	Mag: 21.5293 (0.0137) Goe: n/a Lep: 21.5300 (.0423)
L-lys	Mag:172.56 (0.11)	Mag: 148.49 (0.3) Goe: 148.39 (0.3)	Mag: 27.07 (0.02) Goe: n/a Lep: 84.48 (0.12)	Mag: 53.1941 (0.0360)	Mag: 138.2929 (0.1614) Goe: 138.2929 (0.0694)	Mag: 21.5293 (0.0131) Goe: n/a Lep:21.5300 (0.0414)
L-met	Mag: 291	Mag: 62 Goe: 62.24	Mag: 30 Lep: 44.59	Mag: 12.42	Mag: 24.25 Goe: 24.25	Mag: 40.50 Lep: 40.50
L-asp	Mag: 175.13 (0.13) Goe: 24.73 (0.04)	Mag: 62.97 (0.08)	Mag: 55.42 (0.06) Goe: 46.61 (0.10) Lep: 69.10 (0.10)	Mag: 175.13 (0.13) Goe: 48.2004 (0.0881)	Mag: 21.5293 (0.0050)	Mag: 21.5293 (0.0220) Goe: 21.530 (0.0114) Lep: 68.0787 (0.0674)
L-arg	Mag: 255.24 (.04)	Mag: 65.46 (0.06) Goe: 126.66 (0.34)	Mag: 53.01 (0.05) Goe:35.66 (0.06) Lep: 69.08 (0.07)	Mag: 12.2453 (0.0101)	Mag: 35.4443 (0.0179) Goe: 149.0564 (0.1372)	Mag: 1038,9541 (1.3328) Goe: 70.2676 (0.1419) Lep:21.5298 (0.0281)
L-his	Mag: 294.24 (0.02)	Mag: 104.50 (0.09)	Fer: n/a	Mag: 52.9516 (0.0476)	Mag: 29.0648 (0.373)	Fer: n/a
L-thr	Mag: 95.13 (0.13) Goe: 13.95 (0.01)	Mag: 44.04 (0.2) Goe:47.08 (0.03) Lep: 80.27 (0.13)	Fer: n/a	Mag: 48.2074 (0.0572) Goe: 48.2029 (0.0938)	Mag: 21.5293 (0.0137) Goe: 21.5301 (0.0560) Lep: 21.4295 (0.0319)	Fer: n/a
L-cys	Mag: 232 Goe: 113 Lep: 305	Lep: 52		Mag: 13.70 Goe: 72.55 Lep: 72.55	Lep: 14	

* Maximum concentrations are 80 mM for L-threonine and 60 mM for L-histidine.

3. Concentration-induced TiO_2 sphere-tube-fiber transition in oligovaline organogels and silica structure preparation

Alexandre Mantion[1] and Andreas Taubert[1,2,]*

Department of Chemistry, Klingelbergstr. 80, University of Basel, CH-4056 Basel, Switzerland

1 University of Basel

2 Current address: Institute of Chemistry, University of Potsdam, Karl-Liebknecht-Str. 24-25, Building 26, D-14476 Golm and Max-Planck-Institute of Colloids and Interfaces, D-14476 Golm. Tel.: ++49 (0)331 977 5773, Email: ataubert@uni-potsdam.de

Accepted as a paper in *Macromolecular Bioscience*

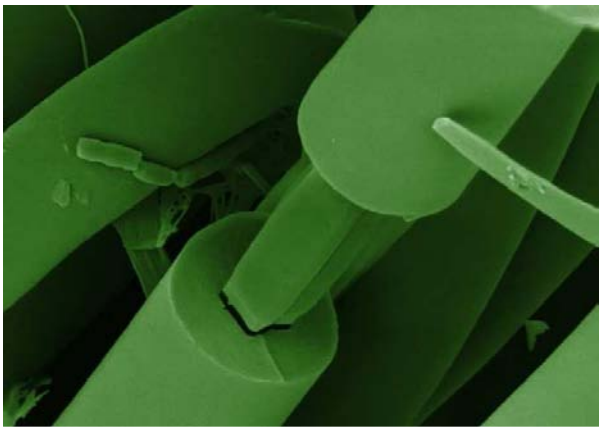

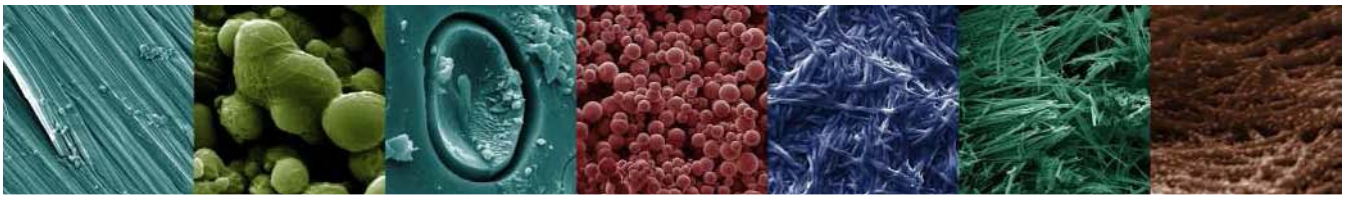

3.1 Introduction

Peptide self-assembly has in recent years attracted much interest because peptide-based structures often combine advantages like biocompatibility with a simple chemistry and structural adaptability, see e.g.[1-5] Peptide gels are but one example where the flexibility of the peptide chemistry and the peptide structure opens the door to new or greatly improved materials. Peptides have therefore found applications in hydro- and organogels, i.e., soft materials that are useful for a variety of applications like drug delivery or in food technology. Simple peptide gelators that are easily manufactured in large amounts are thus of great interest to the (bio)materials community and are currently intensely researched.[6-20]

Peptide-controlled mineralization has been used for the fabrication of various well-defined inorganic materials like calcium phosphate,[21] calcium carbonate,[22, 23] and silica.[14, 24-30] These approaches have led to a variety of interesting and useful geometries and topologies of the inorganics. However, some of these processes require the synthesis of rather long and elaborate peptide sequences,[21] the synthesis of large amounts of (block-co)polypeptides,[22, 24] the extraction of natural polypeptides from diatoms or similar organisms,[31-34] or genetical engineering of proteins.[35-38]

We demonstrate in this section that complex titania architectures can be fabricated using peptide organogels made from simple Z-(L-Val)$_n$-OMe or Z-(L-Val)$_n$-OH oligopeptides that are easy to synthesize and purify. Moreover, the peptides allow for the tuning of the shape and connectivitiy of the resulting TiO_2 structures by simple concentration variation.

We tried the preparation of silica based materials using Z-(L-Val)$_n$-OMe but with a limited success.

3.2 Experimental Section

Materials. Amino acids were purchased from Bachem AG (Bubendorf, Switzerland) and all other chemicals from Fluka (Buchs, Switzerland). All chemicals were used as received.

Peptide synthesis. **Z-L-Val-L-Val-OMe 1a**. 13 mL (99.5 mmol) of isobutyl chloroformate were added to a salt/ice-cooled solution of Z-L-Val-OH (25.0 g, 99.5 mmol) and 4-methylmorpholine (10.9 mL, 99.5 mmol) in 100 mL of chloroform under argon. The reaction mixture was stirred for two minutes. Then 16.7 g (99.4 mmol) of L-valine methyl ester hydrochloride in 10.9 mL (99.5 mmol) of 4-methylaminomorpholine were added. After 15 minutes, the cooling was removed and the solution was allowed to warm up to room temperature. The solution was stirred for 24 hours and the solvents were then removed by rotary evaporation. The residue was dissolved in 200 mL of ethyl acetate and washed three times with 100 mL of saturated hydrogen carbonate solution, once with deionized water, three times with 100 mL of 10 % citric acid, and twice with deionized water. The organic phase was dried with sodium sulfate, concentrated to dryness, and the residue was crystallized from ethyl acetate/petroleum ether to give a white solid (25 g, 70 %). IR (neat, cm^{-1}) 3294, 2970, 1740, 1688, 1650, 1528, 1468, 1453, 1434, 1390, 1371, 1339, 1288, 1242, 1205, 1143, 1117, 1081, 1039, 1026, 884, 966, 925, 911, 894, 862, 840, 779, 751, 740, 695. ^{13}C-NMR (δ in ppm vs. TMS, d_6-DMSO, 100 MHz) 172.70, 172.51, 156.90, 137.98, 129.16, 128.59, 128.47, 66.17, 58.26, 52.41, 31.23, 30.61, 19.93, 19.73, 19.10, 19.06. ^{1}H-NMR (δ in ppm vs. TMS, d_6-DMSO, 400 MHz) 8.06 (d, ^3J = 7.58 Hz, 1 H, amide), 7.07 (m, 6 H, benzyl + amide), 5.01 (s, 2 H, benzylic), 4.14 (t, 1 H, α L-Val), 3.95 (t, 1 H, α L-Val), 3.60 (s, 3 H, methyl ester), 2.00 (hept, 1H, ^3J = 6.56 Hz, β L-Val), 1.91 (hept, 1 H, ^3J = 6.56 ppm, β L-Val), 0.85 (m, 12 H, γ L-Val). Elemental analysis: calc. C 62.62, H 7.74, N 7.69; measured C 62.40, H 7.75, N 7.52. FAB-MS: calculated m/z $[M-H]^+$ = 365; measured $[M-H]^+$ = 365.

Z-L-Val-L-Val-OH 1b. 100 mL of an aqueous 1M NaOH solution were added to a rapidly stirred solution of 25 g (68.7 mmol) of Z-L-Val-L-Val-OMe **1a** in 200 mL of acetone at room temperature. After three hours the organic solvents were removed under reduced pressure, water was added, and the residual **1a** was extracted with ethyl acetate (three times 100 mL). The aqueous solution of **1b** was cooled to 0°C and the pH was adjusted to 1 with 1 M HCl. The slurry was again extracted with ethyl acetate (three times 100 mL) and dried over magnesium sulfate. After removal of the ethyl acetate, the residue was crystallized from ethyl acetate/diethyl ether to give 15 g of white solid (62 %). IR (neat, cm^{-1}) 3291, 2964, 1693, 1629, 1531, 1456, 1392, 1371, 1337, 1239, 1145, 1101, 1030, 1001, 970, 927, 910, 841, 831,779, 733, 695. ^{13}C-NMR (δ in ppm vs. TMS, d_6-DMSO, 100 MHz) 173.70, 172.31,

171.16, 156.90, 137.97, 129.16, 128.57, 128.44, 66.18, 60.81, 57.98, 31.26, 30.68, 20.02, 19.81, 19.00, 18.86, 14.92. ^{1}H-NMR (δ in ppm vs. TMS, d_6-DMSO, 400 MHz) 12.06 (s, 1 H, acid proton), 8.06 (d, ^{3}J = 7.58 Hz, 1 H, amide), 7.07 (m, 6 H, benzyl + amide), 5.01 ppm (s, 2 H, benzylic), 4.14 (dd, 1 H, ^{4}J = 2.02 Hz, ^{3}J = 6.06 Hz, α L-Val), 3.95 (dd, 1 H, ^{4}J = 2.02 Hz, ^{3}J = 7.06 Hz, α L-Val), 2.00 (hept, 1H, ^{3}J = 6.06 Hz, β L-Val), 1.91 (hept, 1 H, ^{3}J = 7.06 ppm, β L-Val), 0.87 (t, 9 H, ^{3}J = 7.07 Hz, γ L-Val), 0.82 (t, 3 H, ^{3}J = 7.07 Hz, γ L-Val). Elemental analysis: calculated C 61.70, H 7.48, N 7.99; measured C 61.55, H 7.55, N 7.78. FAB-MS: calculated m/z $[M-H]^+$ = 351; measured $[M-H]^+$ = 351.

HCl-NH$_2$-L-Val-L-Val-OMe 1c. 7 g (19.2 mmol) of Z-L-Val-L-Val-OMe **1a** were dissolved in a mixture of 100 mL of methanol, 10 mL of 1.25 M HCl in methanol, and 10 mL of water. Argon was bubbled through the solution for ten minutes, followed by the addition of 200 mg of Pd/C. The resulting black slurry was hydrogenated overnight at 50 bar. The solution was filtered through sea sand, centrifuged, and the solvents were removed under reduced pressure. Remaining water was eliminated under high vacuum, leaving 5.1 g (88 %) of a transparent and sticky solid. IR (neat, cm^{-1}) 3183, 2970, 1740, 1666, 1545, 1510, 1464, 1435, 1396, 1373, 1350, 1310, 1263, 1203, 1151, 1020, 995, 971, 931, 912, 882, 840, 766. ^{13}C-NMR (δ in ppm vs. TMS, d_6-DMSO, 100 MHz) 172.41, 171.07, 58.48, 58.36, 56.86, 52.47, 49.34, 31.16, 30.54, 19.66, 19.27, 18.99, 18.25. ^{1}H-NMR (δ in ppm vs. TMS, d_6-DMSO, 400 MHz) 8.53 (d, ^{3}J = 7.59 Hz, 0.8 H, amide), 8.25 (s, 0.2 H, amide), 4.23 (dd, 1 H, ^{3}J = 6.06 Hz, ^{4}J = 2.02 Hz, α L-Val), 3.61 (s, 3 H, methyl ester), 3.55 (d, 1 H, ^{3}J = 5.03 Hz, α L-Val), 2.04 (m, 2 H, β L-Val), 0.90 (m. 12 H, γ L-Val). Elemental analysis: calculated C 49.53, H 8.69, N 10.50; measured C 51.1, H 8.67, N 10.35. FAB-MS: calculated m/z $[M-H]^+$ = 231; measured $[M-H]^+$ = 231.

Z-L-Val-L-Val-L-Val-OMe 2a. **2a** was prepared analogous to **1a**, but 2.61 mL (20 mmol) of isobutyl chloroformate and 7 g (20 mmol) of Z-L-Val-L-Val-OH (7 g, 20 mmol) and 2.19 mL (20 mmol) of 4-methylmorpholine were used. 6.5 g (71 %) of a white solid were obtained. IR (neat, cm^{-1}) 3278, 2957, 1735, 1641, 1510, 1457, 1429, 1334, 1210, 1151, 1116, 1091, 1043, 1027, 1003, 987, 923, 862, 842, 796, 774, 735, 696. ^{13}C-NMR (δ in ppm vs. TMS, d_6-DMSO, 100 MHz) 172.76, 172.57, 172.15, 171.88, 156.93, 137.97, 129.16, 128.57, 128.44, 66.18, 61.14, 58.27, 58.01, 52.48, 52.38, 31.62, 31.08, 30.48, 20.13, 20.10, 20.02,

19.89, 19.81, 19.70, 19.01, 18.94, 18.90, 18.32. ^{1}H-NMR (δ in ppm vs. TMS, d_6-DMSO, 400 MHz) 8.11 (m, ^{3}J = 7.57 Hz, 1 H, amide), 7.89 (d, 0.3 H, ^{3}J = 8.58 Hz, 0.3 H, amide), 7.75 (d, ^{3}J = 9.09 Hz, 0.7 H, amide). 7.32 (m, 6 H, benzyl + amide), 5.02 (s. 2 H, benzylic), 4.32 (m, 1 H, α L-Val), 4.15 (m, 1 H, α L-Val), 4.05 (m, 0.3 H, α L-Val), 3.90 (m, 1 H, 0.7 H, α L-Val), 3.60 (m, 3 H, methyl ester), 2.02 (m, 2 H, β L-Val), 1.94 (m, 1 H, β L-Val), 0.84 (m, 18 H, γ L-Val). Elemental analysis: calculated C 62.18, H 8.07, N 9.06; measured C 62.22, H 8.02, N 8.91. FAB-MS: calculated m/z $[M-H]^+$ = 464; measured $[M-H]^+$ = 464.

Z-L-Val-L-Val-L-Val-OH 2b. **2b** was prepared analogous to **1b**. The solution was initially turbid but turned translucent with time. After purification, 3.5 g (72 %) of a white solid were isolated. IR (neat, cm^{-1}) 3278, 2957, 1708, 1629, 1528, 1464, 1342, 1293, 1249, 1221, 1151, 1136, 1115, 1087, 1039, 991, 961, 927, 865, 842, 794, 756, 736, 696. ^{13}C-NMR (δ in ppm vs. TMS, d_6-DMSO, 100 MHz) 173.60, 171.98, 171.89, 156.93, 137.97, 129.16, 128.57, 128.43, 66.18, 61.15, 58.08, 58.01, 31.60, 31.07, 30.51, 21.59, 20.34, 20.17, 20.04, 19.97, 19.87, 19.02, 18.94, 18.79. ^{1}H-NMR (δ in ppm vs. TMS, d_6-DMSO, 400 MHz) 12.52 (s, 1 H, acid proton), 8.55 (d, ^{3}J = 7.53 Hz, 0.2 H, amide), 7.93 (d, ^{3}J = 8.08, 1 H, amide), 7.75 (d, ^{3}J = 9.09 Hz, 0.8 H, amide), 7.32 (m, 6 H, amide + benzyl), 5.02 (s, 2 H, benzylic), 4.30 (m, 1 H, α L-Val), 4.11 (m, 1 H, α L-Val), 3.91 (m, 1 H, α L-Val), 2.03 (m, 2 H, β L-Val), 1.94 (m, 1 H, β L-Val), 0.84 (m, 18 H, γ L-Val). Elemental analysis: calculated C 61.45, H 7.85, N 9.35; measured C 59.65, H 7.83, N 9.35. FAB-MS: calculated m/z $[M-H]^+$ = 450; measured $[M-H]^+$ = 450.

Z-L-Val-L-Val-L-Val-L-Val-OMe 3a. 2.61 mL (20 mmol) of isobutyl chloroformate was added to a salt/ice-cooled solution of 7 g (20 mmol) of Z-L-Val-L-Val-OH **1b** and 2.19 mL (20 mmol) of 4-methylmorpholine in 200 mL of chloroform under argon. After two minutes of stirring, 5 g (16.9 mmol) of L-valine-L-valine methyl ester hydrochloride **1c** in chloroform and 4-methylaminomorpholine (2.19 mL, 20 mmol) were added. After 15 minutes, the solution was allowed to warm up to room temperature and was stirred for 24 hours. Purification was as for **1a** and **2a** and after crystallization from chloroform/petroleum ether 6 g (55 %) of a white solid were obtained. IR (neat, cm^{-1}) 3278, 2957, 1735, 1691, 1633, 1524, 1457, 1339, 1293, 1214, 1153, 1118, 1089, 1041, 1027, 1005, 984, 925, 860, 839, 806, 777, 696. ^{13}C-NMR (δ in ppm vs. TMS, d_6-DMSO, 100 MHz) 172.59, 172.05, 171.90,

171.69, 171.57, 156.92, 137.97, 129.17, 128.44, 128.58, 66.16, 58.17, 52.42, 30.52, 20.07, 19.95, 19.85, 19.75, 19.13, 19.06, 19.06, 18.99, 18.96, 31.41, 30.52. ^{1}H-NMR (δ in ppm vs. TMS, d_6-DMSO, 400 MHz) 8.12 (d, ^{3}J = 7.58 Hz, 0.4 H, amide), 8.03 (d, ^{3}J = 7.58 Hz, 0.6 H, amide), 7.89 (d, ^{3}J = 9.09 Hz, 0.3 H, amide), 7.85 (d, ^{3}J = 8.58 Hz, 0.3 H, amide), 7.84 (d, ^{3}J = 9.09 Hz, 0.7 H, amide), 7.78 (d, ^{3}J = 8.58 Hz, 0.5 H, amide), 7.32 (m, 6 H, benzyl + amide), 7.18 (d, ^{3}J = 8.58 Hz, 0.2 H, amide), 5.00 (s, 2 H, benzylic), 4.24 (m, 2 H, α valine), 4.15 (m, 2 H, α valine), 4.00 (dd, ^{3}J = 7.07 Hz, ^{4}J = 2.02 Hz, 0.3 H α valine), 3.9 (dd, ^{3}J = 7.07 Hz, ^{4}J = 2.02 Hz, 0.7 α valine), 3.56 (m, 3H, methyl ester), 2.00 (hept, ^{3}J = 6.56 Hz, 2 H, β L-Val), 1.9 (hept, ^{3}J = 6.06 Hz, 2 H, β L-Val), 0.80 (m, 24 H, γ L-Val). Elemental analysis: calculated C 61.90, H 8.24, N 9.96; measured C 61.75, H 8.17, N 9.83. FAB-MS: calculated m/z $[M-H]^+$ = 563; measured $[M-H]^+$ = 563.

Z-L-Val-L-Val-L-Val-L-Val-OtBu 3c. 0.151 mL (1.068 mmol) of isobutyl chloroformate was added to a salt/ice-cooled solution of 0.400 g (890 μmol) of Z-L-Val-L-Val-L-Val-OH **2b** and 0.1 mL (1.068 mmol) of 4-methylmorpholine in 200 mL of chloform under argon. The reaction mixture was stirred for one hour at room temperature and 0.5 g (1.69 mmol) of L-valine-L-valine t-butyl ester hydrochloride **1c** and 0.1 mL (1.068 mmol) of 4-methylaminomorpholine were added. The solution was allowed to warm up to room temperature and was stirred for 24 hours. Purification was as for **1a** and **2a** and after precipitation and centrifugation 260 mg (50%) of a white solid were obtained. IR (neat, cm^{-1}): 3276, 2959, 1729, 1634, 1512, 1460, 1393, 1369, 1291, 1220, 1153, 1088, 1041, 1026, 1003, 983, 906, 923, 848, 773, 732. ^{13}C-NMR (δ in ppm vs. TMS, d_6-DMSO, 100 MHz) 171.82, 171.57, 171.20, 163.41, 137.97, 128.58, 129.18, 128.44, 81.32, 66.16, 58.75, 31.40, 31.24, 31.10, 30.69, 28.47, 19.94, 19.84, 19.73, 19.02, 18.94, 18.84. ^{1}H-NMR (δ in ppm vs. TMS, d_6-DMSO, 400 MHz) 8.02 (d, 0.2 H, ^{3}J = 8.04 Hz, amide), 7.94 (d, 0.7 H, ^{3}J = 8.08, amide), 7.89 (d, 0.2 H, ^{3}J = 9.09 Hz, amide), 7.81 (dd, 1.6 H, ^{3}J = 9.09 Hz, ^{4}J = 5.05 Hz), 7.33 (m, 6 H, amide + benzyl), 5.00 (s, 2 H, benzyl), 4.32 (m, 0.3 H, α L-Val), 4.23 (m, 1.5 H, α L-Val), 4.10 (m, 1.2 H, α L-Val), 3.90 (m, 0.9 H, α L-Val), 2.05-1.85 (m, 4 H, β L-Val), 1.36 (m, 9 H, t-Bu ester), 0.82 (m, 24 H, γ L-Val) Elemental analysis: calculated C 63.55 H 8.67 N 9.26; measured C 63.47 H 8.56 N 9.22 FAB-MS: calculated m/z $[M-H]^+$ = 605; measured $[M-H]^+$ = 605.

Z-L-Val-L-Val-L-Val-L-Val-OH 3b. To a solution of 220 mg of Z-L-Val-L-Val-L-Val-L-Val-OtBu (360 μmol) 8 mL of trifluoroacetic acid were added under vigorous stirring and the mixture was stirred for 15 minutes at room temperature. The trifluoroacetic acid was evaporated under reduced pressure, leaving a colorless oil. Dissolution in chloroform and precipitation from pentane (twice) yielded a white oily solid, which turned solid (190 mg, 95%) after overnight drying under high vacuum. IR (neat, cm^{-1}): 3292, 2966, 1741, 1640, 1516, 1458, 1370, 1229, 1218, 1158, 1028, 930, 900, 801, 774, 738, 694. ^{13}C-NMR (δ in ppm vs. TMS, d6-DMSO, 100 MHz) 173.59, 171.90, 171.58, 156.92, 131.97, 129.18, 128.58, 128.43, 66.16, 61.05, 57.91, 57.02, 31.40, 31.36, 31.10, 30.54, 20.07, 19.98, 19.91, 19.89, 19.04, 19.01, 18.96, 18.72 ^{1}H-NMR (δ in ppm vs. TMS, d6-DMSO, 400 MHz) 8.02 (d, 0.2 H, ^{3}J = 8.04 Hz, amide), 7.94 (d, 0.7 H, ^{3}J = 8.08, amide), 7.89 (d, 0.2 H, ^{3}J = 9.09 Hz, amide), 7.81 (dd, 1.6 H, ^{3}J = 9.09 Hz, ^{4}J = 5.05 Hz), 7.33 (m, 6 H, amide + benzyl), 5.00 (s, 2 H, benzyl), 4.32 (m, 0.3 H, α L-Val), 4.23 (m, 1.5 H, α L-Val), 4.10 (m, 1.2 H, α L-Val), 3.90 (m, 0.9 H, α L-Val), 2.05-1.85 (m, 4 H, β L-Val), 0.82 (m, 24 H, γ L-Val). Elemental analysis: calculated C 61.29, H 8.08, N 10.21; measured C 58.89, H 7.82, N 9.95 FAB-MS: calculated m/z $[M-H]^{+}$ = 549, measured $[M-H]^{+}$ = 549; calculated $[M-M]^{+}$ = 1097, measured $[M-M]^{+}$ = 1097; calculated [M-M-Bzl] = 963, measured 963.

Mineralization. **Titania synthesis.** The peptide and $Ti(OBut)_4$ were dissolved in a vial containing n-butanol, heated to ca. 70 ºC, vortexed, and allowed to cool to room temperature in a closed vial. Typically 800 μL of butanol and 150 μL of alkoxide were used. The resulting gels were stored in open vials at room temperature between 4 and 15 days to allow for hydrolysis of the metal alkoxide. The samples were calcined at 400 ºC for several hours to remove the organic components. **Silica synthesis**. The silica structures are prepared in a similar way. Peptide is mixed in a vial with TEOS (800 uL), heated up to 80°C until the solid dissolves. Then are added 50 uL of distilled water, the mixture is vortexed and left closed to cool. After this, the samples are treated the same way as in titania synthesis.

Spectroscopy. ^{1}H and ^{13}C NMR spectra were recorded on an Avance 400 MHz NMR spectrometer. Infrared spectra were obtained from the neat samples on a Shimadzu FTIR 8300 with a Golden Gate ATR unit. Spectra were recorded from 300 cm^{-1} to 4500 cm^{-1} with a resolution of 1 cm^{-1}. FAB-MS spectra were taken on a Finnigan MAT 312.

Microscopy. Scanning electron microscopy was done on a Philips XL30 FEG ESEM operated at 10 kV. Samples were sputtered with gold or platinum prior to imaging. TEM images were taken using a FEI Morgani 268D operated at 80 kV. Samples were deposited on carbon-coated copper grids and directly imaged after drying in air.

X-ray diffraction. Powder patterns were measured at room temperature on a Stoe Stadi P diffractometer equipped with a curved germanium monochromator using Cu*K*α radiation. Rietveld analysis was done using the pattern from 4 to 90 degrees 2θ using Fullprof.[39] The peaks were fitted with a Thompson-Cox-Hastings pseudo-Voigt profile convoluted with an axial divergence asymmetry function.[40]

Thermal analysis. Thermogravimetric analysis (TGA) was done with a Mettler Toledo TGA/SDTA 851e from 25 to 550 ºC with a heating rate of 10 ºC/min in N_2.

3.3 Results and Discussion

Scheme 1 shows the oligo-L-valines used for organogel formation; Table 1 summarizes their gelation behavior in various solvents. The only solvent gelled by a dipeptide (1a) is heptane. The tripeptide 2a gels a wide variety of solvents including TEOS. The tetrapeptide 3a is less efficient than the tripeptide as it is insoluble in many solvents.

In contrast to the methyl ester derivatives the free *carboxylic acid* derivatives are not as efficient and versatile organogelators: the only solvents gelled by the compounds **1b**, **2b**, and **3b** are toluene, chlorobenzene, chloroform, and methylene chloride. However, these are the solvents that are not or only poorly gelled by the methyl ester derivatives. As a result, oligovalines with a terminal Z-group and a variable head group are relatively efficient organogelators that can easily be adapted for a wide variety of organic solvents.

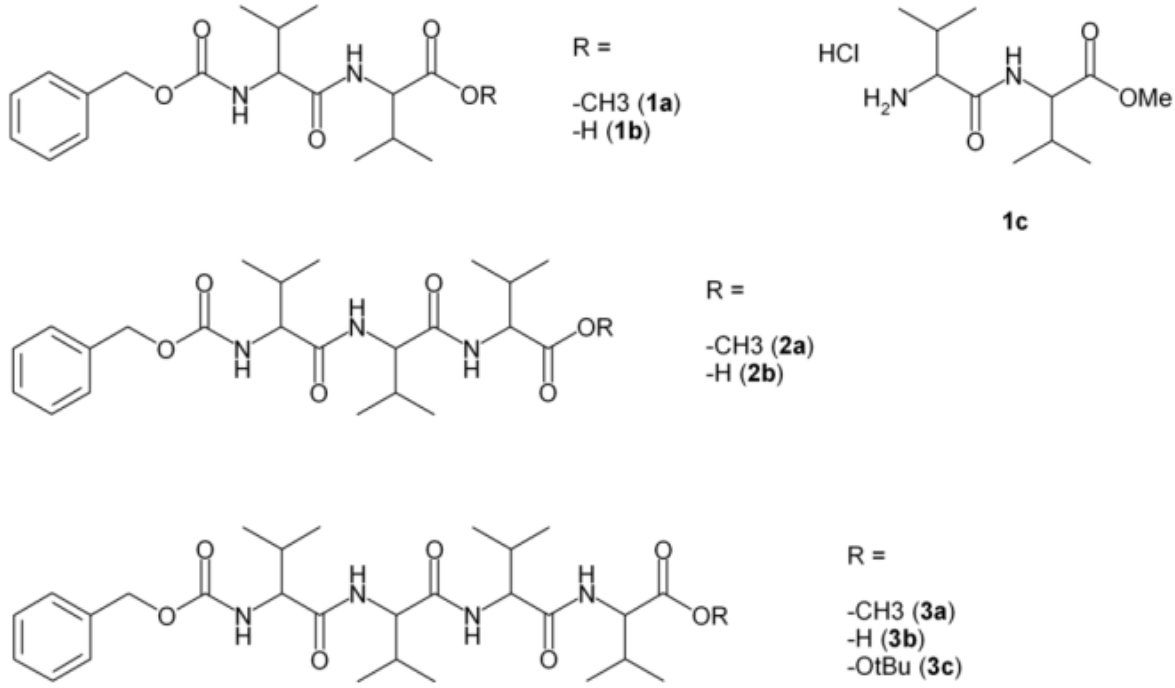

Scheme 1. Chemical structures of **1**, **2**, and **3**. All building blocks are L-amino acids.

Table 1. Behavior of **1**, **2,** and **3** in various solvents grouped according to their chemical composition.[a]

Solvent	1a	2a	3a	1b	2b	3b
Toluene	s	14	i	i	80	30
Chlorobenzene	s	i	i	i	s	30
Methylene chloride	s	s	33	s	80	i
Chloroform	s	s	s	s	80	i
1-decanol	s	9	28	s	s	i
1-octanol	s	16	20	s	s	i
1-hexanol	s	20	25	s	s	i
1-butanol	s	20	33	s	s	i
Ethanol	s	s	i	s	i	i
Methanol	s	s	s	s	s	i
Acetonitrile	s	s	2-phase system (gel + solution)	s	i	i
Acetone	s	s	i	s	i	i
DMSO	s	s	s	s	s	s
Heptane	12	i	i	i	i	i
TEOS	s	10	i	i	i	i
Water (deionized, pH ca. 5.5)	i	i	i	i	i	i

[a] Minimum gelation concentration, mg/mL; i: insoluble; s: soluble.

3.3.1. Gels from the methyl esters 1a, 2a, and 3a. Figure 1 shows a set of representative IR spectra. The neat peptide exhibits broad bands. In contrast, the bands of the gels are relatively sharp and the IR spectra of gels in different solvents are virtually indistinguishable. All spectra show strong bands at around 3280, 1740, 1690, 1640, 1540, and 1220 cm^{-1}. The bands at 1740 and 1690 cm^{-1} have been tentatively assigned to C=O vibrations of the methyl ester and the carbamate.[6] The bands at 3280, 1640, 1540, and 1220 cm^{-1} can be assigned to the amide A, amide I, amide II, and amide III vibrations, respectively. The positions of the bands in the IR spectra indicate that in all cases (crystalline neat peptide and peptide gels) the

structure is predominantly β-sheet, which is very common for fiber forming peptides. IR spectroscopy does not allow for the unambiguous determination of parallel vs. the more common antiparallel β-sheet orientation, because the IR band at ca. 1700 cm^{-1}, which is characteristic for antiparallel sheets is obscured by the presence of the C=O vibrations of the methyl ester and the carbamate.[41, 42]

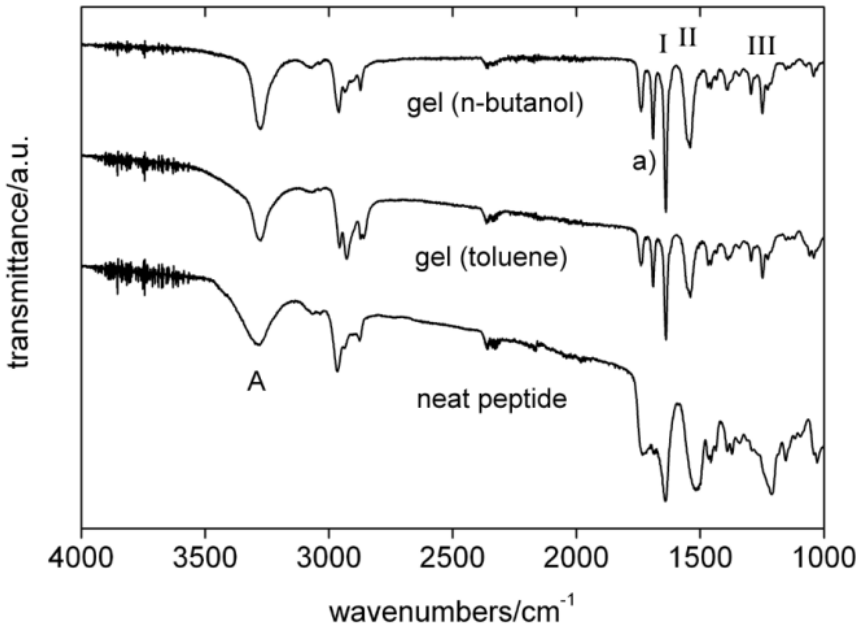

Figure 1. IR spectrum of the peptide **2a** as a neat solid and as a gel in toluene and in n-butanol. A refers to the amide A band. I, II, and III to the amide I, II, and III bands, respectively, and a) denotes the two peaks assigned to the C=O vibrations of COOMe and carbamate groups.

Figure 2 shows scanning electron microscopy (SEM) images of a dried gel. The images reveal that upon gelation the peptides self-assemble into well-defined fibers with a uniform diameter. These primary fibers often form thicker fibers by wrapping themselves around one another. As a result, SEM shows that the self-assembly of our molecular building blocks into long and highly connected peptide nanofibers drives gel formation.

The fiber lengths are more difficult to determine, but they are at least in the tens of microns range, possibly much longer. Higher magnification electron micrographs suggest that

the fibers have a left-handed helix morphology, but due to charging of the sample, a detailed observation is difficult at high magnifications.

Similar to a recent report by Suzuki et al.,[43] the fiber diameter is too big to simply arise from one peptide or a peptide dimer: simple Chem3D estimations of the molecular dimensions show that the dipeptide **1a** is 1.6 nm, the tripeptide **2a** is 2.0 nm, and the tetrapeptide **3a** is 2.4 nm long. These measurements indicate that the fibers must have a three dimensional structure, which is supported by IR (Figure 1) and X-ray experiments presented below. SEM thus implies that, while the fibers have a predominantly 1D shape (the actual fiber), also (limited) self-assembly perpendicular to the fiber axis occurs; this is a possibility of peptide-self-assembly earlier shown by Aggeli et al.[7, 9, 10] A similar process must also take place in the work of Suzuki et al. although they did not comment on this observation.[43]

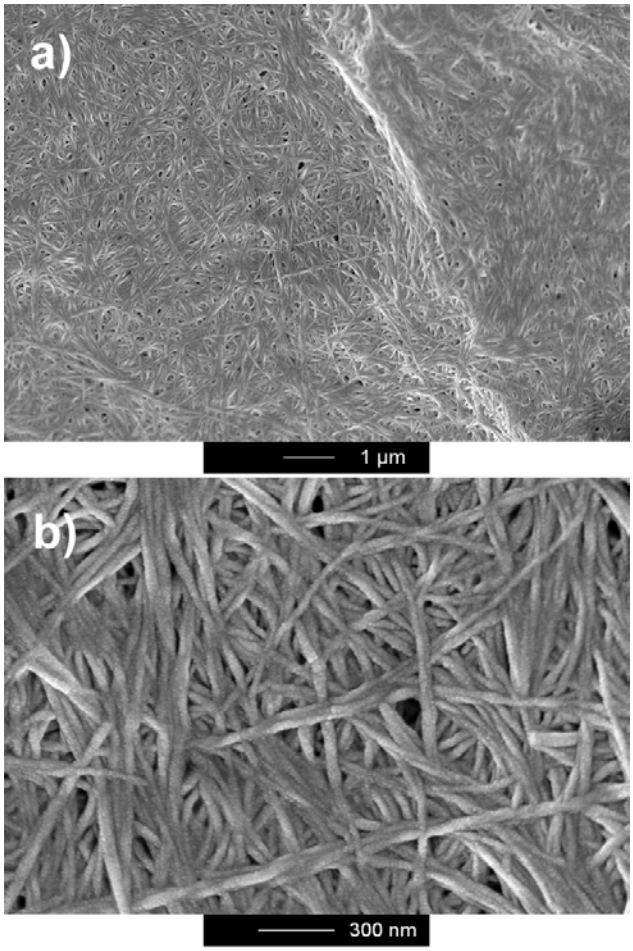

Figure 2. Low magnification (a) and high magnification (b) of a gel of **2a** in butanol.

Figure 3 shows X-ray diffraction (XRD) data of the neat **2a** and gels in toluene and n-butanol. All patterns show a strong reflection at 18.8 (d-spacing of 4.7 Å) and 22.2 (d-spacing of 3.9 Å) degrees 2θ. Furthermore, the neat peptide and the gel in butanol show a strong reflection at 8.2 (d-spacing of 10.8 Å) degrees. Earlier studies have observed similar reflections in β-sheets of poly(L-valine).[44] The spacing of 4.7 Å is due to the interchain spacing in the hydrogen-bonded β-sheets (040 reflection) and a spacing of 3.81 Å has been assigned to the 130 reflection of crystalline poly(L-valine).

The spacing of 10.8 Å in our sample is most likely due to the inter-sheet distance, which is 9.6 Å in poly(L-valine). We explain the slightly larger spacing with the presence of the bulky Z-group in our peptides, which will lead to an increase of the layer-to-layer distance. Because all patterns are virtually identical, X-ray experiments support the IR data and show that the fiber structure in the gels is closely related to the peptide crystal structure.

The X-ray patterns also show that the order in the fibers in toluene is dramatically reduced as the reflection at 8.2 degrees, which is due to the inter-sheet spacing, is either too broad to be observed or is gone altogether. We assign this to the fact that toluene is very similar to the Z-group. It is hence possible that the fibers in toluene form intercalation-like or swollen structures, where the inter-sheet distance varies considerably, leading to a smeared out X-ray signal; a similar model has been proposed for cyclic bis-urea organogelators in various alcohols.[20] In summary however, X-ray experiments confirm the formation of β-sheet structures both in the neat peptide and the fibers.

Interestingly, Jeong et al.[20] have observed similar gels with cyclic bis-urea organogelators in a series of alcohols but in contrast to our gels, the fibers showed no evidence of long-range order in n-butanol and longer alcohols. We assign the higher order in our materials to a stronger interaction between the peptide building blocks due to the higher number of hydrogen bonds.

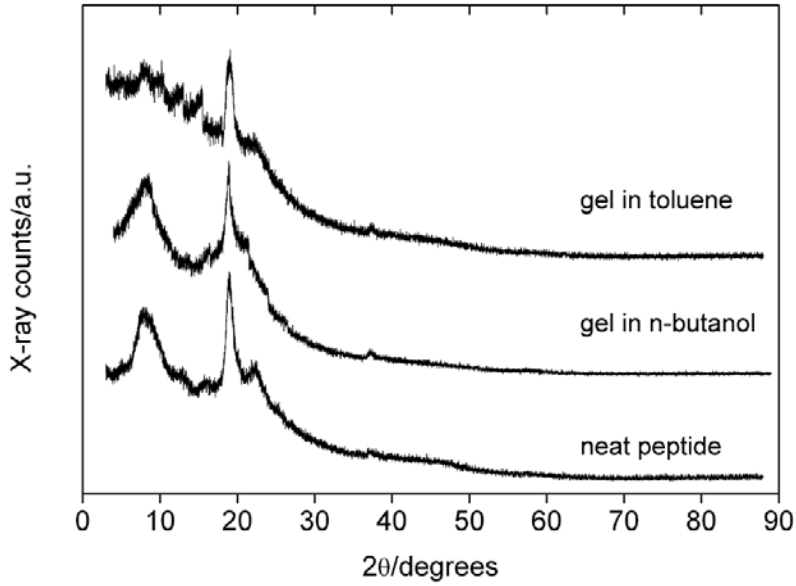

Figure 3. X-ray patterns of the neat peptide **2a** and gels with toluene and n-butanol.

Figure 4 shows that the neat peptide also *crystallizes* in fiber- or needle-like shapes. SEM thus confirms the X-ray and IR data shown above in the sense that both in the crystalline state and in the gel state the peptides adopt fiber-like morphologies. Presumably, the peptides change their orientation only slightly in the presence of organic solvents to accommodate solvent molecules according to their different chemical nature: while aromatic molecules like toluene most likely interact with the aromatic regions (the Z-group) of the peptides, alcohols appear to maintain an almost crystalline-like structure with a high order within the fibers.

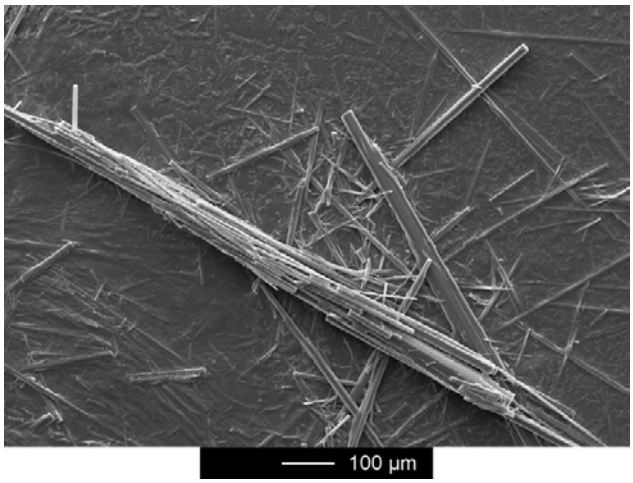

Figure 4. SEM image of crystals of **2a** obtained after crystallization from ethyl acetate.

Figure 5 and Table 2 show representative thermal analysis data obtained from the gels. Thermogravimetric analysis (TGA) of the neat peptide detects a minor weight loss of below 5% at ca. 150 ºC, which we assign to water evaporation. The neat peptides are stable up to ca. 300 ºC, at which temperature they decompose in one rapid step. The thermal stability of the gels is essentially given by the boiling points of the solvents used for gel fabrication (2).

The peptide in the toluene gel starts to decompose much later than expected: the boiling point of toluene is 110 ºC, at which temperature, most of the solvent evaporates, Table 2. However, unlike in the gels with n-alcohols, the remaining peptide only decomposes at 315 ºC. This is roughly 15 ºC higher than the decomposition temperature of the neat peptide. We may speculate that this additional stability is due to the formation of an intercalation or similar compound, which is stabilized at higher temperatures. In contrast, the peptide decomposition temperature decreases with increasing chain length of the n-alcohols, which points to a destabilizing effect.

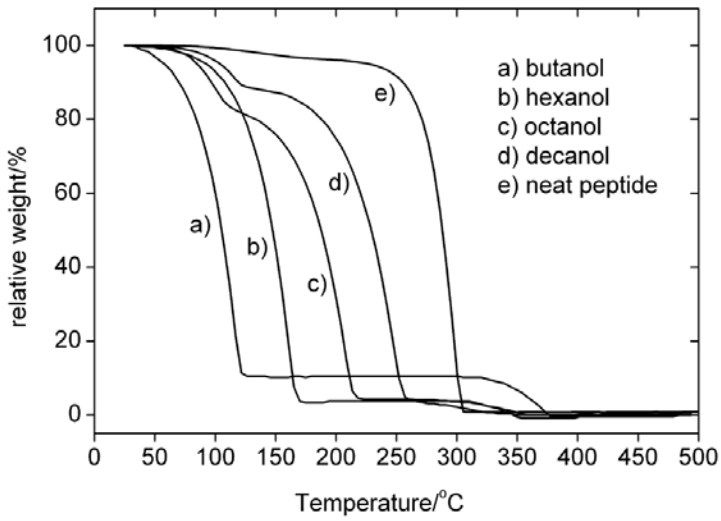

Figure 5. TGA curves of the neat peptide **2a** and various gels.

Table 2. TGA data of gels of **2a** in various solvents. Table 2 shows that the inflection points of the TGA curves measured on the gels coincide with the boiling points of the respective

solvents. Above a chain length of six carbon atoms, we also observe a first weight loss below 100 ºC, which we assign to a separate water loss from the gel.

	T1 (ºC) Water loss	T2 (ºC) Solvent loss	T3 (ºC) Peptide decomposition	Boiling point of pure solvent[54] (ºC)
Neat **2a**			298	
butanol		97	300	117-118
hexanol		133	283	157
octanol	86	168	282	194-195
decanol	97	203	252	234
toluene		97	315	110

3.3.2. Gels from the free carboxylic acids 1b, 2b, and 3b. IR spectroscopy again confirms the formation of β-sheets in the fibers and in the neat peptide, Figure 6.

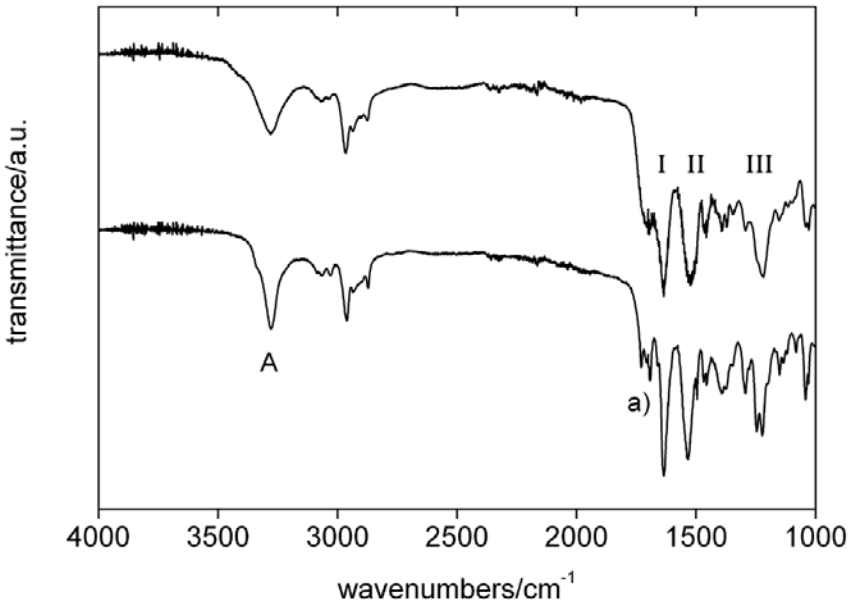

Figure 6. IR spectrum of the neat peptide **2b** (bottom) and of a gel of **2b** in toluene (top). A refers to the amide A band. I, II, and III denote the amide I, II, and III bands, respectively, and a) denotes the peaks assigned to the C=O vibrations of the COOH and carbamate groups.

^{1}H-NMR (Figure 7) supports the IR data: spectra of **2b** in DMSO do not show a signal of the acid proton, but the addition of 1 equivalent of $GaCl_3$ yields a clear peak at ca. 12.6 ppm.[45] This indicates that the original signal of the acid proton is very broad and that the acid proton is involved in some hydrogen bonding in the peptide assembly. Moreover, the signal of the carbamate protons at around 7.9 ppm changes slightly with Ga(III) addition. Ga(III) therefore modifies the interaction between carbamate groups, possibly by coordinating to the carbamate nitrogen and oxygen.

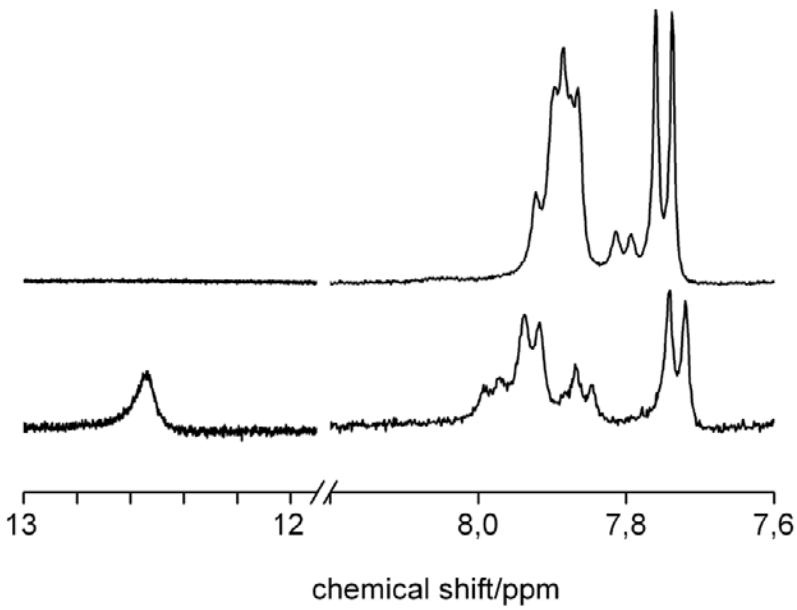

Figure 7. ^{1}H-NMR spectra of **2b** in DMSO (6 mg/mL) before (top) and after (bottom) addition of 1 equivalent of $GaCl_3$. The conformational equilibrium is responsible for the apparently lower than 1 signal of the amide protons. The remaining is probably too broad and vanishes in the background or overlaps with the neighboring signals of the phenyl residue. As the gel forms with increasing concentration, we observe a broadening of the peaks until the signal vanishes due to too slow relaxation in the gel state. We suggest that the carboxylic acid groups are engaged in hydrogen bonding in dimers, but also interact with the carbamate moiety of the Z-group, thereby stabilizing the assembly. As the NMR signals of the amide backbone remain unchanged, we infer that there is only a negligible interaction of the Ga(III) with the amides.

SEM and transmission (TEM) electron microscopy (Figure 8) reveal that also the free acid derivatives **1b**, **2b**, and **3b** assemble into fibers. Their outer diameter strongly depends on the solvent (Figure S4): in toluene individual fibers with a narrow size distribution and an average diameter of 117 nm form. In chloroform, the distribution is much broader and the average diameter is 397 nm (although this number has no significance). The differences are due to the fact that in toluene the peptide fibers are present as individual, well-dispersed fibers, whereas in chloroform the fibers are highly aggregated, pretending larger fibers. TEM however reveals that in both cases the primary fibers are around 60 nm in diameter.

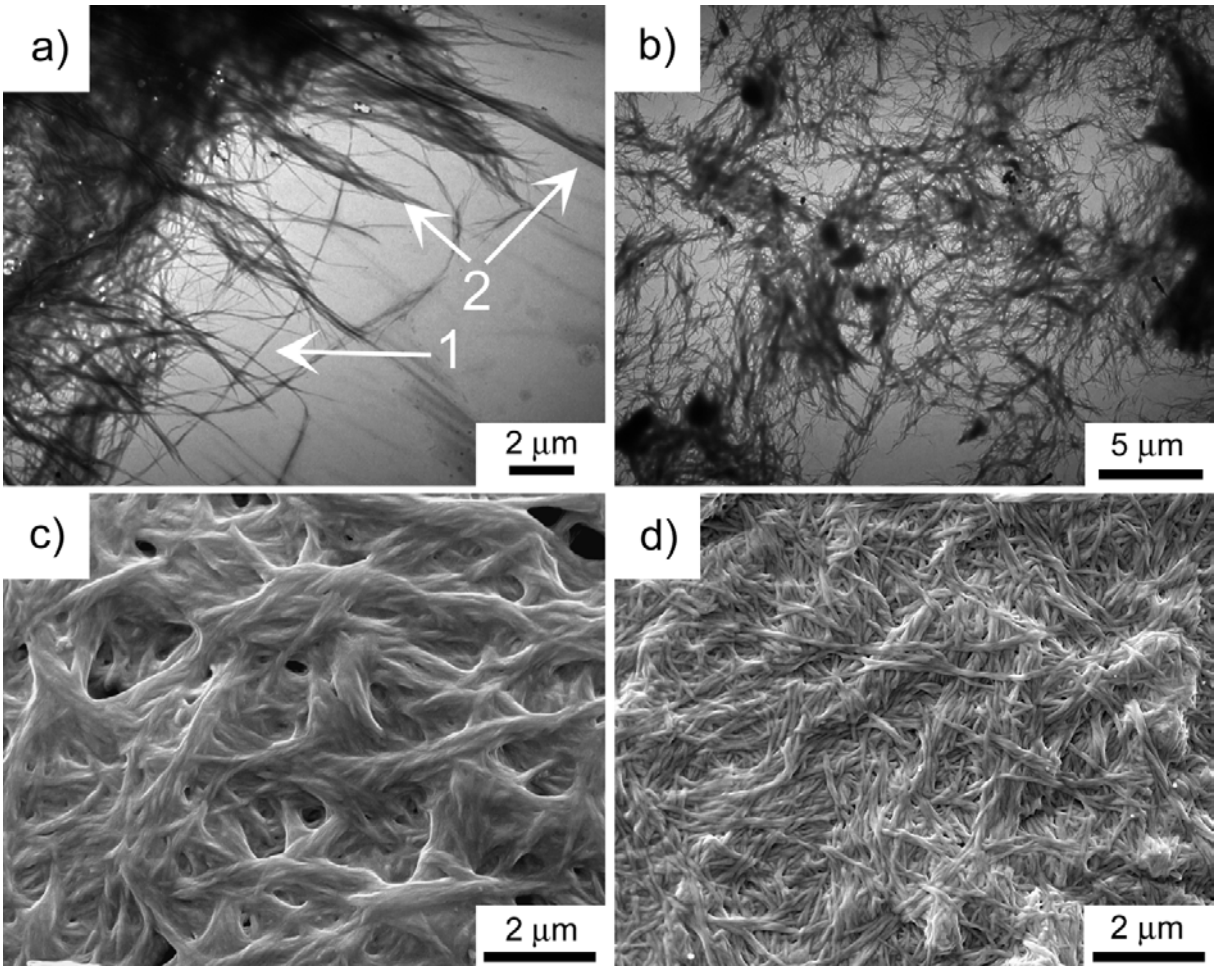

Figure 8. TEM and SEM images of gels of **2b** in $CHCl_3$ (a, c) and toluene (b, d). (1) individual fiber of ca. 60 nm in diameter, (2) aggregated fibers with a diameter much larger than 60 nm. These fibers are less common in toluene than in chloroform.

Representative X-ray data of the free acid **2b** are shown in Figure 9. Essentially, the free acid derivatives show the behavior of the methyl esters. The patterns of the neat **2a** and **2b** show evidence for β-sheet formation in the solid state with almost identical dimensions. However, while X-ray patterns of the gels of the *methyl esters* in toluene (Figure 3) do not show any clear peak at low angles, we observe a small but clear peak at 8.2 degrees (d-spacing of 10.8 Å) in the case of the free acid **2b**. This indicates that the inter-sheet spacing is more uniform in the case of the free acids than with the methyl esters. This may be due to additional hydrogen bonding between the free carboxylic acids or between the carboxylic acids and the carbamate. Both interpretations are also in line with the IR and NMR data. Also, the fibers have again a higher order than similar materials reported by Jeong et al.[20]

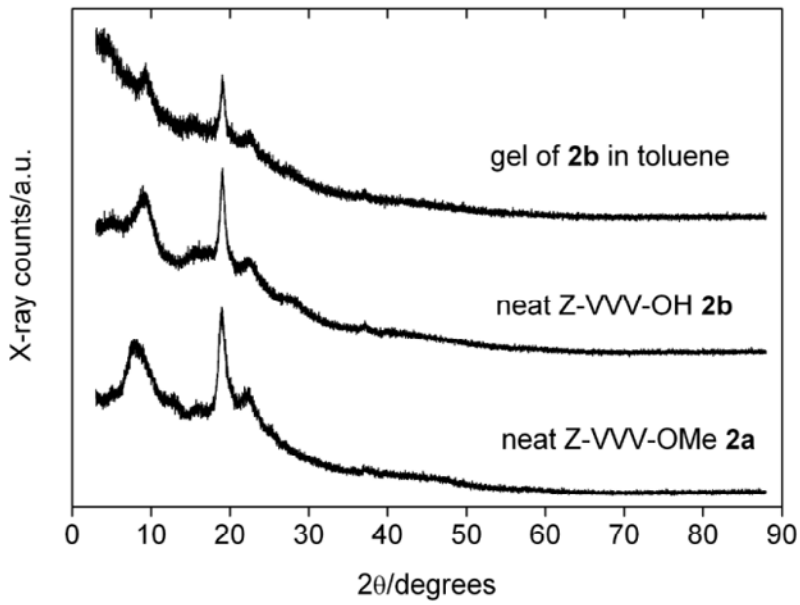

Figure 9. XRD patterns of pure **2a** and **2b**, and a gel of **2b** in toluene.

3.3.3 Titania formation in the gels. As the methyl esters are the more efficient organogelators, we have focused on **2a** to study the formation of inorganic structures within the gels by hydrolyzing $Ti(OBut)_4$ in butanol at different peptide concentrations. At 5 mg/mL of peptide the mixture is a liquid. At 15 mg/mL, a solution with long fibrillar structures that are visible by the naked eye, form. The samples with peptide concentrations of 20 mg/mL and higher form gels that do not flow under the influence of gravity.

Figure 10 shows some of the resulting titania architectures. Without peptide and at low peptide concentrations (below 10 mg/mL) micrometer-sized spherical particles with a broad size distribution form. We assign this to the liquid-like character of the solution, which exerts a rather low control over the mineralization. At 15 mg/mL rodlike features with a unique segmented morphology form. Our interpretation is that these features form by mineralization of coaxial bundles of peptide fibers that form, even though at this state, the mixture is not a gel. Indeed the original peptide fibers are still visible and support this interpretation, which is also supported by the large diameter variation of the rods. The reason for the segmentation however is unclear to date.

At even higher concentration, big blocks of material are observed. Higher magnifications reveal that at 25 mg/mL the large blocks are composed of micrometer long, more or less parallel fibers with a diameter of a few 100 nm. At 50 mg/mL however, the material is a mixture of solid pieces, fibers and also spherical particles. These data show that the real gel state is possibly too unflexible or contains too much organic material for the formation of uniform and well-defined titania structures.

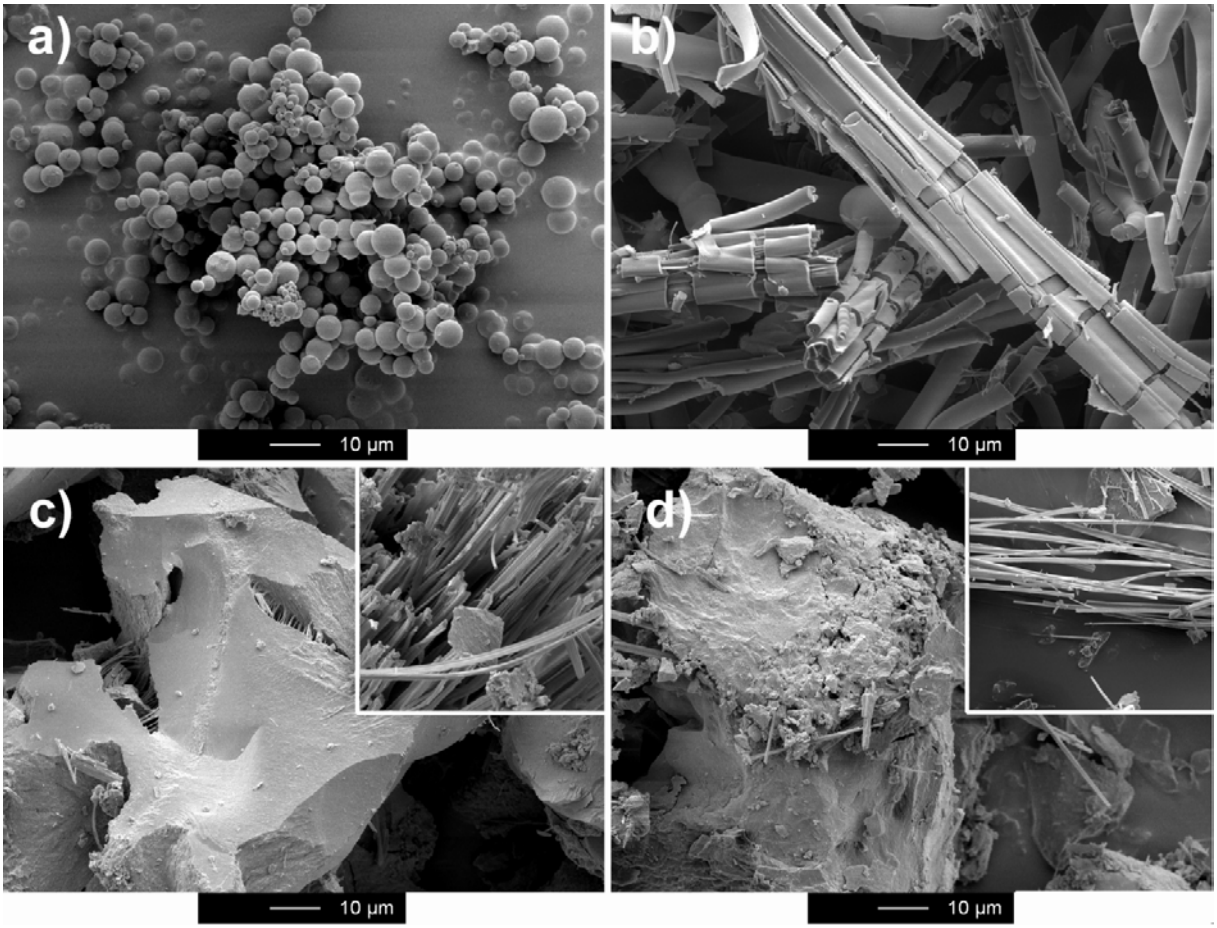

Figure 10. SEM images of titania obtained at different peptide concentrations of **2a** before calcination. (a) 5 mg/mL, (b) 15 mg/mL, (c) 25 mg/mL, (d) 50 mg/mL. Insets are higher magnification views of the fibers described in the text.

Figure 11 shows the samples after calcination. Calcination does not affect the spheres obtained at low concentrations. At higher concentrations, several changes can be observed: the rodlike structures obtained at 15 mg/mL are transformed into tubular structures. This further supports our above explanation of the rodlike morphology: the peptide fibers are mineralized either as a bundle of different numbers of peptide fibers (and hence different diameters) or as individual fibers. The different tube (outer and inner) diameters are a result of this process. Above 20 mg/mL however, the structures observed before calcination do not appear to be stable: at 25 mg/mL, a mixed morphology of spheres and fibers is observed and at 50 mg/mL large blocks with an uncontrolled morphology form. As a result, peptide fibers forming below the actual gelation concentration appear to be the most efficient templates, as here tubular titania with a reasonably well-controlled morphology and uniformity forms.

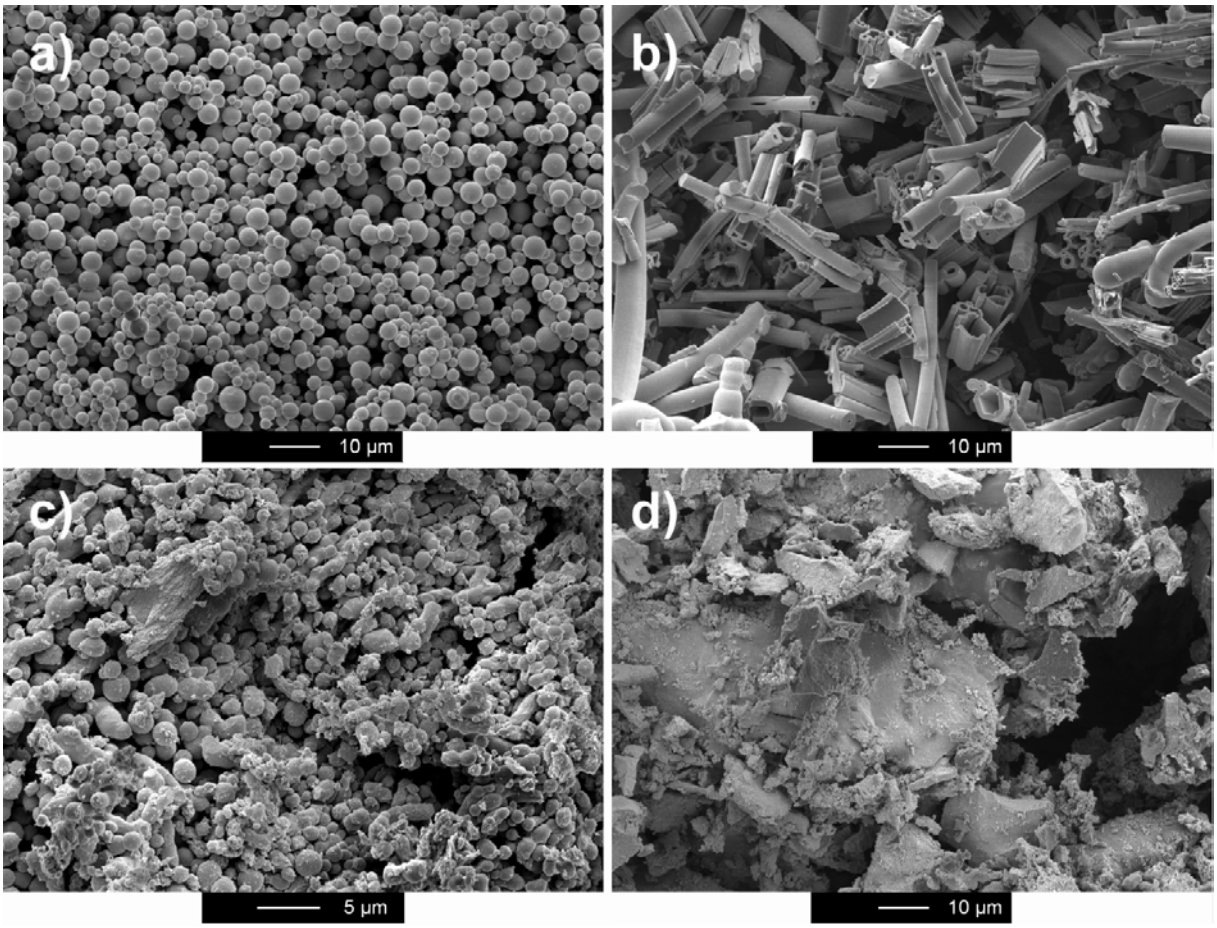

Figure 11. SEM images of titania obtained at different peptide concentrations of **2a** after calcination. (a) 5 mg/mL, (b) 15 mg/mL, (c) 25 mg/mL, (d) 50 mg/mL. Note the different scale bar in (c).

Figure 12 and Table 3 show XRD and TGA data of the mineralized samples. XRD shows that, crystallographically, all samples are pure anatase. Rietveld analysis finds grain sizes (coherence lengths) between 100 and 300 Å, but no trend allowing for the development of a growth model. TGA shows a linear relationship between peptide concentration and weight loss in the mineralized samples: all samples show a weight loss below 100 ºC due to evaporating n-butanol and water. A second weight loss is observed (with the samples made at higher peptide concentration) between 250 and 280 ºC. We assign this loss to peptide decomposition, a further loss of solvent trapped in the inorganic, and possibly also the decomposition of residual titanium butoxide. Finally, a smaller weight loss is observed at 330 ºC, which is most likely due to the decomposition of the peptide *within* the inorganic.

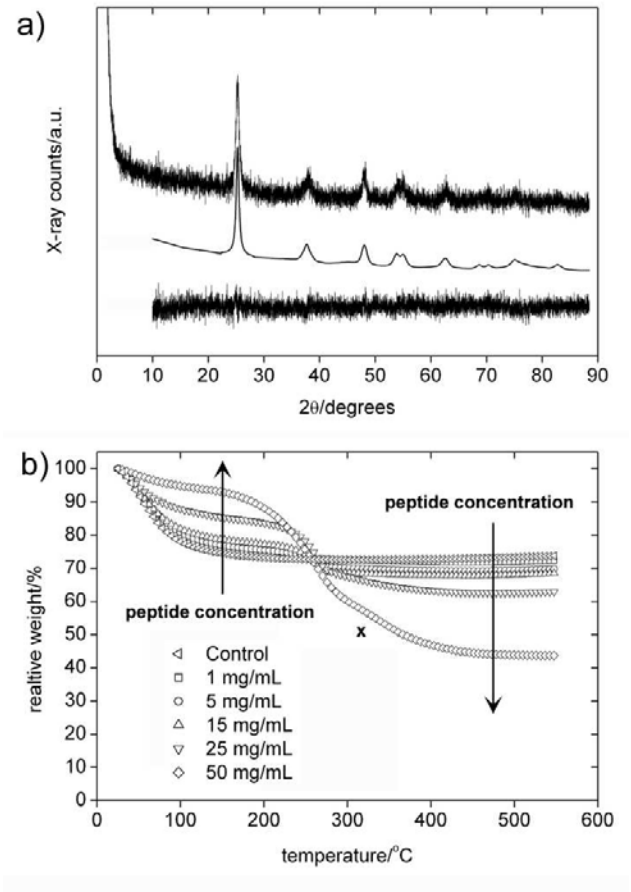

Figure 12. a) Representative X-ray pattern and Rietveld refinement of a sample formed in a gel with 15 mg/mL of peptide (titania tubes, see Figure 7a) after calcination. Top: Y_{obs}, center: Y_{calc}, bottom: Y_{obs}-Y_{calc}. Y_{obs} and Y_{calc} are vertically displaced for better visibility. b) TGA curves of samples formed with peptide concentrations between 0 (control sample) and 50 mg/mL of peptide. (x) denotes the third weight loss described in the text.

Table 3. X-ray results from Rietveld analysis and fraction of organic component from TGA.

Peptide [mg/mL]	Apparent size [Å, XRD]	Weight loss 1 [wt%, TGA]	Weight loss 2 [wt%, TGA]	Weight loss 3 [wt%, TGA]	Total weight loss [wt%, TGA]
0	294.83	27			27
1	124.71	26			26
5	167.90	24	6		30
15	101.81	22	9		31
25	134.92	15	16	6	37
50	152.51	6	33	16	45

3.3.4 Silica formation.

We have also explored the capability of the peptide organogels to form controlled silica architectures. However, the efficiency to generate ordered and uniform structures is, unlike with titania, relatively low. Unlike Stucky and coworkers who have been able to synthesize uniform and well-defined silica nanowires using polypeptides,[24] in our organogels, mixtures of long bundles of wires and spherical particles form. Figure 13 shows fibers formed in the presence 20 mg/mL of the oligopeptide **2a.** The images clearly show that micrometer long bundles of silica fibers form along with aggregated spherical particles. The bundles vary in length but even short bundles are ca. 120 μm long. Figure 13 also shows that the bundles are composed of thin fibers with a diameter between 100 and 200 nm. While there is some variation in the overall fiber diameter of the fibers of the bundle, the diameter of individual fibers (as measured at different locations of one and the same fiber) varies only by ca. 5 %, i.e. 5 to 10 nm.

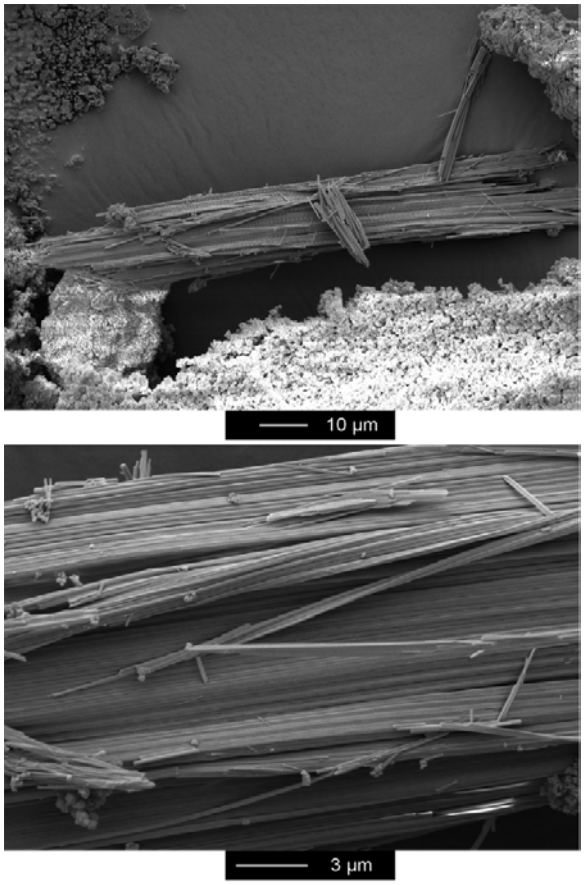

Figure 13. SEM image of a sample obtained with a peptide concentration of 20 mg/mL. a) Low magnification SEM showing a fiber bundle along with aggregated spherical particles; b) higher magnification images showing details of the bundles.

Figure 14 shows the X-ray patterns of several samples. The patterns are essentially identical and show a broad peak due to the amorphous silica at ca. 23 degrees 2θ. In addition, the X-ray patterns of samples with higher peptide concentrations exhibit a small peak at 7.6 degrees 2θ, which we assign to the inter-sheet spacing of the β-sheet of the oligovaline fibers that form the gel.

The inter-sheet spacing of 11.6 Å is slightly larger than in the neat gels (10.8 Å) and also larger than in poly(L-valine) β-sheets (9.6 Å).[44] This increase could is most likely due to the swelling of the peptide fibers with ethanol: as the hydrolysis of TEOS proceeds, ethanol is released into the solvent, which is a good solvent for **2a**, see Table 1.

Determination of the peak widths of the amorphous part show no significant influence of the peptide concentration as all peaks have a full width at half maximum between 7.4 and 8.6 degrees 2θ. These results show that – not surprisingly – the peptide has no influence on the short-range order in the silica.

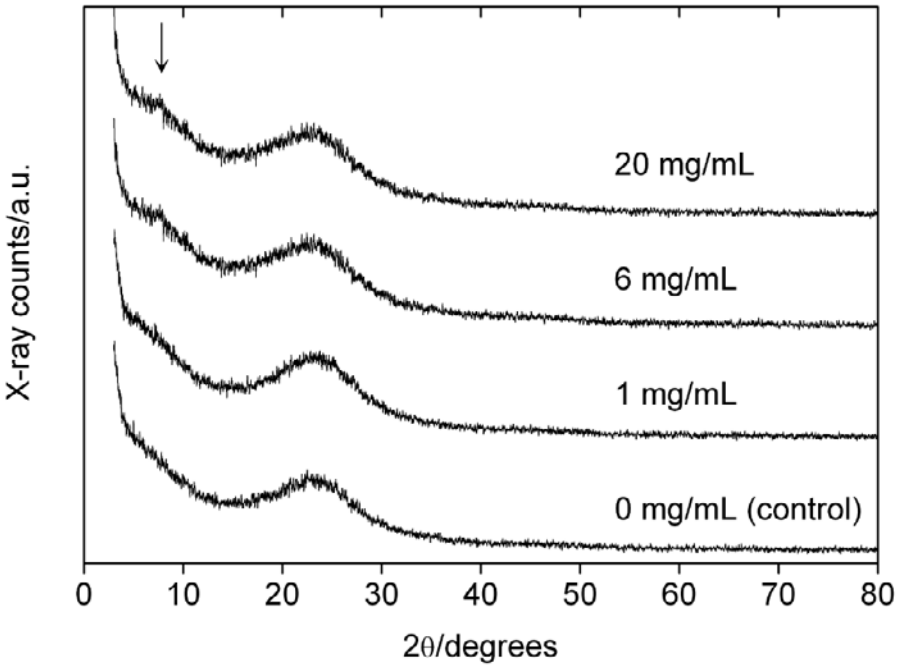

Figure 14. X-ray patterns of silica samples obtained with different peptide concentrations. The arrow highlights the additional reflection appearing at higher peptide concentrations.

Figure 15 shows that the pure peptide loses ca. 4 % of its original weight at 150 ºC and another 94 % at 298 ºC. We assign the first weight loss to water in and on the peptide; the second transition is due to thermal decomposition of the peptide. In contrast, the silica samples lose between 7 and 10 % of their original weight below 100 ºC. We assign this weight loss to both desorption of surface water and to thermal crosslinking of free silanol groups which also leads to a net water loss from the samples. All silica samples show a further weight loss between 270 and 350 ºC. The weight loss increases roughly linearly with the original peptide concentration in the gel, Table 4.

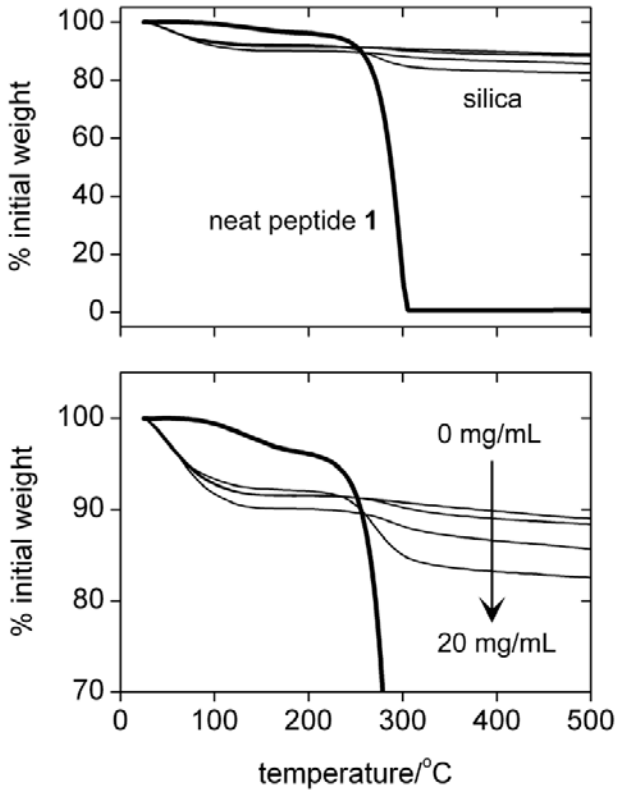

Figure 15. TGA curves of the silica samples and the pure peptide (bold line).

Table 4. Weight loss and temperatures of the respective step from TGA.

Sample	T1 [ºC]	Weight loss [%]	T2 [ºC]	Weight loss [%]
Control	51	-8.2	361	-2.4
1 mg/mL	48	-8.1	314	-2.4
6 mg/mL	61	-10	297	-3.5
20 mg/mL	42	-7.7	270	-8.6
Neat **1**	150	-4	298	-94.0

In summary, we have introduced a simple tool for the controlled fabrication of peptide/anatase, pure anatase and silica materials with a preprogrammed morphology. Titania nanotubes (and many other shapes) have been reported before,[43, 46-53] but this study is to the best knowledge of the authors the first report, where a simple concentration variation in an

organogel allows for titania particle morphology tuning, although the fine tuning and the stabilization of the fibers and other structures is only beginning.

3.4 Conclusions

Simple L-valine-based oligopeptides can act as efficient organogelators. The gelation is similar to other peptide-based organogelators and the synthesis is simple, which is an advantage for large-scale gel fabrication. Furthermore, the peptide organogels are efficient templates for the fabrication of complex titania structures. The exact formation mechanism of those different morphologies is currently under investigation. Further efforts are directed towards a better understanding of the structure of the fibers and the selectivity of these organogelators.

3.5 Acknowledgement

We thank Prof. E.C. Constable for access to his IR spectrometer, M. Düggelin and D. Mathys for SEM measurements, Prof. K.M. Fromm for access to her TGA, and Dr. M. Neuburger for help with the XRD measurements. The Swiss National Science Foundation and the NCCR Nanosciences are acknowledged for financial support. A.T. thanks the Holcim Stiftung Wissen for a Habilitation Fellowship.

3.6 References

[1] E. G. Bellomo, M. D. Wyrsta, L. Pakstis, D. Pochan, T. J. Deming, *Nature Mater.* **2004**, *3*, 244.

[2] S. Zhang, *Nature Biotech.* **2003**, *21*, 1171.

[3] S. Zhang, X. Zhao, *J. Mater. Chem.* **2004**, *14*, 2082.

[4] K. Zhang, M. R. Diehl, D. A. Tirrell, *J. Am. Chem. Soc.* **2005**, *127*, 10136.

[5] J. M. Smeenk, M. B. J. Otten, J. Thies, D. A. Tirrell, H. G. Stunnenberg, J. C. M. van Hest, *Angew. Chem. Int. Ed.* **2005**, *44*, 1968.

[6] K. Hanabusa, K. Okui, K. Karaki, M. Kimura, H. Shirai, *J. Colloid Interface Sci.* **1997**, *195*, 86.

[7] A. Aggeli, M. Bell, N. Boden, J. N. Keen, P. F. Knowles, T. C. McLeish, M. Pitkeathly, S. E. Radford, *Nature* **1997**, *386*, 259.

[8] R. Jayakumar, M. Murugesan, C. Asokan, M. Aulice Scibioh, *Langmuir* **2000**, *16*, 1489.

[9] A. Aggeli, I. A. Nyrkova, M. Bell, R. Harding, L. Carrick, T. C. McLeish, A. N. Semenov, N. Boden, *Proc. Natl. Acad. Sci. USA* **2001**, *98*, 11857.

[10] A. Aggeli, G. Fytas, D. Vlassopoulos, T. C. McLeish, P. J. Mawer, N. Boden, *Biomacromolecules* **2001**, *2*, 378.

[11] A. P. Nowak, V. Breedveld, L. Pakstis, B. Ozbas, D. J. Pine, D. Pochan, T. J. Deming, *Nature* **2002**, *417*, 424.

[12] J. Becerril, M. I. Burguete, B. Escuder, S. V. Luis, J. F. Miravet, M. Querol, *Chem. Commun.* **2002**, 738.

[13] R. Claussen, B. Rabatic, S. I. Stupp, *J. Am. Chem. Soc.* **2003**, *125*, 12680.

[14] J. E. Meegan, A. Aggeli, N. Boden, R. Brydson, A. P. Brown, L. Carrick, A. R. Brough, A. Hussain, R. J. Ansell, *Adv. Funct. Mater.* **2004**, *14*, 31.

[15] M. Suzuki, S. Owa, M. Yumoto, M. Kimura, H. Shirai, K. Hanabusa, *Tetrahedron Lett.* **2004**, *45*, 5399.

[16] M. Moniruzzaman, P. R. Sundararajan, *Langmuir* **2005**, *21*, 3802.

[17] J. Becerril, B. Escuder, J. F. Miravet, R. Gavara, S. V. Luis, *Eur. J. Org. Chem.* **2005**, 481.

[18] F. Fages, F. Voegtle, M. Zinic, *Top. Curr. Chem.* **2005**, *256*, 77.

[19] Y. Yang, M. Suzuki, H. Shirai, A. Kurose, K. Hanabusa, *Chem. Commun.* **2005**, 2032.

[20] Y. Jeong, K. Hanabusa, H. Masunaga, I. Akiba, K. Miyoshi, S. Sakurai, K. Sakurai, *Langmuir* **2005**, *21*, 586.

[21] J. D. Hartgerink, E. Beniash, S. I. Stupp, *Science* **2001**, *294*, 1684.

[22] L. E. Euliss, T. M. Trnka, T. J. Deming, G. D. Stucky, *Chem. Commun.* **2004**, 1736.

[23] D. Volkmer, M. Fricke, T. Huber, N. Sewald, *Chem. Commun.* **2004**, 1872.

[24] J. N. Cha, G. D. Stucky, D. E. Morse, T. J. Deming, *Nature* **2000**, *403*, 289.

[25] S. V. Patwardhan, S. J. Clarson, *J. Inorg. Organomet. Polymers* **2003**, *13*, 193.

[26] D. Belton, G. Paine, S. V. Patwardhan, C. C. Perry, *J. Mater. Chem.* **2004**, *14*, 2231.

[27] M. Sumper, N. Kröger, *J. Mater. Chem.* **2004**, *14*, 2059.

[28] F. Rodriguez, D. D. Glawe, R. R. Naik, K. P. Hallinan, M. O. Stone, *Biomacromolecules* **2004**, *5*, 261.

[29] D. D. Glawe, F. Rodriguez, M. O. Stone, R. R. Naik, *Langmuir* **2005**, *21*, 717.

[30] S. V. Patwardhan, R. Maheshwari, N. Mukherjee, K. L. Kiick, S. J. Clarson, *Biomacromolecules* **2006**, *7*, 491.

[31] N. Kröger, G. Lehmann, R. Rachel, M. Sumper, *Eur. J. Biochem.* **1997**, *250*, 99.

[32] N. Kröger, R. Deutzmann, M. Sumper, *Science* **1999**, *286*, 1129.

[33] N. Kröger, S. Lorenz, E. Brunner, M. Sumper, *Science* **2002**, *298*, 584.

[34] N. Poulsen, N. Kröger, *J. Biol. Chem.* **2004**, *279*, 42993.

[35] K. K. W. Wong, T. Douglas, S. Gider, D. Awschalom, S. Mann, *Chem. Mater.* **1998**, *10*, 279.

[36] T. Douglas, V. T. Stark, *Inorg. Chem.* **2000**, *39*, 1828.

[37] D. Resnick, K. Gilmore, Y. U. Idzerda, M. Klem, E. Smith, T. Douglas, *J. Appl. Phys.* **2004**, *95*, 7127.

[38] R. M. Kramer, C. Li, D. C. Carter, M. O. Stone, R. R. Naik, *J. Am. Chem. Soc.* **2004**, *126*, 13282.

[39] *http://www-llb.cea.fr/fullweb/fp2k/fp2k.htm* **2006**, *August*.

[40] L. W. Finger, D. E. Cox, A. P. Jephcoat, *J. Appl. Cryst.* **1994**, *27*, 892.

[41] M. Palumbo, S. Da Rin, G. M. Bonora, C. Toniolo, *Makromol. Chem.* **1976**, *177*, 1477.

[42] M. H. Baron, C. De Loze, C. Toniolo, G. D. Fasman, *Biopolymers* **1979**, *18*, 411.

[43] M. Suzuki, J. Nakajima, T. Sato, H. Shirai, K. Hanabusa, *Chem. Commun.* **2006**.

[44] O. Yamashita, T. Yamane, T. Ashida, S. Yamashita, T. Yamashita, *Polymer J.* **1979**, *11*, 763.

[45] M. V. Deshmukh, G. Voll, A. Kühlewein, H. Mäcke, J. Schmitt, H. Kessler, G. Gemmecker, *J. Med. Chem.* **2005**, *48*, 1506.

[46] T. Kasuga, M. Hiramatsu, A. Hoson, T. Sekino, K. Niihara, *Adv. Mater.* **1999**, *11*, 1307.

[47] Y. Zhu, H. Li, Y. Koltypin, Y. H. Rosenfeld, A. Gedanken, *Chem. Commun.* **2001**, 2616.

[48] S. Kobayashi, N. Hamasaki, M. Suzuki, M. Kimura, H. Shirai, K. Hanabusa, *J. Am. Chem. Soc.* **2002**, *124*, 6550.

[49] J. H. Jung, H. Kobayashi, K. J. C. van Bommel, S. Shinkai, T. Shimizu, *Chem. Mater.* **2002**, *14*, 1445.

[50] C. N. R. Rao, M. Nathab, *Dalton Trans., 2003, 1-24* **2003**, 1.

[51] A. Collins, D. Carriazo, S. A. Davis, S. Mann, *Chem. Commun.* **2004**, 568.

[52] J. Zhao, X. Wang, T. Sun, L. Li, *Nanotechnology* **2005**, *16*, 2450.

[53] M. A. Khan, H.-T. Jung, O. Yang, *J. Phys. Chem. B* **2006**, *110*, 6626.

[54] M. Windholz, S. Budavan, P. G. Stecher, *Merck Index*, 8. ed., Merck, Rahway, N.J., **1968**.

4. Silver nanoparticle growth controlled by modular oligovaline organogels

Alexandre Mantion,[1] Géraldine Guex,[1] Annette Foelske,[2] Laurent Mirolo,[3] Katharina M. Fromm,[3] Monika Painsi,[4] and Andreas Taubert[1,5,]*

1 Department of Chemistry, Klingelbergstr. 80, University of Basel, CH-4056 Basel, Switzerland

2 Electrochemistry Laboratory, Paul Scherrer Institute, CH-5232 Villingen, Switzerland

3 Department of Chemistry, University of Fribourg, Chemin du Musée 9, CH-1700 Fribourg, Switzerland

4 Institute of Geological Sciences, University of Bern, Baltzerstrasse 1-3, CH-3012 Bern, Switzerland

5 Institute of Chemistry, University of Potsdam, D-14476 Golm, Germany and Max-Planck-Institute of Colloids and Interfaces, D-14476 Golm, Germany.

Accepted as a paper to *Soft Matter*

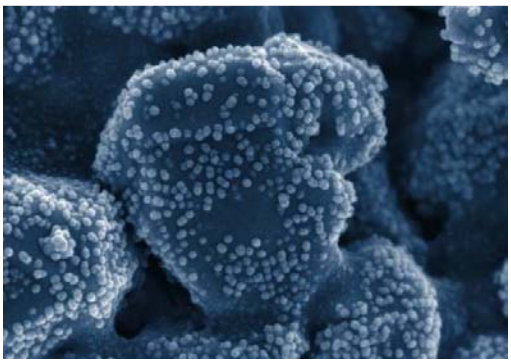

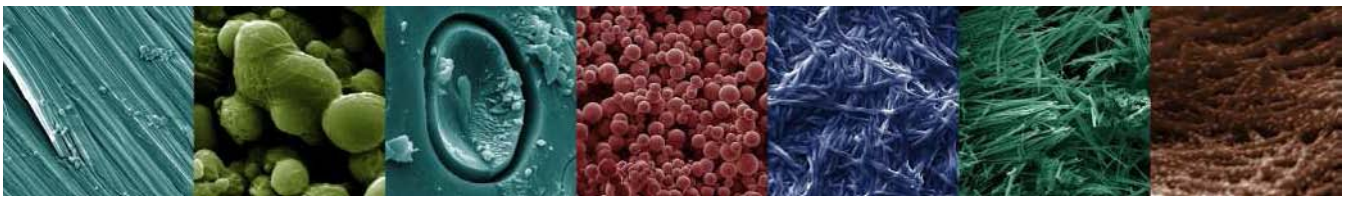

4.1 Introduction

Metal colloids and their assemblies have arguably become one of the most popular research fields since the original discovery of colloidal gold by Michael Faraday and their subsequent rediscovery in the late 20th century.[1-3] Since the development of the so-called Brust-Shiffrin method,[4, 5] extensive work on the synthesis and physical properties of colloidal metal particles has been done. This includes studies on the role of particle composition (pure particles vs. doping or alloying), surface modification with organic or inorganic structures like additional shells or (bio)molecules, particle shape and size etc. on the optical and electronic properties of such nanoparticles and nanoparticle arrays.[6, 7] Interestingly however, there are only a few reports on the formation of metallic particles in organogels, in particular in peptide organogels.[8-10] This is intriguing because peptide chemistry and peptide self-assembly is nowadays quite well understood. Peptide scaffolds should therefore be prime candidates for the fabrication of ordered nanoparticle arrays with more or less rationally designed structures and properties.

There are only a few examples of silver nanoparticle synthesis and supramolecular organization using small peptides and proteins as templates or scaffolds. Tryptophane and tyrosine-containing peptides have been used as gelators and growth modifiers for silver colloids in aqueous solution and organic solvent/water mixtures.[11-13] Djalali et al. and Slocik and Wright have used histidine-rich residues for templating gold nanocrystals and other noble metal nanoclusters.[14, 15] These studies all show that peptides can act as *in situ* reducing agents and/or as nucleation centers for the formation of silver particles with various shapes.

Proteins have also been reported to control the spatial organization of silver nanoparticles in one and two dimensions. This is done by exploiting the spatial organization of cysteine residues on the protein surface and the corresponding thiol-metal nanoparticle interactions. Alternatively, weak interactions like peptide non-specific adsorption, metal pre-concentration, or amine stabilization on the fiber also play a role.[14-17] However, up to now, there have been no reports on thiol or thioether incorporation into rather stiff (stiff compared to thiols in solution) supramolecular assemblies like peptide fibers and the effect of such templates on metal nanoparticle formation.

Our group has recently reported the formation of oligovaline organogels where the peptide fibers act as templates for various TiO_2 morphologies.[18] Here we report that by simply replacing the C-terminal valine with a benzyl-protected cysteine, Scheme 1, the same oligovaline family can be used for the fabrication of supramolecular scaffolds for silver nanoparticle mineralization. The ratio of the pure oligovaline **1** vs. sulfur-containing peptide **2** in the gel allows for a simple control over the silver mineralization reaction.

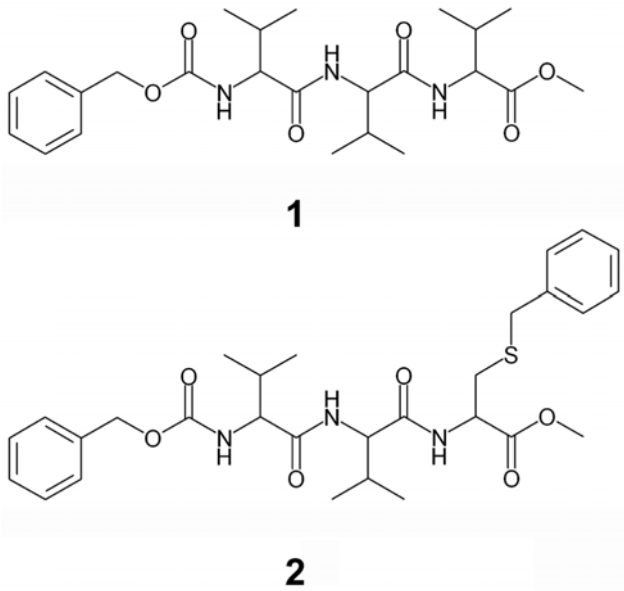

Scheme 1. Oligopeptides used in the current study. All amino acids are L-amino acids.

4.2 Experimental

Peptide synthesis. Amino acids were purchased from Bachem AG (Bubendorf, Switzerland) and chemicals from Fluka (Buchs, Switzerland). All chemicals were used as received. ZVV-OH and Z-$(Val)_3$-OMe **1** was obtained as described before.[18]

Synthesis of ZVVC(SBzl)OMe 2. 1.4 mL (10.3 mmol) of isobutyl chloroformate were added to a salt/ice cooled solution of ZVV-OH (3.0 g, 8.6 mmol) and 4-methylmorpholine (1.7 mL, 14.6 mmol) in 25 mL of acetonitrile under argon. The reaction mixture was stirred for two minutes. Then 2.7 g (10.3 mmol) of L-cysteine-S-benzyl methyl ester hydrochloride and 1.7 mL (14.6 mmol) of 4-methylaminomorpholine were added. After

15 minutes, the cooling was removed and the solution was allowed to warm up to room temperature, upon which the solution was stirred for 24 hours. The solvents were removed by rotary evaporation. The residue was dissolved in 200 mL of a mixture of chloroform and methanol (3:1). The organic solution was washed three times with 100 mL of a saturated hydrogen carbonate/sodium chloride solution and once with sodium chloride solution. Then 100 mL of methanol were added, and the solution was washed three times with 100 mL of a mixture of 10 % citric acid and sodium chloride solution, and finally twice with a sodium chloride solution. The organic phase was dried with sodium sulfate, concentrated to dryness, and the residue was triturated with pentane to give a white to slightly yellowish solid (3.1 g, 65 %) after drying in vacuum overnight. IR (neat, cm^{-1}): 3284, 3080, 2950, 1741, 1686, 1638,1537, 1454, 1342, 1290, 1246, 1217, 1073, 1006, 990, 967, 921, 879, 863, 843, 808, 770, 755, 738, 696, 660, 609. ^{13}C-NMR (δ in ppm vs. TMS, d6-DMSO, 100 MHz, signals of all conformers in brackets): 172.24, 171.82, 171.77, {157.10 - 156.95}, 138.90, {137.96 - 137.88}, 129.77, 129.77, 129.74, 129.24, 129.18, 128.60, 128.47, 127.76, {66.27 - 66.20}, {61.15 - 61.10}, {57.97 - 57.90}, {52.92 - 52.85}, {52.62 - 52.42}, {52.92 - 52.85}, {52.60 - 52.46}, 36.25, 32.62, 20.10, 19.90, 19.08. ^{1}H-NMR (δ in ppm vs. TMS, d6-DMSO, 400 MHz): 8.46 (m, 1 H, H amide), 7.91 (m, 0.3 H, H amide), 7.73 (m, 0.7 H, H amide), 7.27 (m, 11 H, H carbamate + cysteine benzyl ring + benzyl), 5.01 ppm (s, 1 H, benzylic), 4.99 ppm (s, 0.7 H, benzylic), 4.45 (m, 1 H, α Val-1), 4.27 (m, 1 H, α Val-2), 3.96 (m, 1 H, α Cys), 3.72 (m, 2 H, benzyl Cys), 3.60 (m, 3 H, methyl ester), 2.76 (m, 1 H, β cys), 2.64 (m, 1 H, β cys), 1.96 (m, 2 H, β Val-1 + β Val-2), 0.85 (m, 12 H, γ Val-1 + γ Val-2). Elemental analysis: calculated: C 62.46, H 7.05, N 7.53, O 17.21, S 5.75; measured: C 62.52, H 6.95, N 7.55. FAB-MS: calculated $M\text{-}H^+$ = 557, measured $M\text{-}H^+$ = 557.

Silver nanoparticle synthesis. In a typical experiment, 25 mg (0.054 mmol) of ZVVVOMe **1** were mixed with 75 mg (0.135 mmol) of ZVVC(SBzl)OMe **2** in a vial. Then 1 mL of n-butanol and 100 µL of DMF were added. The vial was heated to 80 to 100°C, and as soon as the peptide was dissolved, 26 mg (0.153 mmol) of silver nitrate dissolved in 60 µL of distilled water are added to the vial. The mixture is then shaked for 30 s, followed by rapid heating with a hotplate to 80 °C. Then the vial was closed and left untouched in the dark for 5 days.

Spectroscopy. ^{1}H and ^{13}C NMR spectra were recorded on an Avance 400 MHz NMR spectrometer. Infrared spectra were obtained from the neat samples on a Shimadzu FTIR 8300 with a Golden Gate ATR unit. Spectra were recorded from 300 cm^{-1} to 4500 cm^{-1} with a resolution of 1 cm^{-1}. FAB-MS spectra were taken on a Finnigan MAT 312. UV/Vis spectroscopy was performed in a quartz cuvette with an optical path length of 1 cm on a Perkin Elmer Lambda 25 or an Agilent 8453 using the same cuvette for the titration experiment. Data deconvolution was performed using Fytik and the Chemstation Agilent software was used to retrieve data values.

Surface Enhanced Raman Scattering. Silver wafers of 1 cm x 1 cm x 0.05 cm were degreased with acetone, dried with argon, and etched for 3 min in 3.5 M nitric acid under stirring.[42] The silver was dried with argon and immersed in a hot methanolic, approximately 1 mM peptide solution. After 10 minutes, the wafer was removed from the solution, the excess of solution was removed by argon flushing, and the wafer was dried at 40 °C in a vacuum oven overnight. Microscopy was done with an Olympus BX 41 (100 x objective) optical microscope coupled to a Labram HR800 Jobin Yvon Horiba Raman spectrometer with a 514 nm laser and a power of 5.20 mW. The confocal hole was 400 µm and the slit 150 µm.

Microscopy. Scanning electron microscopy was done on a Hitachi S-4800 operated at 10 kV. Samples were sputtered with 5 nm of platinum prior to imaging. TEM images were taken using an FEI Morgani 268D operated at 80 kV. Samples were deposited on carbon-coated copper grids and directly imaged after drying in air. Some samples were diluted prior to imaging to allow for better imaging conditions.

X-ray diffraction. X-ray patterns were measured at room temperature on a Stoe Stadi P diffractometer equipped with a curved germanium monochromator. X-ray radiation was CuKα radiation and data analysis was done with OriginLab Origin 6.1.

X-Ray Photoelectron Spectroscopy. XPS was done on a VG ESCA Lab 220iXL with a Mg Kα (1253.6 eV) source. Take-off angle was 90° and the pressure during measurements was 10^{-10} mbar. The silver wafer had dimensions of ca. 1.5 cm x 1.5 cm x 0.05 cm. Wafers were first degreased with acetone, then three times chemically etched with concentrated nitric acid, rinsed with distilled water, and finally dried with argon. The clean

silver wafers were immersed in a rapidly stirred, hot methanolic solution of the peptides or in neat methanol for the control measurements. After ten minutes and two hours of immersing, the wafers were removed from the solution, the excess solution was removed by flushing the wafer with argon and the wafers were then dried overnight vacuum at 40°C. Data analysis was done using Unifit 2006 (evaluation version) and XPSPEAKS 4.1.

4.3 Results

Gels before mineralization. The structural similarity between gels of either pure **1** or pure **2** and mixed gels containing **1** and **2** was studied via by X-ray diffraction and IR spectroscopy. Figure 1 shows IR spectra of various gels. IR spectroscopy reveals that the gels form via β-sheet formation of the individual peptide building blocks. The IR spectra of all gels are virtually indistinguishable, indicating that they all have the same structural organization. However, much like in our previous study,[18] we cannot unambiguously distinguish between parallel or anti-parallel β-sheet due to the presence of the carbamate and methyl ester carbonyl bands which overlap with the diagnostic antiparallel/parallel β-sheet vibrations at 1700 cm^{-1}.

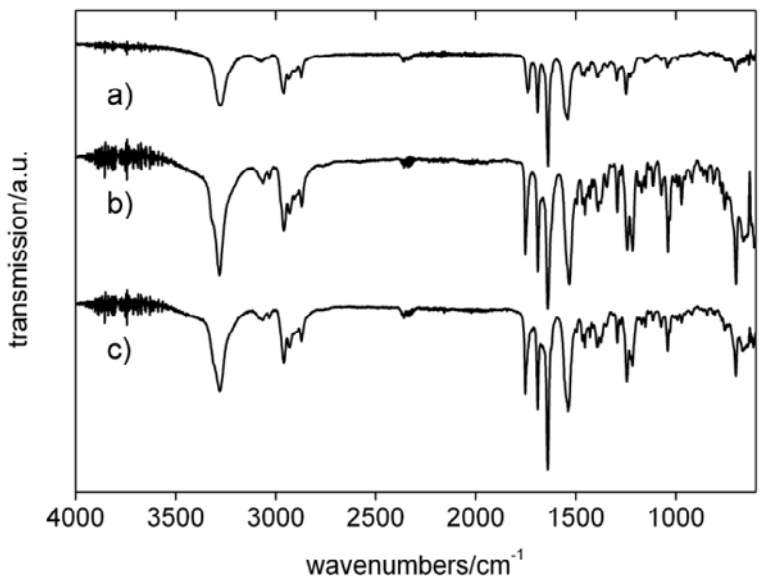

Figure 1. IR spectra of gels with (a) pure **2** (b) 50 % of **1** and 50 % of **2**, and (c) pure **1**.

Figure 2 shows X-ray patterns of the same gels. Overall, XRD indicates a moderately ordered structure without any particular features. XRD patterns of gels of pure **1** exhibit two reflections at 18.8 (d-spacing of 4.7 Å) and 22.2 (d-spacing of 3.9 Å) degrees 2θ, which were earlier assigned to a fiber structure similar to polyvaline.[18] Interestingly, the current XRD data show that the addition of peptide **2** to peptide **1** improves the order within the fibers. The increasing number of (narrow) reflections observed with increasing fraction of **2** in the gels suggests that the additional thioether functionality and the additional aromatic ring further stabilize the peptide **2** when compared to the pure tri-valine peptide **1**. It also suggests and that peptide **2** leads to a somewhat more crystalline order in the fibers.

Overall, XRD shows that all samples have a similar structural organization, which is consistent with IR spectroscopy. Closer inspection reveals minute shifts (below 0.8 degrees 2θ) in the XRD patterns of the different samples. This indicates that there are slight differences between samples containing different fractions of **1** and **2**, which however does not affect the overall organization of the peptide assemblies. These differences are attributed to minor size differences between **1** and **2**, similar to a study by Sunde et al.[19] The absence of abrupt structural changes between fibers of pure **1** and pure **2** implies that the two peptides are structurally similar enough to not disturb their respective supramolecular order upon co-assembly.

Finally, XRD indicates that all peptide fibers adopt an amyloid quaternary structure upon gelation, regardless of their composition (pure peptides or mixtures of **1** and **2**). The helical pitch of the structure is 115 Å, as determined from the reflections at 18.3(5), 18.8(3), 30.9(0), 39.6(9) degrees 2θ. This matches earlier data by Sunde et al.[19] on proteins self-assembling into amyloid fibrils. The pitch corresponds to 25 peptides in the helical repeating unit as is classically accepted for amyloid fibers.[19, 20]

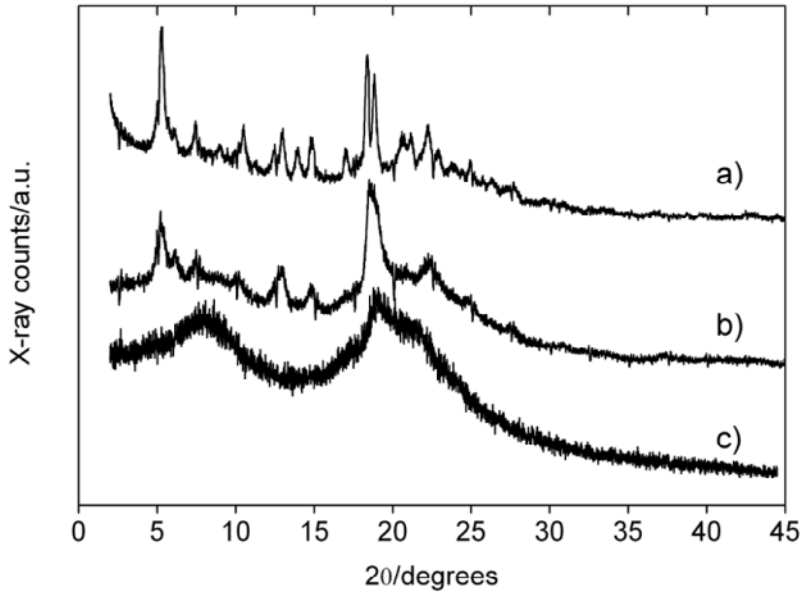

Figure 2. XRD patterns of gels with (a) pure **1** (b) 50 % of **1** and 50 % of **2**, and (c) pure **2**.

Figure 3 shows representative SEM images of some gels. SEM shows that in all cases the peptides self-assemble into long fibers with a diameter of ca. 60 nm (pure **1**), 25 nm (mixtures of **1** and **2**), and 500 nm (pure **2**). The latter value may not be from the individual fibers, as those large fibers seem to be composed of thinner fibers as well. These could, however, not be resolved.

The fibers of pure **2** often appear somewhat "crystalline" in that they exhibit edges or flat areas that could be poorly developed crystal faces. This is further supported by the fact that gels formed from pure **2** show additional reflections in XRD, Figure 2. We therefore conclude that **2** forms peptide fibers and gels, but SEM and XRD also provide circumstantial evidence that **2** crystallizes more readily than **1**. This higher tendency towards crystallization is assigned to the presence of an additional aromatic ring in the thioether moiety of **2**. The resulting π-π stacking interaction at least partially favors crystallization of **2**. The combination of **1** and **2** in one fiber, however, completely inhibits the formation of larger crystalline units. This finding is further evidenced by the fact that the gels with (large fractions) of **2** are opaque, whereas the gels with **1** and mixtures of **1** and **2** are transparent to very slightly opaque.

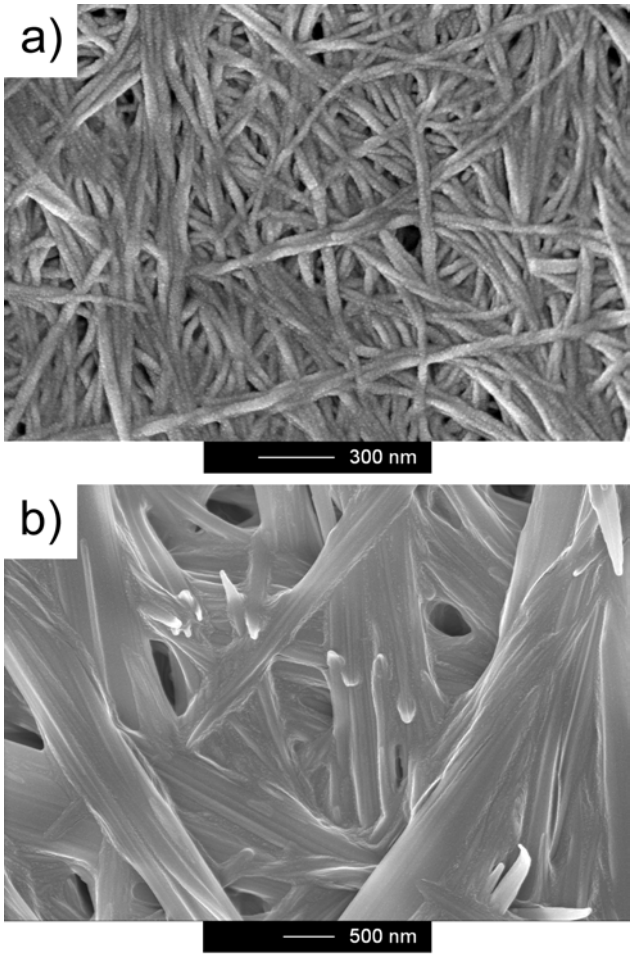

Figure 3. SEM images of gels before mineralization. (a) Pure **1** and (b) pure **2**.

Mineralized gels. Figure 4 shows that the IR spectra of the organogels remain unaffected by the mineralization process. This indicates that there is no change in the supramolecular structure of the self-organized fibers upon silver deposition. Specifically, IR spectroscopy shows that the vibration at 1634 cm^{-1} indicative of the β-sheet is conserved.[18] Furthermore, IR shows that the chemical integrity of the peptides is maintained and the peptides are not damaged during mineralization because the spectra of the precursor gels and the mineralized gels are identical. Even the thioether moiety is unaffected by silver mineralization. This is evidenced by the fact that no –S-H band (indicative of thioether cleavage) is observed at ca. 2550 cm^{-1}. Moreover, there are no sulfone or sulfoxide bands at 1100 to 1300 and at 1050 cm^{-1} indicative of sulfur oxidation.

The only significant change between the non-mineralized and the mineralized gels are several peak shifts. The carbonyl band of the methyl ester at 1738 cm^{-1} shifts by 24 cm^{-1} compared to the pure organogel. This shows that the methyl ester is not hydrolyzed, because the band persists, but that its local environment changes. Contrary to the work of Si et al.,[11] our approach to silver deposition does not involve strong bases or alkaline conditions. As a result, the methyl ester is not cleaved and remains intact. Furthermore, the amide II band at 1529 cm^{-1} shifts by 3 cm^{-1}, but remains strong and intact, showing that the integrity of the peptide backbone is unaffected by the silver deposition and there is no significant structural change either.[11]

Overall, IR spectroscopy shows that there are some interactions of the peptides with the silver crystals, most prominently via the carbonyl group of the methyl ester. The quite large shift of over 20 cm^{-1} indicates that the interaction is quite strong. However, the fact that the band does not disappear upon mineralization shows that also the methyl ester is not cleaved during mineralization. IR spectroscopy therefore clearly confirms that the silver deposition using DMF in oligovaline organogels is a soft method leaving the peptide scaffold intact.

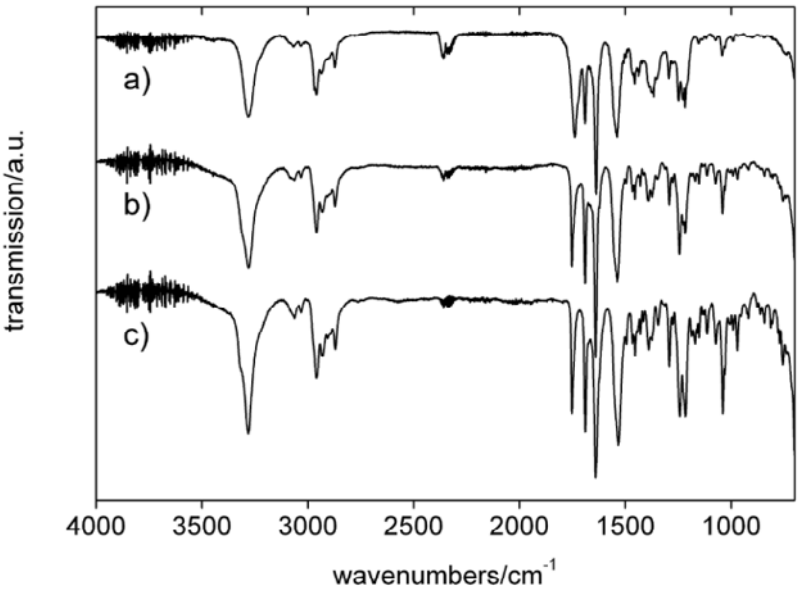

Figure 4. IR of the gels after mineralization. (a) Pure gel of **1**, (b) mixture of 50% **1** and **2**, (c) pure **2**.

Figure 5 shows SEM images of the mineralized gels. The images clearly show that the gel structure is conserved, that is, that the fibers are intact even after mineralization. In all cases, the peptide fibers are comparable to their non-mineralized analogs, but they are covered with particles of different shapes and sizes.

The fibers containing only **2** or a large fraction of **2** are densely covered small particles with a diameter of ca. 9 nm. Some larger particles are also present. As the fraction of **2** in the fibers decreases, the particles grow larger. Also, the decreasing fraction of **2** leads to the formation of more diverse particle shapes. Particles with triangular and related shapes are the predominant species at 50% of **2.** At even lower contents of 25% of **2**, most silver particles are above 100 nm in size and partly have well-defined triangular and related shapes. Mineralization of gels of pure **1** leads to samples with large particles of various shapes where the silver particles appear not tightly associated with the peptide fibers anymore. In all cases some fraction of the ca. 9 nm particles are also visible.

These data show that the gels composed of just peptide **1** are only weak growth modifiers for silver, whereas increasing fractions of **2** make them more and more efficient growth modifiers. This is not surprising, as thioethers and thiols are known to interact with silver particles[21] and the thioether is therefore most likely the unit controlling silver nanoparticle growth on the fibers. Removal of the strong silver-sulfur interaction leads to a system, which allows for much less control over the mineralization process and the entirely hydrophobic peptide **1** will lead to crystal growth, which is essentially unrestricted by strongly interacting moieties.

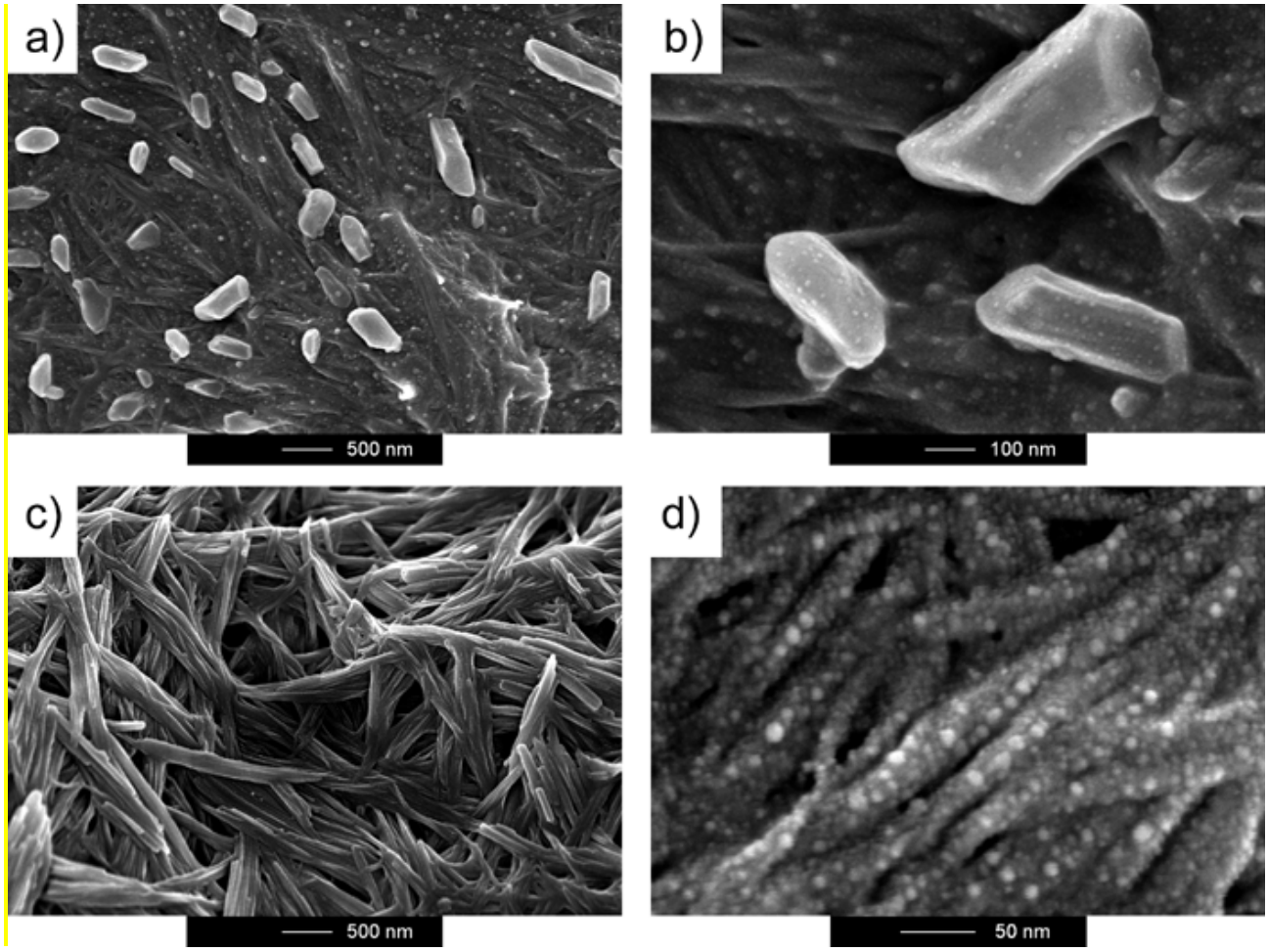

Figure 5. SEM images of the gels after mineralization. (a, b) Gel with pure **1**, (c, d) gel with pure **2**.

More detailed SEM and transmission electron microscopy (TEM) investigations show that some of the particles formed at different ratios of **1** and **2** have quite complex morphologies. Figure 6 shows that, besides the ca. 9 nm particles and the large particles discussed above, also more complex particle morphologies form. With decreasing content of **2**, plates are increasingly observed, including plates with holes that have presumably formed via fusion of separately grown platelike crystals. Furthermore, larger spheres, sometimes organized in chains, are observed. Finally, at contents below ca. 25% of **2**, we also observe what appears to be bandlike structures, which, interestingly, are single crystalline particles or particles with a single crystal texture, as is evidenced by electron diffraction of several samples (Figure 6e, f).

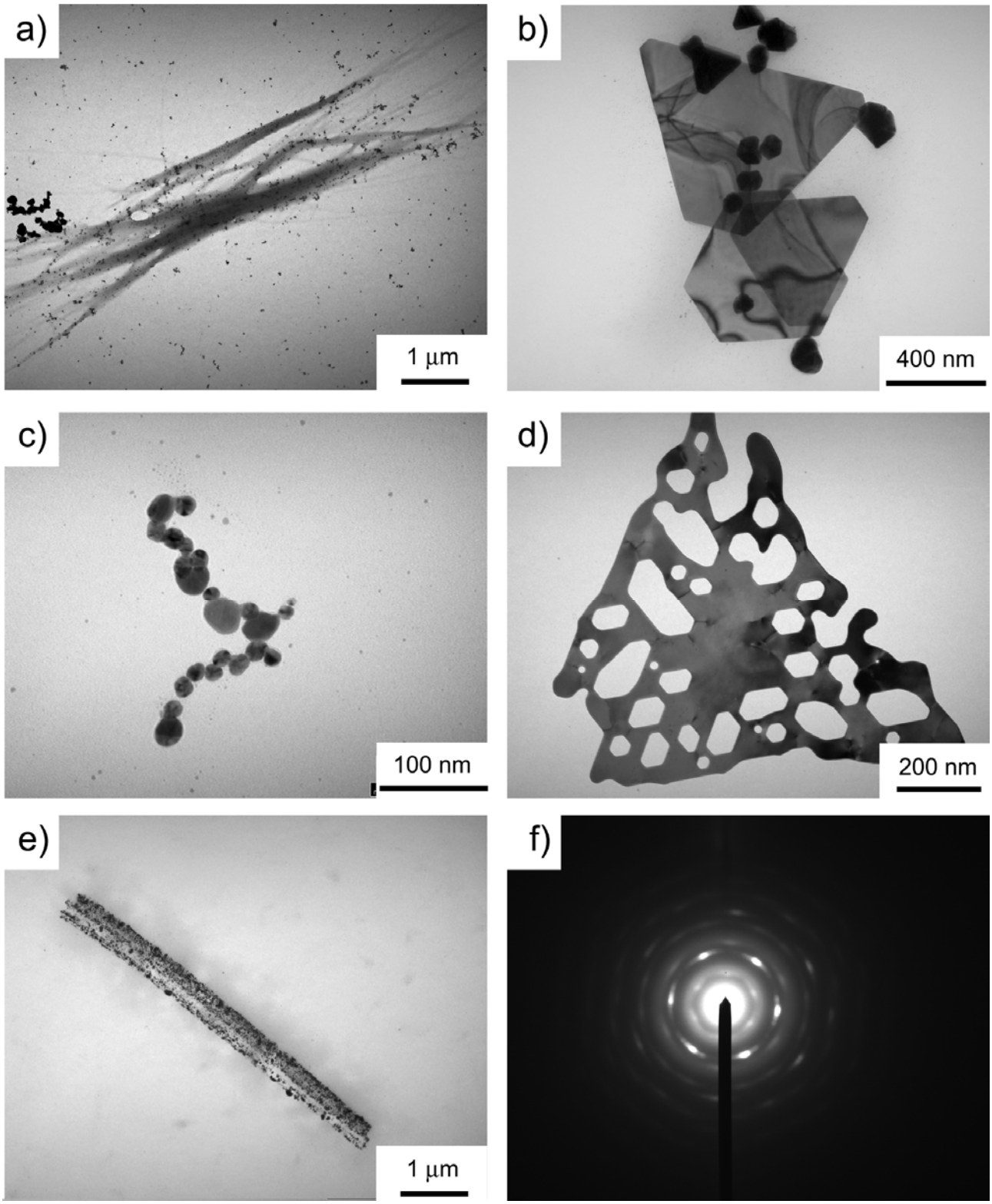

Figure 6. TEM images of select peptide/nanoparticle aggregates. (a) 100% of **2**, (b, c) 50 % of **2**, (d, e) 0 % of **2**, (f) Electron diffraction pattern of the sample shown in (e).

Figure 7 shows additional SEM images of samples grown at contents of **2** of 20% and 15%. These particles often appear to have been covered with a second generation of smaller particle or particles with a “raspberry” morphology. We currently explain these features with heterogeneous nucleation on already existing silver particles (mostly plates), which seems to be energetically more favorable than further nucleation on the peptide fibers. We speculate that in the first deposition process, where the larger particles (Figure 7b) form, nucleation and growth is preferred at locations with a high local concentration of the thioether moiety, that is, with a high concentration of **2**. As a result, further nucleation and growth at other locations may be less favorable than heterogeneous (epitaxial) nucleation and growth on existing silver crystals.

In summary, SEM and TEM show that there is a transition from pure, ca. 9 nm spheres at 100% of **2** (Figures 5c,d and 7a) to samples containing the same spheres along with plates and larger spheres (Figure 7b, c) at 50% of **2**. A further decrease of the content of **2** yields samples containing the small spheres, plates (occasionally with quite complex “holey” triangular or ribbon-like shapes) between 25 and 0% of **2** (Figures 5a, b, 7d, e). In the same regime, we also often observe particles that appear to have been covered with a second generation of smaller particle or particles with a “raspberry” morphology. This can be explained by secondary nucleation and growth, which is preferred over growth on predominantly oligovaline fibers, which only slightly interact with the particles.

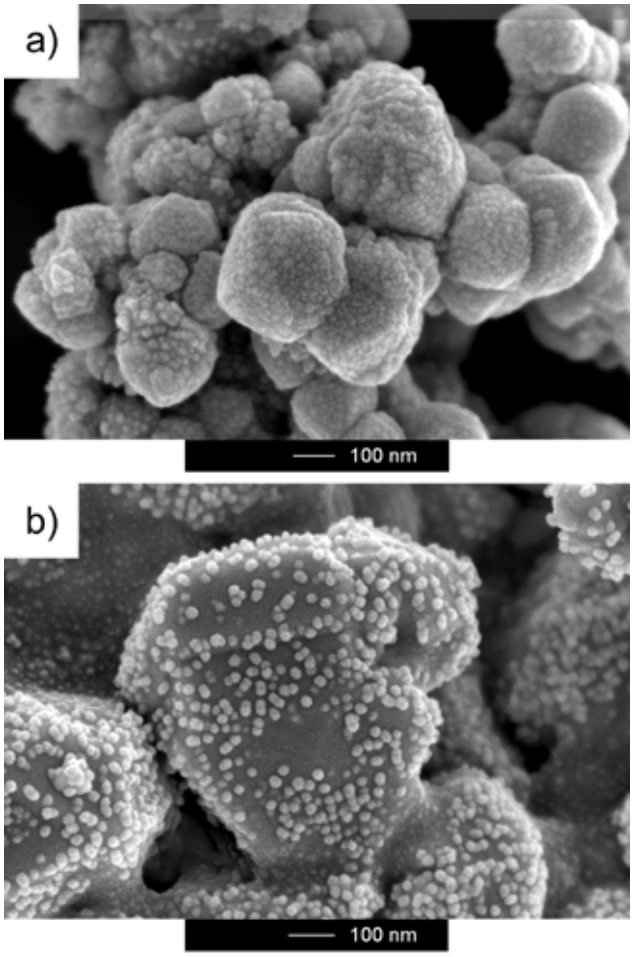

Figure 7. SEM images of select silver nanocrystals. (a) Sample precipitated with 85% of **1** and 15% of **2** and (b) sample precipitated with 80% of **1** and 20% of **2**. The sample shown in (a) has a raspberry-like morphology and the sample shown in (b) clearly shows evidence for heterogeneous nucleation and growth on preexisting silver plates or larger crystals.

Visual inspection shows that the color of the gels changes from purple (gels containing pure **2**) to green with increasing fraction of **1**. Gels from pure **1** have a silverish luster. UV/Vis spectroscopy has been successfully used for the characterization of nanoparticle shapes and sizes, including silver particles.[22-24] Figure 8 shows a representative UV/Vis spectrum of silver particles isolated from a sample containing 50% of **1** and 50% of **2**. Essentially, all spectra only exhibit two to three very broad bands or shoulders. The fact that the bands are broad indicates that the silver particles created here are not very homogeneous in size. Fitting the UV spectra with Gaussian profiles shows that the spectra are composed of up to seven overlapping bands. The bands at 340 to 355 nm, 360 to 385, 400 to 430, and 455 to 490 nm

are attributed to overlapping peaks from scattering and plasmon resonances of the silver particles.[22, 23] These bands vary from sample to sample, which can again be explained by the presence of particles with different sizes and shapes. Bands between 525 and 575 can be attributed to distorted nanoparticles (bent plates or particles with distortions in the crystal lattice). If the amount of **2** is 75% or lower, two bands at around 525 and 660 nm are found. The former is again assigned to distorted particles and the latter band is due to the presence of (truncated) triangular nanoparticles.[22]

A further decrease of the fraction of **2** in the gels leads to another broad peak between 630 and 665 nm, which can be assigned to the formation of polygon (twinned) crystals and triangular particles.[23, 25] Samples grown in gels containing only 25% of **2**, exhibit another broad band at around 920 nm. This band has earlier been assigned to self assembled raspberry-like structures or silver nanowires.[23] Without **2**, the particles behave spectroscopically as bulk material, although SEM and TEM show that these samples contain nanoparticles as well. Essentially, UV spectroscopy provides evidence that the mineralized gels contain particles of a diverse size and shape, which is consistent with SEM and TEM, see Figures 6 and 7. Table 1 summarizes the absorption band positions obtained after deconvolution with Gaussian profiles.

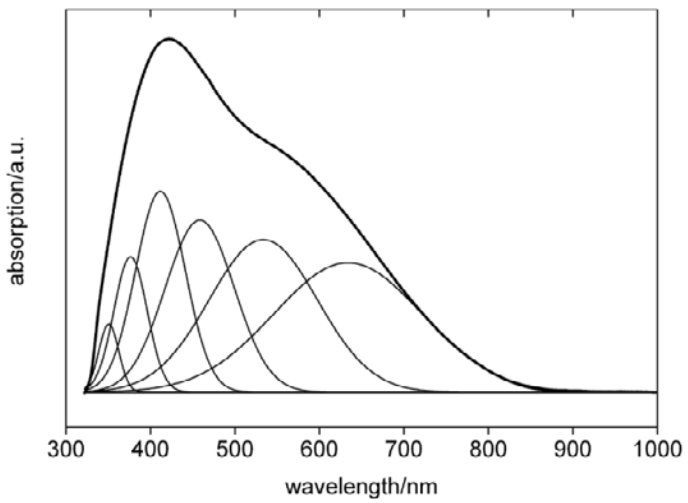

Figure 8. UV/Vis spectrum of particles isolated from a sample containing 50% of **1** and 50% of **2** dissolved in methanol.

Table 1. UV bands determined from Gaussian fitting.

wt% of 2 in the gel fibers	Band position (nm)
100	352, 379, 416, 472, 559, (977, weak)
75	355, 385, 428, 490, 573
50	350, 376, 411,458, 533, 633
25	342, 363, 401, 456, 525, 663, 924
0	No absorption detected

Figure 9 shows X-ray patterns of some mineralized gels. The patterns again exhibit more and sharper peaks as the fraction of **2** increases. This shows that the integrity of the peptide fibers is unaffected by the mineralization process, although slight shifts in the peak positions indicative of minute changes, are found. XRD therefore confirms IR spectroscopy, Figure 4, which shows that overall the peptide fibers do not change upon mineralization.

Furthermore, XRD confirms the presence of metallic silver as additional reflections between 20 and 80 degrees 2θ can be assigned to silver (JPCPS 04-0783). At high fractions of **2** in the fibers, the silver reflections are broad. They become increasingly narrow, as the fraction of **2** decreases. XRD therefore shows a transition from silver nanoparticles with pure **2** to rather well-crystallized particles with pure **1**. This indicates that the interaction of the peptide **2** with the growing silver crystals is much stronger than with peptide **1**. XRD therefore supports SEM, TEM, and UV data showing that a direct tuning of the interaction between the peptide and the growing particles is possible with our gels.

The relative intensities of the reflections allow for a qualitative analysis of the structure directing properties of **2**, although they may contain some experimental error due to preferred orientation effects of, for example, the silver plates observed in the TEM. As long as **2** is present in the fibers in large amounts (over 50%), all reflections are broad. The (200) reflection is not observed in these XRD patterns, presumably due to the fact that the peak is too broad to be detected. This indicates the presence of very small particles, which is consistent with TEM. The presence of small isotropic particles is further supported by the (220)/(111) intensity ratio, which is 0.25. This value is equal to that reported for bulk silver (0.25, JPCPS 04-0783). This indicates that the silver particles have a roughly isotropic distribution and orientation in the mineralized fibers without any preferential orientation. This

is also again consistent with SEM and TEM data showing that most of the silver particles formed in the presence of high fractions of **2** are spherical and have a small diameter.

At 50% of **2**, the (200) reflection appears (although it is still very broad and weak). Again the (220)/(111) ratio is 0.25 to 0.28, which is in consistent with roughly spherical silver particles without preferred orientation. However, the (200)/(111) intensity ratio is 0.18, which is much lower than the expected value of 0.4. This indicates that in this case also other particle shapes are present in the sample. This is again consistent with the TEM data, which show the appearance of plate-like particles. With pure **1**, the (200)/(111) intensity ration increases to 0.29 (expected 0.4), while the (220)/(111) ratio of 0.23 is again close to the expected value of 0.25. This further confirms the weak influence of peptide **1** on particle growth.

Overall, the (220)/(111) ratio is always the same within the experimental error, regardless of the fiber composition. However, with increasing contents of **1**, the (200)/(111) ratio increases from inexistent (200 absent) to a value closer to what it should be for an isotropic sample. We currently interpret this behavior as due to the much weaker interaction of **1** with the growing crystals. As a result of this weaker interaction and the absence (or low concentration) of a growth inhibitor like the thioether, the particles grow bigger.

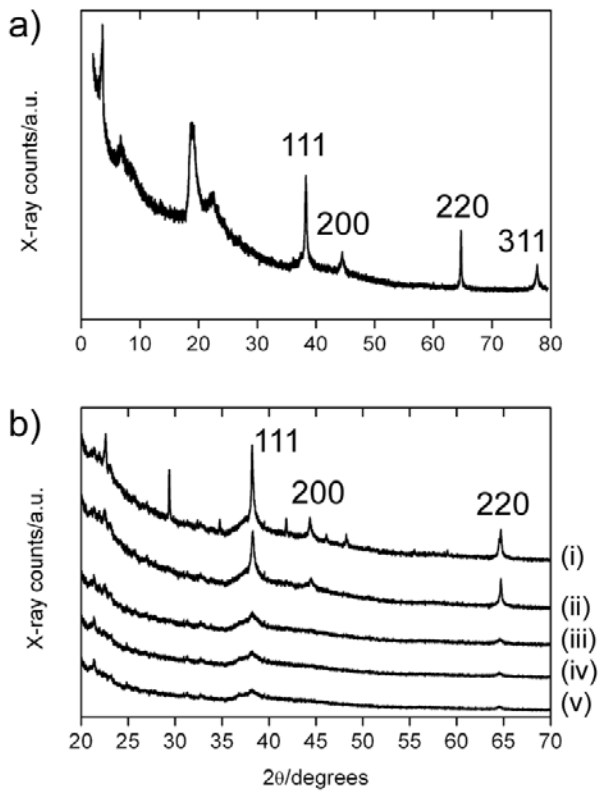

Figure 9. (a) XRD pattern of a mineralized gel with 50 % of **1** and 50 % of **2**. Although there are slight shifts in the peak positions compared to the control sample, the signal of the peptide fibers is not affected by the mineralization. (b) XRD patterns of gels mineralized with silver. Magnified view of the area showing the Ag reflections. (i) pure **1**, (ii) 75 % of **1** and 25 % of **2**, (iii) 50% each, (iv) 25% of **1** and 75% of **2**, and (v) pure **2**. The other reflections are from the peptide fibers.

Peptide-silver interactions. To further quantify the interactions of the peptides with the growing silver particles, we have performed X-ray photoelectron spectroscopy (XPS) experiments on both peptides deposited on silver wafers. This system serves as a model for the peptide-silver nanoparticle interaction at the molecular scale and provides information about the binding modes of **1** and **2** to silver.

Figure 10 shows silver and sulfur XPS spectra of **2** on a silver wafer. All signals (including carbon, oxygen, and nitrogen) have a full width at half maximum (FWHM) of around 1 eV, which is rather broad. The line broadening suggests that the peptides adopt a variety of conformations on the surface, which in turn indicates that there is no (highly)

preferred orientation or interaction of the peptide with the surface. The silver $3d_{5/2}$ and $3d_{3/2}$ peaks do not vary with immersion time of the wafer in the peptide solution. They are in all cases located at around 368.2 and 374.2 eV, which is indicative of an oxidized metallic silver surfaces.[26-28]

Unlike the silver peaks, the S 2p signals vary slightly. After deconvolution, all spectra show a peak at around the S $2p_{3/2}$ energy of 161.15 eV, which is indicative of S^{2-}.[29] As the same signal is also present in the control samples (samples immersed in hot methanolic solution without the peptide), this signal may be due to some contamination or to degradation of **2** on the surface during the peptide deposition.

The $2p_{3/2}$ peak at 161.5 eV is due to thiols chemically bound to the silver surface. This is not surprising as silver surfaces can cleave thioethers, in particular S-benzyl ethers.[30, 31] The signal at around 163.8 eV is attributed to chemisorbed thioether. Signals for $2p_{1/2}$ at 164.7 eV and 166.0 eV arise from thioether physisorbed on top of peptides bound to the surface, respectively. The $2p_{3/2}$ peak at 168.2 eV is only present in the samples immersed for 10 minutes. This peak arises from oxidized forms of the thioether, most likely upon exposition to air.

In summary, XPS provides evidence of a variety of sulfur species that can form with silver. XPS supports the observation that peptide **2** is an efficient growth modifier because it provides a sulfur atom, which can be present as a chemisorbed or physisorbed thioether or via the in situ formation of a thiol. As IR spectroscopy and XRD of the gels after mineralization show that the gels remain intact after mineralization, XPS provides evidence that there is still the possibility of a reaction of the peptide with the silver on the fiber surface. This reaction can include rather drastic processes like thioether cleavage and generation of free thiol or thiolate and eventually silver thiolate bonds.

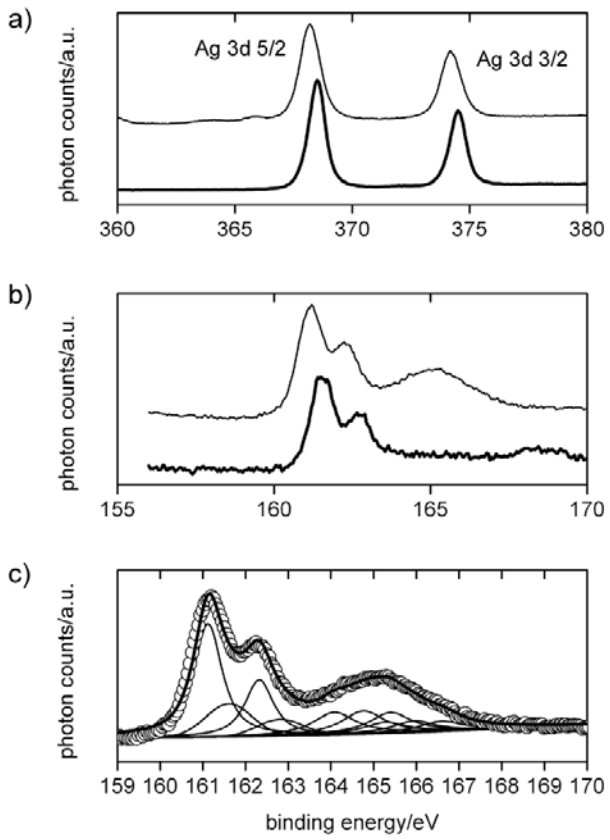

Figure 10. XPS spectra of peptide **2** deposited on a silver wafer. (a) Silver $3d_{5/2}$ and $3d_{3/2}$ peaks. (b) Sulfur $2p_{1/2}$ and $2p_{3/2}$ peaks. Bold lines are samples deposited for ten minutes and thin lines are from samples deposited for two hours. (c) Deconvolution of the sulfur peaks of an XPS spectrum recorded for a sample exposed for 10 minutes. Open symbols are the experimental data, thick line is the peak sum from deconvolution and thin lines are the individual components of the deconvoluted spectrum.

XPS clearly shows that there is an interaction of the sulfur atom of peptide **2** with the silver surface. Surface enhanced Raman spectroscopy (SERS) provides additional insight into the surface orientation and binding mode of the peptides with the surface.[32-35] Figure 11 shows SER spectra recorded from both peptide **1** and **2** on a silver surface. SERS shows that peptide **1** is randomly oriented on the silver surface. Spectra recorded at different locations of the wafers yield the same spectra, but the relative intensities are quite different between measurements. These intensity variations are most obvious for the benzyl ring vibrations at 2900 to 3000 cm^{-1} (ν_{C-H}, ring and aliphatic residue, undistinguished) and at 1007 cm^{-1} (ring breathing vibration), the amide vibrations at 1664 cm^{-1} ($\nu_{C=O}$, amide), the carbonyl vibrations

at 1747 cm^{-1} ($\nu_{C=O}$, methyl ester), and the aliphatic chain vibrations at 1336 cm^{-1} (δ_{CH3}). SERS therefore shows that the peptide **1** is adsorbed on the surface. However, the interaction of the peptide with the surface is not uniform, but there are several groups, including the amide, the ester, and the benzyl groups, which contribute to the binding.

In contrast to **1**, all spectra recorded for **2** are essentially identical, including the relative band intensities. The spectra exhibit a broad band at 660 cm^{-1} attributed to ν_{C-S} in thioethers. A further band at 650 cm^{-1} is also attributed to ν_{C-S} in thiols. This band indicates that some of the thioether is present as a chemisorbed thioether or in a cleaved stage, as thiol.[30] In the current case, however, SERS does not allow for an unambiguous distinction of thiol vs. chemisorbed thioether because of a broad emission peak at 200 to 320 cm^{-1}. This peak is assigned to either an Ag-O bond from air oxygen or Ag_2O which may form upon air exposition of activated surfaces,[36] an Ag-N bond from the peptide,[37] or, less likely, from a sulfur containing contamination as the XPS shows that the atomic compositions at the surface are compatible with the atomic composition of the peptide. This peak overlaps with the position of the ν_{Ag-S} vibration,[30] which would confirm the presence of a thiol bond. No significant signal of thiol formation on a silver wafer was determined by ATR-IR, either. In summary, therefore, SERS confirms the XPS data, although SERS cannot confirm the generation of some thiol in the sample.

A SERS signal is observed if the electric field vector at the silver surface is collinear with the polarizability vector of a bond of the adsorbed molecule. If the field vector and the polarizability vector, however, are perpendicular to one another, there is no emission in the spectra. As a result, the bands at 975, 1000, 1586, and 2935 cm^{-1} clearly show that peptide **2** binds to the silver via the carbamate benzyl ring and the thioether benzyl group. The presence of the signal at 1350 cm^{-1} further shows that the alkyl groups of the peptide are perpendicular to the surface. In contrast, the absence of a band over 1600 cm^{-1} shows that the amide moieties are parallel to the surface, because there is no SERS signal from this part of the molecule. This is consistent with the interpretation of the broad emission peak at 200 to 320 cm^{-1}, which was assigned to an Ag-O or Ag-N bond. While the Ag-O was assigned to Ag_2O on the surface via XPS, the Ag-N bond is due to bonding between the peptide nitrogen atoms and the silver wafer.

Overall, SERS indicates that the peptide lies flat on the silver surface and does not form (perpendicular) brushes. This is in stark contrast to peptide **1**, which adopts a variety of conformations on the surface, although it also contains benzyl and amide groups that could in principle lead to the same organization. However, SERS indicates that the second benzyl group and the sulfur atom introduced via the thioether are a key part for uniform peptide-silver interactions.

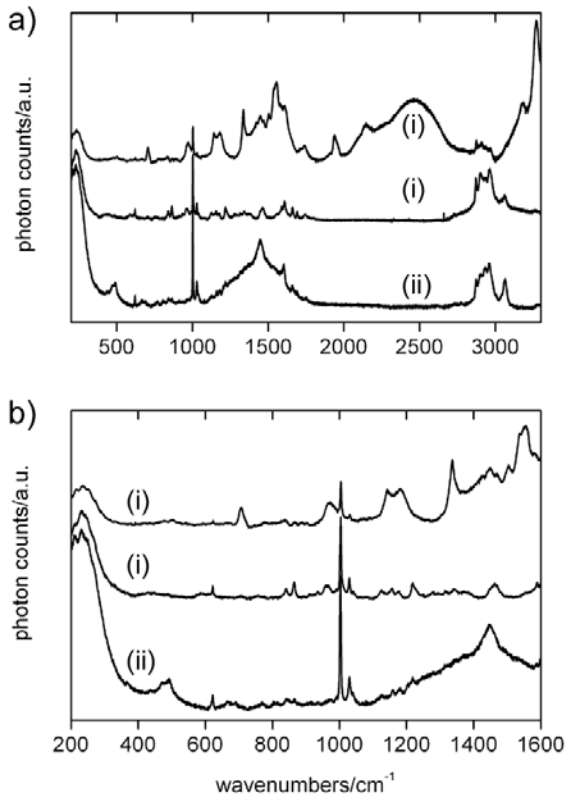

Figure 11. (a) SER spectra of a silver surface (i) coated with **1** and (ii) coated with **2**. (b) Magnified view of the lower wavenumber region.

Interaction of silver ions with peptide 2. We have shown above that the peptide **2** is a much stronger growth modifier for silver nanoparticles than **1**. In part this is due to the strong interaction of the thioether or thiol moiety, which is shown by XPS to directly interact with silver. Furthermore, SERS provides evidence that peptide **2** also interacts with silver via the additional benzyl group from the thioether side chain. A further point of interest is how and how strongly the Ag^+ ions interact with the peptide fibers prior to nucleation and growth of the particles. This question has been addressed via ^{13}C NMR and UV/Vis titration.

Figure 12 shows UV/Vis spectra and UV/Vis titration data of a 1 mM solution of **2** in DMSO with a 1 mM solution of $AgNO_3$ in DMSO. The spectra of the peptide and silver nitrate solutions quite strongly overlap. This indicates that the data may have a rather large error. Nevertheless, Figure 12 shows that the absorption spectra change as the peptide **2** is titrated with silver nitrate. All bands at 290, 314, and 340 nm slowly increase in intensity until an Ag/peptide ratio of 1:1 is reached. Thereafter, the band at 314 nm levels off to a constant value and the band at 290 and 340 nm slowly decrease again. These data therefore indicate a 1:1 Ag/peptide complex.

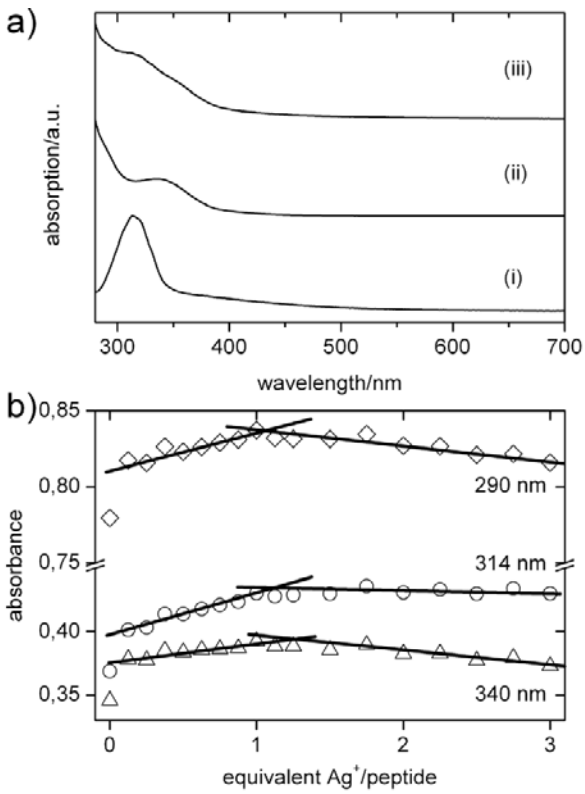

Figure 12. UV/Vis spectra and titration data. (a) UV/Vis spectra of (i) $AgNO_3$ in DMSO, (ii) peptide **2** in DMSO, and (iii) mixture of $AgNO_3$ and peptide **2** in DMSO. (b) UV/Vis titration data recorded at 290, at 314, and at 340 nm.

Figure 13 shows ^{13}C-NMR titration data of peptide **2** with silver nitrate. Addition of $AgNO_3$ gradually shifts the ^{13}C signal of the carbons in the α position of the sulfur from ca. 36.1 to 37.2 ppm until at 2 equivalents of Ag^+ no further shift is observed. Control

experiments with $NaNO_3$ show that Na^+ does not lead to a shift of the respective signals. This confirms that the shift is due to a true Ag^+-peptide interaction and not an effect of ionic strength. Furthermore, the fact that the shift is observed for the carbon atoms next to the sulfur clearly indicates that the interaction as determined from UV titration is a silver-sulfur interaction. UV/Vis and ^{13}C NMR therefore show that there is an interaction between the silver ions and the thioether moiety already prior to nucleation and growth of the silver nanoparticles. The discrepancy between the UV/Vis and the NMR data in terms of the number of silver equivalents is to date unresolved. However, further NMR studies show that also the benzyl ring of the thioether, but not the benzyl group of the Z-group, interacts with the silver cations, most likely via cation-π interaction. This suggests that the binding of the silver cations to the peptides can occur via multiple binding modes, which makes a quantitative analysis rather difficult.

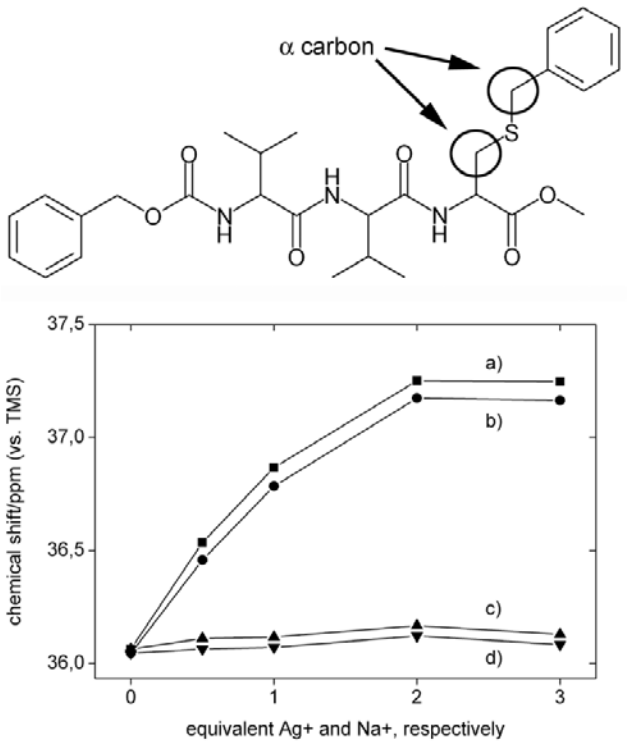

Figure 13. ^{13}C NMR titration of carbon atoms in the α position of the sulfur in **2** in d_6-DMSO. Lines (a, b) show the shift of the two α carbon atoms upon titration with $AgNO_3$. (c, d) Shift of the two α carbon atoms upon titration with $NaNO_3$. The position of the α carbons is shown in the molecular structure of peptide **2**.

4.4 Discussion

Particle formation Peptide-controlled mineralization of silver particles has so far been achieved with redox active peptides, most often based on tyrosine or tryptophane. They were either in solution or incorporated into gels.[11-13, 17] Histidine rich peptides have also been used as scaffolds, but there, an additional reducing agent, sodium borohydride, was used.[14, 15] The major drawback of this approach is that the samples require extensive purification after synthesis. Both approaches using sodium borohydride and using redox active peptides are therefore different from the current approach, which uses DMF as a reducing agent.

Avoiding an external reducing agent may seem an advantage, but the disadvantage is that the template (peptide) concentration, the silver ion concentration, and the reaction temperature are the only variables in the system. This allows for some control over nucleation and growth, but the use of an independent reducing agent offers many more possibilities for reaction tuning. For example, if the concentration of the reducing peptide increases, also the amount of the peptide scaffold and therefore the internal surface, which interacts with the growing particles, changes. That is, there is no independent variation of both the scaffold and the reducing agent (unless mixtures of a redox active and a redox-inactive peptide are used).

The current paper shows that mixtures of two different peptides can in some cases be interesting for the fabrication and tuning of organic/inorganic composites. This is particularly interesting in cases where one peptide is regarded (and designed) as a “structural” unit, which does not interact with the growing inorganic material. In our case, peptide **1** can be regarded as structural and non-interacting peptide. If however, the other peptide contains functional groups, for example, thiols (that is, coordination or nucleation promoters) or alcohol moieties (that is, reducing agents) it is possible to combine a wide variety of functions in one self-assembling system. Because the peptides can be fabricated individually and combined later, mixtures of **1**, **2**, and a peptide containing e.g. tyrosine can be envisioned. The resulting gels would provide an interesting reactive scaffold for silver/peptide hybrid materials. As such, the current paper is just one example of such a modular peptide toolbox.

Proteins, which also provide control over the spatial organization of nucleation and growth,[16] can be viewed as more complex varieties of our approach. That is, the peptides used

here form a primitive, but still functional, "protein" scaffold for controlling silver mineralization. As XRD and IR do not show a clear segregation of both peptides within the fibers, mixed fibers of **1** and **2** can be viewed as a simplified large protein with statistically distributed sulfur moieties on the surface.

Earlier studies have mainly commented on the reduction mechanisms, which have been studied by exploiting the tryptophane or tyrosine fluorescence, IR, EPR, solid state ^{13}C-NMR, and UV/Vis spectroscopy.[11, 12, 17, 38] The present study also reports on the interactions of the peptides with the silver surface. Based on the current data, the following model can be derived.

NMR and UV/Vis titrations provide evidence for an association of the silver cations with the sulfur atom in the thioether. This is the first step required for controlled particle nucleation and growth. Indeed, similar surface enrichment processes close to peptide moieties have been described for histidine, methionine, cysteine, tryptophan, and arginine-rich peptides.[2, 15, 16, 28, 39] Once nucleation has occurred and the silver colloids start forming, the outcome of the mineralization process is largely governed by the concentration of the thioether moieties on the peptide fiber surface, because the main interaction between the peptides and the growing silver particles occurs via bonding of the thioether (thiol), amide, and benzyl groups of the peptide, as evidenced by XPS and SERS.

The main interaction is a silver-sulfur interaction. This approach therefore adds another type of functional group to the peptide family, which can be used besides amines, free thiols, and unspecific adsorption of the peptides to silver[11-16] for nucleation and crystallization control. As the Ag-S interaction is quite strong, peptide fibers with high contents of **2** are efficient growth modifiers and hence these fibers are covered with silver particles of ca. 9 nm in diameter. The particles are trapped and further growth (for example via Ostwald ripening) is prevented. Because of the strong binding of the silver to the sulfur, the resulting particles have a rather low mobility and essentially remain attached to the location where they initially form.

As the content of **2** in the fibers decreases to below 50 %, the interaction between silver ions, silver particles, and the peptide fibers decreases. Nucleation in solution (that is,

homogeneous nucleation) is still not favorable due to the presence of a large internal surface provided by the peptide fibers. However, the surface energies of the peptide fibers change, as the thioether is increasingly removed. Assuming that the particles still form via heterogeneous nucleation, the formation of large particles observed with low contents of **2** can be explained with Ostwald ripening. Initially there is a silver-peptide interaction, as evidenced by ^{13}C NMR. However, after nucleation, the interaction between the particles and the peptide fibers is too weak to completely suppress Ostwald ripening (or regular crystal growth) and rather large crystals with various shapes form.

As the content of **2** decreases below 25 %, nucleation and growth is largely governed by the hydrophobic surface of the peptide fibers. Sulfur containing peptides still interact with the growing clusters. As the sulfur containing moieties are being covered by the growing large crystals, further reduction of silver ions leads to growth according to a model developed by Naik et al.[40] According to this model, peptides modify crystal growth by allowing accumulation of the silver atoms on the lowest surface energy face where the peptide is accumulated. As in face centered cubic (fcc) metals the surface energy γ of the 111 faces is lower than for other faces,[41] there is a preferential interaction of the peptide fibers with the 111 faces. Therefore, growth will have to occur along other crystallographic axes and the resulting anisotropic particles will have large 111 faces and thus predominantly a plate-like morphology. This is evidenced by TEM and electron diffraction data.

Finally, the peptides not only control the growth of the particles, they also control their organization. The presence of the thioether moieties on the fiber surface provides a simple, yet efficient, scaffold because the strong silver-sulfur interaction defines the location of nanoparticle nucleation and growth and the orientation of the particles on the fibers. This is again similar to earlier reports in the literature. Naik et al.[40] have shown that peptides interact with lower energy surface to influence the shape of the particle. Mo et al.[16] have shown that silver colloids can be organized on a protein like scaffold.

Potential of the approach. The current approach to silver (and potentially other metal)-peptide hybrid structures has a few advantages over other “bioinspired” systems reported in the literature. First, our peptides are in principle fully recyclable because they are not involved in the silver colloid formation (although there is some evidence of thioether

cleavage from XPS). This is unlike earlier examples where the peptides are mostly oxidized during particle formation and could therefore not be reused.[11, 13, 38] Here, the peptide can be separated from the colloidal silver by dissolution of the composite in methanol. After centrifugation and solvent evaporation, the peptide can be recovered.

More interestingly, our peptide scaffold is (with only 3 amino acids) a much simpler scaffold than many others, that is, it is easy to fabricate on a large scale. Nevertheless it is possible to prepare gels which act as templates for hybrid material formation. XPS and SERS also suggest that under certain conditions it might be possible to generate surfaces with a relatively high order. Possibly, 2D and 3D structures similar to protein arrays[16, 17] can be fabricated, without the need to prepare highly complex bioengineered structures.

4.5 Conclusion

In summary, we have introduced a simple tool for the controlled fabrication of peptide/silver nanoparticle hybrid fibers and gels with a preprogrammed silver nanoparticle size and shape. This study shows that the Brust-Shiffrin concept of nanoparticle size-selection by metal ion/thiol ratio variation[4, 5] also works when the thiols or thioethers are incorporated in a rather stiff supramolecular assembly like peptide fibers. The paper also shows that mixtures of simple L-valine-based oligopeptides provide a flexible mineralization platform for the tuning of hybrid nanostructures. As a result, our findings open the way towards a better control of metal/organic hybrid materials via the variable incorporation of functional (peptide **2**) and (almost) purely structural (peptide **1**) building blocks into a supramolecular scaffold. Formation kinetics and related questions are currently under investigation.

4.6 Acknowledgement

We thank Prof. E.C. Constable for access to his IR spectrometer, M. Düggelin, D. Mathys, and G. Morson for SEM measurements, Prof. L. Diamond for access to his Raman microscope, Prof. J. Wirz for access to the Agilent spectrophotometer, Dr. R. Kötz for comments about the manuscript. The Swiss National Science Foundation, the University of Potsdam, the Max-Planck-Institute of Colloids and Interfaces, and the NCCR Nanosciences

are acknowledged for financial support. A.T. thanks the Holcim Stiftung Wissen for a Habilitation Fellowship.

4.7 References

[1] M. Faraday *Philos. Trans. Royal Soc. London* 1857, *147*, 145.

[2] U. Kreibig *Z. Phys. D* 1986, *3*, 239.

[3] A. Henglein *Chem. Rev.* 1989, *89*, 1861.

[4] M. Brust; J. Fink; D. Bethell; D.J. Shiffrin; C. Kiely *J. Chem. Soc., Chem. Commun.* 1995, 1655.

[5] M. Brust; M. Walker; D. Bethell; D.J. Shiffrin; R. Whyman *J. Chem. Soc., Chem. Commun.* 1994, 801.

[6] G. Schmid *Nanoparticles. From Theory to Application*; Wiley-VCH: Weinheim, 2003.

[7] M.C. Daniel; D. Astruc *Chem. Rev.* 2004, *104*, 293.

[8] C. Zhan; J. Wang; J. Juan; H. Gong; M. Liu *Langmuir* 2003, *19*.

[9] C.S. Love; V. Chechik; D.K. Smith; K. Wilson; I. Ashworth; C. Brennan *Chem. Commun.* 2005, 1971.

[10] P. Gao; C. Zhan; M. Liu *Langmuir* 2006, *22*.

[11] S. Si; T.K. Mandal *Chem. Eur. J.* 2007, *13*, 3160.

[12] S. Bhattacharya; A.K. Das; A. Banerjee; D. Chakravorty *J. Phys. Chem. B* 2006, *110*, 10757.

[13] S. Ray; A.K. Das; A. Banerjee *Chem. Commun.* 2006, 2816.

[14] Y.-F. Djalali; H.M. Chen *J. Am. Chem. Soc.* 2003, *125*, 5873.

[15] J.M. Slocik; D.M. Wright *Biomacromolecules* 2003, *4*, 1135.

[16] X. Mo; M.P. Krebs; S.M. Yu *Small* 2006, *2*, 526.

[17] Q. Dong; H. Su; D. Zhang *J. Phys. Chem. B* 2005, *109*, 17429.

[18] A. Mantion; A. Taubert *Macromol. Biosci.* 2007, *7*, 208.

[19] M. Sunde; L.C. Serpell; M. Bartlam; P.E. Fraser; M.B. Pepys; C.C.F. Blake *J. Mol. Biol.* 1997, *273*, 729.

[20] J.A. Jarvis; D.J. Craik; M.C.J. Wilce *Biochem. Biophys. Commun.* 1993, *192*, 991.

[21] A. Manna; B.D. Kulkarni; K. Bandyopadhyay; K. Vijayamohanan *Chem. Mater.* 1997, *9*, 3032.

[22] J.J. Mock; M. Barbic; D.R. Smith; D.A. Schultz; S. Schultz *J. Chem. Phys.* 2002, *116*, 6755.

[23] I.O. Sosa; C. Noguez; R.G. Barrera *J. Phys. Chem. B* 2003, *107*, 6269.

[24] K.L. Kelly; E. Coronado; L.L. Zhao; G.C. Schatz *J. Phys. Chem. B* 2003, *107*, 668.

[25] T.C. Deivaraj; N.L. Lala; J.Y. Lee *J. Coll. Interface Sci.* 2005, *289*, 402.

[26] S.Y. Kang; K. Kim *Langmuir* 1998, *14*, 226.

[27] A. Kumar; H. Joshi; R. Pasricha; A.B. Mandale; M. Sastry *J. Colloid Interf. Sci.* 2003, *164*, 396.

[28] C.D. Wagner; W.M. Riggs; C.E. Davis; J.F. Moulder In *Handbook of X-ray Photoelectron Spectroscopy*; Muilenberg, G. E., Ed.; Perkin-Elmer Corporation: Eden Praire, 1979, pp 122.

[29] J.C. Munro; C.W. Frank *Polymer* 2003, *44*, 6335.

[30] C.J. Sandroff; D.R. Herschbach *J. Phys. Chem.* 1982, *86*, 3277.

[31] C.-J. Zhong; M.D. Porter *J. Am. Chem. Soc.* 1994, *116*, 11616.

[32] H. Lee; M.S. Kim; S.W. Suh *J. Raman. Spectroscopy* 1991, *22*, 91.

[33] G. Xue; M. Ma; J. Zhang; Y. Lu; K.T. Carron *J. Coll. Interface Sci.* 1992, *150*, 1.

[34] E. Podstawka; Y. Ozaki; L. Proniewicz *Appl. Spectroscopy* 2004, *58*, 570.

[35] E. Podstawka; Y. Ozaki; L. Proniewicz *Appl. Spectroscopy* 2004, *58*, 581.

[36] B.A. Sexton; R.J. Madix *Chem. Phys. Lett.* 1980, *76*, 294.

[37] B. Pettinger; H. Wetzel *Chem. Phys. Lett.* 1981, *78*, 398.

[38] S. Si; R.R. Battacharjee; A. Banerjee; T.K. Mandal *Chem. Eur. J.* 2006, *12*, 1256.

[39] P.R. Selvakannan; S. Mandal; S. Phadtare; A. Gole; R. Pasricha; S.D. Andyanthaya; M. Sastry *J. Coll. Interface Sci.* 2004, *269*, 97.

[40] R.R. Naik; S.J. Stringer; G. Agarwal; S.E. Jones; M.O. Stone *Nature Mater.* 2002, *1*, 169.

[41] Z.L. Wang *J. Phys. Chem. B* 2000, *104*, 1153.

[42] G. Xue; J. Dong *Anal. Chem.* 1991, *63*, 2393.

5. Metal-peptide frameworks (MPFs) – "bioinspired" metal organic frameworks

Alexandre Mantion,[1,*] Lars Massüger,[2] Pierre Rabu,[3] Cornelia Palivan,[1] Lynne McCusker,[2] and Andreas Taubert[1,4,*]

1 Department of Chemistry, Klingelbergstr. 80, University of Basel, CH-4056 Basel, Switzerland

2 ETH Zürich, Laboratorium für Kristallographie, Wolfgang-Pauli-Str. 10, CH-8093 Zürich, Switzerland

3 IPCMS - Groupe des Matériaux Inorganiques, 23, rue du Loess, BP 43, F-67034 Strasbourg CEDEX 2, France

4 Institute of Chemistry, University of Potsdam, and Max-Planck-Institute of Colloids and Interfaces, D-14476 Golm, Germany.

* corresponding author: A. Taubert, Institute of Chemistry, University of Potsdam, Karl-Liebknecht-Str. 24-25, Building 26, D-14476 Golm, Germany. Email: ataubert@uni-potsdam.de, Tel.: ++49 (0)331 977 5773, Fax: ++49 (0)331 977 5055.

* corresponding author: A. Mantion, Department of Chemistry, Klingelbergstr. 80, University of Basel, CH-4056 Basel, Switzerland Email: a.mantion@unibas.ch, Tel.: ++41 (0)61 267 38 50.

Accepted as a paper to *J. Am. Chem. Soc., currently in press.*

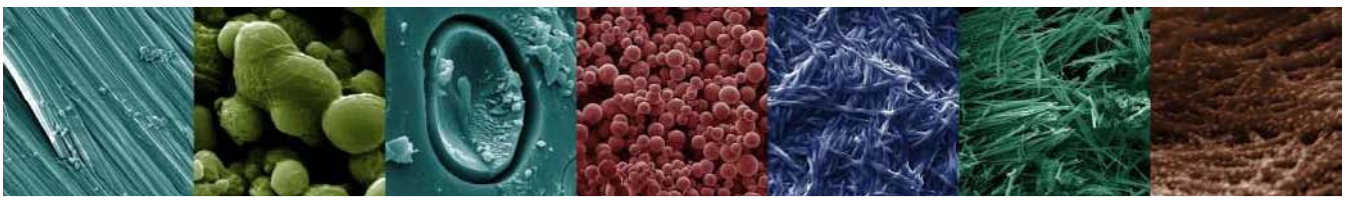

5.1 Introduction

Metal organic frameworks (MOFs) have attracted tremendous attention over the last few years. This is due to the fact that they are porous, have large surface areas of over 5000 m^2/g, and have tunable pores sizes and topologies.[1-4] MOFs are constructed from relatively simple organic building blocks, which act as connectors between transition metals or lanthanides. Because of their "infinite" connectivity, MOFs can be viewed as porous inorganic polymers.[5] Furthermore, like zeolites and aluminophosphates, MOFs are crystalline materials. However, while zeolites and other microporous materials are purely inorganic, MOFs are organic/inorganic hybrids. Despite the presence of organic building blocks, MOFs are robust materials. Their low density and high surface area are useful for gas sorption and energy technologies,[6,7] filtration,[8] or possibly even lightweight building materials. Other MOFs have useful optical[9] and electric properties[10] or have been proposed as transport vessels for biological applications.[11]

MOFs can be synthesized using a wide variety of methods from hydrothermal to simple diffusion methods.[1,4,12,13] To date, most ligands used as connectors are rigid and do not carry additional functionalities, which could modify the properties of the MOF pores. There are only a few studies on flexible connectors and connectors that also self-assemble in the absence of a metal ion. For example, several groups have studied MOFs obtained from adipic acid, auxiliary bases, and Ca^{2+}, lanthanides, or 3d transition metals.[14-21]

Interestingly, there have been no reports on the use of peptides or peptidomimetics as connectors. This is particularly intriguing because peptide chemistry offers a virtually unlimited structural diversity, including additional metal coordinating sites etc. Moreover, peptides are intrinsically chiral, which should make them prime candidates for the fabrication of chiral MOFs. Chiral MOFs are, beyond the more fundamental search for new topologies, highly attractive as asymmetric catalysts, for chiral recognition, and applications requiring non-centrosymmetric crystal structures like non-linear optical devices.[22-26]

There are essentially three approaches for the preparation of chiral MOFs: (i) the exploitation of molecules, where the chiral resolution happens without further assistance,[27] (ii) the use of chiral co-ligands in addition to achiral connectors,[23] or the use of a chiral

connector.[25,28] The chiral connector approach is currently most often used because of its flexibility.[22-28]

We have recently introduced a family of self-assembling peptides based on oligovalines. These peptides gel a variety of solvents, including the inorganic liquid tetraethylorthosilicate (TEOS). Furthermore, they act as templates for complex titania and silver/peptide nanostructures.[29,30] The current paper shows that replacing one valine unit with a glutamic acid, Scheme 1, leads to peptides that can form peptide analogs of MOFs, which we have termed metal peptide frameworks (MPFs). The peptides form strong bonds with Cu^{2+} and Ca^{2+}, and the resulting crystalline materials precipitate from solution as long needle-like micrometer-sized particles.

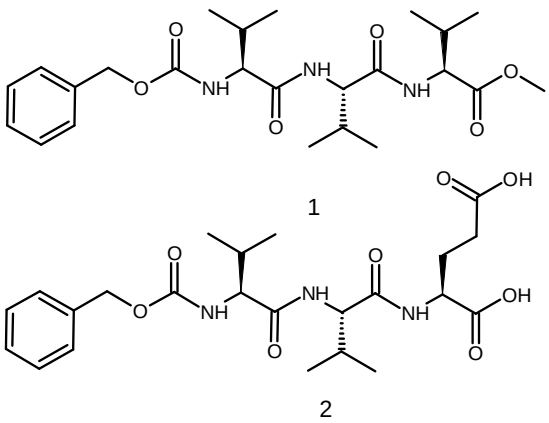

Scheme 1. Oligovaline peptides. **1** is the parent compound used in our earlier studies.[29,30] **2** is the peptide ligand used for construction of the MPFs and for magnetic dilution in the EPR experiments in the current paper.

5.2 Experimental

Materials. Amino acids were purchased from Bachem AG (Bubendorf, Switzerland) and all other chemicals from Fluka (Buchs, Switzerland). All chemicals were used as received.

Ligand synthesis. The synthesis of the precursor peptide ZVVOH and of peptide 1 has been described elsewhere.[29]

Z-L-Val-L-Val-L-Glu(OtBu)OtBu. 1.4 mL (10.3 mmol) of isobutyl chloroformate were added to a salt/ice cooled solution of Z-L-Val-L-Val-OH (3.0 g, 8.6 mmol) and 4-methylmorpholine (1.7 mL, 14.6 mmol) in 25 mL of acetonitrile under argon. The reaction mixture was stirred for two minutes. Then 3.0 g (10.3 mmol) of L-glutamic acid di-tert-butyl ester hydrochloride and 1.7 mL (14.6 mmol) of 4-methylaminomorpholine were added. After 15 minutes, the cooling was removed and the solution was allowed to warm up to room temperature, upon which the solution was stirred for 24 hours. The solvents were removed by rotary evaporation and the residue was dissolved in 200 mL of chloroform. The organic solution was washed three times with 100 mL of a mixture of saturated hydrogen carbonate solution and sodium chloride, once with aqueous sodium chloride, three times with 100 mL of 10 % citric acid and aqueous sodium chloride, and twice with aqueous sodium chloride. The organic phase was dried with sodium sulfate, concentrated to dryness, and the residue was triturated with pentane to give a white solid (3.4 g, 75 %) after drying. IR (neat, cm^{-1}) 3479, 3277, 3063, 2976, 1633, 1533, 1429, 1393, 1371, 1349, 1283, 1247, 1222, 1153, 1088, 1071, 1038, 1028, 1020, 1005, 987, 920, 908, 864, 846, 799, 774, 753, 740, 698, 667. Elemental analysis calculated: C 62.92, H 8.35, N 7.10, O 21.63; measured: C 62.97, H 8.32, N 7.19. FAB-MS calculated $[M-H]^+$ = 592, measured $[M-H]^+$ = 592. ^{13}C-NMR (δ in ppm vs. TMS, d6-DMSO, 100 MHz) 172.25, 171.84, 171.70, 171.51, 156.91, 137.96, 129.16, 128.56, 128.52, 128.45, 81.40, 80.56, 66.19, 61.11, 57.94, 52.58, 31.71, 31.12, 28.56, 28.43, 27.04, 20.11, 20.01, 18.99, 18.96. ^{1}H-NMR (δ in ppm vs. TMS, d6-DMSO, 400 MHz) 8.23 (d, 0.9 H, H amide), 8.1 (d, 0.1 H, H amide), 7.92 (d, 0.1 H, H amide), 7.72 (d, 0.8 H, H amide), 7.33 (m, 6 H, H phenyl + H carbamate), 5.01 (s, 2 H, benzyl), 4.22 (t, 1 H, α Val-1), 4.12 (m, 1 H, α Val-2), 3.94 (m, 1 H, α Glu), 2.22 (m, 2 H, γ Glu), 1.92 (m, 3 H, β Val-1 + β Val 2 + β Glu), 1.72 (m, 1 H, β Glu), 1.36 (m, 18 H, tertiobutyl ester x 2), 0.83 (m, 12 H, γ Val-1 + γ Val-2)

Z-L-Val-L-Val-L-Glu(OH)OH 2. 2 g of Z-L-Val-L-Val-L-Glu(OtBu)OtBu were reacted with 25 mL of a 95% aqueous TFA solution for 30 minutes under argon. Then the solvent was removed under reduced pressure. The residue was treated three times with 30 mL of chloroform. After evaporation of the chloroform, the slightly yellow solid was triturated with diethyl ether, filtered, and the whitish solid was dried overnight under vacuum, leaving 1.29 g of white solid **2** (80 %). IR (neat, cm^{-1}) 3289, 3074, 2976, 1637, 1530, 1419, 1340,

1293, 1242, 1217, 1179, 1150, 1075, 1043, 1029, 995, 965, 934, 917, 859, 842, 798, 778, 756, 736, 697. FAB-MS: calculated $[M-H]^+$ = 480; measured $[M-H]^+$ = 480. Elemental analysis calculated: C 57.61, H 6.94, N 8.76, O 26.69; measured: C 56.91, H 6.90, N 8.60. ^{1}H-NMR (δ in ppm vs. TMS, d6-DMSO, 400 MHz) 12.35 (very broad, 2 H, acidic protons), 8.17 (d, 0.94 H, H amide), 8.03 (d, 0.17 H, H amide), 7.90 (d, .12 H, H amide), 7.72 (d, 0.9 H, H amide), 7.36 (m, 6 H, H carbamate + H phenyl), 5.01 (s, 2 H, H benzylic), 4.18 (m, 2 H, α Val-1 + α Val-2), 3.92 (m, 1 H, α Glu), 1.94 (m, 3 H, 1H β-Glu + β Val-1 + β Val-2), 1.76 (m, 1 H, 1 H β Glu), .82 (m, 14 H, 2 H γ Glu + 6 H γ Val-1 + 6 H γ Val-2). ^{13}C-NMR (δ in ppm vs. TMS, d6-DMSO, 100 MHz) 174.59, 173.91, 172.95, 171.82, 156.94, 137.95, 129.99, 129.39, 129.25, 66.20, 61.13, 58.13, 51.98, 31.63, 31.08, 30.80, 27.04, 20.08, 19.96, 19.03, 18.95.

Complex synthesis. The metal complexes were prepared by dissolving peptide 2 in a 60/40 (v/v) ethanol/water mixture. The pH of the solution was adjusted to pH 8 with diluted aqueous ammonia. In a typical experiment, 56 μL of a 3 mM copper(II) or calcium nitrate in water were added to the ligand solution at room temperature under stirring. After copper or calcium salt addition, the pH was readjusted to 8. The copper complex (MPF-9) immediately precipitated and the calcium complex (MPF-2) precipitated after one hour at 80 °C. To complete the reaction, the reaction mixture was further reacted for 48 hours at 80 °C in a closed vessel. Then, the solids were centrifuged, washed with ethanol, and dried under vacuum overnight. Various metal/peptide ratios were used during the synthesis, but all precipitates had a 1:1 metal/peptide stoichiometry. Yields were above 99%. Elemental analysis (MPF-2, $C_{23}H_{39}CaN_3O_{12}$) calculated: C 46.85, H 6.67, N 7.13, O 32.56, Ca 6.80; measured: C 47.80, H 6.29, N 7.57. Elemental analysis (MPF-9 corresponding to the dibasic form of **2** plus 1 Cu^{2+} plus 2 NH_3 plus 2 H_2O: $C_{23}H_{41}CuN_5O_{10}$), calculated: C 45.20, H 6.76, N 11.46, Cu 10.40, O 26.18; measured: C 45.98, H 6.38, N 10.39.

Spectroscopy. ^{1}H and ^{13}C NMR spectra were recorded on an Avance 400 MHz NMR spectrometer. Infrared spectra were obtained from the neat samples on a Shimadzu FTIR 8300 with a Golden Gate ATR unit. Spectra were recorded from 300 cm^{-1} to 4500 cm^{-1} with a resolution of 1 cm^{-1}. FAB-MS spectra were taken on a Finnigan MAT 312.

Microscopy. Scanning electron microscopy was done on a Philips XL30 FEG ESEM operated at 10 kV. Samples were sputtered with gold or platinum prior to imaging.

X-ray diffraction. Powder diffraction patterns were measured on the Swiss-Norwegian Beamlines (SNBL) at the European Synchrotron Radiation Facility (ESRF) in Grenoble. Details of the data collection are given in Table 1.

Table 1. X-ray powder diffraction data collection

Synchrotron facility	SNBL (Station B) at ESRF
Wavelength	0.50007 Å
Diffraction geometry	Debye-Scherrer
Analyzer crystal	Si 111
Sample	rotating 1.0 mm capillary
2θ range	1.020-30.501˚
Step size	0.003˚2θ
Time per step	1.0s

Voids volume evaluation. After refinement and before evaluating the voids size and position, non refined hydrogen atoms were added using the hydrogen addition functionality in Crystals[35] using an average C-H distance of 1 Å. Plotting and structure analysis was performed using Platon[36,37] and CrystalMaker (CrystalMaker Software Ltd).

Thermal analysis. Thermogravimetric analysis (TGA) was done with a Mettler Toledo TGA/SDTA 851e from 25 to 550 ºC with a heating rate of 10 ºC/min in N_2.

SQUID Measurements. The magnetic properties of MPF-9 were investigated on neat powder samples with a Quantum Design MPMS-XL SQUID magnetometer between 1.8 and 300 K. The magnetic field strength was varied from -5 to +5 T. All magnetic data were corrected for diamagnetism of the sample and the sample holder. To evaluate the antiferromagnetic coupling between the neighboring Cu(II) centers, we analyzed the susceptibility by using a model of Heisenberg S = ½ spin chains. Writing the exchange hamiltonian $\hat{H}=-J\sum_{i,j}\hat{S}_i\hat{S}_j$, we used the expression of the susceptibility χT given in the literature.[41]

$$\chi T = \frac{N\mu_B^2 g^2 \left(0.25 + 0.0750y + 0.15047y^2\right)}{k\left(1 + 0.9931y + 0.34427y^2 + 3.0313y^3\right)} \quad (1)$$

In expression (1), $y = |J|/kT$, where J is the exchange interaction between electron spin moments S_i.

Electron paramagnetic resonance spectroscopy. EPR spectroscopy was done on an EPR Bruker ElexSys E500 operating at 9.6 GHz spectrometer equipped with an Oxford Instruments cryostat. All complexes were measured as powders at 75 and 293 K. The complexes were magnetically diluted with 2 to a maximum extent of 10% of Cu(II). Spectra were recorded using 100 kHz modulation frequency and a microwave power of 0.5 to 2 mW. The diphenylpicrylhydrazyl (DPPH) radical was used as a field marker (g = 2.0036). The spectra for the Cu(II) species were simulated using Symfonia software (Bruker), which is based on a third order perturbation theory treatment and assumes Gaussian shapes for the linewidth tensors. The isotopes were considered in their natural abundance for each spectrum.

5.3 Results and discussion

Figure 1 shows representative scanning electron microscopy (SEM) images of the calcium complex MPF-2 and the copper complex MPF-9. Both samples have a fiber-like morphology with lengths ranging up to several micrometers and widths of ca. 200 nm. The calcium based MPF-2 crystals are somewhat shorter but have a more regular morphology with well developed crystal faces and edges. The copper-based MPF-9 appears less crystalline and seems to consist of smaller “blobs” that make up the rodlike particle.

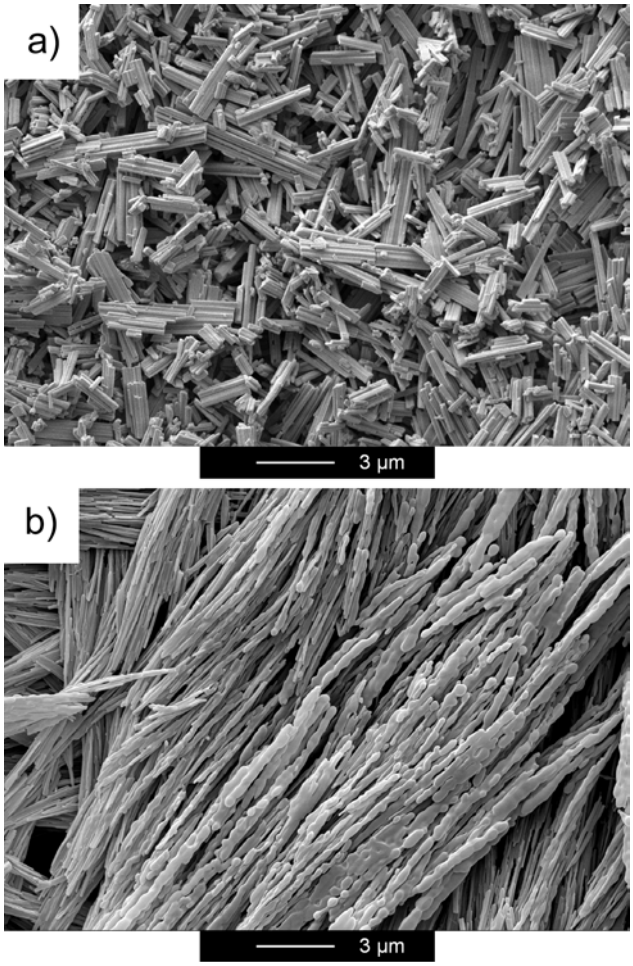

Figure 1. SEM images of (a) MPF-2 and (b) MPF-9.

Figure 2 shows thermogravimetric analysis (TGA) data. The pure ligand 2 exhibits a single sharp weight loss at 272 °C. There is no indication of the presence of water or other volatile substances, and no indication of decarboxylation. TGA curves of MPF-2 show four steps. The first one, at 35 °C, is relatively small (5%) and is caused by solvent or water evaporation. A clear weight loss of 19% is then observed at 262 °C. This weight loss is attributed to the loss of four molecules of water strongly bound in the crystal lattice or to solvent trapped in the structure. The third step is less clear, and has an inflection point at 340 °C and a loss of 27 %. The last weight loss of 14 % is observed at 429 °C. The total mass loss indicates (assuming that Ca is present as CaO after TGA) that one Ca ion is bonded to one ligand molecule.

MPF-9 behaves similarly, except that there are only three thermal events. The first weight loss takes place at 91 °C, which is due to solvent evaporation. This weight loss of 6 % is assigned to one equivalent of ethanol or two equivalents of adsorbed water. The second

event occurs at 160 °C and is assigned to the loss of crystallographically bound solvent, most likely solvent molecules coordinated to the metal center. A final weight loss of 66% is observed at 260 °C. These data are consistent with a ratio of one copper to one ligand molecule, where the copper is possibly surrounded by one or two water or ammonia molecules (see elemental analysis and EPR results below, which suggest that two molecules of ammonia are bonded to the copper center) in the coordination sphere.

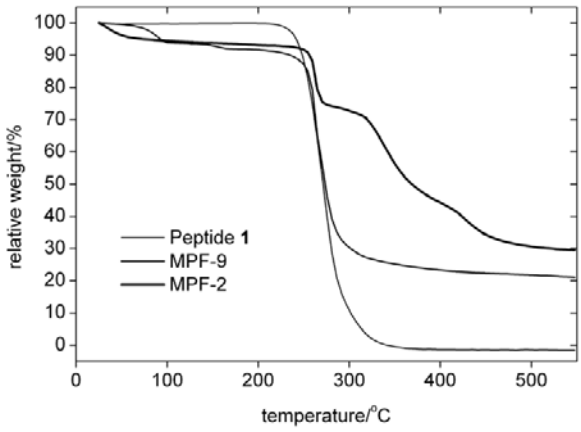

Figure 2. TGA curves of the pure peptide and the MPFs.

Figure 3 shows representative IR spectra of the pure peptide 2, MPF-2, and MPF-9. The ligand bands at 3066, 1705, 1390, 1290, and 918 cm^{-1} can be assigned to O-H stretch, C=O stretch, C-O stretch, and O-H bending vibrations, respectively. Bands at 3280, 1637, 1528, and 1221 cm^{-1} can be assigned to the amide A, amide I, amide II, and amide III vibrations, respectively. The band at 1690 cm^{-1} can be attributed to the C=O vibration of the carbamate moiety. As in our previous work,[29] the amide band positions are indicative of a β sheet structure. However, also as in our earlier work, IR does not reveal whether the organization of the β-sheet is parallel or antiparallel, because the diagnostic bands are obscured by vibrations of the N-benzylcarboxy group.[42,43] The β sheet in the peptide is conserved after reaction with calcium and copper, respectively, because the three bands at 1688, 1628, and 1533 cm^{-1} (MPF-2) and 1688, 1633, and 1533 cm^{-1} (MPF-9), indicative of the β-sheet, are still visible in the crystalline precipitates.

Besides the conservation of the β-sheet, IR also shows differences between the pure peptide and the metal complexes MPF-2 and MPF-9. After reaction of the ligand with the

metal ions, the C=O stretch vibration of the glutamic acid at 1705 cm^{-1} disappears. This is in line with the fact that the ligand interacts with the metal ion via its acid moiety. Finally, differences between the peak positions of the asymmetric $\nu_{C=O}$ and the symmetric $\nu_{C=O}$ vibrations (1533 cm^{-1}, difference 116 cm^{-1} in MPF-2, and 1564 cm^{-1}, difference 182 cm^{-1} in MPF-9) suggest that a carboxylic acid acts as a bridging unit between metal centers in MPF-2 and as an asymmetric monodentate ligand in MPF 9.[44,45]

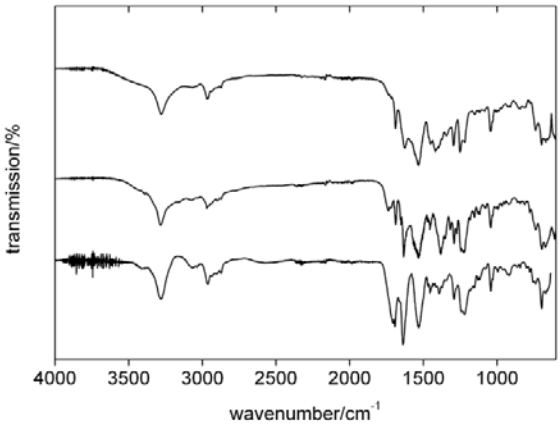

Figure 3. IR spectra of (a) the pure peptide 2, (b) MPF-2, and (c) MPF-9.

Figure 4 shows EPR spectra of MPF-9 powders measured at 75 and 293 K. Both spectra have an anisotropic overall shape, but because the signals are broad, the hyperfine pattern of Cu(II) is invisible. Therefore, simulation of the spectra was done using an orthorhombic gyromagnetic tensor, because a slight orthorhombic character of the gyromagnetic tensor has been previously obtained for other systems where Cu(II) was bonded to glutamic acid.[46] The hyperfine tensor could not be obtained due to the large linewidths. Table 2 summarizes the results from the simulation.

The presence of the half-field EPR signal shows that spin-spin interactions are present in MPF-9. This indicates, in accordance with the very low solubility of MPF-9 in organic solvents, that there is a network of Cu(II) ions connected by bridging moieties. In most Cu complexes where the metal ions are bonded to two amino acid molecules this is realized by carboxylate as well as by hydrogen bond bridges. Both paths are in principle able to transfer spin polarization and therefore provide the dominant pathways for super-exchange.[46]

For two S = 1/2 centers with gyromagnetic values near 2 and an electron-electron distance r > 4.5 Å, the integrated intensity of the half-field signal is determined only by the interspin distance r.[47] By assuming in this simple model that the anisotropic exchange is negligible, the integrated intensity ratio between the ΔMS = ± 1 and ΔMS = ± 2 transitions has been used to estimate a Cu(II)-Cu(II) distance of 5.75 Å. Since the gyromagnetic tensor is anisotropic, the anisotropic exchange interaction is not negligible, and therefore the calculated electron-electron distance has an error of ca. 10 %.

The values for the gyromagnetic tensor suggest that the first coordination sphere around the copper ion is distorted and involves, besides the oxygen atoms from the carboxylate groups, two nitrogen atoms. These two atoms are most likely from ammonia used in the synthesis of MPF-9. The distortion around the copper center is suspected to arise from the extended coordination ring of the glutamic acid moiety. This extended cycle is different from the more conventional 5-coordination ring in Cu(II)-L-arginine complexes where the 2N2O square planar geometry is preserved.[48] Moreover, these values indicate that the main contribution to the ground state wave function is given by the d(x^2-y^2) orbital.

The EPR spectrum measured at 293 K exhibits the same shape, although the signal intensity slightly decreases. To simulate this spectrum, an octahedral gyromagnetic tensor and large linewidths, as in the case of low temperature measurements, were used. The values of the gyromagnetic tensor differ slightly from those obtained for the low temperature measurements, but did not show a fluxional behavior of the copper ions.

The absence of any hyperfine structure has been previously observed for ferromagnetic chain complexes involving carboxylate bridges. There, carboxylate groups involving a copper-apical oxygen bond are more effective to transfer spin polarization than hydrogen bonds.[49] However, the relatively large electron-electron distance suggests that in the case of MPF-9, the bridging does not involve carboxylate, but hydrogen bonds, which stabilize the hybrid system by forming long copper-copper 1-D chains. Moreover, the observed spectra are clearly different from spectra observed for copper(II) complexes of linear-chain fatty acids.[50]

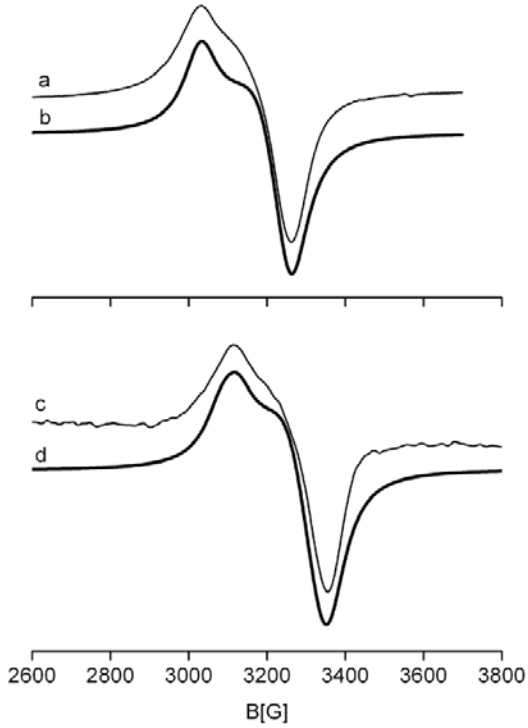

Figure 4. EPR spectra and spectrum simulations of MPF-9 powder measured at 75K and 293 K. (a) Spectrum measured at 75 K, (b) spectrum simulation, (c) spectrum measured at 293 K, and (d) spectrum simulation.

Table 2. EPR parameters obtained by simulating the experimental spectrum of MPF-9.

Complex	T/K	g			g_{iso}	A	Γ/G		
		g_{xx}	g_{yy}	g_{zz}			Γ_{xx}	Γ_{yy}	Γ_{zz}
MPF-9	75	2.082	2.113	2.235	2.143	-	55	80	62
	293	2.083	2.126	2.252	2.154	-	65	75	68

Besides EPR, magnetic measurements were used to further characterize MPF-9. Figure 5 shows a Curie-Weiss plot of MPF-9 and Figure 6 shows the corresponding saturation curve recorded at 1.8 K. The χ^{-1} dependence of T in the Curie-Weiss plot and the saturation curve clearly show that the structure is composed of independent S = ½ Cu(II) ions and

constitutes 1D Heisenberg S = ½ chains.[51] The Curie-Weiss law is well-followed, and the fittings leads to C = 0.437 K cm^3 mol^{-1} and θ = -0.30 K.

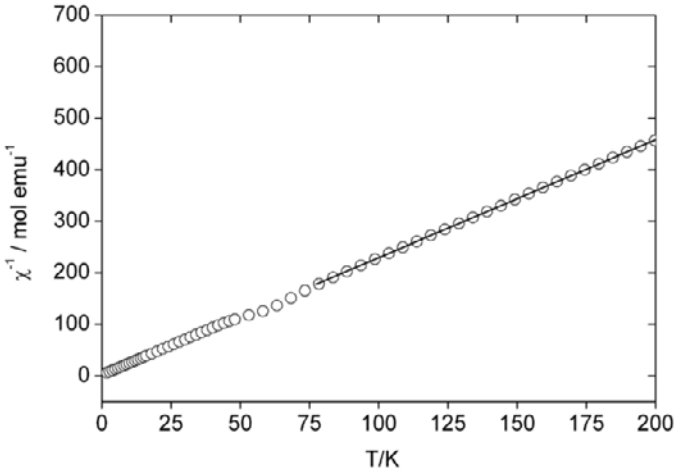

Figure 5. Curie-Weiss Plot of MPF-9.

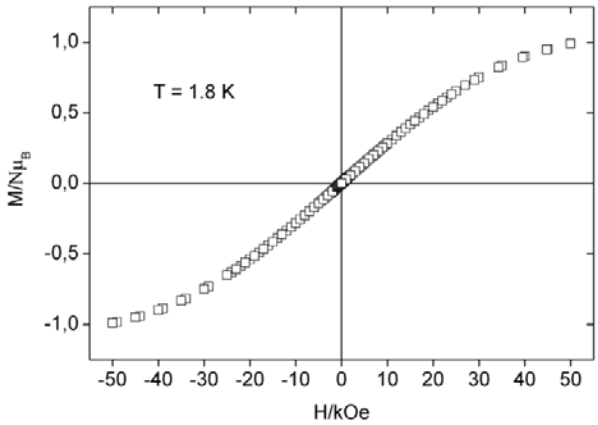

Figure 6. Magnetization versus field curve for MPF-9 recorded at 1.8 K.

Figure 7 shows the corresponding χT vs. T curve. χ is almost constant down to 50 K and is well fitted using the Hattfield model of 1D Heisenberg S = ½ chains.[41] A small hump at 50 to 60 K, not observed in the susceptibility vs. T curve, was revealed when plotting the χT product variation. This can be attributed either to very small amount of impurity or to the presence of oxygen, the signal of which is apparent due to the low mass of sample used for the measurement (3.2 mg). This anomaly however does not prevent interpreting the global behavior of MPF-9. Fitting of the curve leads to g = 2.164(1) and J/k = -1.38(1) K. The

negative J value is characteristic for a singlet ground state in the case of an antiferromagnetic coupling, as already observed from the EPR data.[52]

Both values are of the same order of magnitude and are in good agreement with the EPR values, as is the small Curie-Weiss constant θ. A small decrease in the Curie-Weiss constant θ is observed from 0.437 K*cm^3*mol^{-1} at 295 K to 0.283 K*cm^3*mol^{-1} at 1.8 K. The decrease of χT, and the negative sign of θ confirm the existence of small antiferromagnetic exchange interactions.[53] The weak J value confirms that the magnetization exchange occurs through nitrogen atoms and H-bonds and not through carboxylate-mediated interactions like in amino-acid copper(II) complexes.[54] As the behavior of complexes with a single carboxylate bridge indicates that J vanishes at distances over 3 Å because the direct interaction predominates over the superexchange mechanism, we exclude a single carboxylate bridge network in the case of MPF-9.[52]

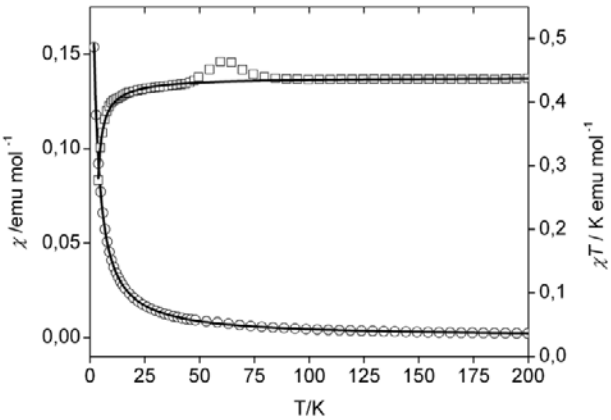

Figure 7. Temperature variation of the magnetic susceptibility, χ (circles) and of the χT product (squares) of MPF-9 recorded in a 5000 Oe field. The full line corresponds to the fit carried out with the expression for Heisenberg S = ½ chains.

Because neither MPF-2 nor MPF-9 crystallize as single crystals, powder diffraction methods had to be used for structure solution. The X-ray powder diffraction patterns for MPF-2 and MPF-9 are shown in Figure 8. They were indexed using Topas academic[31,32] and the results are shown in Table 3.

The quality of the powder diffraction pattern for MPF-2 did not allow structure solution. However, the powder pattern does suggest a lamellar structure. The peaks at 2θ values of 0.9068°, 1.92°, 2.88°, and 3.88° (d-spacings of 29.85 Å, 14.91 Å, 9.95 Å and 7.46 Å) can be indexed as 001, 002, 003 and 004. This indicates a lamellar structure perpendicular to the *c* direction, which in turn suggests a β-sheet structure.

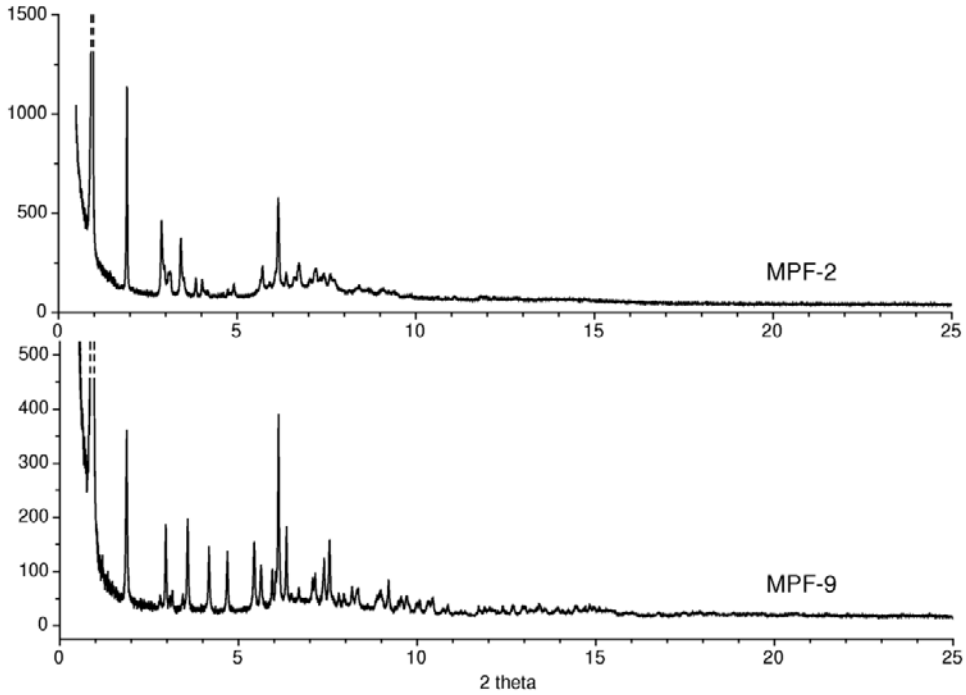

Figure 8. Synchrotron powder diffraction patterns of MPF-9 and MPF-2 (λ = 0.50007Å). In both cases, the first peak has been cut at approximately 25% of its full height to show more detail at higher angles.

Table 3. Unit cells for MPF-2 and MPF-9.

Sample	*a* (Å)	*b* (Å)	*c* (Å)	α (°)	β (°)	γ (°)	Space group
MPF-2	13.6714	9.7210	29.9315	90	94.826	90	Monoclinic *P*
MPF-9	19.2610	4.8885	30.5096	90	92.524	90	Monoclinic *C*2

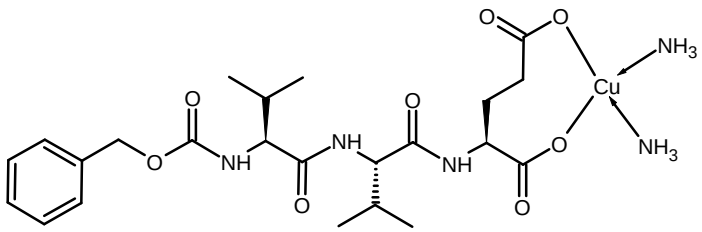

3

Scheme 2. Chemical structure used as input for FOX analysis.

The diffraction pattern of MPF-9 was of better quality, and a crystal structure model could be obtained using the direct-space global-optimization algorithms implemented in the computer program FOX.[35,36] The chemical information used as input for these optimizations (connectivity, bond distances and angles) is shown in Scheme 2. Le Bail extraction was performed to determine Cagliotti parameters and the η ratio with Fullprof using a Pseudo-Voigt profile.[33,34] The best of the copper complex structures generated by FOX is shown in Figure 9. Elemental and thermogravimetric analyses indicated that there is also one water molecule per copper ion present in the structure, but to keep the model as simple as possible, this was not included in the FOX simulations. Some of the torsion angles were fixed or restricted to a certain range to limit the possibility of unrealistic torsion angles. For the optimization, data to sin $\theta/\lambda = 0.20$ (11.5˚2θ) were used. To allow for the steric requirements of the hydrogen atoms, they were included in the model submitted to Fox.

To complete and refine the model from FOX, a Rietveld refinement using the program XRS-82[38] was undertaken. The complete diffraction pattern was used, and bond distance and angle restraints were included to keep the model chemically sensible. H atoms were added where their positions could be calculated from the connected atoms, but for the ammonia molecules and methyl groups, where the positions of the H atoms are not well defined, the occupancy factor for the corresponding N and C atoms were simply increased to include the three electrons from the attached H atoms (e.g. CH_3 was modeled as 1.5 C) and the atomic displacement factor increased slightly. During the course of the refinement, the weight of the geometric restraints with respect to the diffraction data was reduced progressively, and in the final stages a factor or 1.0 was applied. A water molecule was located in a difference electron density map and added to the structural model as an O atom with an occupancy of 1.25 (to

account for the two unlocated H atoms). To keep the number of parameters to a minimum, the atomic displacement parameters were fixed at typical values and not refined. Refinement of this model converged with the R-values R_F = 0.103, R_p = 0.211 and R_{wp} = 0.266 (R_{exp} = 0.217). The crystal structure including the water molecule is shown figure 10. The profile fit is shown in Figure 11. Further details of the refinement are given in Table 4. The atom numbering convention is given in the supporting information, Figure S1. Atomic positions are given in Table S1, selected interatomic distances in Table S2 and bond angles in Table S3. Platon's CALC Void[40] function log journal is given in Table S4.

Table 4. Rietveld refinement of MPF-9.

Unit Cell	
Space group	*C*2
a (Å)	19.2665(10)
b (Å)	4.8848(2)
c (Å)	30.5146(21)
β (˚)	92.5(1)
Refinement	
Number of observations	4723
Number of contributing reflections	1107
Number of geometric restraints	207
Number of positional parameters	
non-H	113
H	57
Number of profile parameters	11
R_F	0.103
R_{wp}	0.266
R_{exp}	0.217

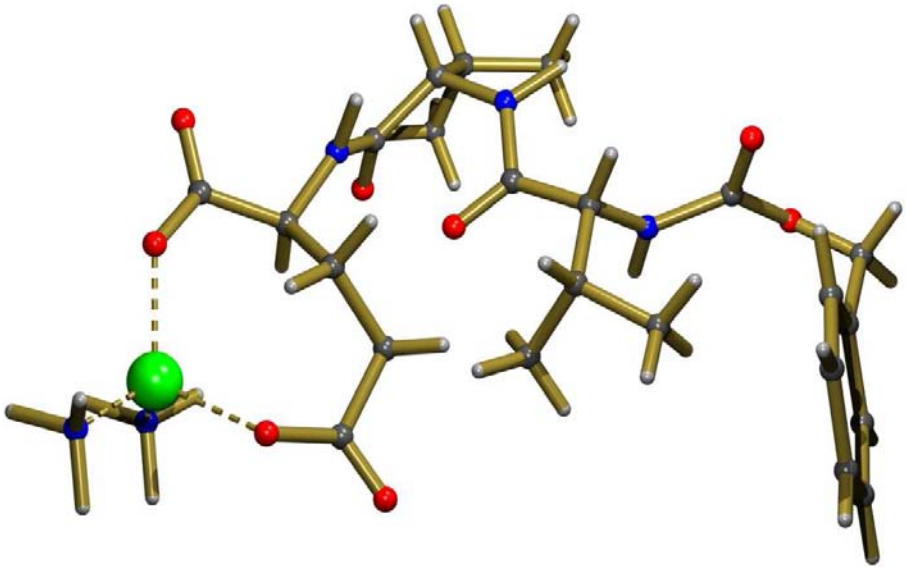

Figure 9. Crystal structure of MPF-9 generated by FOX and before Rietveld refinement, including hydrogen atoms.

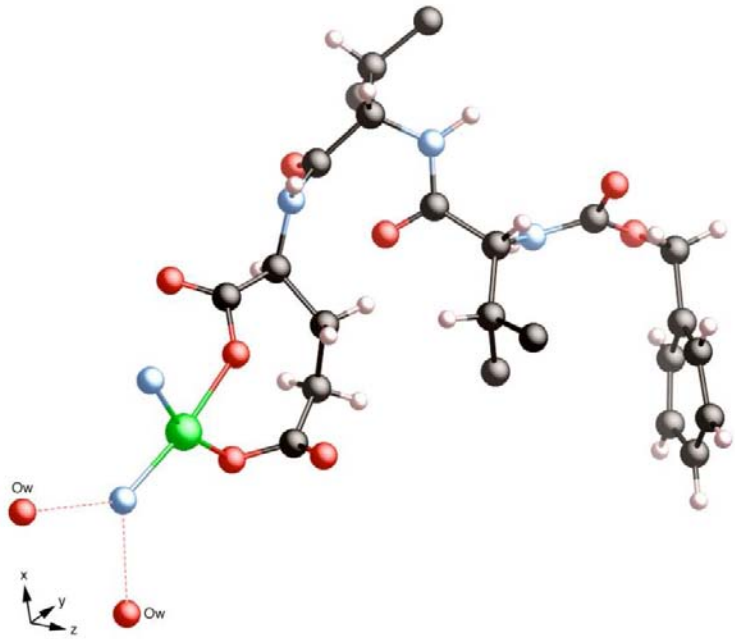

Figure 10. Crystal structure of MPF-9 after refinement of the model generated by FOX, including the water molecule.

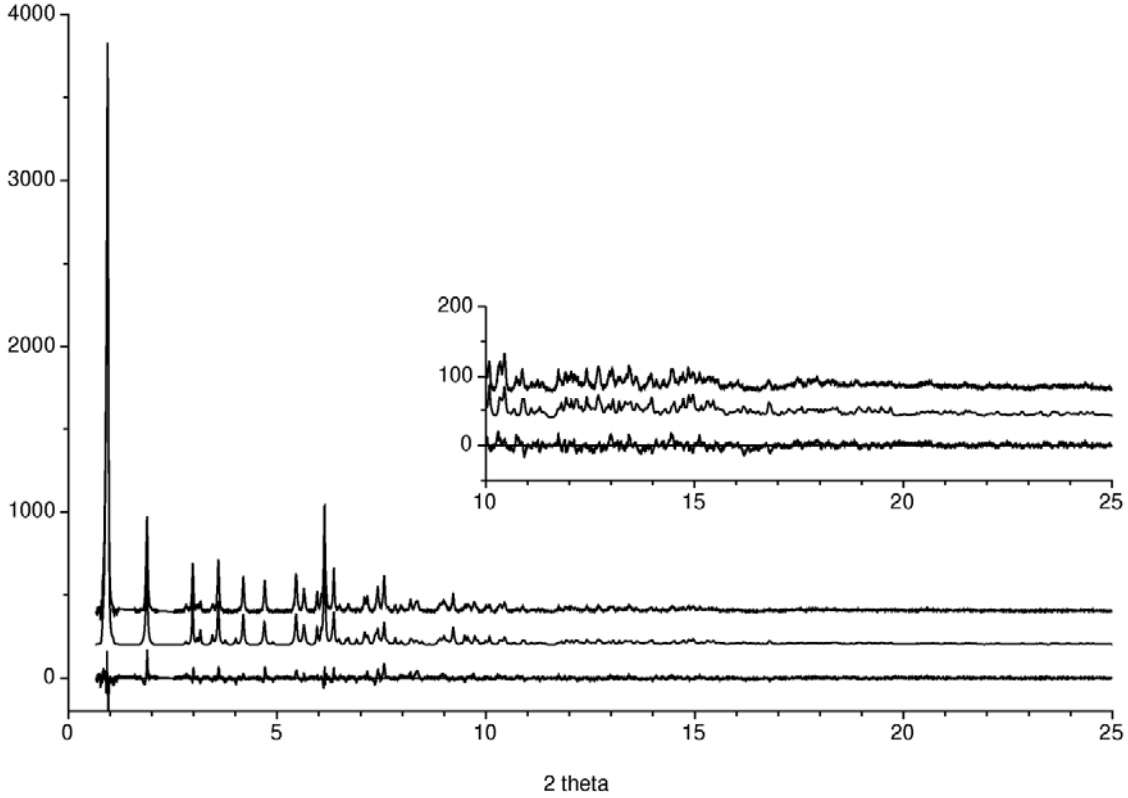

Figure 11. Observed (top), calculated (middle) and difference (bottom) profiles for the Rietveld refinement of MPF-9. The inset has been scaled up by a factor of 5 to show more detail.

The copper center is coordinated to two oxygens of the carboxylic acid and to two ammonia molecules introduced during the synthesis in a distorted square planar geometry. The Cu-N distances of 1.98(3) Å and 1.99(3) Å are in accordance with the generally observed values of 1.90 to 2.02 Å. Similarly, the Cu-O distances of 1.98(3) Å and 1.99(3) Å correspond to those observed in related systems.[55-58] A global view of the crystal structure of MPF-9 is shown in Figure 12, and a magnified view along the crystallographic *a*-axis in Figure 13. Both figures show that there are multiple interactions present in MPF-9. The water molecule forms H-bonds with ammonia molecules of neighboring Cu complexes along the [100] direction (N⋯O 2.88(5) Å and 3.02(4) Å) to create a helical H-bonding network along the [010] direction (Figure 14 and supporting information Figure S2). The other ammonia molecule forms H-bonds with the L-glutamic acid residue of the neighboring Cu complex along the [001] direction (N⋯O 2.87(4) Å). There are two further H-bonds linking the peptides along

the [010] direction (N···O 2.84(4) Å and N···O 3.01(4) Å). Thisdense hydrogen bonding network accounts for the insolubility of this material in both water and organic solvents. The structure is, within the limitations of the method, very well-defined. It is also consistent with the results of the elemental analysis, TGA, EPR, and magnetic measurements.

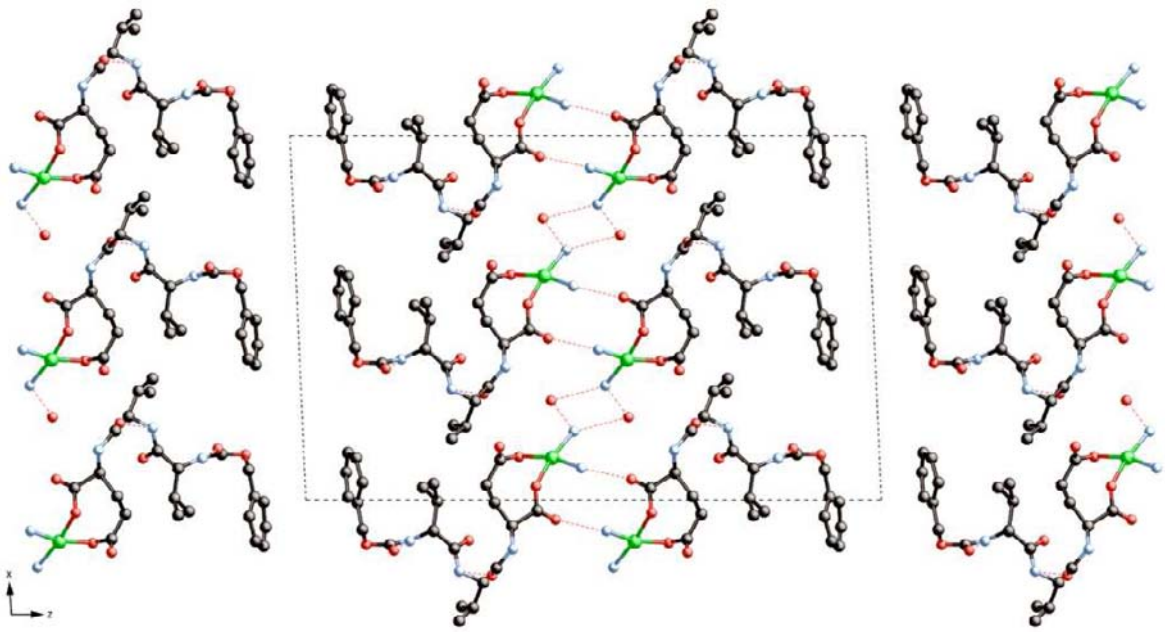

Figure 12. Packing scheme of the crystal. View slightly off the crystallographic *b*-axis. Hydrogen atoms have been removed for clarity.

The structure can be described in terms of two 2D substructures, which are interconnected via hydrogen bonding. However, there is no extended Cu(II) 3D network. The first substructure is composed of a double layer of copper ions in the *ab* plane that are diagonally displaced with respect to one another. Along [010], the copper(II) centers are separated by a distance of 4.9 Å and along [100], by 6.2 Å and 7.0 Å. Such a structure is in line with the magnetic properties of the material, which exhibits a weak antiferromagnetism and thus long Cu(II) – Cu (II) distances. Because of the spacing of the Cu(II) centers, the magnetic transfer cannot be based on carboxylate pathways, and must therefore be based on hydrogen bonding. Despite the existence of hydrogen bonds between adjacent complexes, there is no magnetic coupling between them, because the large number of atoms involved in the hydrogen bonding network limits the magnetic interaction. The large distance of 6.2 Å between two columns of copper (II) as well as the packing of the ligands prevents any

magnetic interactions between them and is in line with the modeling of the magnetic properties as a Heisenberg S = ½ 1D chain.

The second double layer in the *ab* plane is that of the peptide with its long molecule axis oriented roughly along [001]. In addition to the H-bonding between the peptides along [010], the phenyl rings form a column along [010]. The centers of gravity of the individual phenyl residues are 4.9 Å apart, indicating some π–π-stacking interaction. The intercolumn distances are in the same range and the rings form a zig-zag arrangement, which implies that π-π stacking is responsible for both the internal and external column stabilization.

The hydrogen bonding scheme adopted by the peptides in the crystal is shown in Figure 13. There is a β-sheet-like interaction along the crystallographic *b*-axis. The presence of a β-sheet bonding scheme has also been shown by IR spectroscopy (Figure 3), but the crystal structure further shows that not all of the peptide is part of the β-sheet. Only the carbamate and the L-valine-L-valine peptide bond are involved. To maximize the number of hydrogen bonds, the β-sheet is distorted slightly to accommodate the rather large side chains of the valine units. This distortion enables the L-glutamic acid residue to adapt to the metal center coordination geometry. The crystallographic results confirm those of the IR spectroscopy, and also reveal a more complex bonding scheme than simple β-sheets. Furthermore, the crystal structure shows that the β-sheet orientation, which could not be determined from IR, is parallel and not antiparallel along the *b*-axis.

The hydrogen bonding between the water and coordinated ammonia molecules that connects copper centers in adjacent columns is shown in Figure 14. This hydrogen bonding scheme is an effective pathway for transferring magnetization through hydrogen bonding.[46,59] The structure presented here is a new mode of coordination for the well-known glutamic acid ligand,[46,49,60-62] where there is no magnetic exchange through carboxylate centers, although here the glutamic acids are not involved in a peptide-like structure. However, the gain in energy given by the formation of β sheets via hydrophobic interaction, hydrogen bonding and extensive π–π stacking of benzyl rings is highly favorable and compensates the effect of the non-classical bonding scheme.

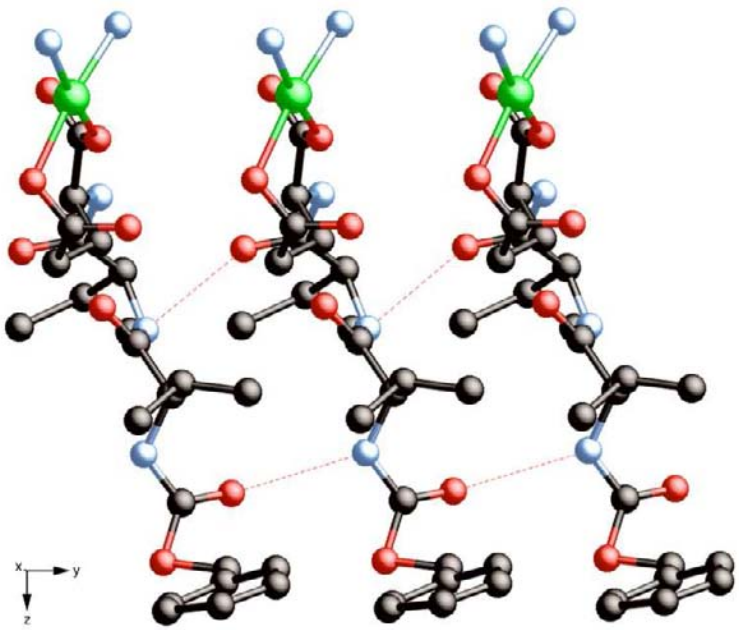

Figure 13. β-sheet-like structure and hydrogen bonding in the peptide backbone of MPF-9. Hydrogen atoms have been removed for clarity and N···O interactions are indicated by a dotted line.

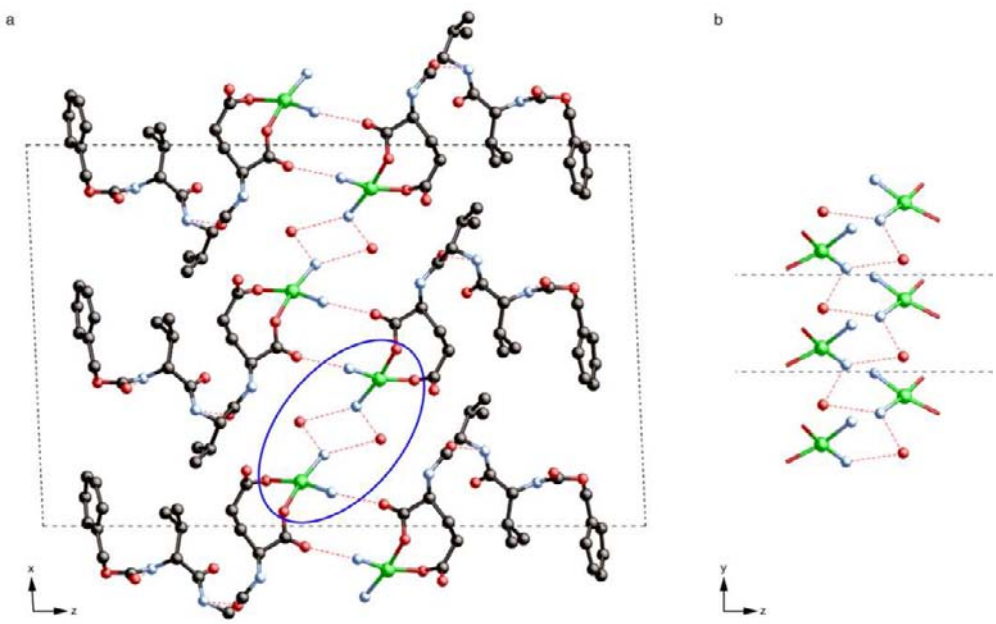

Figure 14. Hydrogen bonding network in the *ac* plane (left) and a perpendicular view of the helical linkage between water and ammonia molecules along [010] (right). The Hydrogen atoms have been removed for clarity.

The porosity of MPF-9 was analyzed using Platon's voids calculation functionality and plotting.[40] Figure 15 shows the pores in MPF-9 that are accessible to small solvent or gas molecules. The total void volume is 387 $Å^3$ for a total unit cell volume of 2867 A^3. This results in a total void volume of just above 13 % of the cell volume. MPF-9 only has chiral channel-like pores parallel to the [010] direction, but two ranges of sizes can be distinguished. The larger pores have a volume of around 101 $Å^3$. This is large enough to accommodate methanol, ethanol, or possibly benzene if the linear molecular shape of the latter three and the possible π-π interactions are considered. The smaller voids are around 20 to 37 $Å^3$. These pores are large enough to accommodate hydrogen and carbon dioxide, or even water (in the pores at the larger end of the spectrum). However, the small connections between the 20 $Å^3$ voids prevent them from forming an extended channel along the *b* axis. As a result, MPF-9 is a candidate for gas adsorption and storage, for purification, or for chiral separation.

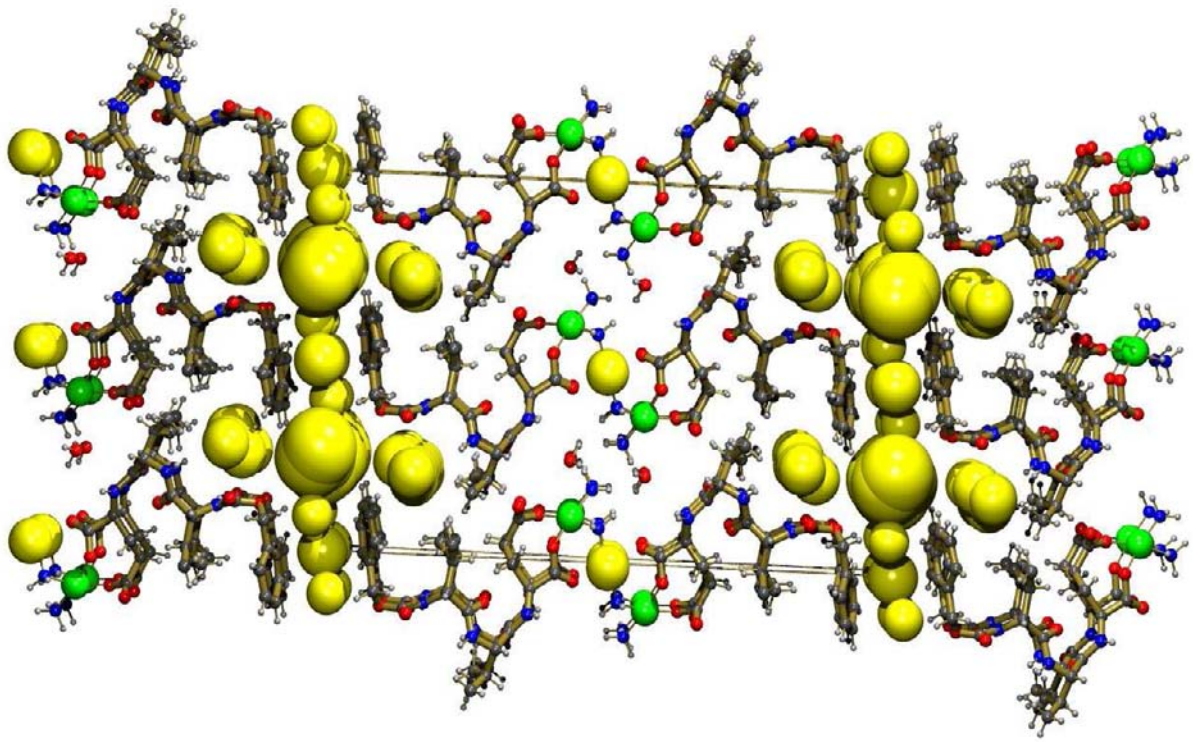

Figure 15. Packing diagram of MPF-9. Yellow balls indicate the voids.

In summary, metal-peptide frameworks are a new and interesting variety of metal-organic frameworks. The coordination mode of MPF-9 differs from other α–ω dicarboxylic

acids. There is no bridging of the carboxylic acid moiety between the metal centers as seen in refs.[14-21] The current paper therefore suggests that peptides with different topologies should, like regular organic dicarboxylic acids, allow for the fabrication of MPFs with different topologies with specifically designed (chiral) inner pores. The ligand acts as a chelator, similar to smaller dicarboxylic acids like malonates.[55,56] This is rather surprising, but can be rationalized via the overall energy gain from the formation of a highly hydrogen-bonded network with π-π-stacking. This energy gain is presumably higher than the energy gained by forming an extensive carboxylate network.

Furthermore, the synthesis conditions are convenient and there is no need for autoclave, microwave, or slow diffusion synthesis protocols, which are often used for MOF's.[5] The ease of synthesis is an important point for any industrial application. Although the overall cost of MPFs is somewhat higher than that of conventional MOFs, the ability to include chiral information and possibly other chemical information like metal coordinating sites *a priori* should alleviate issues of higher cost.

MPF-2 and MPF-9 are just the first examples of MPFs. They demonstrate that new peptide-based materials can be generated using rather simple building blocks and low strength, non-covalent interactions like hydrogen bonding.[63,64] and π–π stacking of benzyl rings,[65,66] along with metal complexation. A structurally interesting point is the role of the amines located around the copper(II). They not only complete the coordination sphere, but also constitute a way of ensuring the stabilization and weak magnetization transfer in a metal column using hydrogen bonding. Moreover, π–π stacking was very useful in stabilizing and organizing the complexes.

5.4 Conclusion

This paper is the first example of metal-peptide frameworks, "bioinspired" analogs to the well-known MOFs. Metal-oxygen and metal-nitrogen bonding and various types of hydrogen bonding along with π-π-stacking are responsible for the formation of a porous network structure, which is stable up to ca. 250 °C. Despite the lack of single crystals, the crystal structure of the copper complex MPF-9 could be determined from powder diffraction

data using the FOX program. The refined crystal structure is consistent with the spectroscopic information.

The 1D channel architecture with two different pore sizes makes MPF-9 an interesting material for gas storage. Further applications include gas or chiral separation or catalysis. Finally, the organization of the Cu(II) ions in a 2D layer pattern yields a material with an interesting paramagnetic character. The current paper therefore clearly shows that small peptides are viable candidates for the preparation of complex metal-organic materials with defined topologies. MPFs thus further broaden the more general field of MOFs and entactic metal systems,[67] which are interesting for a wide range of technical applications.

5.4 Acknowledgements

We thank Prof. E.C. Constable for access to his IR spectrometer, M. Düggelin and D. Mathys for SEM measurements, Prof. K. Fromm for access to her TGA, Prof. M. Meuwly for the access to one of his Linux clusters, F. Schmid for FOX and IT support, Dr. R. Černý and Dr. V. Favre-Nicolin for FOX support, J. Rohlíček providing a computer-grid capable FOX version, and Dr. Markus Neuburger for useful discussions. Experimental assistance from the staff at SNBL is gratefully acknowledged. The Swiss National Science Foundation, the NCCR Nanosciences, the University of Potsdam, and the Max-Planck-Institut of Colloids and Interfaces are acknowledged for financial support. A.T. thanks the Holcim Stiftung Wissen for a Habilitation Fellowship.

5.5 References

(1) Yaghi, O. M.; Li, H.; Davis, C.; Richardson, D.; Groy, T. *Acc. Chem. Res.* **1998**, *31*, 474.

(2) Barton, T. J.; Bull, L. M.; Klemperer, W. G.; Loy, D. A.; McEnaney, B.; Misono, M.; Monson, P. A.; Pez, G.; Scherer, G. W.; Vartuli, J. C.; Yaghi, O. M. *Chem. Mater.* **1999**, *11*, 2633.

(3) James, S. L. *Chem. Soc. Rev.* **2003**, *32*, 276.

(4) Rowsell, J. L. C.; Yaghi, O. M. *Microporous Mesoporous Mater.* **2004**, *73*, 3.

(5) Robin, A. Y.; Fromm, K. M. *Coord. Chem. Rev.* **2006**, *250*, 2127.

(6) Rosi, N. L.; Eckert, J.; Eddaoudi, M.; Vodak, D. T.; Kim, J.; O'Keeffe, M.; Yaghi, O. M. *Science* **2003**, *300*, 1127.

(7) Duren, T.; Sarkisov, L.; Yaghi, O. M.; Snurr, R. Q. *Langmuir* **2004**, *20*, 2683.

(8) Chen, B.; Liang, C.; Yang, J.; Contreras, D. S.; Clancy, Y. L.; Lobkovsky, E. B.; Yaghi, O. M.; Dai, S. *Angew. Chem. Int. Ed.* **2006**, *45*, 1390.

(9) Fan, J.; Zhu, H.-F.; Okamura, T.-A.; Sun, W.-Y.; Tang, W.-X.; Ueyeama, N. *New J. Chem.* **2003**, *27*, 1409.

(10) Ye, Q.; Song, Y.-M.; Wang, G.-X.; Chen, K.; Fu, D.-W.; Chan, W.; Hong, P.; Zhu, J.-S.; Huang, S. D.; Xiong, R.-G. *J. Am. Chem. Soc.* **2006**, *128*, 6554.

(11) Horcajada, P.; Serre, C.; Vallet-Regi, M.; Sebban, M.; Taulelle, F.; Ferey, G. *Angew. Chem. Int. Ed.* **2006**, *45*, 5974.

(12) Kitagawa, S.; Noro, S. *Compreh. Coord. Chem.* **2004**, *7*, 231.

(13) Clegg, W. *Compreh. Coord. Chem.* **2004**, *1*, 579.

(14) Borkowski, L. A.; Cahill, C. L. *Inorg. Chem.* **2003**, *42*, 7041.

(15) Borkowski, L. A.; Cahill, C. L. *Inorg. Chem. Commun.* **2004**, *7*, 725.

(16) de Lill, D. T.; Bozzuto, D. J.; Cahill, C. L. *Dalton Trans.* **2005**, 2111.

(17) de Lill, D. T.; Gunning, N. S.; Cahill, C. L. *Inorg. Chem.* **2005**, *44*, 258.

(18) Dimos, A.; Tsaousis, D.; Michaelides, A.; Skoulika, S.; Golhen, S.; Ouahab, L.; Didierjean, C.; Aubry, A. *Chem. Mater.* **2002**, *14*, 2616.

(19) Kiritsis, V.; Michaelides, A.; Skoulika, S.; Golhen, S.; Ouahab, L. *Inorg. Chem.* **1998**, *37*, 3407.

(20) Lobo, R. F.; Zones, S. I.; Davis, M. E. *J. Inclusion Phenom.* **1995**, *21*, 47.

(21) Kim, Y.; Suh, M.; Jung, D.-Y. *Inorg. Chem.* **2004**, *43*, 245.

(22) Kesanli, B.; Lin, W.-B. *Coord. Chem. Rev.* **2003**, *246*, 305.

(23) Bradshaw, D.; Claridge, J. B.; Cussen, E. J.; Prior, T. J.; Rosseinsky, M. J. *Acc. Chem. Res.* **2005**, *38*, 273.

(24) Zang, S.; Su, Y.; Li, Y.; Zhu, H.; Meng, Q. *Inorg. Chem.* **2006**, *45*, 2972.

(25) Lin, W. *J. Solid State Chem.* **2005**, *178*, 2488.

(26) Sun, D.; Ke, Y.; Collins, D. J.; Lorigan, G. A.; Zhou, H.-C. *Inorg. Chem.* **2007**, *46*, 2725.

(27) Gao, E.-Q.; Yue, Y.-F.; Bai, S.-Q.; He, Z.; Yan, C.-H. *J. Am. Chem. Soc.* **2004**, *126*, 1419.

(28) Wu, C.-D.; Hu, A.; Zhang, L.; Lin, W. *J. Am. Chem. Soc.* **2005**, *127*, 8940.

(29) Mantion, A.; Taubert, A. *Macromol. Biosci.* **2007**, *7*, 208.

(30) Mantion, A.; Guex, G.; Foelske, A.; Mirolo, L.; Fromm, K. M.; Painsi, M.; Taubert, A. *Soft Matter*, submitted.

(31) Cheary, W.; Coelho, A. *J. Appl. Cryst.* **1992**, *25*, 109.

(32) Coelho, A. TOPAS; Academic 4.0 ed., 2006.

(33) Rodriguez-Carvajal, J. *Physica B* **1993**, *192*, 55.

(34) http://www-llb.cea.fr/fullweb/fp2k/fp2k.htm **2006**, *August*.

(35) Favre-Nicolin, V. R.; Cerny, R. *J. Appl. Cryst.* **2002**, *35*, 734.

(36) *Fox, Free Objects for Crystallography*, http://objcryst.sourceforge.net.

(37) Betteridge, P. W.; Carruthers, J. R.; Cooper, R. I.; Prout, K.; Watkin, D. J. *J. Appl. Cryst.* **2003**, *36*, 1487.

(38) Baerlocher, C. *The X-ray Rietveld System (XRS-82)*; ETH Zürich: Zürich, 1982.

(39) Spek, A. L. *J.Appl.Cryst.* **2003**, *36*, 7.

(40) Kueppers, H.; Liebau, F.; Spek, A. L. *J. Appl. Cryst.* **2006**, *39*, 338.

(41) Hatfield, W. E. *J. Appl. Phys.* **1981**, *52*, 1985.

(42) Palumbo, M.; Da Rin, S.; Bonora, G. M.; Toniolo, C. *Makromol. Chem.* **1976**, *177*, 1477.

(43) Baron, M. H.; De Loze, C.; Toniolo, C.; Fasman, G. D. *Biopolymers* **1979**, *18*, 411.

(44) Deacon, G. B.; Phillips, R. J. *Coord. Chem. Rev.* **1980**, *33*, 227.

(45) A. Barth, P. *Prog. Biol. Mol. Biol.* **2000**, *74*, 141.

(46) Brondino, C. D.; Casado, N. M. C.; Passeggi, M. C. G.; Calvo, R. *Inorg. Chem.* **1993**, *32*, 2078.

(47) Eaton, S. S.; More, K. M.; Sawant, B. M.; Eaton, G. R. *J. Am. Chem. Soc.* **1983**, *105*, 6560.

(48) Ohata, N.; Masuda, H.; Yamauchi, O. *Inorg. Chim. Acta* **1999**, *286*, 37.

(49) Colacio, E.; Ghazi, M.; Kivekas, R.; Moreno, J. M. *Inorg. Chem.* **2000**, *39*, 2882.

(50) Sharrock, P.; Dartiguenave, M.; Dartiguenave, Y. *Bioinorg. Chem.* **1978**, *9*, 3.

(51) Carlin, R. L. *Magnetochemistry*; Springer: Berlin-Heidelberg, 1986.

(52) Rodriguez-Fortea, A.; Alemany, P.; Alvarez, S.; Ruiz, E. *Chem. Eur. J.* **2001**, *7*, 627.

(53) Zou, J.-Z.; Liu, Q.; Xu, Z.; You, X.-Z.; Huang, X.-Y. *Polyhedron* **1998**, *17*, 1863.

(54) Gerard, M. F.; Aiassa, C.; Casado, N. M. C.; Santana, R. C.; Perec, M.; Rapp, R. E.; Calvo, R. *J. Phys. Chem. Solids* **2007**, *68*, 1533.

(55) Devereux, M.; McCann, M.; Cronin, J. F.; Ferguson, G.; McKee, V. *Polyhedron* **1999**, *18*, 2141.

(56) Chawla, S. K.; Nättinen, K.; Rissanen, K.; Yakhmi, J. V. *Polyhedron* **2004**, *23*, 3007.

(57) Rodriguez-Martin, Y.; Ruiz-Pérez, C.; Sanchiz, J.; Lloret, F.; Julve, M. *Inorg. Chim. Acta* **2001**, *318*, 159.

(58) Li, J.; Zeng, H.; Chen, J.; Wang, Q.; Wu, X. *Chem. Commun.* **1997**, 1213.

(59) Levstein, P. R.; Calvo, R. *Inorg. Chem.* **1990**, *29*, 1581.

(60) Steren, C. A.; Gennaro, A. M.; Levstein, A. M.; Calvo, P. R. *Condens. Matter* **1989**, *1*, 637.

(61) Colacio, E.; Dominguez-Vera, J. M.; Costes, J. P.; Kivekas, R.; Laurent, J. P.; Ruiz, J. *Inorg. Chem.* **1992**, *31*, 774.

(62) Pushita, W. J.; Odani, A.; Yamauchi, O. *J. Inorg. Biochem.* **1999**, *73*, 203.

(63) Beatty, A. M. *Cryst. Eng. Commun.* **2001**, 243.

(64) Katsura, N.-K. *Chem. Soc. Rev.* **2005**, *34*, 109.

(65) Roesky, H. W.; Andruh, M. *Coord. Chem. Rev.* **2003**, *236*, 91.

(66) Ye, B.-H.; Tong, M.-L.; Chen, X.-M. *Coord. Chem. Rev.* **2005**, *249*, 545.

(67) Comba, P. *Coord. Chem. Rev.* **2000**, *200-202*, 217.

5.6 Supplementary material

Figure S1: ORTEP plot (as implemented in Platon[39,40]) of MPF-9 giving the atom numbering convention

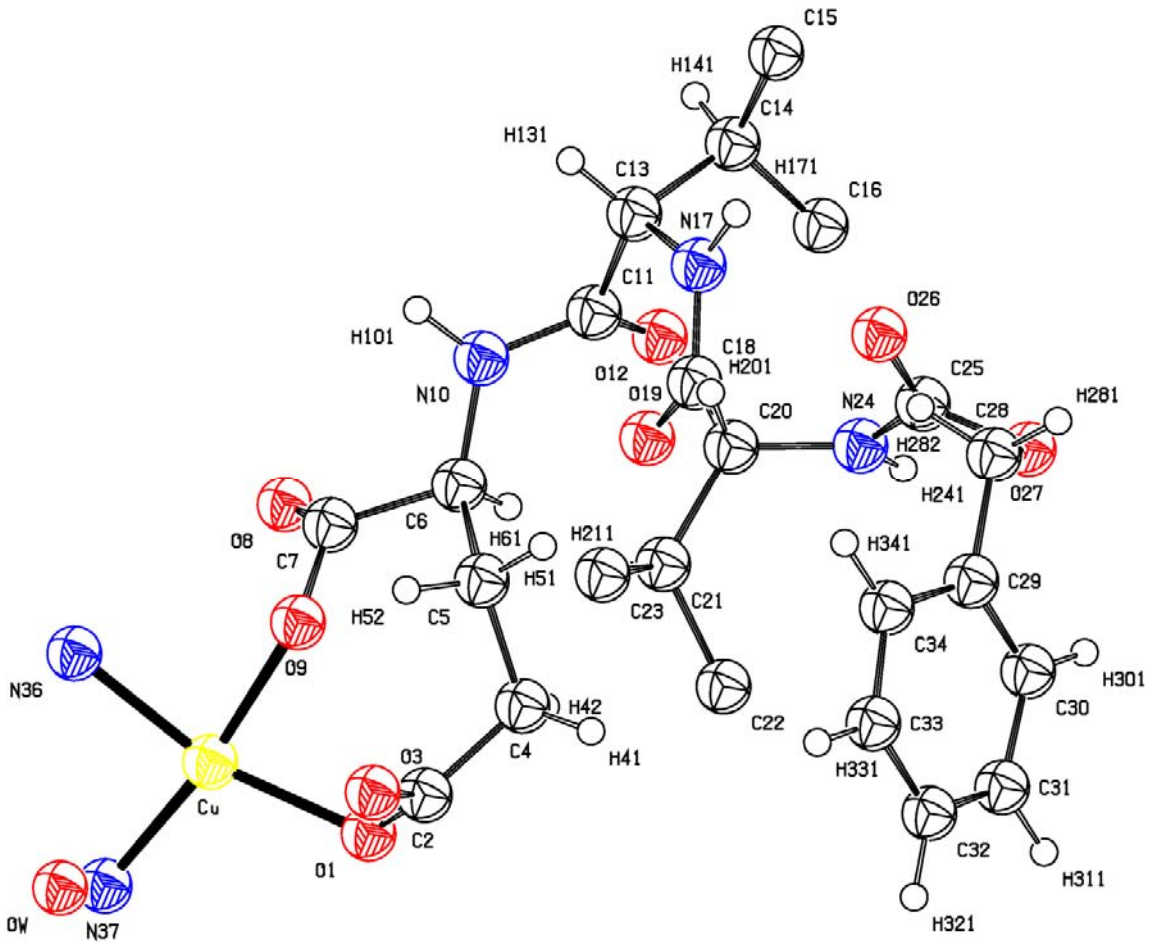

Table S1: Atomic coordinates for MPF-9[a]

Atom	*x*	*y*	*z*	U_{iso}[b]	Occupancy
Cu	0.3850(5)	-0.2586	0.5686(3)	0.010	1.00
O1	0.381(2)	-0.442(7)	0.6268(6)	0.025	1.00
C2	0.390(1)	-0.261(8)	0.659(1)	0.025	1.00
O3	0.355(2)	-0.043(8)	0.659(1)	0.025	1.00
C4	0.460(2)	-0.261(10)	0.686(1)	0.025	1.00
C5	0.509(1)	-0.023(9)	0.673(1)	0.025	1.00
C6	0.573(1)	-0.068(7)	0.6435(8)	0.025	1.00
C7	0.531(1)	-0.074(7)	0.5990(7)	0.025	1.00
O8	0.556(2)	-0.192(9)	0.5674(9)	0.025	1.00
O9	0.463(1)	-0.067(7)	0.5996(9)	0.025	1.00
N10	0.636(1)	0.110(7)	0.6438(7)	0.025	1.00
C11	0.689(2)	0.068(6)	0.675(1)	0.025	1.00
O12	0.709(2)	-0.168(6)	0.683(1)	0.025	1.00
C13	0.729(1)	0.303(6)	0.6983(7)	0.025	1.00
C14	0.798(1)	0.196(7)	0.7173(9)	0.025	1.00
C15	0.833(2)	0.439(9)	0.742(1)	0.040	1.50[c]
C16	0.795(2)	-0.098(8)	0.738(2)	0.040	1.50[c]
N17	0.697(1)	0.372(7)	0.7385(8)	0.025	1.00
C18	0.634(2)	0.268(9)	0.746(1)	0.025	1.00
O19	0.612(1)	0.095(8)	0.7204(8)	0.025	1.00
C20	0.585(1)	0.375(7)	0.7807(7)	0.025	1.00
C21	0.504(1)	0.339(8)	0.7714(8)	0.040	1.50[c]
C22	0.467(2)	0.105(9)	0.796(2)	0.040	1.50[c]
C23	0.457(2)	0.590(10)	0.777(2)	0.025	1.00
N24	0.614(2)	0.277(6)	0.8230(8)	0.025	1.00
C25	0.625(3)	0.453(7)	0.8571(7)	0.025	1.00
O26	0.640(2)	0.694(6)	0.8510(9)	0.025	1.00
O27	0.624(2)	0.367(7)	0.8985(8)	0.025	1.00
C28	0.582(1)	0.611(7)	0.903(1)	0.025	1.00
C29	0.508(1)	0.527(6)	0.911(1)	0.025	1.00

C30	0.493(1)	0.267(8)	0.926(1)	0.025	1.00
C31	0.425(2)	0.180(10)	0.928(1)	0.025	1.00
C32	0.372(1)	0.371(12)	0.923(2)	0.025	1.00
C33	0.386(1)	0.635(11)	0.910(1)	0.025	1.00
C34	0.454(2)	0.706(8)	0.900(1)	0.025	1.00
N36	0.413(2)	-0.021(6)	0.5195(8)	0.040	1.43[c]
N37	0.313(2)	-0.432(8)	0.5289(9)	0.040	1.43[c]
Ow	0.228(2)	0.153(8)	0.5666(8)	0.040	1.25[c]
H41	0.450(3)	-0.247(19)	0.717(1)	0.030	1.00
H42	0.483(3)	-0.440(10)	0.680(3)	0.030	1.00
H51	0.530(3)	0.055(17)	0.700(2)	0.030	1.00
H52	0.479(2)	0.120(12)	0.658(3)	0.030	1.00
H61	0.591(2)	-0.257(8)	0.651(2)	0.030	1.00
H101	0.633(3)	0.290(12)	0.628(3)	0.030	1.00
H131	0.736(3)	0.468(8)	0.680(1)	0.030	1.00
H141	0.827(2)	0.172(11)	0.691(1)	0.030	1.00
H171	0.719(5)	0.520(31)	0.758(4)	0.030	1.00
H201	0.592(3)	0.578(8)	0.782(2)	0.030	1.00
H211	0.498(3)	0.295(16)	0.739(1)	0.030	1.00
H241	0.624(8)	0.076(7)	0.827(2)	0.030	1.00
H281	0.601(3)	0.719(14)	0.929(2)	0.030	1.00
H282	0.584(3)	0.722(12)	0.876(2)	0.030	1.00
H301	0.532(2)	0.134(8)	0.932(2)	0.030	1.00
H311	0.414(2)	-0.010(11)	0.938(2)	0.030	1.00
H321	0.323(1)	0.315(15)	0.928(2)	0.030	1.00
H331	0.347(2)	0.768(15)	0.904(3)	0.030	1.00
H341	0.464(3)	0.895(9)	0.890(2)	0.030	1.00

[a] Numbers in parentheses are the estimated standard deviations in the units of the least significant digit given. Values without an esd were not refined.

[b] Atomic displacement parameters ($Å^{-2}$) were not refined.

[c] These occupancy parameters have been increased to account for the associated H atoms.

Table S2: Selected interatomic distances (Å) for MPF-9[a]

Cu - O1	1.99(3)	C2 - C4	1.53(4)
Cu - O9	1.98(3)	C4 - C5	1.56(5)
Cu - N36	1.99(3)	C5 - C6	1.56(4)
Cu - N37	1.98(3)	C6 - C7	1.55(3)
O1 - C2	1.34(4)	C11 - C13	1.54(4)
O3 - C2	1.27(5)	C13 - C14	1.53(4)
O8 - C7	1.23(4)	C14 - C16	1.57(5)
O9 - C7	1.31(3)	C14 - C15	1.55(5)
O12 - C11	1.24(4)	C18 - C20	1.54(4)
O19 - C18	1.20(5)	C20 - C21	1.59(4)
O26 - C25	1.22(5)	C21 - C22	1.56(6)
O27 - C25	1.33(3)	C21 - C23	1.54(6)
O27 - C28	1.45(5)	C28 - C29	1.52(4)
N10 - C6	1.49(4)	C29 - C34	1.39(4)
N10 - C11	1.38(4)	C29 - C30	1.39(5)
N17 - C18	1.34(4)	C30 - C31	1.39(4)
N17 - C13	1.43(4)	C31 - C32	1.39(6)
N24 - C20	1.46(4)	C32 - C33	1.39(8)
N24 - C25	1.36(4)	C33 - C34	1.39(5)

N17 ⋯ O12	2.84(4)
N24 ⋯ O26	3.01(4)
N36 ⋯ O8	2.87(4)
N37 ⋯ Ow	2.88(5)
	3.02(4)

[a] Numbers in parentheses are the estimated standard deviations in the units of the least significant digit given.

Table S3: Selected bond angles (˚) for MPF-9[a]

O1	-	Cu	-	O9	81(1)	C13	-	C14	-	C15	106(3)
O1	-	Cu	-	N36	163(1)	C13	-	C14	-	C16	114(3)
O1	-	Cu	-	N37	107(1)	C15	-	C14	-	C16	122(3)
O9	-	Cu	-	N36	82(1)	C13	-	N17	-	C18	118(3)
O9	-	Cu	-	N37	171(1)	N17	-	C18	-	O19	117(3)
N36	-	Cu	-	N37	90(1)	N17	-	C18	-	C20	124(3)
						O19	-	C18	-	C20	119(3)
Cu	-	O1	-	C2	111(2)	C18	-	C20	-	C21	117(2)
O1	-	C2	-	C4	118(3)	C18	-	C20	-	N24	107(3)
O1	-	C2	-	O3	120(3)	C21	-	C20	-	N24	117(2)
O3	-	C2	-	C4	118(3)	C20	-	C21	-	C22	118(3)
C2	-	C4	-	C5	113(3)	C20	-	C21	-	C23	118(3)
C4	-	C5	-	C6	123(3)	C22	-	C21	-	C23	104(3)
C5	-	C6	-	N10	125(3)	C20	-	N24	-	C25	121(3)
C5	-	C6	-	C7	96(2)	N24	-	C25	-	O26	121(3)
C7	-	C6	-	N10	114(2)	N24	-	C25	-	O27	121(3)
C6	-	C7	-	O8	120(3)	O26	-	C25	-	O27	117(3)
C6	-	C7	-	O9	118(2)	C25	-	O27	-	C28	83(3)
O8	-	C7	-	O9	116(3)	O27	-	C28	-	C29	109(3)
Cu	-	O9	-	C7	136(2)	C28	-	C29	-	C30	120(2)
C6	-	N10	-	C11	120(3)	C28	-	C29	-	C34	120(3)
N10	-	C11	-	O12	119(3)	C30	-	C29	-	C34	120(3)
N10	-	C11	-	C13	123(3)	C29	-	C30	-	C31	120(3)
O12	-	C11	-	C13	117(3)	C30	-	C31	-	C32	119(4)
C11	-	C13	-	C14	109(2)	C31	-	C32	-	C33	120(3)
C11	-	C13	-	N17	111(2)	C32	-	C33	-	C34	120(4)
C14	-	C13	-	N17	99(2)	C29	-	C34	-	C33	120(4)

[a] Numbers in parentheses are the estimated standard deviations in the units of the least significant digit given.

Table S4: Results of the voids calculation using CALC VOID[40] function of Platon[39,40]

```
van der Waals (or ion) Radii used in the Analysis
==============================================================================
    C    H   Cu    N    O
------------------------------------------------------------------------------
 1.70 1.20 2.32 1.55 1.52

:: Grid: Y-Axis Step = 0.0417 = Points  24, Angstrom Step = 0.20
:: Grid: Z-Axis Step = 0.0064 = Points 156, Angstrom Step = 0.20
:: Grid: X-Axis Step = 0.0104 = Points  96, Angstrom Step = 0.20


:: Total Potential Solvent Area Vol    387.2 Ang^3
                  per Unit Cell Vol   2869.8 Ang^3 [13.5%]

Note: Expected volumes for solvent molecules are:
      A hydrogen bonded H2O-molecule      40 Ang^3
      Small molecules (e.g. Toluene) 100-300 Ang^3

      Values below for gridpoints and volumes in []
      refer to areas where atom centers may reside.

:: Use the CALC SQUEEZE instruction to calculate and optionally correct for
:: Density identified in solvent accessible areas (Reflection data required)

Area #GridPoint VolPerc.  Vol(A^3)  X(av) Y(av) Z(av) Eigenvector(frac) Sig(Ang)
------------------------------------------------------------------------------
 1  12644[  2472]  4   101[  19.7]  0.250-0.044 0.000 1  0.210 1.000 0.117  1.60
                                                      2  0.339-1.000-0.014  1.38
                                                      3  0.133 1.000-0.327  1.12
 2  12644[  2472]  4   101[  19.7]  0.750-0.062 0.000 1 -0.210 1.000-0.110  1.65
                                                      2  0.364 1.000-0.035  1.34
                                                      3  0.080-1.000-0.310  1.11
 3   4668[   123]  1    37[   1.0]  0.222-0.055 0.157 1  0.058 1.000 0.016  1.40
                                                      2 -1.000 0.435 0.792  0.90
                                                      3  0.847-1.000 0.448  0.71
 4   4668[   123]  1    37[   1.0]  0.722-0.100 0.157 1 -0.062 1.000 0.012  1.49
                                                      2 -0.642-1.000 0.678  0.87
                                                      3  1.000 0.752 0.423  0.74
 5   4667[   123]  1    37[   1.0]  0.778-0.061 0.843 1 -0.056 1.000-0.019  1.40
                                                      2 -1.000-0.205 0.929  0.92
                                                      3  0.861 1.000 0.387  0.73
 6   4667[   123]  1    37[   1.0]  0.278-0.099 0.843 1  0.062 1.000-0.013  1.49
```

```
                                                        2 -0.561 1.000 0.789  0.89
                                                        3  1.000-0.792 0.331  0.75
 7   2271[    22]  1    18[   0.2]  0.000 0.265 0.000 1  1.000-0.001-0.014  0.90
                                                        2  0.000 1.000 0.000  0.72
                                                        3  0.104 0.019 1.000  0.62
 8   2271[    22]  1    18[   0.2]  0.500 0.765 0.000 1  1.000-0.002-0.014  0.90
                                                        2  0.000 1.000 0.000  0.72
                                                        3  0.104 0.019 1.000  0.62

      x     y     z              Shortest Contacts within 4.5 Angstrom (Excl. H)
==============================================================================
  1  0.250-0.044 0.000            C32  3.43; O27  3.93; C32  3.96; C33  4.02; C31
4.22; C33  4.24; C28  4.25; C31  4.31; O27  4.34;
  2  0.750-0.062 0.000            C32  3.42; O27  3.92; C32  4.00; C33  4.04; C33
4.20; C31  4.24; C28  4.26; C31  4.28; O27  4.38;
  3  0.222-0.055 0.157            C32  2.98; C33  3.01; O26  3.03; C16  3.36; N24
3.57; C25  3.78; C25  3.85; C31  3.97; O27  3.97;
  4  0.722-0.100 0.157            C25  2.93; O26  3.06; C33  3.15; N24  3.29; C15
3.41; O27  3.45; N17  3.60; C32  3.74; C34  3.92;
  5  0.778-0.061 0.843            C32  2.98; O26  3.02; C33  3.02; C16  3.36; N24
3.58; C25  3.80; C25  3.83; C31  3.96; O27  3.98;
  6  0.278-0.099 0.843            C25  2.93; O26  3.06; C33  3.16; N24  3.29; C15
3.41; O27  3.45; N17  3.60; C32  3.74; C34  3.92;
  7  0.000 0.265 0.000            C29  2.98; C29  2.98; C34  3.14; C34  3.14; C31
3.26; C31  3.26; C30  3.30; C30  3.30; C30  3.42;
  8  0.500 0.765 0.000            C29  2.98; C29  2.98; C34  3.14; C34  3.14; C31
3.26; C31  3.26; C30  3.30; C30  3.30; C30  3.42;

 :: Note: use CALC VOID (not CALC SOLV) for Packing Index.
```

Figure S2: Hydrogen bonding helix along the [010] direction formed by ammonia and water molecules.

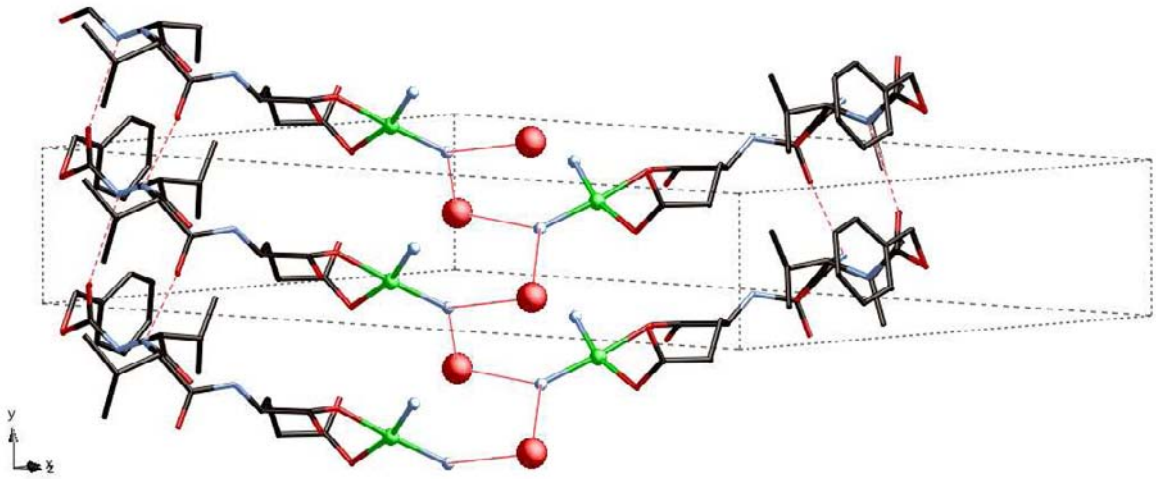

Conclusions - Outlook

The major research lines I followed during my PhD are based on the extensive use of small peptides or even single amino-acids as first steps to understand their role in inorganic materials templating. Small peptides, relying on weak forces like: hydrophobic interactions, π–π stacking, hydrogen bonding or metal-induced self assembly to self assemble; constitute an interesting starting point for the preparation of finely tuned functional materials.

In summary, these are the advances achieved during the scheme of this PhD:

- One of the most challenging project, besides the structural resolution of the MPF structure from powder diffractogramm, was to understand how single amino-acids can interfere with (bio)inspired iron oxide precipitation processes. Despite the simplicity of the system considered, we were able to determine first rules which constitute a beginning for more advanced experiments using more designed peptides.

- Transcription of nanostructures in inorganic materials was possible and opened the track for more complex and more interesting peptides. This shows the applicability of sol-gel processes for the preparation of inorganic materials from small peptides based organogels.

- The concept of mixing small functionalized peptides (i.e. a peptide with a functional part) and non-functionalized material (i.e. a structural part) to obtain more complex structures was successfully verified and applied to the synthesis of silver nano-objects. We demonstrate both a size and shape control on the nanoparticles thus created and have shown that even small peptides can be used to successfully template nanostructures.

- We have for the first time prepared a peptide-based MOF. This will open a new avenue for advanced materials with chiral structures and porosity in many fields.

The work realized during the Thesis timeframe and the successes observed lead to the following outlooks which I would follow:

- The preparation of metal-peptides frameworks is of prime interest because of the potential advances which may arise from this new approach. There is not only potential interest in material science, but these simple to prepare materials could be used as potential asymmetric catalysts or models for entactic systems and to summarize *to prepare simplified bio-catalysts, nanoscaled tools equivalents*.

- The *in-situ* generation of thiols from thioethers opens a clear and interesting direction to prepare *chiral chemically modified surfaces based on cysteine or methionine containing peptides.* Theses surfaces can be further functionalized with other peptides which will be adsorbed and (possibly) start to self assemble on the surface using β sheets (or other schemes). As these peptides could be functionalized, these surfaces will be reactive and they may constitute the start of a new subfield in *bio-inspired surfaces* for the creation of bio-inspired materials.

- As we demonstrated that the large scale synthesis of non-functionalized (and in some extend of simply functionalized) peptides was possible, the last point which uses the technology developed in the group is based on electrospinning of the *non-functionalized* peptide in the presence of a given amount of *functionalized* peptide. This would lead to the preparation of solvent-free, functionalized fibbers which could be used as templates for inorganic materials growth in a (bio)inspired approach.

These points are only the starting elements for a more extensive study scheme. Finishing these studies will lead to the setting of a relatively new platform based on small self assembling peptides either functionalized or not.

Curriculum Vitae & Collaboration list

Alexandre MANTION
36 Rue Charles de Gaulle
F-68550 SAINT-AMARIN
Tel - Fax: +33 (0)3 89 38 75 50
email: a.mantion@unibas.ch

Date of Birth: 19/08/1977
French citizen

Education:

2004	**PhD student in Physical Chemistry** under the supervision of Prof Andreas Taubert	University of Basel Basel, Switzerland
2003	**Master of Science in Chemistry** *with distinction Passable*	Université de Haute-Alsace Mulhouse, France
2001	**Maitrise de Chimie Physique** (MSc equivalent) *with distinction Passable*	Université de Haute-Alsace Mulhouse, France
2000	**Licence de Chimie Physique** (BSc equivalent) *with distinction Assez Bien*	Université de Haute-Alsace Mulhouse, France
1998	**Brevet de Technicien Supérieur** (BTech in Chemistry)	Lycée Lavoisier Mulhouse, France
1996	**Baccalauréat S** (equivalent to A levels) majoring in Maths, Physics and Chemistry *with distinction Assez Bien*	Lycée Scheurer-Kestner Thann, France

Skills, competencies, and further information

Competences in Chemistry : Preparation of low molecular weight molecules (peptides and others) in solution or on solid phase, (peptide) self-assembly, powder X ray diffraction (PXRD), Rietveld analysis, structure determination from PXRD, metal nanoparticle preparation, sol-gel chemistry, iron oxide chemistry, Raman (incl. SERS)-, fluorescence-, UV-Vis-, AA-, IR (incl. PM-IRRAS) spectroscopy, SQUID, X-ray fluorescence, ICP, XPS, Thermogravimetric analysis, TEM, SEM, optical microscopy.

Computers : Microsoft Office and related software, Linux and Linux-based programs.

Teaching assistant : Laboratory course in first year analytical and general chemistry (in German), University of Basel/CH and University of Potsdam/D, since 2004

Collaborations : Organization of collaborations with other laboratories in Switzerland or abroad.

Memberships : Swiss Young Chemists, Swiss Chemical Society, German Chemical Society, and Swiss Society of Crystallography

Languages : French (mother tongue), English (good), German (good)

Award : travel stipend for the Frühjahrstagung from the German Chemical Society

Publications :

Papers

Ionic Liquid Crystal Precursors for Inorganic Particles: Phase Diagram and Thermal Properties of a CuCl Nanoplatelet Precursor.
Andreas Taubert, Pascal Steiner and Alexandre Mantion, *J. Phys. Chem. B*, *2005*, 109 (32), 15542 – 15547.

Concentration-induced TiO2 sphere-tube-fiber transition in oligovaline organogels
Alexandre Mantion and Andreas Taubert
Macromolecular Bioscience (Special Issue on Bioinspired Materials for the Chemical Industry), *2007*, 7, 208.

Amino acid-controlled iron oxide polymorph selection
Alexandre Mantion, Fabia Gozzo, Bernd Schmitt, Willem B. Stern, Yvonne Gerber, Adeline Y. Robin, Katharina M. Fromm, Monika Painsi, and Andreas Taubert
J. Phys. Chem. C, accepted with minor revisions

Silver nanoparticle growth controlled by modular oligovaline organogels
Alexandre Mantion, Annette Foelske, Laurent Mirolo, Katharina M. Fromm, Monika Painsi, and Andreas Taubert
Soft Matter, accepted with minor revisions

Metal-peptide frameworks (MPFs) – "bioinspired" metal organic frameworks
Alexandre Mantion*, Cornelia Palivan, Pierre Rabu, Lars Massuger, Lynne MacCusker and Andreas Taubert*
J. Am. Chem. Soc., in press

Oral communications

X-Ray Diffraction and Raman Microscopy: Complementary Tools for Iron Oxide Biomineralization studies Alexandre Mantion, Andreas Taubert
Scholarship from The German Chemical Society obtained to present this talk
GDCh JCF Frühjahrsymposium 2005
07-09/04/05 Humboldt-Universität zu Berlin, Institut für Chemie, Berlin/D

Amino acids: Bioinspired templating agent for iron oxyde and hydroxide templating
Alexandre Mantion, Andreas Taubert
SFC Eurochem 2005
28-1/08/05, Nancy/F

Bioinspired iron oxide synthesis
Alexandre Mantion, Andreas Taubert
European Congress of Young Chemists, Youngchem 2005
12-16/10/05 Rydzyna/PL

Peptide-based low molecular weight organogelators and their transcription in inorganic materials
Alexandre Mantion, Andreas Taubert
EMPA PhD Day 2006
19/10/06 St Gallen/CH

Posters

From rust to magnet: Nature triggers structures of iron oxide
Alexandre Mantion, Andreas Taubert
Informal Discussion Workshop "Growth Control"
09-10/09/04 Faculté Science et Techniques, Mulhouse/F

Bioinspired Iron Oxide Synthesis
Alexandre Mantion, Andreas Taubert
NRP 47 Summer school - 11-15/04/05 Löwenberg center, Murten/CH

Self assembling peptides as new inorganic materials templates
Alexandre Mantion, Andreas Taubert
BASF Symposium on Bioinspired Materials - 07-08/08/06 Strasbourg/F

A simple model for iron oxide biomineralization - synchrotron X-ray scattering analysis of iron oxide precipitated in the presence of amino acids
Alexandre Mantion, Andreas Taubert
7th Swiss Light Source Users' Meeting - 28-29/09/06 Paul Scherrer Institute, Villingen/CH

Self assembling small peptides and their use to prepare new materials
Alexandre Mantion, Andreas Taubert
Swiss Chemical Society - Fall Meeting - 13/10/2006 Irchel Campus, Zurich/CH

Work experience

Worker in Logistic Department
TFL France, Huningue/F (July/August 1999, 2001, and 2003)
Société Chimique Roche, Village-Neuf/F (August 1997)

Worker in Production Department
Ciba Specialty Chemicals, Huningue/F (July/August 1998)

Technician in Quality Control Department
Albemarle PPC, Thann/F (July/August 2000)

Technician in Drug Discovery
Organic Synthesis Department, Actelion Pharmaceuticals, Allschwil/CH (one year: 2001/2002)

Personal interests and activities:

Volunteering : tutoring students in library works, secretary works
Leisure activities : do-it-yourself job, newspapers, tactical PC games, digital photography, mineralogy

Collaborations

Name	Location	Objectives	Started by
Dr Conception Domingo	Instituto de Estructura de la Materia, CSIC - Madrid, Spain	Raman Microscopy	AT
Prof. Dr. Larry Diamond	Institute for Geology, University of Bern - Bern, Switzerland	Raman Microscopy, SERS	AM
Dr Annette Foelske	Paul Scherrer Institute - Villigen, Switzerland	XPS	AM
Prof. Dr. Katharina Fromm	Institute for Chemistry, University of Fribourg - Fribourg, Switzerland	Powder X-Ray diffraction	AM/AT
MS-X04 Beamline scientists	Paul Scherrer Institute - Villigen, Switzerland	Powder X-Ray diffraction	AT
Lars Massüger and Dr Lynne McCusker	Laboratory for cristallography, ETH Zurich - Zurich, Switzerland	Powder X-Ray diffraction	AM
Dr Holger Frauenrath	Department of Materials Polymer Chemistry, ETH Zürich - Zurich, Switzerland	Sol-gel chemistry	AT
Dr Pierre Rabu	IPCMS - GMI - Strasbourg, France	Magnetic measurements	AM
Dr Pierre Rabu	IPCMS - GMI - Strasbourg, France	Material preparation	AT + AM for some sections
Prof Dr Edwin Constable Prof Dr Catherine Housecroft	Department of Chemistry, University of Basel - Basel, Switzerland	Various analytical techniques	AM/AT
Dr Ovidiu Ersen	IPCMS - GSI - Strasbourg, France	TEM tomography	AM
Prof Dr Thomas Bürgi	Institut de Microtechnique, University of Neuchâtel - Neuchâtel, Switzerland	PM-IRRAS	AM
Prof. Dr Willem-B. Stern Yvonne Gerber	Institute of Mineralogy and Petrography, University of Basel - Basel, Switzerland	Powder X-Ray diffraction XRF	AM/AT

AT: opened by Prof. Andreas Taubert - AM: opened by Alexandre Mantion
AM/AT : opened by Prof Andreas Taubert - continued by Alexandre Mantion on new projects

Dozenten involved in my Doctoral formation.

Prof Dr Katharina Fromm
Prof Dr Catherine Housecroft
Prof Dr Edwin Constable
Prof Dr Michael Oehme
Dr. Herrmann

Appendix 1 Ionic liquid crystal precursors for inorganic particles: phase diagram and thermal properties of a CuCl nanoplatelet precursor

Andreas Taubert,* Pascal Steiner, and Alexandre Mantion

Accepted as a paper in *J. Chem. Phys. B*

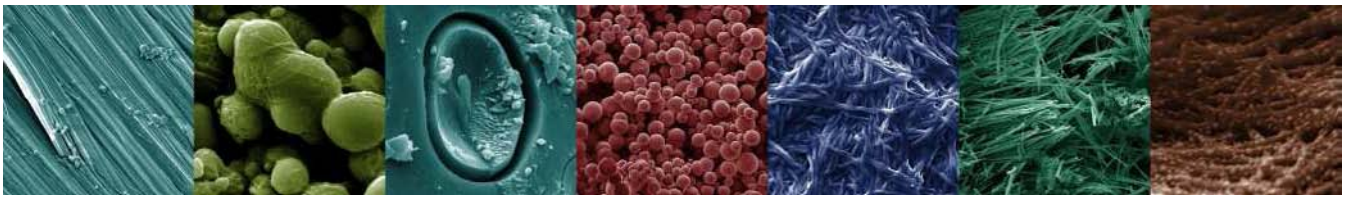

Appendix-1.1 Introduction

Ionic liquids (ILs) have been widely promoted as green and efficient solvents for many reactions in organic chemistry, for electrochemical applications, or for industrial extraction problems.[1] Ionic liquid crystals (ILCs), i.e. ionic liquids with a long range order, have also been studied in some detail by Neve et al.,[2-6] Lee et al.,[7] Seddon et al.,[8-12] and a few other groups.[13-16] For a recent review about the structural organization in ionic liquids see also ref.[17]

More recently, ILs have also been investigated by the (inorganic) materials community because ILs can easily be tuned to interact with various surfaces and chemical environments. Inorganic materials chemistry has mainly focused on the fabrication and stabilization of ordered metal oxides[18-22] or metal, metal alloy, metal oxide, and metal sulfide nanoparticles.[23-33] These developments have recently also been reviewed.[34]

Combining ILCs and inorganic materials chemistry, we have recently reported the formation of an ILC from a 50/50 (wt/wt) mixture of bis(dodecyl pyridinium) tetrachlorocuprate 1 and 6-O-palmitoyl ascorbic acid 2, Scheme 1.[35] We have suggested from the analysis of the optical micrographs and from interpolation of the self-assembly behavior of the individual components 1 and 2 that the mixture forms a layered LC. Furthermore, this so-called ionic liquid crystal precursor (ILCP) templates the formation of CuCl nanoplatelets at elevated temperatures, which further supports the claim of a layered ILCP.

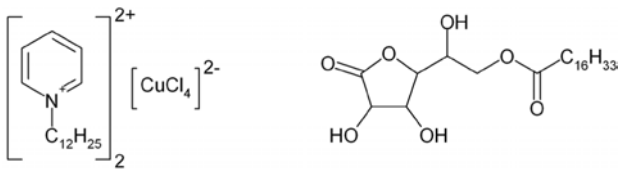

1 2

Scheme 1: Bis(dodecyl pyridinium) tetrachlorocuprate 1 and 6-O-palmitoyl ascorbic acid 2.

Here we present a detailed study on the structure and reactivity of these ILCPs. Specifically, we use an improved method to fabricate the mixtures of 1 and 2 and report on the full phase diagram and the thermal behavior of the ILCPs.

Appendix-1.2 Experimental Section

Compound 1 was obtained as described previously,[35] but we have increased the reaction time from 10 to 60 minutes. 6-O-palmitoyl ascorbic acid 2 was obtained from Fluka and used without further purification. Instead of mechanically mixing the two components to obtain the ILCP, 1 and 2 were dissolved in THF, the THF was removed by rotary evaporation, and the resulting dark brownish to light yellow materials were dried under vacuum overnight. The samples obtained with this procedure are more homogeneous than those employed in our previous study. Solutions of 1 and 2 in THF are stable without any visible precipitation for up to 5 months. Thereafter, a green precipitate forms. In the remainder of the text, samples are labeled Cu###, where ### is the weight fraction of 1 in the respective mixture. Cu000 thus designates pure 2, Cu020 is a 20/80 (wt/wt) mixture of 1 and 2, etc.

Optical polarization microscopy (OPM) experiments were made on a Leica DM-RP microscope with a hotstage. DSC experiments were made on a Perkin-Elmer DSC 6 calibrated with indium. Typically, measurements were done from –5 to 200 ºC with a heating rate of 10 ºC/min. Samples were held at –5 ºC for 120 minutes before the first and 15 minutes before the second heating cycle. Reaction enthalpies were calculated by using an apparent molecular weight of the mixture of 1 and 2 computed from the molecular weights (702.2 and 430.6 g/mol, respectively) and the weight fractions of the two components in each mixture. Activation energies for CuCl formation were determined via the Kissinger peak method[36] with heating rates of 5, 10, 20, and 30 ºC/min. Measurements were done with Cu050; repeat measurements showed that the peak temperature T_p is reproducible to ± 2 ºC and in most cases to ± 1 ºC. Thermogravimetric analysis (TGA) was done with a Mettler Toledo TGA/SDTA 851e from 25 to 300 ºC with a heating rate of 10 ºC/min in N_2. Estimations of the molecular dimensions were done with ChemOffice Chem3D.

X-ray scattering experiments were done at the powder diffraction station of the Swiss Light Source´s (Paul Scherrer Institute, Villigen) materials science beamline X04SA equipped with the new MYTHEN microstrip detector.[37] For scattering experiments, samples were mounted on 1 mm mark tubes (Hilgendorf) and measured at room temperature while rotating the sample. Beam energy was 17.5 keV and the X-ray wavelength λ was 0.708 Å. Typical measurement times were ten or twenty seconds. Further low angle X-ray experiments were done on a Siemens D5000 using CuK_{α} radiation (λ = 1.5408 Å).

Appendix-1.3 Results and Discussion

Pure Components. Figure 1 shows OPM images and DSC traces of 1, 2, and of the ligand dodecyl pyridinium chloride. 1 melts at 50 to 53 ºC and has a liquid crystal-isotropic (LC-iso) transition at 74 to 76 ºC. Despite the different sample preparation procedure, the melting point and the LC-iso transition temperature are consistent with literature,[3-5] but deviate somewhat from our earlier melting point of 66 – 70 ºC.[35] We explain this with the improved sample preparation, where we have allowed for a longer reaction time.

2 melts at 113 to 116 ºC and the liquid crystal (LC) observed above the melting temperature has a clear point at 160 ºC in the OPM. Correspondingly, DSC shows an endothermic peak (ΔH = 0.8 kJ/mol) at 160 ºC. This is to the best knowledge of the authors the first report on a thermotropic LC from an ascorbic acid derivative, but lyotropic phases have been described.[38]

The pure ligand dodecyl pyridinium chloride melts at 60 to 65 ºC. DSC of the ligand also shows endothermic peaks at 118 ºC (ΔH = 0.5 kJ/mol) and 150 ºC (ΔH = 1.3 kJ/mol), which indicates a crystalline – LC1 – LC2 – isotropic transition, where the transition temperatures are 65, 118, and 150 ºC, respectively. OPM images support this interpretation as they show an LC texture between 65 and 117–120 ºC. We currently assign the texture to a smectic liquid crystal. Above 120 ºC, the mixture is isotropic in OPM; we may thus infer that LC2, which is detected in the DSC, has another, non-birefringent, symmetry.

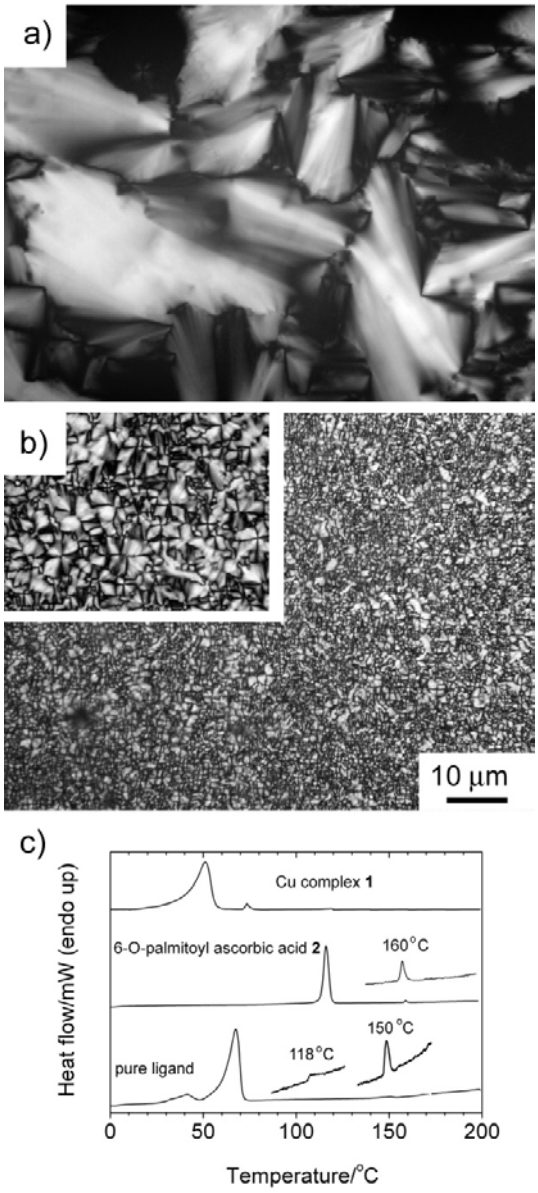

Figure 1: a) Optical micrograph (crossed polarizers) of the ligand dodecyl pyridinium chloride at 110 ºC. b) Optical micrograph (crossed polarizers) of pure 2 at 134 ºC; the scale bar applies to a) and b). Inset: magnified view of the texture of 2. c) DSC first heating trace of 1, 2, and dodecyl pyridinium chloride. Insets show the endothermic peaks associated with the further transitions mentioned in the text.

ILCPs. We will now focus on the mixtures of 1 and 2, i.e. the ILCPs. They are light yellow at low weight fractions of the Cu complex 1 and become increasingly dark yellow to brown on increasing concentration of 1. Cu010, Cu020, Cu030, Cu080, and Cu090 have a

wax-like appearance and easily break into smaller pieces. The other mixtures are honeylike and flow under the pressure of a spatulum.

Phase Diagram. Figures 2a to 2d are representative OPM images of various ILCPs. At 20 ºC and below, only Cu 040, Cu050, Cu060, and Cu070 exhibit an LC texture and the other samples appear crystalline in the OPM. Above ca. 30 ºC all ILCPs exhibit a single LC texture up to the clear point. This is similar to pure 1 where only one LC is observed.[3,4] We currently assign our textures to smectic LCs, even though often they are not very characteristic and even though pure 1 is columnar.[3] Our assignment is however supported by X-ray scattering (see Figure 4 below). Furthermore, bis(*hexa*decylpyridinium) tetrachlorocuprate, i.e. the C_{16} analog of 1 with the same alkyl tail length as 2, exhibits a SmA phase.[3]

DSC of the ILCPs reveals a broad endothermic phase transition from ca. 5 up to 40 ºC, see Figure 2e. We assign this transition to the crystalline – Sm transition observed in the OPM. DSC thus confirms the presence of a broad crystalline – Sm phase transition just around room temperature.

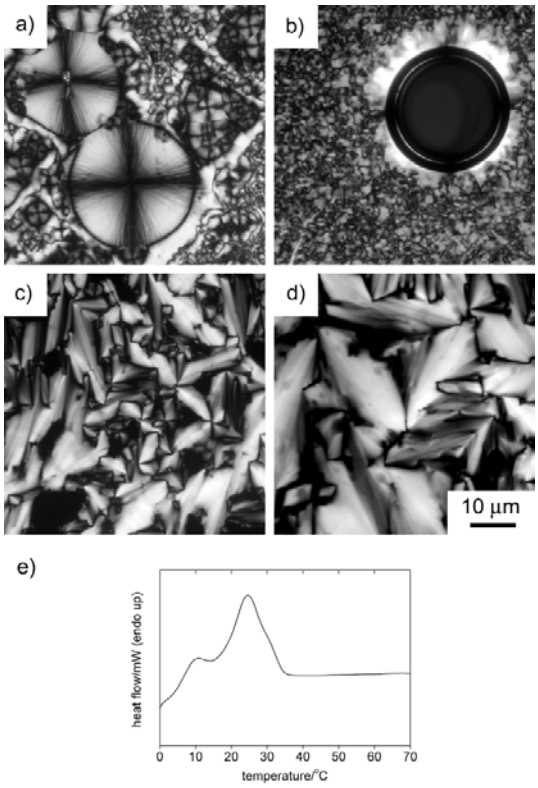

Figure 2: Representative optical micrographs (crossed polarizers) of a) pure 2 at room temperature after slow cooling from 150 ºC, b) Cu050 at 85 ºC on first heating, c) Cu060 at 69 ºC on rapid cooling from the isotropic melt, d) Cu070 on rapid cooling from the isotropic melt at 60 ºC. The scale bar applies to all images. e) DSC peak of the melting transition of Cu050 showing that the transition is broad.

Figure 3 is the ILCP phase diagram obtained from OPM and DSC. All ILCPs exhibit a crystalline – Sm – isotropic transition and the LC region is largest (up to 90 ºC) at weight fractions of 1 between 0.3 and 0.7. The error bars correspond to the breadth of the transition observed in the DSC; they show that some of the transitions are broad, which makes them difficult to observe in the OPM. This applies in particular to the crystal – LC transition, whereas the LC – iso transition is clearly visible in the OPM.

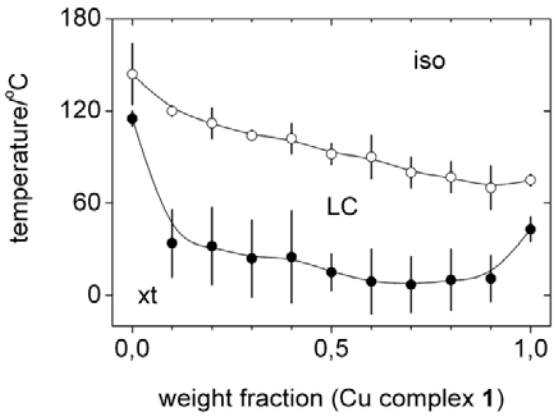

Figure 3: Phase diagram of ILCPs of 1 and 2 obtained from OPM and DSC. Xt: crystalline region, LC: liquid crystalline region, iso: isotropic region (dark in the OPM). The error bars give the width of the observed transition, i.e. the range between the onset and the upper end of the corresponding DSC peak (see Figure 2e for a typical melting peak width).

Structure of the ILCP. Figure 5 shows the X-ray patterns of Cu050 and Cu090. Cu090 is representative of samples at either end of the phase diagram, Cu050 for ILCPs at the center of the phase diagram. The pattern of Cu050 exhibits two reflections at 2.67 and 5.29 degrees 2θ, which we assign to the 100 and 200 reflection of a layered LC with a spacing of 33.1 Å.

However, even with a fully extended C_{16} chain, **2** (the longest molecule in the system) is only 28.7 Å long, which is 4.4 Å shorter than the long period of the LC of 33.1 Å. This discrepancy can be accounted for in different ways: (i) if the $CuCl_4^{2-}$ counterion is loosely bound in the LC, the layer spacing could be larger than the calculated molecular length of the longest component. However, 4.4 Å is a large difference between observed and calculated spacings. It is thus more likely that (ii) **1** and **2** form a mixed tilted bilayer with a layer spacing of 33.1 Å. This assumption is supported by Chem3D measurements showing that an untilted bilayer of 2 is 37 to 38 Å thick, which is ca. 5 Å thicker than the X-ray thickness (see supporting information). The most straightforward way to obtain a layered structure with a spacing of 33.1 Å would thus be tilting.

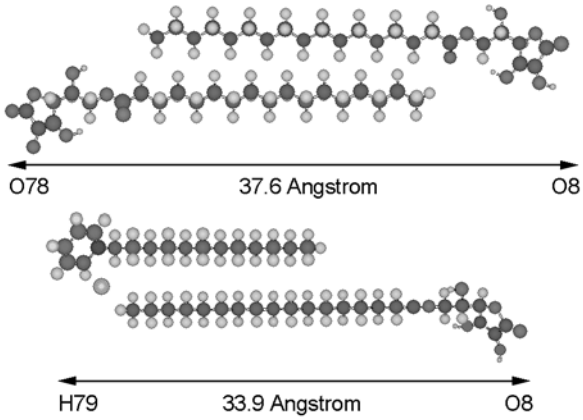

Figure 4: Calculated (Chem3D) bilayer of 2 (top) and a mixed bilayer of the pure ligand dodecylpyridinium chloride and 2 (bottom). In the top image the molecules are arranged such that the carbonyl group marks the beginning of the bilayer and the alkyl tails effectively overlap over the whole length. This is a very compact configuration, but other geometries with partial interpenetration (and hence a larger long period) are also possible.

Besides the low angle reflection, the pattern of Cu050 shows a broad hump at ca. 10 degrees 2θ, which we assign to the liquid-like alkyl tails of **1** and **2**. The pattern also shows a few reflections that we cannot assign to an LC phase; we assign them to the fact that these samples are still partly crystalline at room temperature. This is consistent with OPM and DSC, which also show that the crystalline-LC phase transition occurs over a rather broad temperature range between 5 and ca. 40 ºC, see Figure 2e.

Unlike ILCPs from the center of the phase diagram, ILCPs with either low or high weight fractions of **1** (Cu010, Cu020, Cu030, Cu080, Cu090) exhibit X-ray patterns with many reflections but with a much less intense hump around 10 degrees. This clearly indicates that these materials are predominantly crystalline. As we have not been able to obtain either single crystals or a calculated structure of the mixed systems, the detailed structure of the crystalline phase is still undetermined.

Overall however, X-ray supports OPM data presented above. X-ray shows that the samples from the center of the phase diagram are predominantly, but not completely, liquid

crystalline at room temperature, but samples from either end of the phase diagram are crystalline. X-ray also confirms the assignment of a layered LC phase.

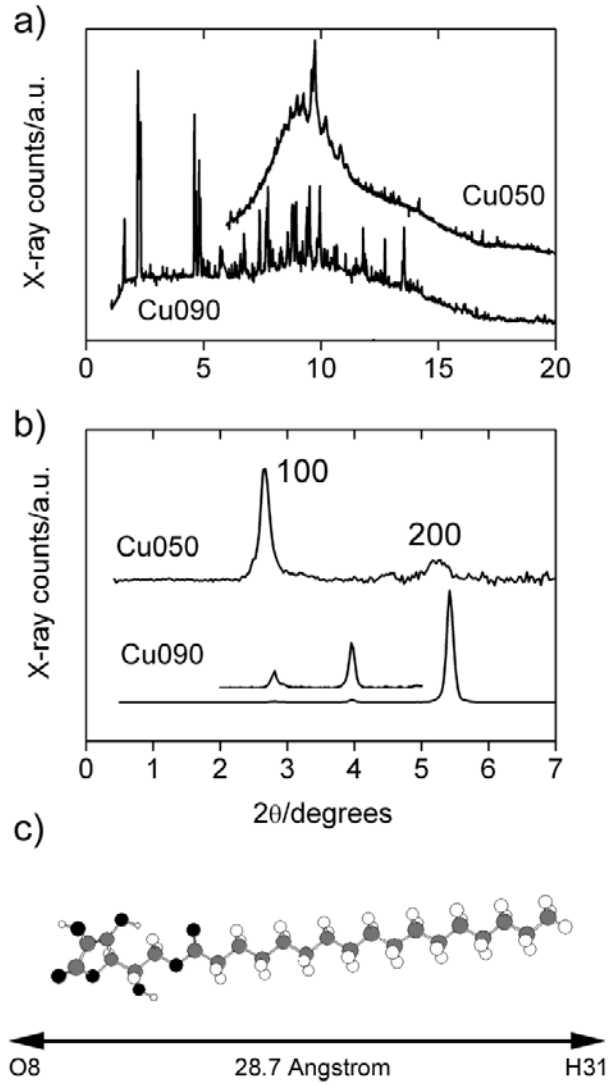

Figure 5: a) Representative synchrotron (λ = 0.708 Å) X-ray patterns of Cu090 and Cu050 at room temperature. The lower end of the Cu050 pattern has been cut for clarity. b) Low angle pattern of Cu050 and Cu090. These patterns were acquired with CuK_α radiation (λ = 1.5408 Å) and the signals are thus shifted with respect to the reflections observed in the above pattern. c) Calculated structure of 2 with a fully extended C_{16} chain. White: hydrogen, gray: carbon, black: oxygen.

The ILCPs are difficult to investigate because they not only exhibit mesomorphism. They are also reactive matrices for CuCl formation.[35] Unlike conventional LCs, we cannot anneal the ILCPs below the LC – isotropic transition temperature to obtain characteristic textures, because heating to over ca. 50 ºC induces CuCl formation. In fact, continued heating destroys the mesophase and crystals become visible in the optical microscope (data not shown). Figure 3 and 4 thus refer to an *unreacted* mixture**.**

Thermal properties. Figure 5 shows a DSC trace of Cu050. Like all other samples, Cu050 exhibits a broad endotherm from 5 to ca. 40 ºC (the melting peak) and a broad exotherm between ca. 70 and 175 ºC (due to the formation of CuCl particles) on first heating. The peak temperature T_p of the exothermic peak lies between 120 and 130 ºC. Only in Cu090 T_p is at 155 ºC.

In addition to the endothermic peak at around room temperature, Cu010 and Cu020 show three endothermic peaks between 55 and 110 ºC on first heating, see the inset in Figure 5. The first peak is sharp and centered around 60 ºC, the second peak is broad and centered around 75 ºC, and the last peak is at ca. 100 ºC and much less intense. On second heating all samples exhibit a sharp endothermic peak between 55 and 65 ºC. Finally, Cu050 and Cu060 exhibit a weak exothermic peak at ca. 100 to 110 ºC also on second heating.

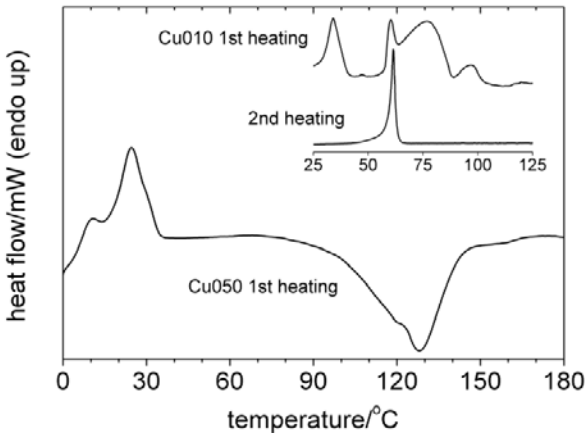

Figure 6: Representative first heating curve of Cu050. The DSC traces exhibit a broad peak from ca. 5 up to 40 ºC and a broad exothermic peak between ca. 70 and 170 ºC. The inset

shows the additional endothermic peaks observed in Cu010 and Cu020 on first heating and a typical second heating curve; both are from Cu010.

We have performed DSC experiments with mixtures of **2** and the pure ligand, i.e. in the *absence* of a reactive Cu(II) center, to elucidate the origin of the various additional peaks in the thermograms of Cu010 and Cu020. Figure 7 shows that mixtures of the pure ligand dodecyl pyridinium chloride and **2** often exhibit a double peak on both first and second heating. By comparison with the data from Figure 1, we assign the smaller peak at 55 ºC to the melting of some dodecyl pyridinium chloride. We do not observe a melting peak due to pure **2** (113 – 116 ºC) and we assign the more intense peak at ca. 75 ºC to the melting transition of the mixture of **2** and the ligand. The samples are thus quite homogeneous because only a minor fraction of one compound (the ligand) shows an individual melting transition. More importantly, the mixture melts at a temperature similar to where the sharp peak on second heating is observed in the Cu-containing ILCPs, see the inset in Figure 6.

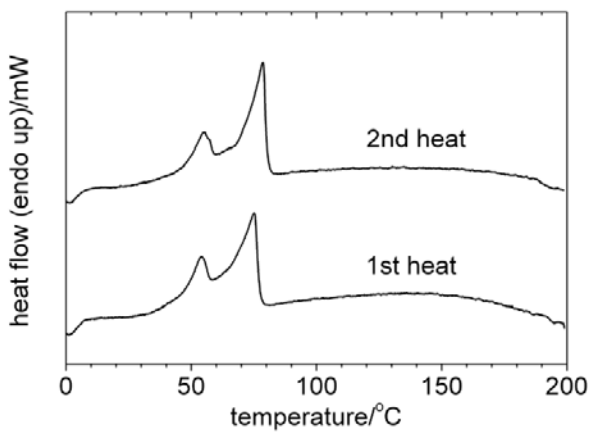

Figure 7: DSC traces of a 1:2 (wt/wt) mixture of **2** and dodecyl pyridinium chloride.

Figure 8 shows that the melting temperature of the mixtures of 2 and dodecyl pyridinium chloride (i.e. the peak position of the more intense peak in Figure 7) only weakly depends on the mixing ratio. For example, the addition of 20 wt% of dodecyl pyridinium chloride (the pure ligand) to **2** reduces T_{melt} to 65 ºC. Higher weight fractions of ligand do not dramatically alter this temperature, as all melting temperatures of the mixtures are between 60

and 75 ºC. This further supports the interpretation that the peak observed in the DSC of the ILCPs on second heating is due to a mixture of ligand and (oxidized) **2**.

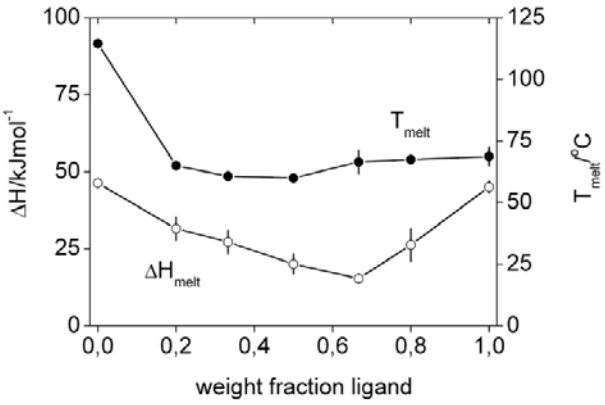

Figure 8: Mean melting temperatures (T_{melt}) and mean ΔH_{melt} values of various mixtures of pure ligand and **2**. Values and errors were determined from the most intense peak (see Figure 7) and by averaging data from three measurements.

By combination of the data above, we now propose an explanation for the additional peaks observed in the DSC curves of Cu010 and 020 and for the sharp peak observed in all samples on second heating. On first heating, the sharp peak observed at 55 – 65 ºC in the thermograms of Cu010 and Cu020 can be assigned to the melting of the pure ligand dodecyl pyridinium chloride by comparison to figure 1. The broad peak around 75 ºC is most likely due to a mixture of **2** and the pure ligand, i.e. without copper, see Figures 7 and 8. We can rule out the possibility that the latter peak arises from the LC-iso transition in pure **1** (73-75 ºC) because ΔH is far too large for an LC-iso transition. The peak at ca. 100 ºC could be from some free crystals of **2**. If this, currently rather speculative, assignment is correct, the crystals are probably small because the melting temperature is ca. 10 ºC lower than in bulk **2**.

Finally, the sharp peak observed on second heating in all samples is caused by a mixture of free ligand (released from **1** on CuCl formation) and (oxidized) **2**. This mixture melts at 55 – 65 ºC, i.e. the location of the sharp peak in the traces of Cu010 and Cu020 and in all DSC second heating traces.

The presence of free ligand in the ILCPs suggests that during sample preparation from THF some ligands are released from **1**. This could imply a disproportionation reaction leading to dodecyl pyridinium chloride and a dodecylpyridinium-$CuCl_3^-$ complex. Possibly, the ascorbic acid head groups of ***2*** interact with the disproportionation complex and lead to a (dodecylpyridinium-$CuCl_3^-$)(2) adduct. If this is indeed the case, we may postulate that such centers could act as the nucleation sites for CuCl precipitation, as here the reducing agent is already in close contact with a Cu(II) ion. This hypothesis is currently being verified with EPR, IR, UV, and solid-state NMR.

Figure 9 shows ΔH values for the melting (ΔH_{endo}) and exothermic (ΔH_{exo}) transitions as a function of ILCP composition. ΔH_{endo} decreases from 45 to 4 kJ/mol with increasing weight fractions of 1 on first heating. On second heating, the ΔH_{endo} values (in this case from the sharp peaks at 55 to 65 ºC) show the same trend and range from 88 to 15 kJ/mol. The values are roughly comparable to bis(*hexa*decylpyridinium) tetrachlorocuprate (ΔH_{melt} = 51.7 kJ/mol) and to **1** (ΔH_{melt} = 29.3 kJ/mol),[3] but they span a much larger window. For comparison, Figure 8 also shows that the melting enthalpies of the mixtures of pure ligand and 2 decrease up to a ligand weight fraction of 0.66 after which they increase again to approximately 45 kJ/mol for the free ligand, i.e. they are comparable to the ILCPs.

Unlike the approximately linear behavior of ΔH_{endo}, ΔH_{exo} values have a minimum at Cu050 and Cu070 on first heating. ΔH_{exo} of Cu060 is reproducibly higher than either one of the latter values on first heating. On second heating, only Cu050 and Cu060 exhibit a measurable and reproducible exothermic peak. The *sum* of the measured exothermic signals from the first and second heating has only one minimum of –151 kJ/mol at Cu050. An ILCP with a molar ratio of 1:1 contains 62 wt% of **1** and one would thus expect the largest reaction enthalpy in Cu060. However, as the error bars are relatively large around Cu050, the difference is likely within the experimental error.

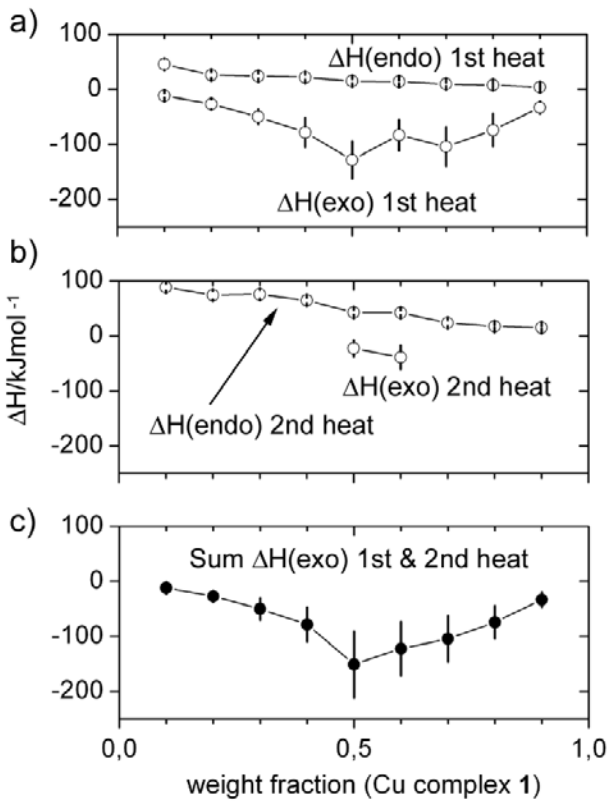

Figure 9: a) ΔH values for ILCPs on first heating. b) ΔH values for ILCPs on second heating. c) Sum of ΔH_{exo} values for ILCPs on first and second heating.

From DSC it is also possible to estimate the activation energy E_a of CuCl formation. Because the exothermic peaks are broad and the onset of the exothermic peak is poorly defined, we have used the quite simple Kissinger peak method,[36] even though there are more advanced approaches for the determination of E_a available.[39,40] In the Kissinger method, the peak temperatures T_p of the exothermic peak are determined at different heating rates β. A plot of $1/T_p$ vs. $\ln(T_p^2/\beta)$ is linear and the slope of the linear regression gives E_a/R (R = 8.314 J/K*mol) from which the activation energy E_a is obtained.

Figure 10 shows the Kissinger plot of a fresh Cu050 and a sample that was aged for six weeks at room conditions. The activation energies are 190.8 kJ/mol for the fresh and 192.4 kJ/mol for the aged sample; they are comparable, which indicates that at ambient conditions the formation of CuCl is strongly inhibited and does not proceed even after extended storage

time. Other solid–solid transformations have activation energies between 30 and over 300 kJ/mol. For example the activation energy for the precipitation in copper-chromium alloys is ca. 120 kJ/mol in undeformed alloys[41] and a quasicrystalline-crystalline phase transition in Al_6CuMg_4 is ca. 260 kJ/mol.[42] While the activation energy obtained here is thus not exceedingly high, it certainly points to a cooperative effect,[40] i.e. the nucleation and growth of CuCl crystals within the ILCP.

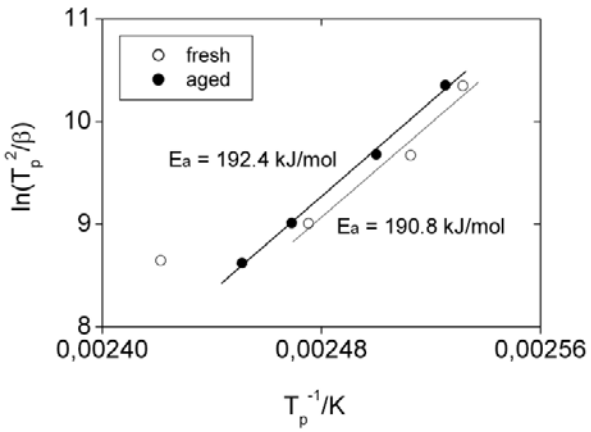

Figure 10: Kissinger plot obtained from averaging three measurements per heating rate of a freshly prepared Cu050 and a Cu050 aged for 6 weeks at room temperature and ambient pressure and humidity. The peak temperatures are reproducible to within ± 2 ºC and the error bars are thus smaller than the dot size. In the fresh sample, heating rates of 30 ºC/min and above could not be evaluated, as there T_p shows a nonlinear behavior (see for example the open circle on the far left). In the aged sample, heating rates of 40 ºC/min and more were not evaluated for the same reason.

Finally, we have evaluated the thermal stability of our samples using thermogravimetric analysis (TGA), Figure 11. All samples lose between 6 and 12 % of their original weight (presumably water) between 110 and 125 ºC and all samples lose 45 to 60 % of the original weight above ca. 180 ºC. The latter process is important because we have studied the samples up to 200 ºC in the DSC.

However, the sharp peak observed in the DSC on second heating (see inset in Figure 6) is not due to a decomposition product as DSC experiments with mixtures of dodecyl pyridinium chloride and 2 that were held at 150 ºC rule out this possibility. 150 ºC is below

the presumed decomposition temperature of 180 ºC and these mixtures do not contain a reactive Cu(II) ion. Nevertheless, these samples exhibit the same peak on second heating as the samples heated to 200 ºC.

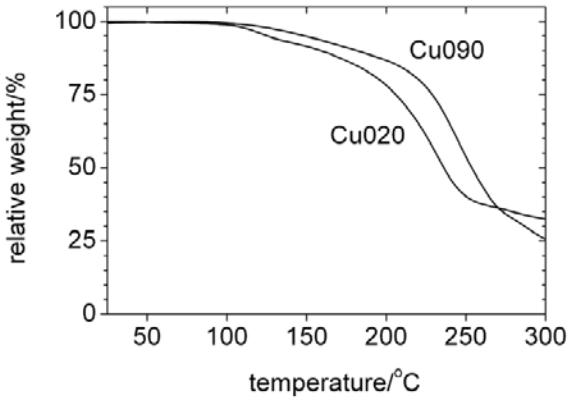

Figure 11: Representative TGA curves of Cu020 and Cu090.

Appendix-1.3 Conclusion

The current paper shows that not only Cu050, the original ILCP used for CuCl platelet formation,[35] exhibits mesomorphism, but that all ILCPs composed of **1** and **2** show the same general crystalline – smectic LC – isotropic phase behavior. The system is fairly complicated because thermal reduction of **1** by **2** leads to CuCl, oxidized forms of **2**, HCl, and Cl^-. As the reaction proceeds by heating the mixture, DSC measurements are not equilibrium measurements and the contributions of the reaction products vary as the reaction proceeds. These issues are currently being addressed by time-resolved in-situ high-temperature X-ray, solid state NMR, IR, and UV measurements as well as with ex situ mass spectrometry (MS) and GC-MS experiments.

However, our data show that the system is stable at ambient conditions and that the thermally induced formation of CuCl already occurs in a controlled manner at temperatures well below 100 ºC. As the ILCPs can be dissolved in THF, one may thus envision applications, where the ILCP is cast onto a surface, reacted at 50 to 80 ºC, yielding a (macro)porous CuCl network, which can be removed from the surface and used e.g. as a

heterogeneous catalyst. We currently explore these possibilities along with ILCPs with other symmetries that could lead to other morphologies of the final inorganic.

Appendix-1.4 Acknowledgement

The authors thank Prof. W. Meier (U. of Basel) and Dr. A.R. McGhie (U. of Pennsylvania) for useful discussions, Prof. W.B. Stern (U. of Basel) for access to the X-ray setup at the Earth Sciences Department, Prof. K. Fromm (U. of Basel) for access to her TGA, and Dr. F. Gozzo, Dr. B. Patterson, and Dr. B. Schmitt (Swiss Light Source, Villigen) for help with the synchrotron experiments. We also thank the Swiss National Science Foundation for financial support and A.T. acknowledges the Holcim Stiftung Wissen for a Habilitation Fellowship.

Appendix-1.5 References

[1] *Ionic liquids in synthesis*; Wiley-VCH: Weinheim, **2002**.

[2] Neve, F.; Crispini, A.; Armentano , S. *Chem. Mater.* **1998**, *10*, 1904.

[3] Neve, F.; Francescangeli, O.; Crispini, A.; Charmant, J. *Chem. Mater.* **2001**, *13*, 2032.

[4] Neve, F.; Francescangeli, O.; Crispini, A. *Inorg. Chim. Acta* **2002**, *338*, 51.

[5] Neve, F.; Imperor-Clerc, M. *Liq. Cryst.* **2004**, *31*, 907.

[6] Neve, F.; Francescangeli, O. *J. Cryst. Growth* **2005**, *5*, 163.

[7] Lee, C. K.; Peng, H. H.; Lin, I. J. B. *Chem. Mater.* **2004**, *16*, 530.

[8] Bowlas, C. J.; Bruce, D. W.; Seddon, K. R. *Chem. Commun.* **1996**, 1625.

[9] Gordon, C. M.; Holbrey, J. D.; Kennedy, A. R.; Seddon, K. R. *J. Mater. Chem.* **1998**, *8*, 2627.

[10] Holbrey, J. D.; Seddon, K. R. *J. Chem. Soc, Dalton Trans.* **1999**, 2133.

[11] Carmichael, A. J.; Hardacre, C.; Holbrey, J. D.; Nieuwenhuyzen, M.; Seddon, K. R. *Mol. Phys.* **2001**, *99*, 795.

[12] Hardacre, C.; Holbrey, J. D.; McCormac, P. B.; McMath, S. E. J.; Nieuwenhuyzen, M.; Seddon, K. R. *J. Mater. Chem.* **2001**, *11*, 346.

[13] Bowers, J.; Butts, C. P.; Martin, P. J.; Vergara-Gutierrez, M. C.; Heenan, R. K. *Langmuir* **2004**, *20*, 2191.

[14] Yoshio, M.; Mukai, T.; Ohno, H.; Kato, T. *J. Am. Chem. Soc.* **2004**, *126*, 994.

[15] Firestone, M. A.; Dzielawa, J. A.; Zapol, P.; Curtiss, L. A.; Seifert, S.; Dietz, M. L. *Langmuir* **2002**, *18*, 7258.

[16] Yoshio, M.; Mukai, T.; Kanie, K.; Yoshizawa, M.; Ohno, H.; Kato, T. *Chem. Lett.* **2002**, 320.

[17] Dupont, J. *J. Braz. Chem. Soc.* **2004**, *15*, 341.

[18] Nakashima, T.; Kimizuka, N. *J. Am. Chem. Soc.* **2003**, *125*, 6386.

[19] Zhou, Y.; Antonietti, M. *Adv. Mater.* **2003**, *15*, 1452.

[20] Zhou, Y.; Antonietti, M. *Chem. Commun.* **2003**, 2564.

[21] Zhou, Y.; Antonietti, M. *J. Am. Chem. Soc.* **2003**, *125*, 14960.

[22] Dai, S.; Ju, Y. H.; Gao, H. J.; Lin, J. S.; Pennycook, S. J.; Barnes, C. E. *Chem. Commun.* **2000**, 243.

[23] Dupont, J.; Fonseca, G. S.; Umpierre, A. P.; Fichtner, P. F. P.; Teixeira, S. R. *J. Am. Chem. Soc.* **2002**, *124*, 4228.

[24] Desmukh, R. R.; Rajagopal, R.; Srinivasan, K. V. *Chem. Commun.* **2001**, 1544.

[25] Swatloski, R. P.; Spear, S. K.; Holbrey, J. D.; Rogers, R. D. *J. Am. Chem. Soc.* **2002**, *124*, 4974.

[26] Fonseca, G. S.; Umpierre, A. P.; Fichtner, P. F. P.; Teixeira, S. R.; Dupont, J. *Chem. Eur. J.* **2003**, *9*, 3263.

[27] Scheeren, C. W.; Machado, G.; Dupont, J.; Fichtner, P. F. P.; Ribeiro Texeira, S. *Inorg. Chem.* **2003**, *42*, 4738.

[28] Rossi, L. M.; Dupont, J.; Machado, G.; Fichtner, P. F. P.; Radtke, C.; Baumvol, I. J. R.; Teixeira, S. R. *J, Braz. Chem. Soc.* **2004**, *15*, 904.

[29] Trewyn, B. G.; Whitman, C. M.; Lin, V. S.-Y. *Nano Lett.* **2004**, *4*, 2139.

[30] Yoo, K.; Choi, H.; Dionysiou, D. D. *Chem. Commun.* **2004**, 2000.

[31] Cassol, C. C.; Umpierrre, A. P.; Machado, G.; Wolke, S. I.; Dupont, J. *J. Am. Chem. Soc.* **2005**, *127*, 3298.

[32] Jiang, Y.; Zhu, Y.-J. *J. Phys. Chem B* **2005**, *109*, 4361.

[33] Wang, Y.; Yang, H. *J. Am. Chem. Soc.* **2005**, *127*, 5316.

[34] Antonietti, M.; Kuang, D.; Smarsly, B.; Zhou, Y. *Angew. Chem. Int. Ed.* **2004**, *43*, 4988.

[35] Taubert, A. *Angew. Chem. Int. Ed.* **2004**, *43*, 5380.

[36] Kissinger, H. E. *J. Res. Natl. Bur. Standards* **1956**, *57*, 217.

[37] Schmitt, B.; Brönnimann, C.; Eikenberrya, E. F.; Gozzo, F.; Hörmann, C.; Horisberger, C.; Patterson, B. *Nuclear Instruments and Methods in Physics Research A* **2003**, *501*, 267.

[38] Lo Nostro, P.; Ninham, B. W.; Fratoni, L.; Palma, S.; Hilario Manzo, R.; Allemandi, D.; Baglioni, P. *Langmuir* **2003**, *19*, 3222.

[39] Shanker Rao, T. L.; Lad, K. N.; Pratap, A. *J. Thermal Analysis and Calorimetry* **2004**, *78*, 769.

[40] Starink, M. J. *Thermochim. Acta* **2003**, *404*, 163.

[41] Szablewski, J.; Kuznicka, B. *Physica Status Solidi A* **1988**, *108*, K5

[42] Sanyal, M. K.; Sahni, V. C.; Dey, G. K.; Varshney, L. *Phys. Rev. B* **1987**, *36*, 2443.

Beantwortung der Frage: Was ist Aufklärung?

„Aufklärung ist der Ausgang des Menschen aus seiner selbst verschuldeten Unmündigkeit. Unmündigkeit ist das Unvermögen, sich seines Verstandes ohne Leitung eines andern zu bedienen. Selbst verschuldet ist diese Unmündigkeit, wenn die Ursache derselben nicht am Mangel des Verstandes, sondern der Entschließung und des Muthes liegt, sich seiner ohne Leitung eines andern zu bedienen. Sapere aude! Habe Muth, dich deines eigenen Verstandes zu bedienen! ist also der Wahlspruch der Aufklärung.

Faulheit und Feigheit sind die Ursachen, warum ein so großer Theil der Menschen, nachdem sie die Natur längst von fremder Leitung frei gesprochen (naturaliter majorennes), dennoch gerne Zeitlebens unmündig bleiben; und warum es Anderen so leicht wird, sich zu deren Vormündern aufzuwerfen. Es ist so bequem, unmündig zu seyn. Habe ich ein Buch, das für mich Verstand hat, einen Seelsorger, der für mich Gewissen hat, einen Arzt, der für mich die Diät beurtheilt, u. s. w, so brauche ich mich ja nicht selbst zu bemühen.

2ter Band. Xx

Immanuel Kant, Beantwortung der Frage: Was ist Aufklärung. Beginn des Traktats. (EA 1784). (Imanuel Kant's vermischte Schriften; Hrsg.: Johann Heinrich Tieftrunk; Bd. 2. Halle 1799)

"Aufklärung ist der Ausgang des Menschen aus seiner selbstverschuldeten Unmündigkeit. Unmündigkeit ist das Unvermögen, sich seines Verstandes ohne Leitung eines anderen zu bedienen. Selbstverschuldet ist diese Unmündigkeit, wenn die Ursache derselben nicht am Mangel des Verstandes, sondern der Entschließung und des Mutes liegt, sich seiner ohne Leitung eines andern zu bedienen. 'Sapere aude!' Habe Mut, dich deines eigenen Verstandes zu bedienen! ist also der Wahlspruch der Aufklärung.

Faulheit und Feigheit sind die Ursachen, warum ein so großer Teil der Menschen, nachdem sie die Natur längst von fremder Leitung freigesprochen, dennoch gerne zeitlebens unmündig bleiben; und warum es anderen so leicht wird, sich zu deren Vormündern aufzuwerfen. Es ist so bequem, unmündig zu sein. Habe ich ein Buch, das für mich Verstand hat, einen Seelsorger, der für mich Gewissen hat, einen Arzt, der für mich die Diät beurteilt usw., so brauche ich mich ja nicht selbst zu bemühen."

Fini d'imprimer en Novembre 2007 à Bâle, Suisse